SEISMIC BEHAVIOUR OF A SHEAR-CRITICAL REINFORCED CONCRETE FRAME: AN EXPERIMENTAL AND NUMERICAL INVESTIGATION

by

Kien Vinh Duong

A thesis submitted in conformity with the requirements

for the degree of Masters of Applied Science

Graduate Department of Civil Engineering

University of Toronto

ABSTRACT

Many reinforced concrete structures that were built 30 or 40 years ago were built without consideration for seismic design. As such, these buildings are of great concern because they failed (or may fail) in a catastrophic brittle shear manner. Unlike moment critical structures, shear-critical structures have not been well studied, and reliable analytical tools to accurately evaluate shear-critical buildings are scarce. A corroborative experimental and analytical investigation was carried out to study the behaviour of a shear-critical reinforced concrete frame under seismic loading. A single-span, two-storey, reinforced concrete frame with shear-critical beams was constructed. This frame was tested in a lateral reverse cyclic manner until severe shear damage took place, repaired with carbon fibre reinforced polymer (CFRP), and re-tested. The damage mode changed from shear to flexure after repair. In addition, great improvements were observed in the peak lateral load, ductility, maximum displacement, and energy dissipation. The experimental findings concluded that the strain limitations proposed by ISIS Canada on the CFRP were conservative. The frame was analyzed in a nonlinear finite element analysis software called VecTor2. Analytical results indicated that the frame behaviours such as load-displacement response, failure mode, and crack pattern were predicted well prior to repair, but poorly after repair.

ACKNOWLEDGEMENTS

The experimental portion of this thesis was challenging, labour intensive, but fun and rewarding at the same time. Building the formwork and assembling the steel cage could be compared to an orthodontist surgeon trying to install braces. The working space was very limited, but every detail had to be aligned precisely. The completion of this thesis could not be realized without the advice and help of many people.

I would like to express my sincere acknowledgement to my supervisors Professor Frank. J. Vecchio and Professor Shamim A. Sheikh for their guidance and knowledge. In addition, the advice of Professor Evan Bentz was invaluable. I would also like to thank the other Professors in the Structural Department who taught me over the past two years. Their teaching and knowledge made this experience much more fulfilling.

The assistant and expertise of the Stuctural Laboratory staff is recognized. Renzo Basset, John MacDonald, Joel Babbin, Giovanni Buzzeo, and Alan McClenaghan are acknowledged for their contributions to this project.

NSERC and ISIS Canada are recognized for their generous financial support. The Vector Construction Group and Fyfe Co. are recognized for their expert technical support.

Life is so much more enjoyable when the experiences are shared with others. I would like to thank the numerous graduate and undergraduate students who took part in this project, gave me advice, and made this experience satisfying. To David Ho, Karen Liu, Phillip Miller, and Selcuk Saatci, thank you for the great laughs and conversations in the VecTor office. To Michael Montgomery, Tarek Moukhtar, and Liping Xie, thank you for making homework dynamic and fun. To Ciyan Cui, Serhan Guner, Katrin Habel, Dan Laine, Adam Lubell, Nabil Mansour, Mohammed Semelawy, Ted Sherwood, and

Jimmy Susetyo, thank you for everything. To Saidal Akbari, Ryan Chan, Andy Chu, Jenny Lam, Vladimir Maleev, Danny Rosanova, Raymond Tam, Sylvio Tam, and Anson Yeun, I had the privilege to be both your TA and friend. You all showed up unexpectedly to brighten up the day.

Last but not least, I would like to thank my family for their support throughout these years. To my parents, grandmother, and aunts, thank you for your sacrifice in order to give me a chance at education. To my older sister and brother, we have great things to look forward to. Life has just begun!

"To infinity and beyond" Buzz Lightyear in Toy Story

TABLE OF CONTENTS

LIST OF TABLES

CHAPTER 3

CHAPTER 4

CHAPTER 5

CHAPTER 6

LIST OF FIGURES

CHAPTER 1

CHAPTER 2

CHAPTER 3

CHAPTER 4

NOTATION

a	depth of equivalent rectangular concrete stress block
A_c	area of concrete
A_{frp}	Cross-sectional area of CFRP
A_s	area of tensile longitudinal steel reinforcement
A_v	area of transverse steel reinforcement
b_w	Effective web width
C_c	internal force due to concrete compression
C_s	internal force due to steel compression
d	Distance from the extreme compression fibre to the centroid of the longitudinal tension reinforcement
d_v	Effective shear depth taken as 0.9d
E	elastic modulus of concrete
E_s	elastic modulus of steel
f'c	Specified compressive strength of concrete
F_{lt}	required tension force in the longitudinal steel reinforcement
f't	specified tensile strength
f’r	modulus of rupture strength
f_v	yield stress of stirrup
f_y	yield stress of steel reinforcement
h	height of beam
I	moment of inertia of cross-section
M_f	moment
M_r	moment resistance
N_f	axial load normal to cross-section
P	axial load normal to cross-section
s	stirrup spacing

S_{frp}	spacing of FRP wrap
T_s	internal force due to steel tension
V_c	shear strength of concrete
V_f	shear force
V_{frp}	shear strength of CFRP
V_r	shear resistance
V_s	shear resistance of reinforcement
X_1	top horizontal distance of Zurich grid
X_2	bottom horizontal distance of Zurich grid
XY_{+45}	positive diagonal distance of Zurich grid (Appendix B)
XY_{-45}	negative diagonal distance of Zurich grid (Appendix B)
Y_1	left vertical distance of Zurich grid
Y_2	right vertical distance of Zurich grid
β	factor accounting for shear resistance of cracked concrete
δ_{max}	maximum displacement (Appendix B)
δ_y	yield displacement determined from the tangent stiffness (Appendix B)
Δ_y	yield displacement determined from the cross-section
ε_{bot}	strain at the bottom of the CFRP wrap
ε_{frpe}	effective strain of FRP
ε_{mid}	strain at the middle of the CFRP wrap
ε_s	tensile strain in longitudinal steel reinforcement
ε_{top}	strain at the top of the CFRP wrap
ε_x	horizontal strain
ε_{x1}	longitudinal strain at mid-depth of the member
ε_y	vertical strain
γ	shear strain

μ_Δ	displacement ductility (δ_{max} / δ_y) (Appendix B)
θ	angle of crack inclination
θ_1	positive angle of shear deformation
θ_2	negative angle of shear deformation
ρ_x	longitudinal tensile steel reinforcement ratio
ρ_y	transverse steel reinforcement ratio

Introduction

1.1 BACKGROUND

Over the past few decades, structural engineers have taken great strides in our understanding of seismology and seismicity. This knowledge, combined with modern day practice, enables us not only to design buildings that can safely withstand earthquake loading, but also allows us the capability to design buildings that can remain in full operation during and after an earthquake. On the other hand, we have no such certainty regarding the stability of buildings built 30 or 40 years ago. Some buildings designed at that time failed (or will fail) in a catastrophic brittle manner, because ductility was not well understood. In contrast, the 2005 Canadian National Building Code lays out stringent seismic design guidelines that encompass a wide range of requirements, such as detailing requirements, ductility requirements, and detailed steps on the derivation of the earthquake demand. If buildings that were built several decades ago were assessed according to today's design code, many of them would be considered inadequate. Many such structures exist throughout the world and are still in use, but are they safe for occupancy?

Two common deficiencies in inadequate buildings relate to moment and shear. Reinforced concrete structures that are inadequate in moment have been well studied, and there exist numerous reliable analytical tools that can be used to evaluate the structural reliability of such buildings. On the other hand, reinforced concrete framed structures that are deficient in shear have not been well studied, and reliable analytical tools to accurately evaluate shear-critical buildings are scarce. This lag in shear research is directly correlated to the complex nature of predicting shear behaviour. Engineers have only recently developed the theoretical models to fully understand shear behaviour through principles such as the Compression Field (Collins 1978) and Modified Compression Field theories (Vecchio and Collins 1986).

Although we may not know when existing shear-critical buildings might fail, we do know how they will fail. Unlike moment-critical buildings where flexural failure is ductile, shear-critical failures are usually associated with much less forgiving brittle failure mechanisms. The potential danger of such failures is all too clearly demonstrated by many lives lost in the 1995 Kobe earthquake: a tragedy caused by the catastrophic shear failure of numerous buildings (NISEE 1997).

1.2 ANALYSIS OF STRUCTURES

In practice, reinforced concrete structures are typically designed based on linear elastic principles. Analysis procedures that follow these principles are generally plausible if the buildings are designed according to code. In other words, strength and serviceability requirements are met, joints are detailed correctly, rebar lengths are developed sufficiently, and failure modes are ductile. Buildings designed to code are usually conservative. The precise knowledge of their structural behaviour is not necessary, but rather these buildings are designed to withstand the load requirements safely. Alternatively, when inspected buildings are deemed to be deficient according to current standards, a more accurate structural analysis is required to reassess the capacity of these deficient buildings for safety. For these buildings, second-order effects such as material and geometric nonlinearities become prominent. These effects can influence the ultimate capacity and failure mode; therefore, a detailed structural analysis is required to account for these second-order effects. Such an analysis will not only be useful for evaluating the rehabilitation strategy, but also provide a predicted cracking pattern that can be used as a forensic tool to warn engineers of potential failure. The nonlinear response of reinforced concrete structures has to be developed to a sufficient level of confidence in order to assess the seismic behaviour of deficient buildings, and to implement repair strategies where needed.

Over the past 25 years at the University of Toronto (U of T), much effort has been focused towards improving and implementing nonlinear numerical analysis procedures

for reinforced concrete structures. Simple but realistic behaviour models from test data are implemented into analysis procedures and design formulations. These procedures and formulations are then applied to the design and assessment of real structures. VecTor2 is a nonlinear finite element program developed at U of T and was used in this thesis project (refer to Section 1.6). The conceptual basis behind VecTor2 is based on the Modified Compression Field Theory (MCFT).

1.3 MODIFIED COMPRESSION FIELD THEORY

The Modified Compression Field Theory was developed by Vecchio and Collins (1986). The constitutive relations behind the MCFT were derived from the experimental testing of thirty reinforced concrete panels subjected to pure shear or in combination of shear and axial loads. From these test results, equilibrium, compatibility, and stress-strain relationships were formulated in terms of average stresses and average strains. Equilibrium conditions ensure balance of the externally applied loads to the internal element forces; compatibility enforces agreement between deformation experienced by the concrete to an identical deformation to the reinforcement; and constitutive relationships relate average stresses to average strains for both cracked concrete and reinforcement.

The MCFT considers cracked reinforced concrete elements as an orthotropic material in which smeared cracks can fully rotate and freely re-orient. This theory also accounts for compression softening, which refers to the reduced concrete compressive strength in the presence of large transverse tensile strains. As well, tension stiffening is incorporated and this accounts for the tensile concrete stresses that exist between cracks. Local failure mechanisms are considered with yielding or fracture of reinforcement at crack locations, and sliding shear failure along cracks.

1.4 CEMENT PLANT TOWER IN EL SALVADOR, CENTRAL AMERICA

Cemento de El Salvador is a seven-storey cement tower located in the seismically active country of El Salvador, Central America. Although this reinforced concrete tower was built in the late 1990s, its design is typical of construction 30 or 40 years ago in this region and numerous other similar towers exist in other parts of the world. The main structural components of this tower consist of four exterior corner columns, which support seven sets of four exterior beams (one set per storey) (refer to Figure 1.1). Preliminary investigations concluded that this tower will behave critically in shear under seismic loading. Specifically, the beams on the narrow side, with a clear span-to-depth ratio of approximately 3.8, are the most vulnerable to shear failure. Other deficiencies that this cement tower exhibits are inadequate column splice and poor beam joint anchorage detailing. The characteristics of this cement tower served as the real-life example for this thesis investigation. For example, the tower's beam span-to-depth ratio, low percentage of beam shear reinforcement, concrete strength, and magnitude of column loading were mimicked, where possible, in this test experiment (refer to Chapter 3).

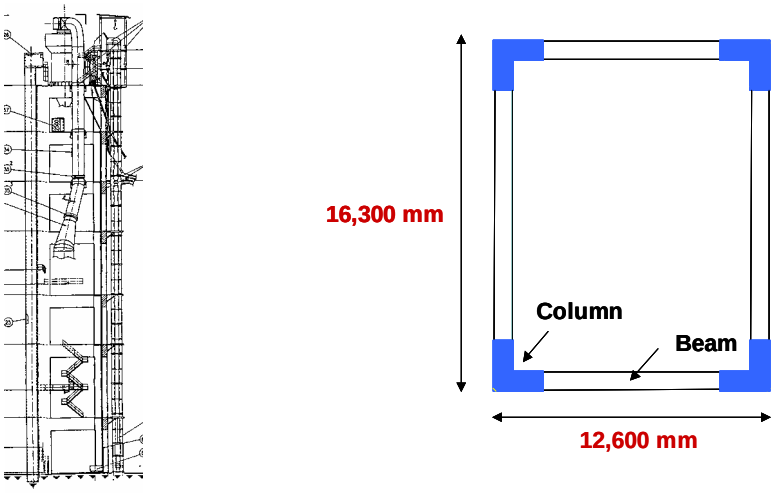

Narrow Elevation of Structure (80 m high) Floor Plan

Figure 1.1 Structural Layout of Cement Plant Tower

1.5 EXPERIMENTAL PROGRAM

An experimental investigation was undertaken to lend insight into the behaviour of shear-critical reinforced concrete frames under seismic loading. A single-span, two-storey, shear-critical reinforced concrete frame with a fixed base condition was constructed and tested. This two-third scaled frame (storey scale of a typical building) stood 4600 mm tall and 2300 mm wide. The beams and columns were 300 mm wide x 400 mm deep. A fixed base condition at the bottom was provided with a reinforced concrete base 800 mm wide, 400 mm thick, and 4100 mm long. The base was post-tensioned to the strong floor prior to testing. The beam clear span was 1500 mm, and the column clear storey height was 1700 mm. Typical beam and column sections contained 4 No.20 bars as top and bottom reinforcement, with US No.3 closed stirrups spaced at 300 mm in the beams and No.10 double closed hoops spaced at 130 mm in the columns. The base section contained 8 No.20 top and bottom bars, with No.10 triple closed hoops spaced at 175 mm. The frame was tested under quasi-static loading (push-over analysis), then repaired with carbon fibre reinforced polymer wrap upon significant shear damage, and cycled under lateral load. Refer to Chapter 3 (Experimental Program) for details of the test specimen.

1.6 FINITE ELEMENT PROGRAM

To corroborate with the experimental work, the test specimen was modeled using VecTor2: a nonlinear analysis program. Experimental and analytical results were compared to facilitate changes in analytical procedures.

VecTor2 is a nonlinear finite element program capable of analyzing two-dimensional reinforced concrete membrane structures subjected to quasi-static load conditions. This program uses a smeared, rotating-crack formulation for reinforced concrete based on the MCFT and the Disturbed Stress Field Model (Vecchio 2000). VecTor2 incorporates second-order effects such as compression softening, tension stiffening, and shear slip along crack surfaces. Additional analysis capabilities include

modeling cyclic loading, bond slip of rebars, and repaired or rehabilitated structures. VecTor2 uses low-powered elements to represent structural elements. These computational elements include a 4-node rectangular or quadrilateral element which have eight degrees of freedom (d.o.f.), a 3-node triangular element (6 d.o.f.), and a 2-node truss bar element (4 d.o.f.). Bar slip and adhesion loss are handled with 2-node bond link element or a 4-node contact element.

1.7 OBJECTIVE OF WORK

The goal of this project is not only to increase our knowledge of how shear-critical reinforced concrete structures behave, but also to provide much needed experimental data for further theoretical and analytical development in this subject. To accomplish this goal, a combined experimental and analytical research program was carried out on a shear-critical large scaled reinforced concrete frame. The data collected from the experimental testing will provide an extensive database to facilitate modifications to current analytical models and / or to provide a basis for new formulations. Analytical results from VecTor2 were assessed with respect to the experimental results.

Catastrophic failure of shear deficient structures in seismic regions is inevitable. The accurate assessment of the seismic structural response of such buildings, particular those built 30 or 40 years ago, is urgently needed. A better understanding of shear deficient structures will allow engineers to properly evaluate and accordingly retrofit these structures before failure takes place.

1.8 CHAPTER LAYOUT

This thesis focuses on the presentation of the experimental details, results, and discussion of experimental and analytical behaviours. Subsequent chapters contain information concerning reinforced concrete frames from literature (Chapter 2), details of test specimen, material properties, and instrumentation (Chapter 3), experimental results

(Chapter 4), discussion of results (Chapter 5), finite element analysis (Chapter 6), and finally conclusions and recommendations for future research (Chapter 7). At the end of the thesis, appendices are included which contain material stress-strain curves, sample calculations, condensed experimental data, and experimental photos.

Literature Review of Reinforced Concrete Frames

2.1 INTRODUCTION

To augment the research in this thesis, a literature review was carried out on previous experimental work of monotonically and / or cyclically-loaded reinforced concrete frames. The testing of reinforced concrete frames at the University of Toronto was reviewed (Section 2.2), along with summaries of previous work on ductile moment and shear-critical frames (Section 2.3), shear-critical beam-column joints (section 2.4), and retrofitting strategies using fibre reinforced polymer (Section 2.5).

2.2 TESTING OF REINFORCED CONCRETE FRAMES AT THE UNIVERSITY OF TORONTO

Over the past 15 years, research at the University of Toronto has been carried out to study the behaviour of reinforced concrete frames. Specifically, two frames tested by Vecchio and Balopoulou in 1990 and Vecchio and Emara in 1992 are elaborated below. These two projects established the basis of the design and test setup for the experiment in this thesis.

2.2.1 Vecchio and Balopoulou 1990: *On the Nonlinear Behaviour of Reinforced Concrete Frames*

Vecchio and Balopoulou (1990) examined the factors that contributed to the nonlinear behaviour of reinforced concrete frames under short-term loading. They carried out testing of a large-scale reinforced concrete frame. An investigation was also performed on the then-current formulations that were used to analytically predict the response of reinforced concrete. Specifically, problems that involved the formulation of nonlinear frame analysis procedures were identified. In this regard, the nonlinear analysis program TEMPEST (now known as VecTor5) was examined.

In this research, a large-scale, single-bay, two-storey reinforced concrete frame was constructed and tested. This test specimen was built with a centre-to-centre span of 3500 mm, a storey height of 2000 mm, and an overall height of 4600 mm. The frame dimensions and reinforcement layout are given in Figure 2.1. Fixed support conditions were imposed on the frame by integrally building a large reinforced concrete base attached to the frame columns. All rebars used complied with the Canadian Grade 400 steel specifications. Reinforcement anchorage was achieved by welding the ends of the rebars to bearing plates. The structure was cast in a reclined position using 29 MPa strength concrete. The specimen was lab cured for 25 days, and tested six months after casting.

During testing, a vertical monotonic point load was applied at the midspan of the first-storey beam with two 350 kN capacity servo-controlled actuators. These actuators were attached to the two ends of a steel I-beam which in turn rested across the first-storey beam. To monitor frame behaviour during testing, extensive electronic instrumentation was installed throughout the frame; included were twenty-two strain gauges to measure rebar strains, twelve linear variable displacement transducers (LVDTs) to measure frame displacements, and a continuous 200 mm square pattern of Zurich gauges to record deformations on the concrete surface. A total of thirty-six load stages were performed.

When examining the frame response, the authors concluded that several second-order effects can significantly influence the overall frame behaviour. These effects include material nonlinearities, geometric nonlinearities, concrete shrinkage, tension stiffening effects, shear deformations, and membrane action. The frame failed at 517 kN in a combination of tensile yielding of steel and crushing of concrete at the midspan of the first-storey beam. As well, flexural hinging at the first-storey beam-column joints were developing near the failure load. Figure 2.2 shows the vertical load versus displacement response with the load stages marked on the graph. Overall, the computer program TEMPEST predicted the frame's response accurately; however, the analysis procedure could not account for shear-related influences. This deficiency caused an

underestimated structural flexibility; as well the final failure mechanism was not captured correctly. Improvements suggested were to refine the tension stiffening model and to incorporate shear effects into the analysis procedure.

At the time when this project was undertaken, the large-scale testing of reinforced concrete frame was scarce. Therefore, this experiment was considered a pilot project of its kind. Nevertheless, the testing regiment was limited; only gravity load was applied. In order to fully understand the behavioural mechanisms of reinforced concrete frames, further testing with more complex loading conditions was required.

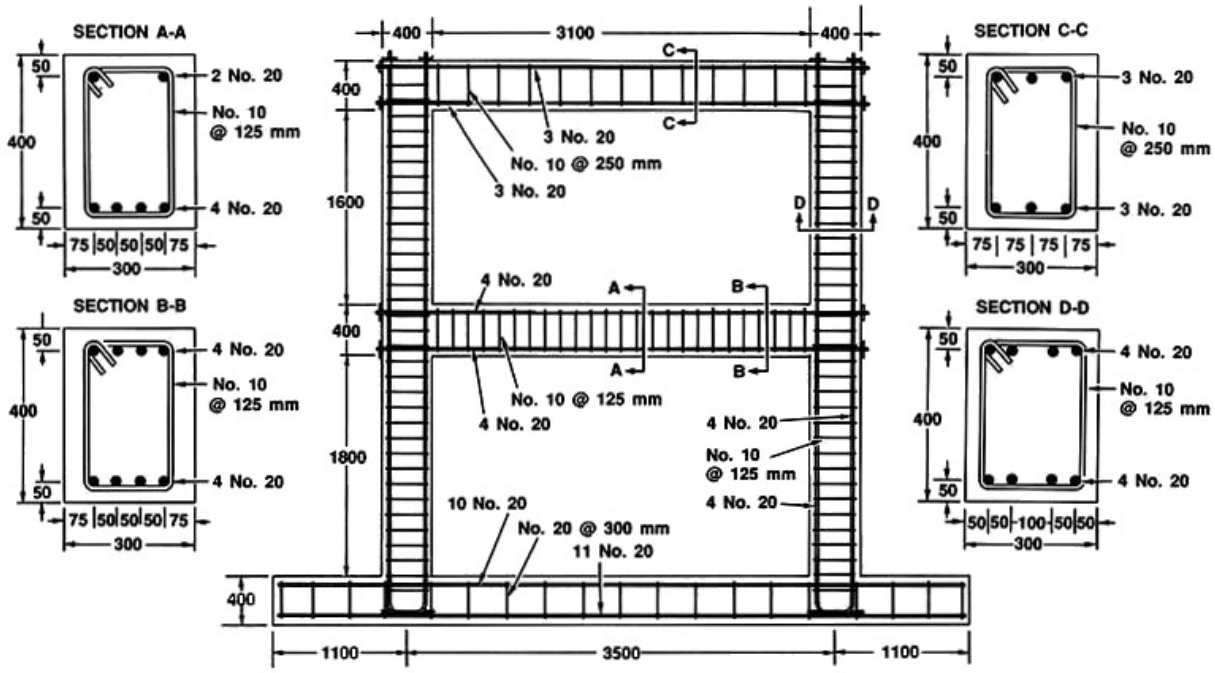

All dimensions in mm

Figure 2.1 Frame Dimensions and Reinforcement Layout
(Vecchio and Balopoulou 1990)

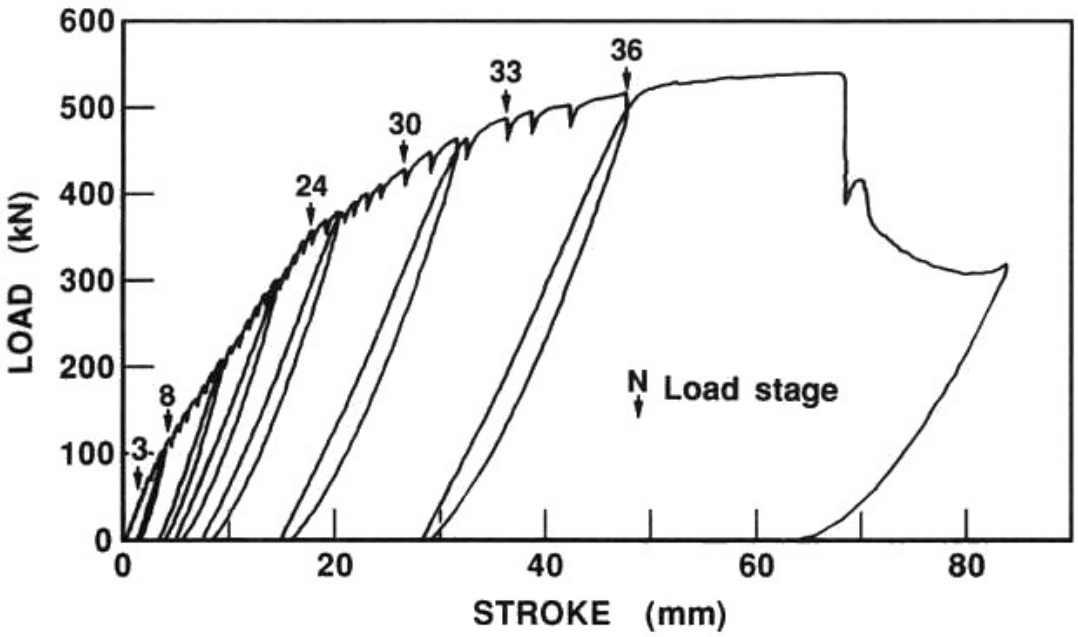

Figure 2.2 Vertical Load vs. Vertical Displacement at the Midspan of the First-Storey Beam *(Vecchio and Balopoulou 1990)*

2.2.2 Vecchio and Emara 1992: *Shear Deformations in Reinforced Concrete Frames*

Second-order effects such as shear deformations are now understood to have important influences on the response of reinforced concrete frames. Progressing from the pilot test completed by Vecchio and Balopoulou (1990), Vecchio and Emara (1992) proceeded to investigate the magnitude and influence of shear deformations on the response of reinforced concrete frames. Furthermore, the program TEMPEST was modified from the previous findings by Vecchio and Balopoulou (1990) and was reassessed for accuracy.

A large-scale reinforced concrete frame was tested with concrete dimensions identical to Vecchio and Balopoulou (1990) (refer to Figure 2.1), but the reinforcement layout was modified as illustrated in Figure 2.3. The concrete and steel material properties, the casting procedure, and the types of instrumentation used were similar to

those reported by Vecchio and Balopoulou (1990). The testing involved applying two constant column axial loads (700 kN per column), combined with a monotonically increasing lateral load located at the top storey beam. The column loads were provided by four 450 kN capacity, force-controlled hydraulic jacks (two per column), while the lateral load was supplied by a 1000 kN displacement-controlled actuator mounted laterally against a reacting strong wall.

The frame failed at 329 kN of lateral load by developing flexural hinges at both ends of the first and second-storey beams, as well as both column bases. Refer to Figure 2.4 for the lateral load versus displacement plot. While some shear cracks were observed in the beams and columns, the failure mode in these members were predominantly flexural. However, a post-analysis of the test data indicated that shear strains were of significant magnitude, particularly in the latter load stages. In this experiment, shear related deformations contributed to approximately 20% of the frame lateral deflection. The magnitude of influence will vary depending on the frame geometry, load condition and load level. Shear strains can also reduce the lateral stiffness of the frame, lower the flexural and axial rigidity of the members, and increase the members' rotational and axial strains. In situations where the frame displacement is notably affected by secondary effects, the increase in deflection can influence the failure mechanism (i.e. by the P-Δ effect). The analytical procedures developed in TEMPEST were found to provide reasonable predictions of the frame response such as the load-deformation response, ultimate load capacity, and failure mechanism.

Progress was made from the pilot testing in 1990 by Vecchio and Balopoulou to the second iteration in 1992 by Vecchio and Emara. Further insight was gained into the effect of shear deformations on the frame response. Nonetheless, the frame tested by Vecchio and Emara predominantly failed in flexure. In order to fully understand the magnitude and significance of shear behaviour in reinforced concrete frames, a frame that is critical in shear needs to be tested.

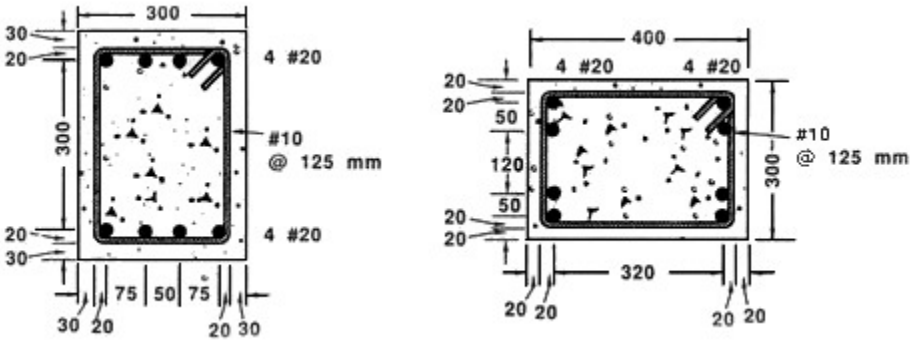

Beam Section Column Section

Figure 2.3 Beam and Column Cross-Sections
(Vecchio and Emara 1992)

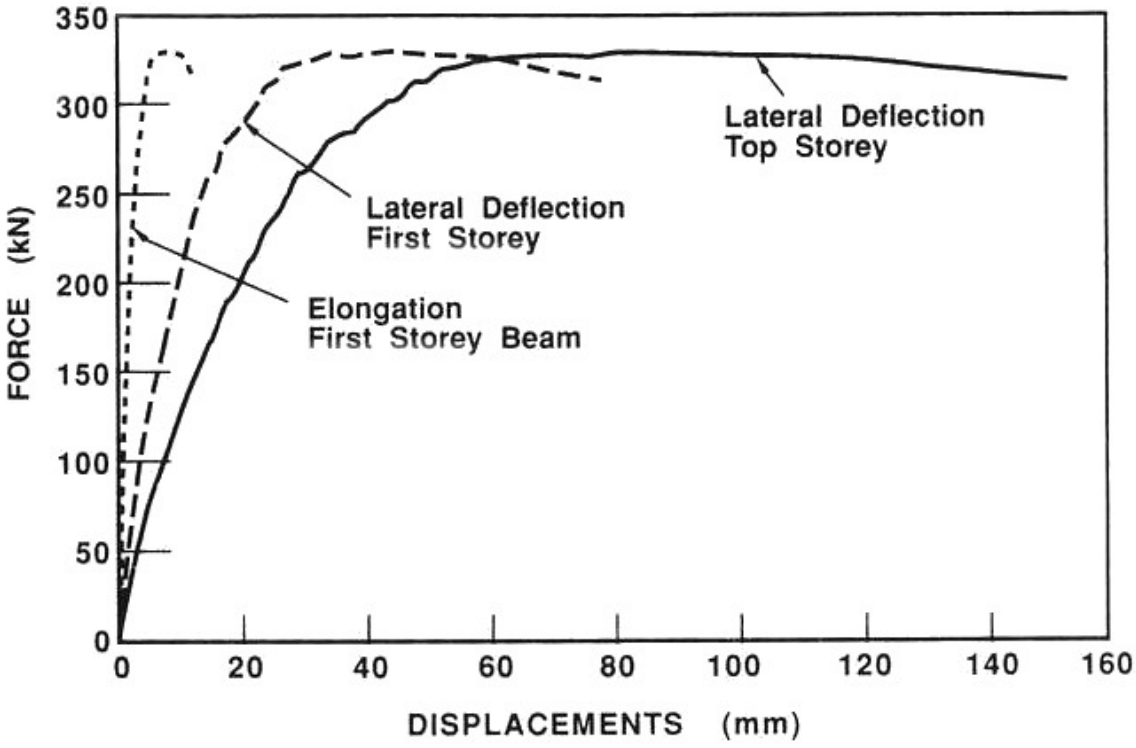

Figure 2.4 Second-Storey Lateral Force vs. Lateral Storey Deflection
(Vecchio and Emara 1992)

2.3 TESTING OF REINFORCED CONCRETE FRAMES AT OTHER INSTITUTIONS

Over the past 50 years, research on the large-scale testing of reinforced concrete frames has been carried out throughout the world. The majority of research has been performed on moment-critical, ductile reinforced concrete frames. For example, Cranston (1965) applied vertical and lateral load combinations to a one-storey ductile portal frame with a pinned base support. Clough and Gidwani (1976) tested a ductile two-storey double bay frame on a shake table, as well as in a push-over manner. Furthermore, Lee and Woo (2001) examined gravity reinforced concrete frames (frames that were designed without seismic consideration) under seismic loading. Nevertheless, due to reasons such as high over-strength inherent in the original non-seismic design, these frames exhibited a ductile behaviour. In contrast to work relating to moment-critical frames, the testing of shear-critical-frames has been scarce. In fact, a comprehensive article was difficult to obtain of a reinforced concrete frame, with either its beams or columns critical in shear, and tested in either a dynamic mode (i.e. shake table) or in a quasi-static manner (i.e. push-over). The following review summarizes a rare example of a shear-critical frame, tested under seismic loading.

2.3.1 Ozden, Akguzel and Ozturan 2003: *Seismic Retrofit of R/C Frames with CFRP Overlays*

The purpose of this research was to study the behaviour of hollow brick infilled reinforced concrete frames strengthened by CFRP. Four one-third scale, single bay, two-storey reinforced concrete frames were tested under reverse cyclic lateral load, combined with constant column axial loads. Of the four test frames, two were tested without the brick infill to observe the bare frame behaviour, and the remaining two frames were tested with the hollow tile brick infill. The behaviour of the infilled frames is outside the scope of thesis; however, the two bare frames, Pilot and U1, were of interest. Their test details are described below.

Test specimens Pilot and U1 were designed with the following deficiencies: inadequate lap-splice lengths for the column longitudinal reinforcement, poor shear and confining reinforcements for columns and beams, insufficient beam bottom reinforcement anchorage length, lack of ties in the beam-column connections, and strong beam-weak column design. The frame dimensions and reinforcement layout were similar for both specimens and are presented in Figure 2.5. Both Pilot and U1 had fixed base supports, and used plain 8 mm diameter rebar for longitudinal reinforcement with a yield strength of 312 MPa, and 4 mm diameter rebar for transverse reinforcement with a yield strength of 277 MPa. The concrete compressive strengths of Pilot and U1 were 22.4 MPa and 15.4 MPa, respectively. The other differences between the two test specimens were the column rebar splice lengths, and beam rebar anchorage detailing. The column splice lengths of Pilot and U1 were 200 mm and 160 mm, respectively. The minor, but influential, variation in the beam anchorage detail of Pilot and U1 are presented in Figure 2.6.

The test specimens were loaded with a 250 kN capacity displacement controlled hydraulic actuator, in a reverse cyclic manner. In addition, vertical axial loads of 30 kN were applied at the top of each column (approximately 10% of the column capacity). The lateral cyclic load was applied at the second-storey beam in the sequences illustrated in Figure 2.7 and Figure 2.8 for specimens Pilot and U1, respectively. Out-of-plane deformation was unrestrained. A typical electronic data acquisition system was setup to measure the applied load, displacements, rotations, and out-of-plane displacements.

The test specimen Pilot behaved in the following manner (refer to Figure 2.9). First cracking occurred after the first full lateral load cycle, at a peak cycle load of $\pm$5.8 kN. For the next three load cycles, $\pm$8 kN peak load was used. During that time, flexural cracks developed at both ends of the first-storey beam. At the seventh load cycle ($\pm$12.5 kN), flexural cracks at the columns widened. Only then were visible cracks detected at the beam-column joints. This lack of joint deformation prior to the seventh load stage was attributed to the poor joint shear transfer, because the beam longitudinal rebars were

insufficiently anchored. Between the eight and eleventh cycles, the loads ranged from 13 to 14 kN. Flexural cracks at both ends of the first-storey beam and first-storey columns propagated at this point. During the tenth load cycle, concrete cover spalling was observed at the upper far end of the first-storey column. As well, crack widths of 3 mm and 1.5 mm were observed at the column bases and first-storey beams respectively. The first visible x-crack pattern on the connections occurred at the twelfth load cycle. At that time, flexural cracks at the column, just below the first-storey connection, widened concurrently with the widening of column base flexural cracks. Minimal cracking was observed at the second-storey beam and columns.

U1 responded to loading in the following manner (refer to Figure 2.10). The first cracks occurred at the third load cycle ($\pm$7 kN). These cracks were observed at the base of the near column (nearest to the actuator), and alongside the first-storey beam on the far side. Hairline cracks were detected at the beam-column joints at the sixth load cycle ($\pm$9.5 kN). During the seventh and eight load cycles, new cracks were formed near the column bases, as well as at the connections. Beyond the eight load cycle, the frame's lateral load capacity stabilized under increasing lateral displacements. At the end of the thirteenth load cycle, crack widths of 1 mm and 2 mm were evident at the first-storey beam ends and column bases respectively. In addition, the first-storey beam-column joints exhibited heavy cracking compared to Pilot specimen.

For both Pilot and U1, the improper lap splice lengths in the columns mainly governed the ultimate load capacity and failure mode of the specimens. Flexural cracks on the first-storey column, just beneath the first-storey beam, widened and eventually led to sudden failure. The source article also includes plots of lateral load versus column curvature.

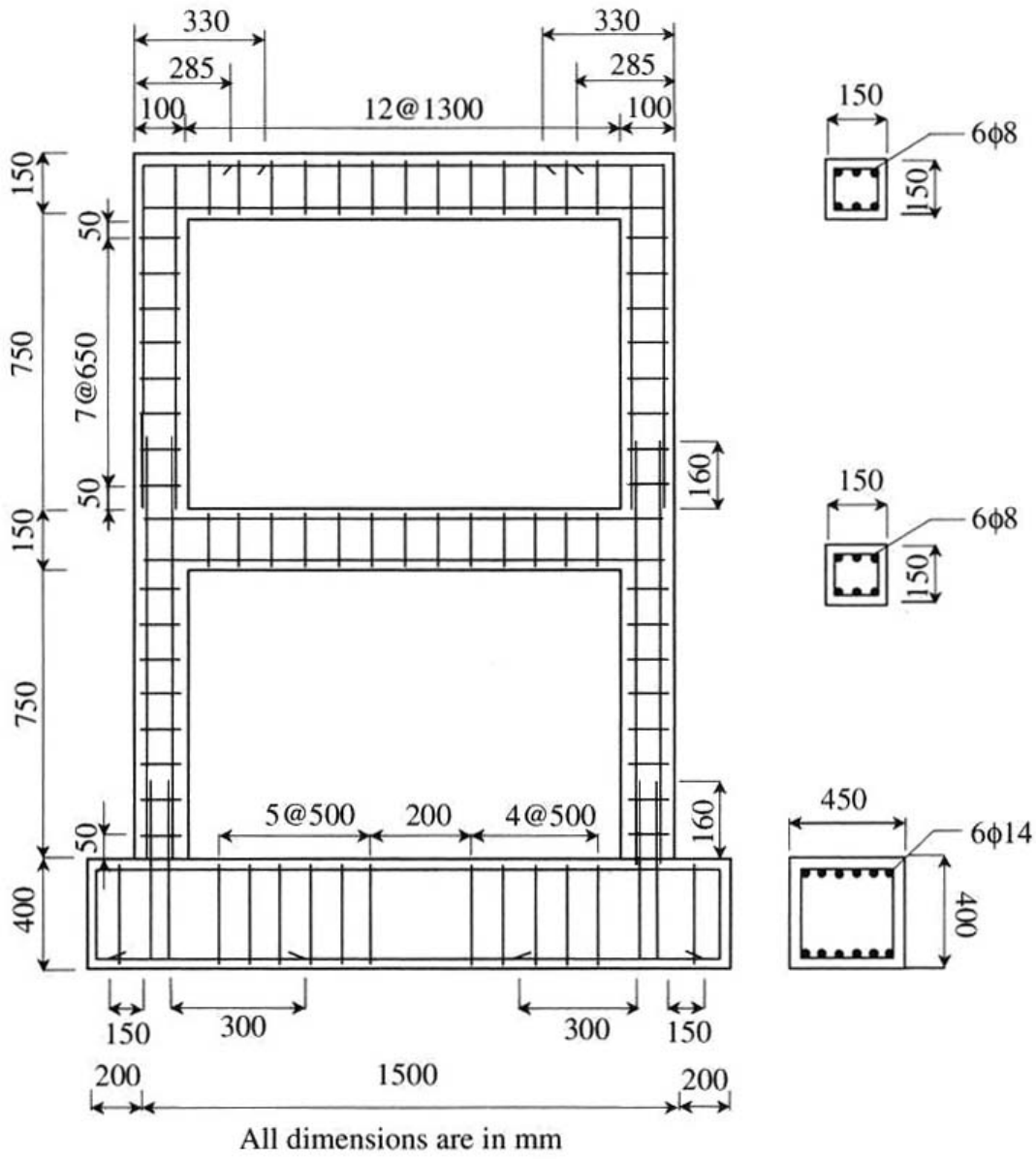

Figure 2.5 Frame Dimensions and Reinforcement Layout *(Ozden et al 2003)*

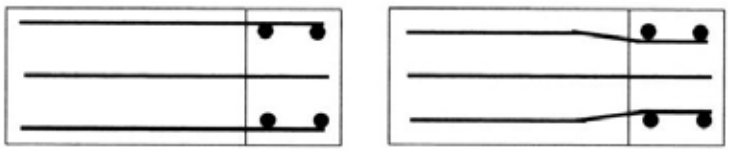

Pilot U1

Figure 2.6 Beam Reinforcement Anchorage Details
(Adapted from Ozden et al 2003)

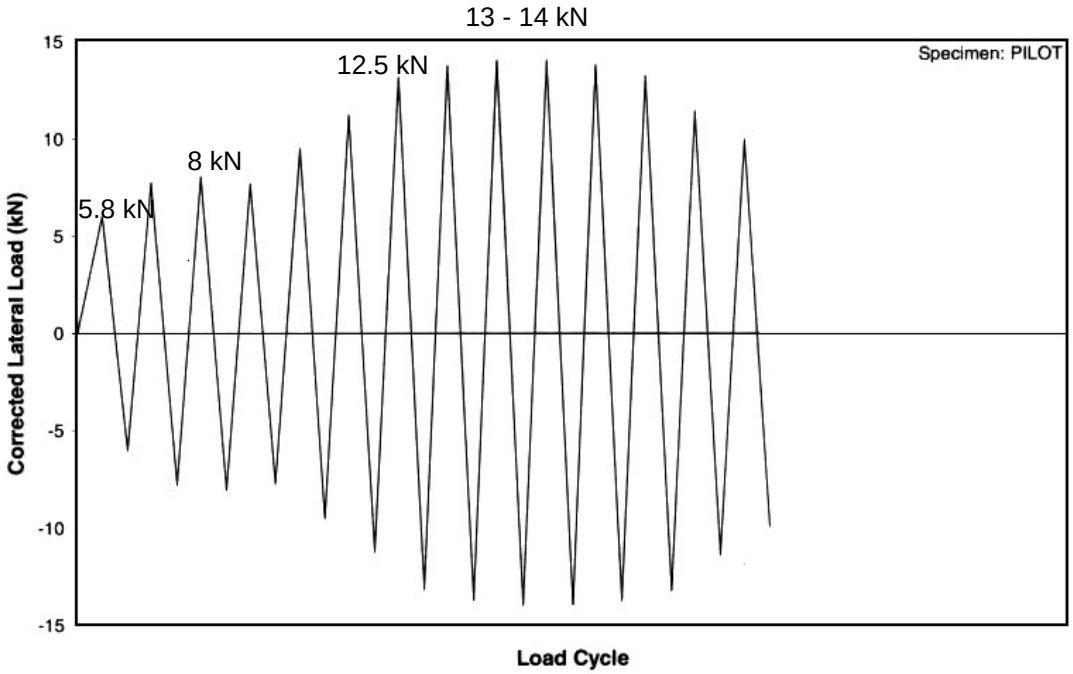

Figure 2.7 Cyclic Load Sequence of Pilot Specimen *(Adapted from Ozden et al 2003)*

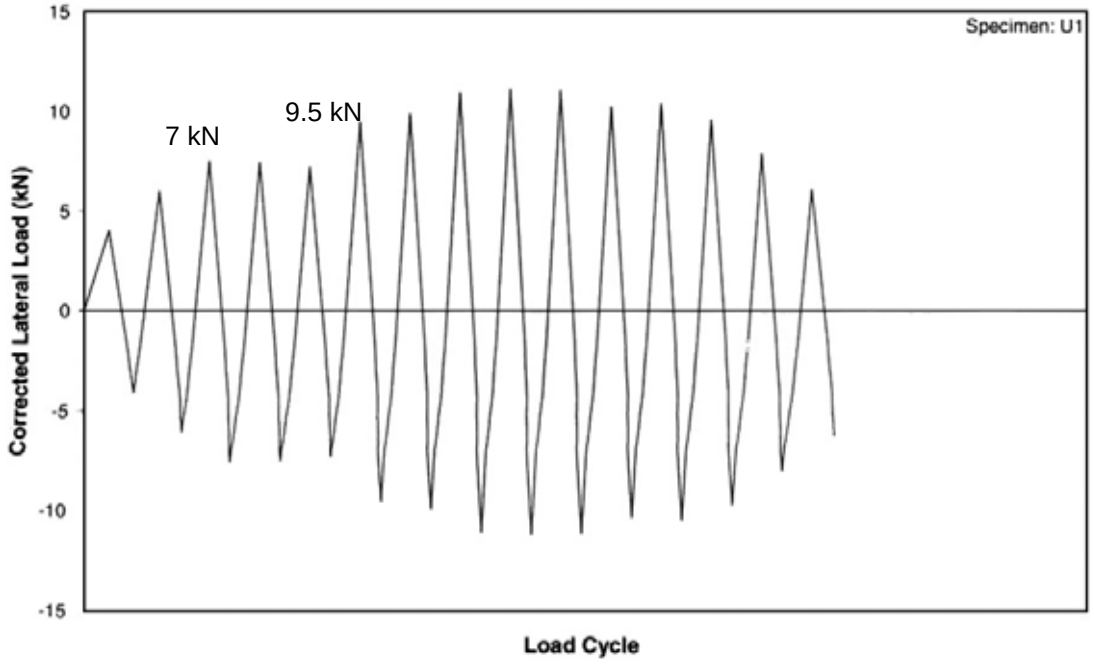

Figure 2.8 Cyclic Load Sequence of U1 Specimen *(Adapted from Ozden et al 2003)*

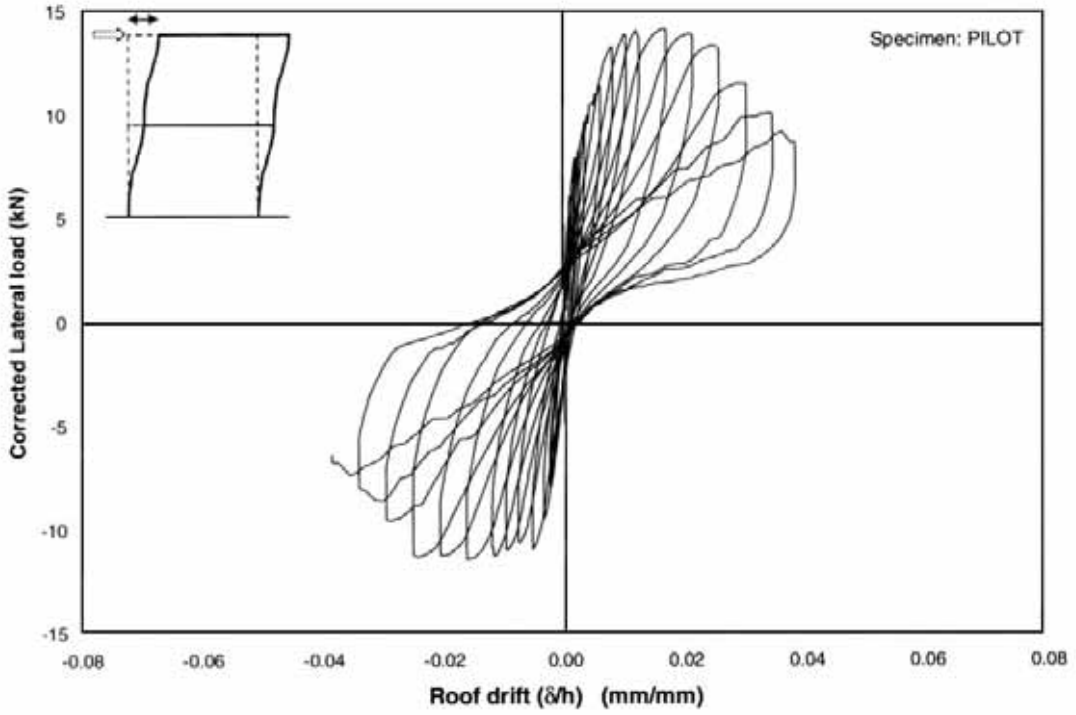

Figure 2.9 Lateral Load vs. Second-storey Roof Drift for Pilot Specimen
(Ozden et al 2003)

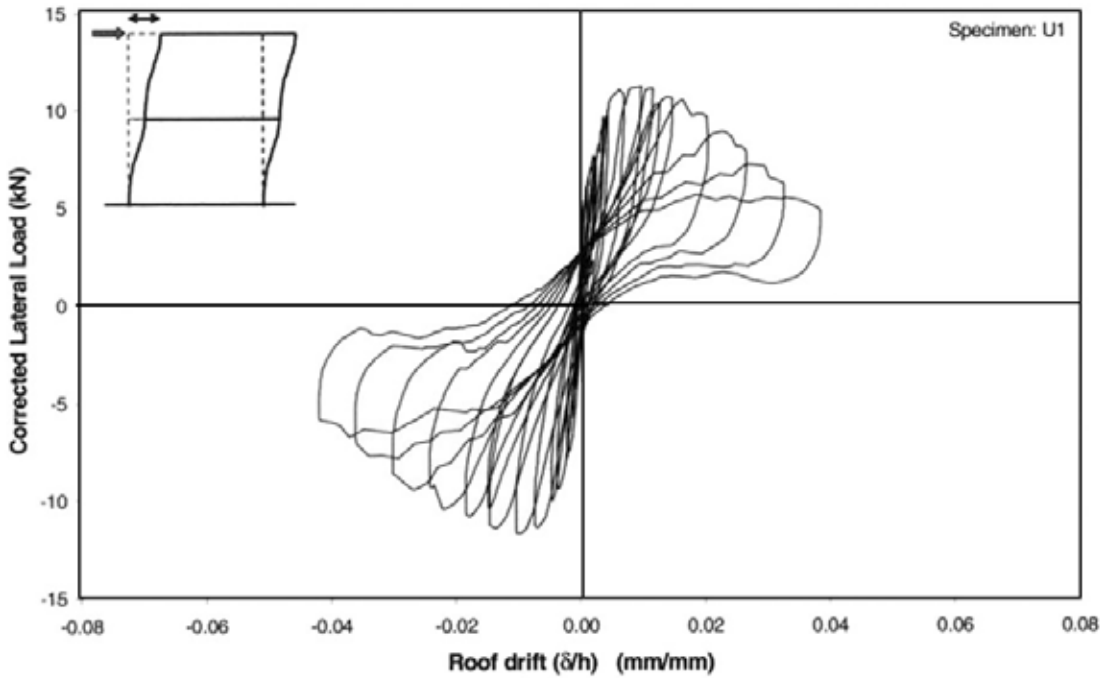

Figure 2.10 Lateral Load vs. Second-storey Roof Drift for U1 Specimen
(Ozden et al 2003)

2.4 BEAM-COLUMN CONNECTIONS

Numerous beam-column connections have been tested in the past to study the behaviour of reinforced concrete structures. By isolating the beam-column joint, one is able to examine the specific connection behaviour without having to construct the entire frame; however, the global frame behaviour inherent in indeterminate structures such as a rigid frame is not fully captured when only the joint is tested. Regardless, the testing of connections is still useful to study the local behaviour. The majority of research performed on beam-column joints, such as panel zone deformation and rebar bond slip, is outside the focus of this thesis. Nevertheless, two studies performed are relevant. In the first research carried out by Celebi and Penzien (1973), the behaviour of reinforced concrete components simulating interior beams with column stubs was investigated. In the second research performed by Ghobarah *et al* (1996), a weak-beam strong-column connection critical in flexural-shear was examined under reserved cyclic loading. The experimental details for both studies are described below.

2.4.1 Celebi and Penzien 1973: *Experimental Investigation into the Behaviour of Critical Regions of Reinforced Concrete Components as Influenced by Moment and Shear*

Celebi and Penzien (1973) tested twelve interior beams with column stubs under reverse cyclic loading. The variables in the beam designs were shear span-to-depth ratio, stirrup spacing, cross-sectional dimension, longitudinal reinforcement ratio, and dynamic versus quasi-static loading rate. The majority of these specimens behaved in a flexural manner except for Beam12 (quasi-static loading only), where shear degradation greatly influenced the cyclic response of the specimen. The properties of Beam12, its test setup, and results are presented below.

Beam12 was 1.83 m in length, and had nominal cross-sectional dimensions of 230 mm in width and 380 mm in depth. A column stub was located at midspan of the specimen. The shear span to effective depth (a/d) ratio was 2.31. The beam was

designed with longitudinal and shear reinforcement percentages of 1.03% and 0.752% respectively, and had a steel yield strength and a concrete compressive strength of approximately 345 MPa and 31.6 MPa, respectively. Figure 2.11 illustrates the concrete dimensions and reinforcement layout.

The beam test setup, instrumentation, and loading sequence were as follow. The two ends of the beam were attached to two vertical columns of a test frame (one fixed at the base and the other hinged), in a manner that allowed for end rotation. This test frame also consisted of an actuator support at the beam midspan where load can be applied. The support columns were post-tensioned to the test floor. Instrumentation utilized included visicorders to record output from all instrumentation, actuator load cell and LVDTs to measure load and displacement, other LVDTs to measure curvature and diagonal displacement, and direct current displacement transducers (DCDTs) to measure steel strains. Vertical reverse cyclic loading was applied at the column stub using a MTS 340 kN capacity displacement-controlled hydraulic actuator with a maximum stroke of $\pm$152 mm. Beam12 was loaded in a continuous quasi-static manner at a rate of 2.54 mm / sec. The loading cycles are depicted in Figure 2.12.

Under reverse cyclic loading, Beam12 exhibited a fair amount of degradation as evident by the pinching in the load-deflection hysteresis (Figure 2.13). The pinching was attributed to the low a/d ratio, as well as the high nominal shear stress present. Shear deformations affected the overall total deformation. The moment-curvature response is also available in the source article.

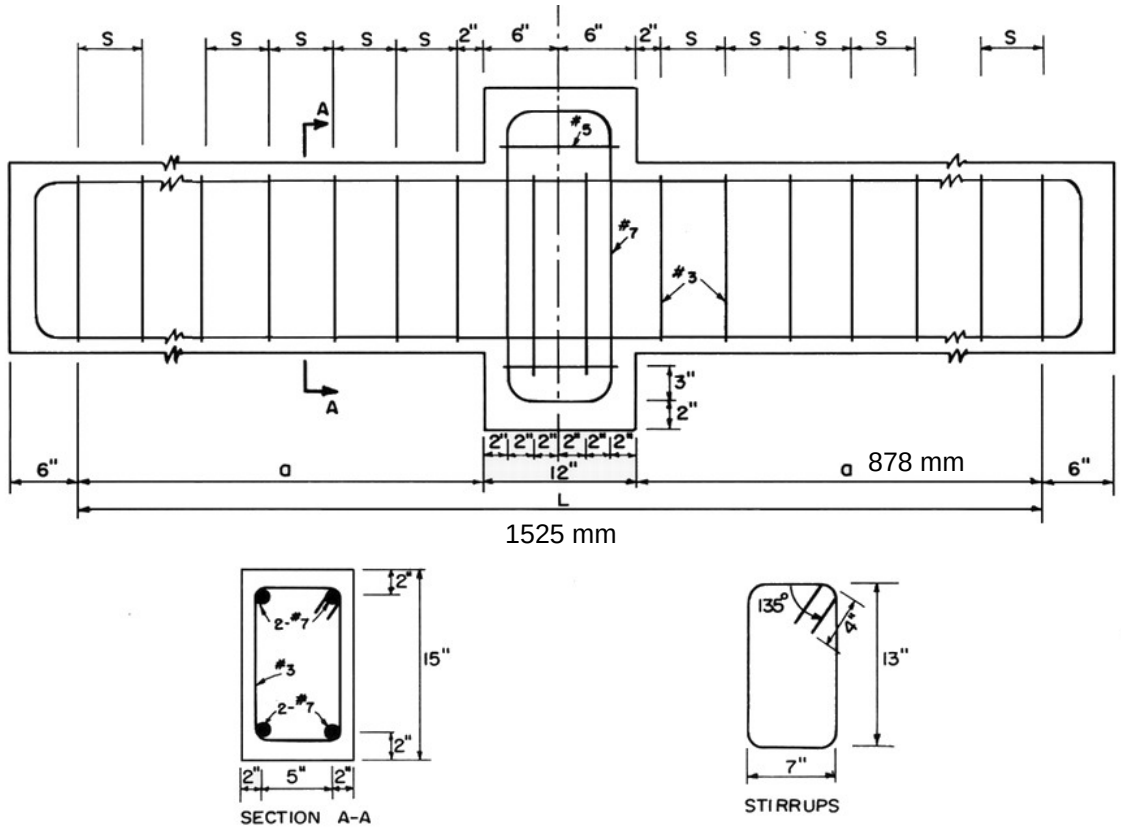

Figure 2.11 Concrete Dimensions and Reinforcement Layout of Beam12
(Celebi and Penzien 1973)

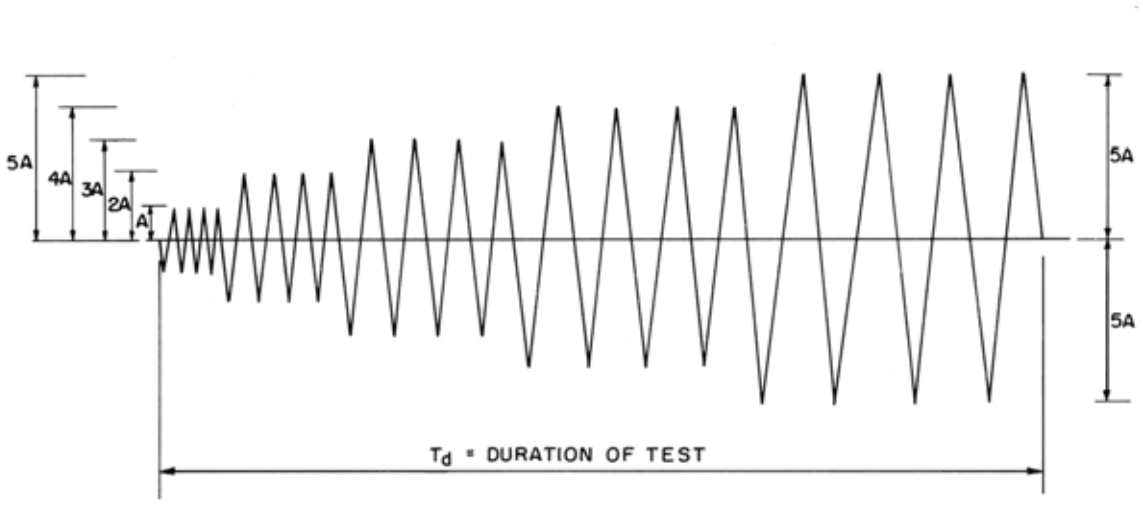

Figure 2.12 Loading Sequence of Beam12 *(Celebi and Penzien 1973)*

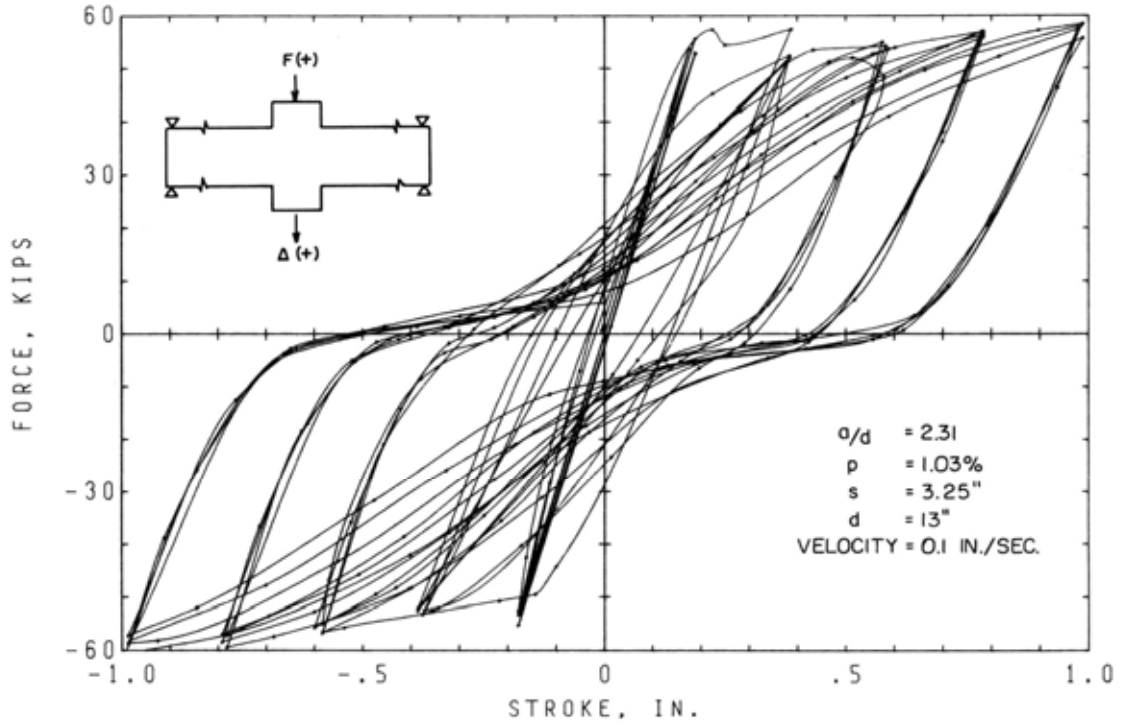

Figure 2.13 Cyclic Response of Beam12 (*Celebi and Penzien 1973)*

2.4.2 Ghobarah, Aziz and Biddah 1996: *Seismic Rehabilitation of Reinforced Concrete Beam-Column Connections*

Ghobarah *et al* (1996) examined the seismic rehabilitation of reinforced concrete beam-column connections. Specifically, the retrofitting technique using corrugated steel jacketing was investigated. Depending on where the deficiencies in the connections were located, the columns, beams, and / or panel zones could be encased with corrugated steel jackets. The gaps between the steel jackets and concrete were filled with a non-shrink grout. Four test specimens were tested. The one of interest, denoted J4, was encased in the column and joint regions, leaving the beam prone to failure. The specimen dimensions, loading sequence, and results are presented below.

J4 was built to one third scale size, and used a concrete strength of 23.0 MPa, transverse reinforcement strength of 448 MPa, and 2.8 mm thick corrugated steel jacket with strength of 363 MPa. The specific characteristics of the jacket can be found in the

source article. Figure 2.14 shows the concrete dimensions and loading points, while Figure 2.15 shows the reinforcement details.

The load cycles were applied in the following manner. First, a column compression load of 505 kN ($0.08A_g f'_c$) was applied and held constant throughout the test. Two initial vertical reverse cycles of approximately 15% of the specimen strength (60 kN) was applied at the beam tip, followed by two cycles to cause cracking (~120 kN), and two cycles to cause initial yield (Δ_y) of beam longitudinally steel (~340 kN). Next, the displacement was increased to two times the lateral yield displacement ($2\,\Delta_y$). Subsequent load stages were increased by multiples of Δ_y, with two cycles applied at each ductility level. Testing was continued until the specimen's load capacity dropped below 25% of its ultimate strength. Surface strains and specimen displacements were measured using strain gauges and displacement transducers.

J4 responded to experimental testing in the following manner (refer to Figure 2.16). The first crack was observed at the beam-column interface, followed by yielding of beam longitudinal reinforcement at approximately 320 kN. At this stage, inclined beam cracks developed. These cracks widened noticeably at the load cycle corresponding to $2\,\Delta_y$. The peak resistance of 430 kN was reached at a factor of $4\,\Delta_y$. The failure was diagnosed as a shear failure at the beam plastic hinge region. The article also includes a beam tip load-strain plot.

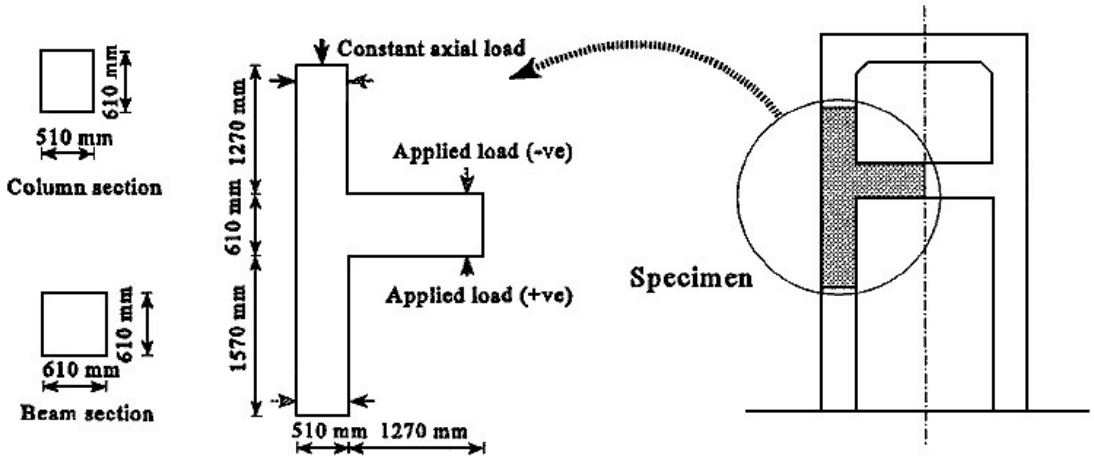

Figure 2.14 Dimensions and Loading Locations of Beam-Column Assemblage
(Ghobarah et al 1996)

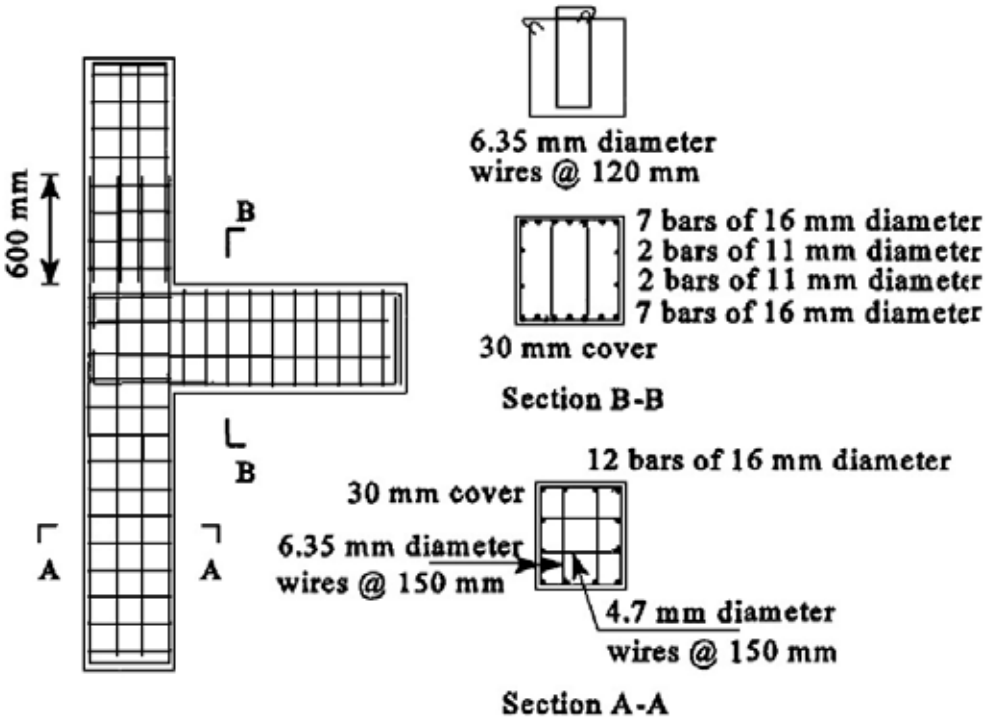

Figure 2.15 Reinforcement Layout of Beam-Column Assemblage
(Ghobarah et al 1996)

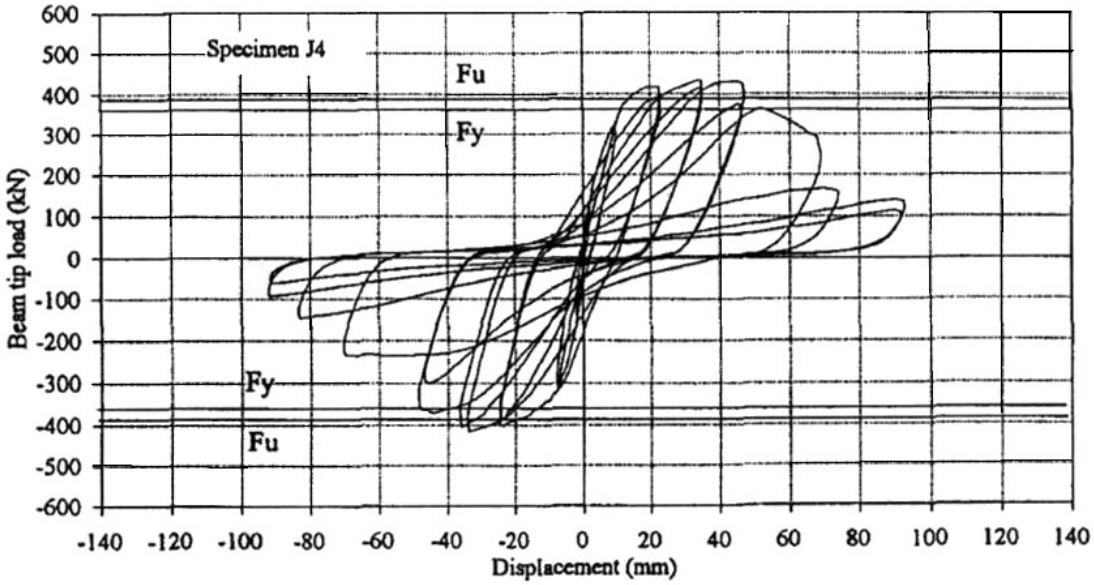

Figure 2.16 Reverse Cyclic Load vs. Beam Tip Displacement
(Ghobarah et al 1996)

2.5 SEISMIC REHABILITATION: FRP RETROFIT

Due to the lack of adequate seismic consideration in structural design over the past 30 or 40 years, a large portion of structures built during that time are now considered seismically substandard and deficient according to today's design codes. With the need for structural upgrading, structural rehabilitation is becoming more important, particularly in seismically active regions. There are several strategies used to seismically upgrade structures. These methods include constructing a shear wall addition to attract the lateral force, and hence protect deflection-sensitive members; reducing the structural stiffness by seismic isolation, thereby decreasing the load demand; reducing the structural dynamic response by increasing the damping via visco-elastic and friction dampers; and increasing the critical member strength with seismic retrofit. The last strategy was of interest in this project; specifically, externally bonded fibre reinforced polymers (FRPs) were examined as a type of retrofit material.

FRPs are gaining popularity in upgrading the shear and / or flexural strengths of reinforced concrete structures. FRPs are manufactured in the form of continuous carbon (C), glass (G) or aramid fibres weaved together and bonded by epoxy, vinylester or polyester. Despite the high material cost of FRPs, they are popular for their high strength-to-weight ratio, immunity to corrosion, and easy handling and installation.

When compared to other retrofit techniques such as steel or concrete jacketing, the FRP solution is advantageous in several ways. These advantages are best explained through an example of a weak beam-strong column connection, with the beam being critical in shear. The beam can be strengthened in shear by wrapping FRP in the transverse direction. This rehabilitation procedure can be executed without altering either the beam's flexural strength or section properties; these properties are attributed to the uni-directional weaving and low thickness characteristics of FRP respectively. On the other hand, steel or concrete jackets are thick and possess strength in both orthogonal directions; therefore, repair with either material will increase both the shear and flexural strengths, and change the sectional properties. These characteristics are undesirable,

because not only will a change in the sectional properties require a reanalysis of the system, but also an increase in beam flexural strength will increase the load demand on the column, and possibly shift the failure mode from a weak beam-strong column system to a strong beam-weak column system. A strong beam-weak column system is undesirable in seismic design, as collapse is more likely when gravity members fail. FRPs are light-weight and easy to install, and can exclusively increase either the shear or flexural strength of a member without affecting its sectional properties. For these reasons, FPRs are preferred over steel and concrete jacket in the repair of reinforced concrete structures.

As mentioned previously, several types of FRPs are manufactured including carbon, glass and aramid fibres. In this experiment, carbon FRP (CFRP) was used over glass or aramid fibres for availability. The following literature review describes an example of the effectiveness of CFRP in improving the shear strength of reinforced concrete members.

2.5.1 Sheikh, DeRose and Markdukhi 2002: *Retrofitting of Concrete Structures for Shear and Flexure with Fibre-Reinforced Polymers*

The objective of this research was to examine the structural distress encountered at various locations in a multi-storey reinforced concrete building. This goal was accomplished through testing large-scale models of wall-slab and beam specimens. Only the beam specimens were of interest in this literature review; their sectional and material properties, test setup, and experimental results are discussed below.

Two large-scale beam specimens, Beam1 and Beam2, were built with dimension 550 mm in width, 1000 mm in depth, and 4800 mm in length. Figure 2.17 summarizes the beams' dimensions and reinforcement details. Beam1 was tested to complete failure to provide a basis for evaluating the effectiveness of the repair. Beam2 was damaged to the same degree as the prototype member in the existing building, and was repaired with CFRP. In the actual building, the beams are framed into the walls. This feature was

simulated by building a haunched region and increasing the amount of reinforcement for half of the beam length. As a result, shear failure was expected in the shallower region of the beam, which is compatible with the observed field damage. Figure 2.17 also illustrates the location of twenty-one electric strain gauges installed on the longitudinal and transverse rebars that were used to collect steel strain readings during testing.

Beam1 and Beam2 were cast in two steps. First, the beams were cast without the haunch and moist cured for three days. Next, the haunch was cast and cured for an additional three days. Concrete strengths of 44.7 and 45.7 MPa were used with 20 mm maximum aggregate size. U.S No.3 bars used were Grade 60 steel, while Canadian size 25M and 30M bars were Grade 400 steel. The CFRP used was designated as 1.0 mm thick. Test coupons for the CFRP were made by impregnating the fabric with epoxy. Results indicated an ultimate CFRP strength of approximately 0.95 kN per mm width, and this occurred at a strain of 0.013.

The beams were tested using a hydraulic jack connected to a rigid 5400 kN testing machine frame. A single-point load was applied at the haunched region near the beam midspan (loading plate is shown in Figure 2.17). LVDTs and dial gauges were installed to monitor the shear strain and deflection, respectively. Beam1, the control specimen, was tested to complete failure, while Beam2 was tested until shear cracks ranged from 0.2 to 0.8 mm (as observed in the field). The imposed displacement on Beam2 was maintained while repair was carried out. Three sheets of CFRP, at 610 mm width each, were saturated in epoxy and wrapped around the beam section to provide one layer of FRP shear reinforcement over about 1.83 m length of the beam. The specimen remained under load for three days for curing of epoxy, and tested until failure.

Figure 2.18 shows the load versus deflection graphs for both specimens. Beam1 failed in brittle shear at 1700 kN with 14 mm of vertical deflection below the point load, while the repaired specimen Beam2 failed in ductile flexure at 2528 kN with a deflection of 143 mm. The ultimate load capacity and displacement were increased by 49% and 1020%, respectively. Energy dissipation capacity or toughness improved by more than

2600%. These results conclude that CFRP was effective in strengthening for shear and improving the ductility of the beam specimen. Additional results including analytical comparison, moment-curvature response, and shear force-strain response are presented in the source article. The article also examined the repair of wall-slab specimens using CRFP and GFRP.

Other researchers have made similar conclusions regarding the shear and ductility improvements of CFRP retrofitting (Kachlakev and McCurry 2000).

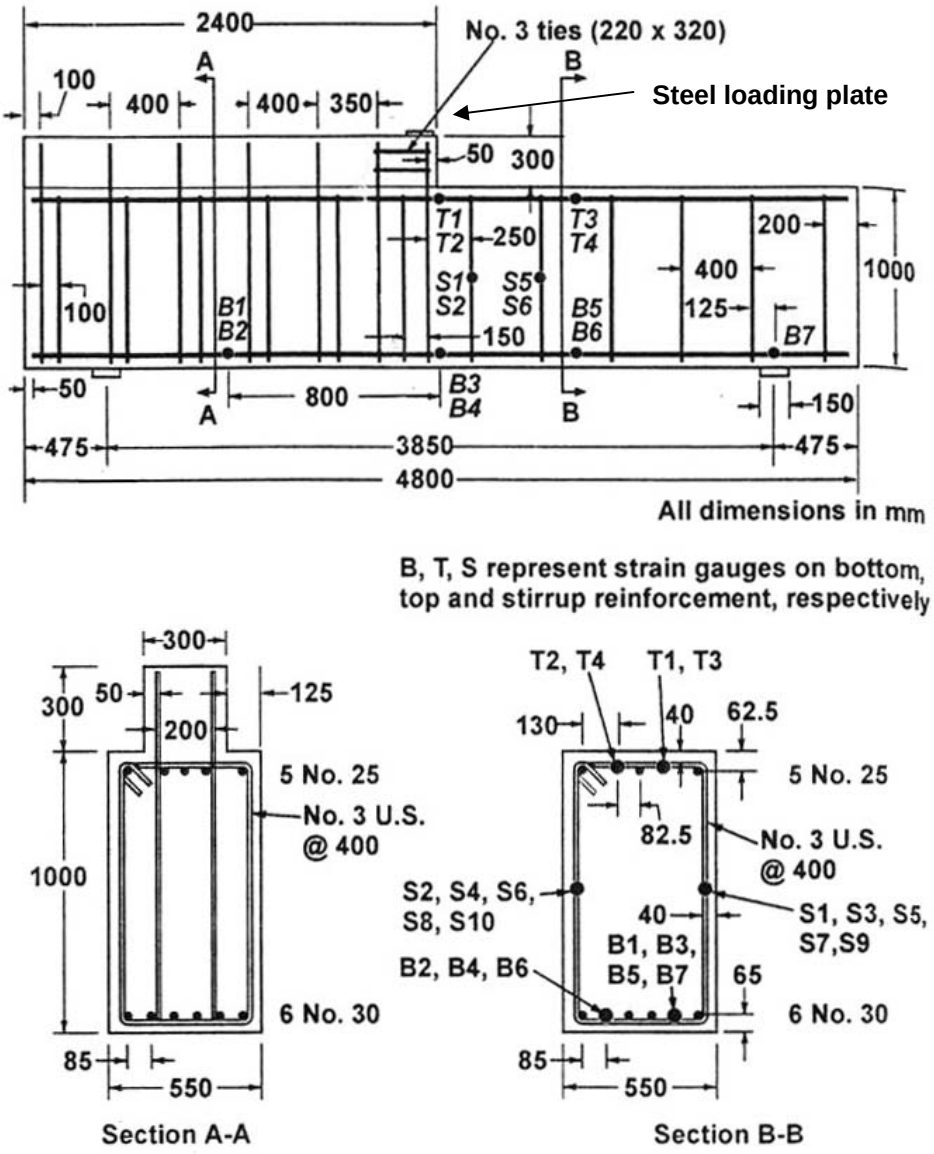

Figure 2.17 Beam Dimensions and Reinforcement Layout *(Sheikh et al 2002)*

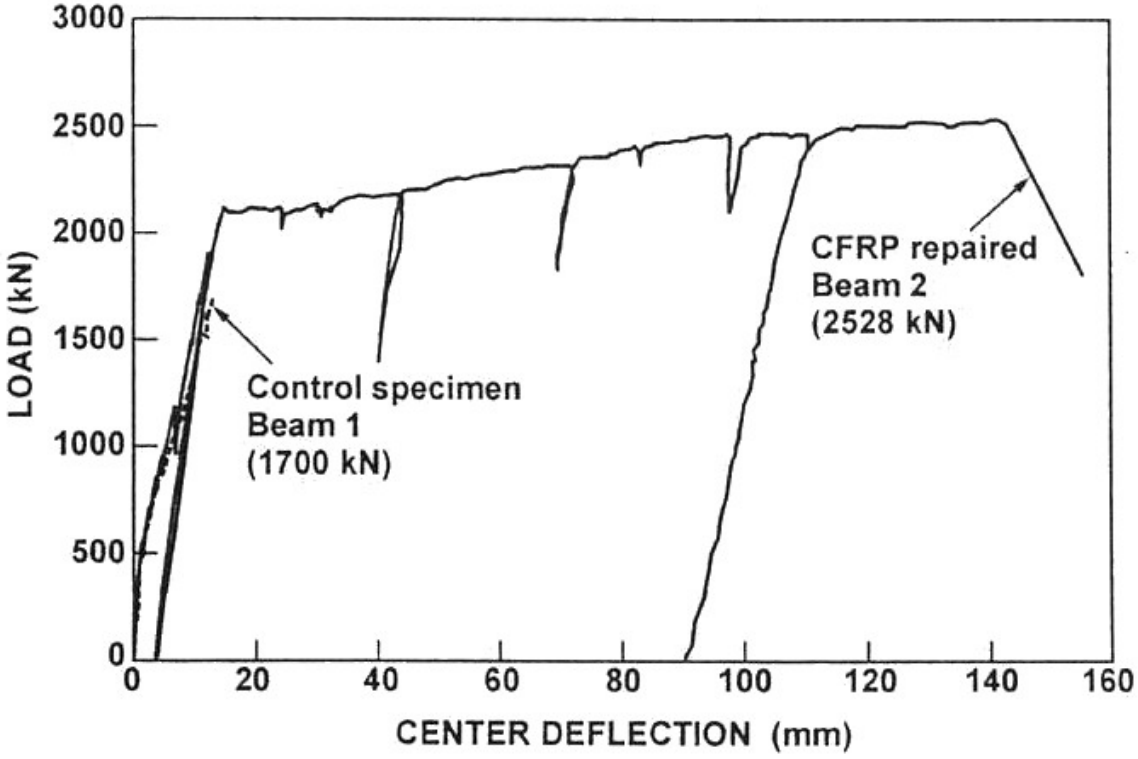

Figure 2.18 Midspan Vertical Load vs. Vertical Deflection
(Sheikh et al 2002)

Experimental Program

3.1 INTRODUCTION

This chapter describes the details of the experimental program, including characteristics of the two-storey reinforced concrete frame, properties of the materials used, the construction procedure, and the repair procedure. Also included are descriptions of the testing facility, data acquisition / instrumentation systems, and loading sequence. The characteristics of the test frame mimicked, where possible, those of the cement tower located in El Salvador (Section 1.4). As such, attempts were made to implement the following cement tower properties to the test frame: a beam clear span-to-depth ratio of 3.8, a concrete compressive strength of 30 MPa, and a column axial load equivalent to 3.5 MPa of compressive stress. The cement tower had several deficiencies including a shear-critical beam design and poor beam anchorage and column splice detailing. Nevertheless, since the focus of this thesis was to study the shear deficient beam design, all other deficiencies from the cement tower were eliminated in the test frame by appropriate design measures.

3.2 TEST SPECIMEN

A single-span, two-storey, shear-critical reinforced concrete frame with a fixed base condition was constructed and tested in the laboratories at the University of Toronto (Figure 3.1 and Figure 3.2). This test frame was two-thirds in scale and stood approximately 4.6 m tall and 2.3 m wide (storey scale of a typical building). Lateral reverse cyclic loading was applied at the top of this test specimen with the lateral force reacted off a strong wall that stood 4.62 m high. The height of the specimen was limited by the height of the strong wall, as well as the lab clearance. The beams were nominally 300 mm wide x 400 mm deep. The columns also had dimensions of 300 mm x 400 mm. To provide fixity at the bottom, a reinforced concrete base 800 mm wide, 400 mm thick,

and 4100 mm long was built integrally with the body of the frame and post-tensioned to the strong floor prior to testing. The beam clear span was 1500 mm and the column clear storey height was 1700 mm. A beam clear span-to-depth ratio of 3.75 was designed to mimic the ratio present in the cement tower (3.8); as well, a high span-to-depth ratio promoted shear failure in the beams.

The deformed reinforcing rebars used in the specimen were No.10, No.20, and US No.3. Typical beam and column sections contained four No.20 bars as top and bottom reinforcement, with US No.3 closed stirrups spaced at 300 mm in the beams and No.10 double closed hoops spaced at 130 mm in the columns. The base section contained eight No.20 top and bottom bars, with No.10 triple closed hoops spaced at 175 mm. Refer to Figure 3.3 for the reinforcement layout, Figure 3.4 for the designed member cross-sections, and Figure 3.5 for the as built member cross-sections. Clear covers of 30 mm and 20 mm were used for the beams and columns, respectively, and 40 mm cover was used for the base. The lateral loads applied to the frame at the top storey induced high bending stresses at the base of the column and at the inner column faces at the top. In order to prevent premature column failure, an extra layer of longitudinal reinforcement consisting of four No.20 bars was added at each of these locations to increase their flexural capacity. Column splices were implemented at the second-storey midheight where stress levels were low under applied loading.

In previous trials of frames built at the University of Toronto, anchorage for longitudinal rebars was provided via externally welded anchor plates (Vecchio and Emara 1992, Vecchio and Balopoulou 1990). This procedure provided clean detailing for analytical modeling purposes; however, in this study, it was deemed important to imitate the actual construction procedures in order to study the behaviours most realistic to construction practice. Thus, hooks and development lengths were used to provide reinforcement anchorage. Given the scaled down frame dimension, a No.20 rebar was the largest longitudinal bar that could be used at the joint region without having any problematic hook bends and / or excessive development lengths. No.10 rebar was used

for the column and base shear reinforcement to compliment No.20 longitudinal steel. For the beam closed stirrups, US No.3 rebar was chosen as it had a lower cross-sectional area than No.10, thereby, lowering the beam shear capacity and encouraging beam shear failure. US No.3 bar was chosen over D6 and D7 as the former had a more reliable material property, even though the latter two had lower cross-sectional areas. Table 3.1 below summarizes the reinforcement bar sizes and ratios used for various frame components.

Figure 3.1 Test Frame after Construction and Casting

Table 3.1 Cross-sectional Details of Frame Components

Member	b (mm)	h (mm)	Bottom Steel	Top Steel	Stirrup (mm spacing)	ρ_x (A_s/bd) %	ρ_y %
Beam	300	400	4 No.20	4 No.20	US No.3 at 300 (single hoop)	1.143	0.158
Column	300	400	4 No.20	4 No.20	No.10 at 130 (double hoop)	1.111	1.018
Column (at top)	300	400	8 No.20	4 No.20	‘ ‘	1.111 or 2.39	1.018
Column (at base)	300	400	8 No.20	8 No.20	‘ ‘	2.39	1.018
Base	800	400	8 No.20	8 No.20	No.10 at 175 (triple hoop)	0.857	0.429

Note: refer to Figure 3.6 for the reinforcement material properties.

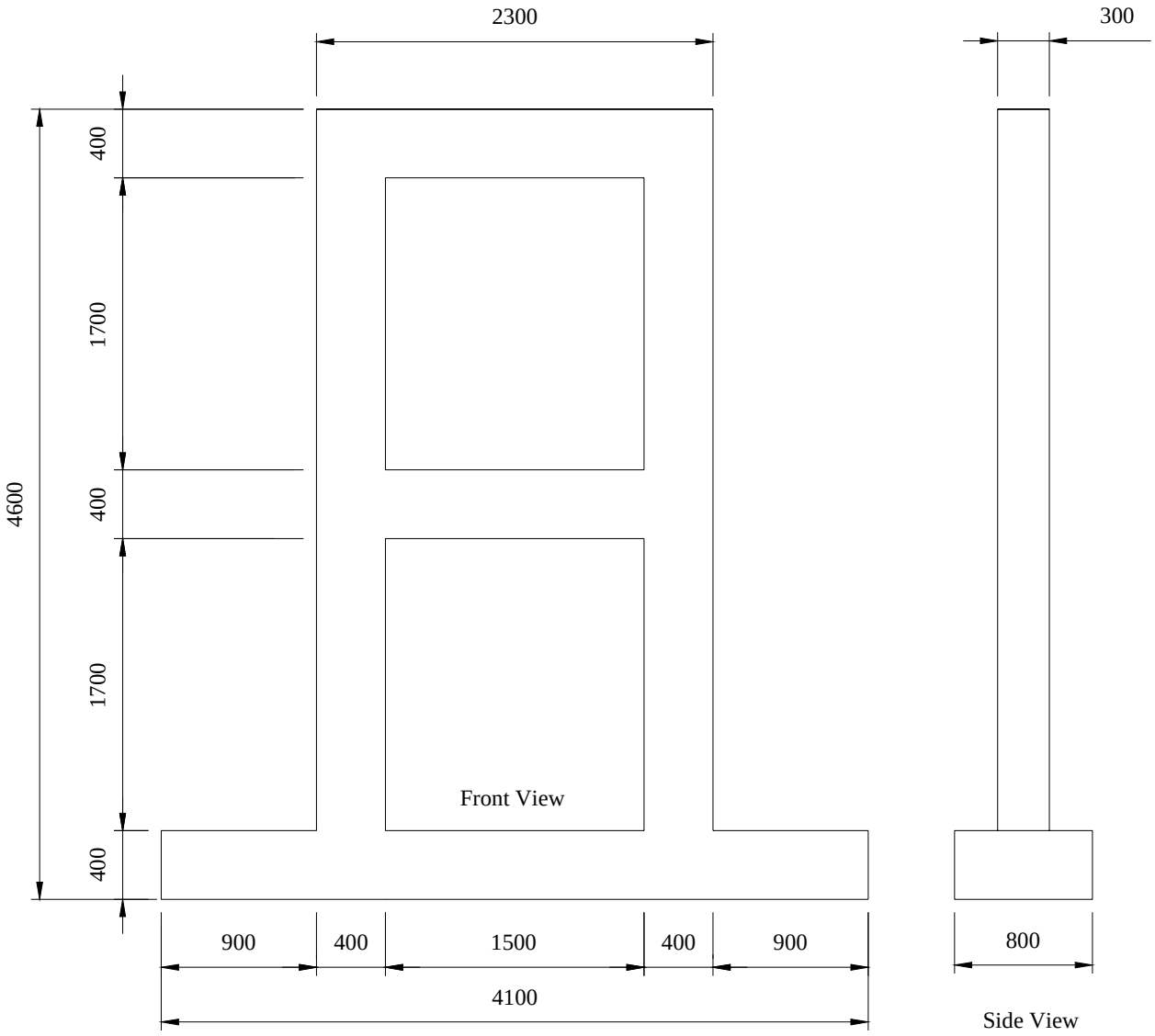

Figure 3.2 Nominal Frame Dimensions

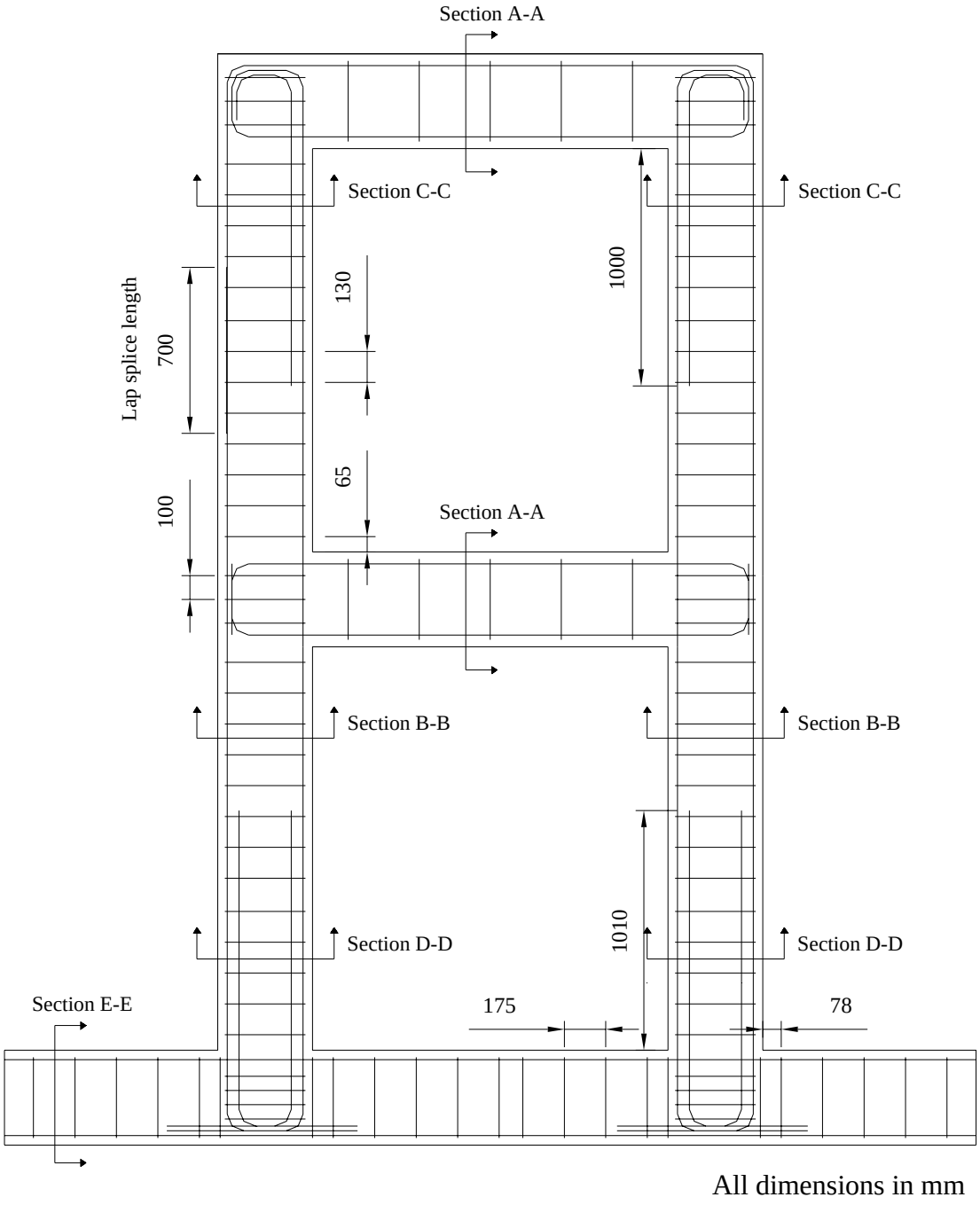

Figure 3.3 Frame Reinforcement Layout

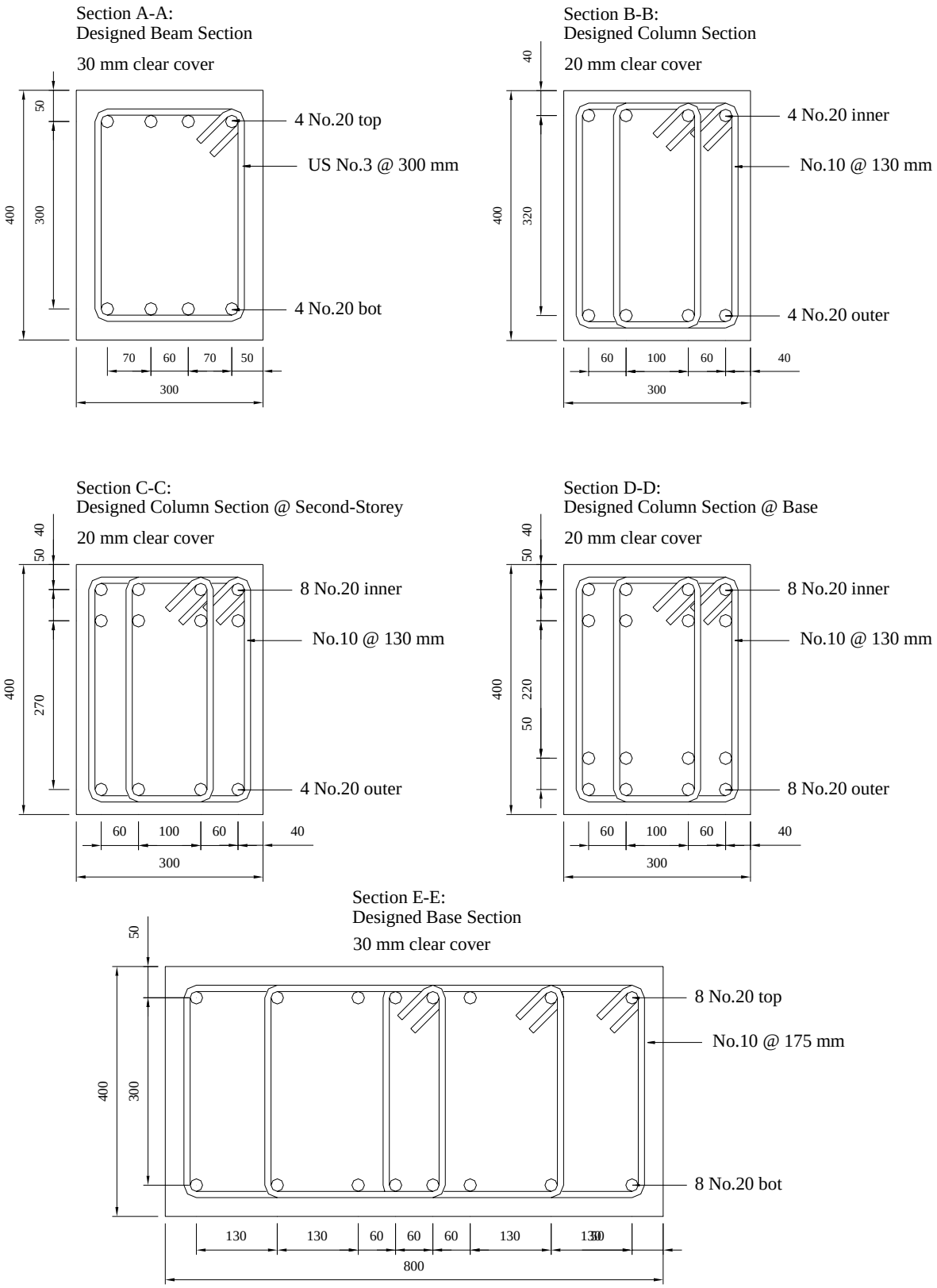

Figure 3.4 Designed Frame Member Cross-Sections

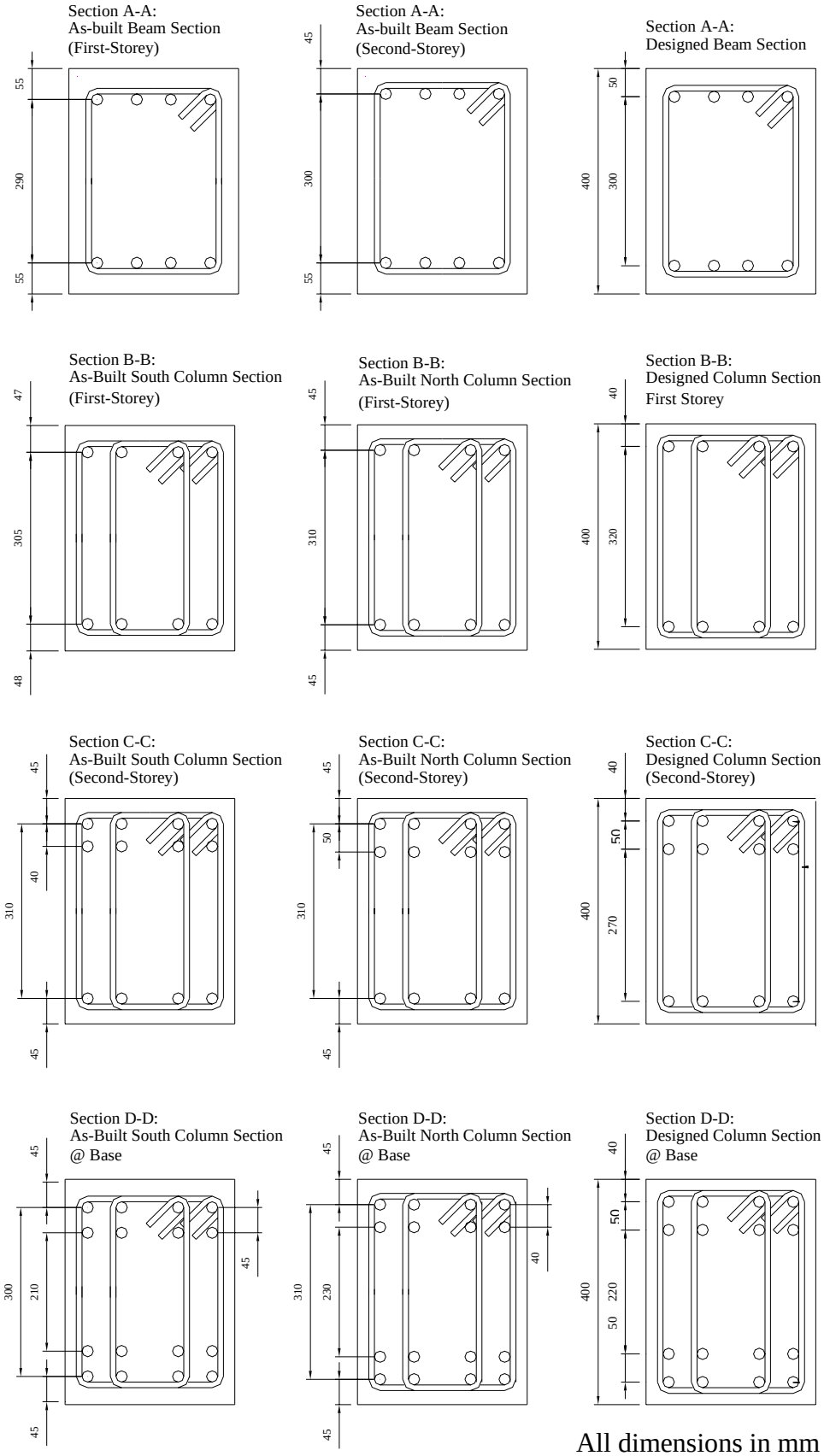

Figure 3.5 As-Built Frame Member Cross-sections

3.3 MATERIAL PROPERTIES

The material properties of concrete, reinforcing steel, and carbon fibre reinforced polymer (CFRP) are presented.

3.3.1 Concrete

Concrete for the specimen was provided by Dufferin-Custom Concrete Group. The concrete specifications are presented in Table 3.2 below:

Table 3.2 Concrete Order Specifications

Product Code	S2019220
Compressive Strength	20 MPa (specified @ 28 days)
Aggregate	10 mm maximum
Air	No additional
Slump	75 mm
Volume	4 m^3
Super-plasticizer	To be sent with truck

Note: Two hours set retarder was added during transportation.

Even though the concrete order had a specified 28 days compressive strength of 20 MPa, the desired 28 days strength for this experiment was actually 30 MPa (same as the Cement Tower). The 10 MPa difference in concrete strength accounted for the overshooting of the targeted strength used by the concrete companies as a safety margin. It was estimated that the concrete order of 20 MPa would yield a 28 days compressive strength of approximately 30 MPa. It was undesirable to acquire a concrete compressive strength drastically greater than 30 MPa since the failure mode would be affected. 10 mm aggregate size and 75 mm slump were specified to provide an adequate level of workability. A two hour set retarder was added during transportation to prevent the concrete mixture from stiffening up during casting. Upon concrete arrival, the initial slump was determined to be 25 mm. Water was added to adjust the slump to 95 mm. In addition, super-plasticizer was added half way through casting to maintain workability.

Cylinder compression tests (150 mm in diameter and 300 mm in height) were performed according to the ASTM C39 Standard at 8 days, 28 days and on the day of testing. Cylinders were subjected to either lab or moist cured conditions, with the former subjected to the same curing condition as the specimen. Lab cured cylinders were tested at the aforementioned days, while moist cured cylinders were only tested at 28 days maturity. Both lab and moist cured modulus of rupture tests (152 x 152 x 508 mm prism) were performed at 28 days according to the ASTM C78-94 Standard. Table 3.3 summarizes these concrete test results. Refer to Appendix A for the concrete stress-strain responses.

Table 3.3 Concrete Strength Test Results

Days After Cast	f'c (MPa) Lab Cured	f'c (MPa) Moist Cured	f'r (MPa) Lab Cured	f'r (MPa) Moist Cured
8	21.3	-	-	-
28	34.4	35.1	3.33	5.69
9 months (test date)	42.9	-	-	-

Note: Strengths were obtained from an average of three specimens.

3.3.2 Steel Reinforcement

Three different sizes of deformed reinforcing bars were used in this experiment: No.10, No.20, and US No.3. Their nominal diameters, cross-sectional areas, and locations of usage are listed in Table 3.4. Standard tensile coupon tests were performed on a 1000 kN MTS testing machine. Results are listed in Table 3.5. Refer to Appendix A for the typical reinforcement stress-strain responses.

Table 3.4 Reinforcement Size and Location of Usage

Bar Size	Nominal Diameter (mm)	Cross-sectional Area (mm^2)	Location of Usage
No. 10	10	100	Column & base transverse steel
No. 20	20	300	Longitudinal steel
US No.3	9.5	71	Beam transverse steel

Table 3.5 Steel Reinforcement Material Properties

Bar Size	Sample	εy ($x10^{-3}$)	εsh ($x10^{-3}$)	fy (MPa)	fu (MPa)	E (MPa)	Esh (MPa)
No. 10	1	2.25	22.0	455	585	202 000	1190
	2	2.25	23.8	450	575	200 000	1163
	3	2.63	22.5	460	590	175 200	1232
	Mean	*2.38*	*22.8*	*455*	*583*	*192 400*	*1195*
No. 20	1	2.25	16.80	447	600	198 700	1337
	2	2.25	17.75	453	607	201 000	1354
	3	2.25	16.75	440	603	195 600	1424
	Mean	*2.25*	*17.1*	*447*	*603*	*198 400*	*1372*
US #3	1	2.38	27.5	503	618	212 000	1070
	2	2.40	25.8	507	613	211 000	1029
	3	2.45	31.5	507	613	207 000	977
	Mean	*2.41*	*28.3*	*506*	*615*	*210 000*	*1025*

3.3.3 Fibre Reinforced Polymer

Carbon fibre reinforced polymer (CFRP) was used to repair the damaged specimen. The type of CFRP used was Tyfo® SCH41S Composite: a high strength graphite Fibrwrap® system with carbon fibres orientated in the longitudinal direction and Kelvar 49 weft in the transverse direction. The epoxy resin used for the bonding of the CFRP was Tyfo® S Epoxy: a two part epoxy adhesive which consisted of components A (Shell epoxy) and B (Texaco Hardener). The mixing ratio by volume was 100 parts of A to 42 parts of B. Approximately one litre of epoxy was mixed to cover each square meter of FRP surface. The material properties of the composite are summarized in Table 3.4. Refer to Appendix A for the CFRP composite material datasheet.

Table 3.6 CFRP Material Properties

Product Name	f't (MPa)	E (MPa)	ε_{ult} (10^{-3})	Laminate Thickness (mm)
Tyfo® SCH41S	876	72400	12.1	1.0 mm

Note: Material properties were based on ASTM D 3039 standard coupon tests and a laminate thickness of 1.0 mm.

3.4 CONSTRUCTION

Construction of the test specimen commenced in June of 2004, and was completed in October of 2004. The entire procedure can be broken down into four stages: formwork construction and initial assembly, preparation and placement of the reinforcement, final assembly of formwork and lateral support system, and concrete casting. In a conventional building system, concrete frames are cast in an upright position, with the floor slabs, columns, and roof slabs cast in several stages. However, for constructability and casting considerations, this single-span two-storey reinforced concrete frame had all its members integrally built and cast in a reclined horizontal position as depicted in Figure 3.6. Discussions and figures presented in this section henceforth will describe the frame with reference to this reclined construction setup.

3.4.1 Construction Phase 1: Formwork Construction and Initial Assembly

Formwork construction and its initial assembly involved cutting plywood sheets to the appropriate dimensions, constructing the wall panels, partially assembling the formwork, and installing custom corner mouldings. In preparation of formwork assembly, 250 mm deep spacers were placed under the body region of the frame to accommodate the elevation difference between the base and body (Figure 3.6a). A surveying level was used to check the relative elevations of these spacers to ensure a leveled casting platform.

a) Formwork Spacers b) Partial Formwork c) Corner Moulding

Figure 3.6 Construction Phase 1: Formwork Construction and Initial Assembly

Plywood sheets, 19 mm (¾") in thickness, were cut into side and bottom panel pieces according to the formwork layout and design presented in Appendix A. Side panels were stiffened with 50 x 100 mm (2"x4") spruce wailers, and panel pieces were assembled together in a manner depicted in Figure 3.6b. At this stage, several side panels were omitted from the assembly to allow space for placing steel reinforcement during phase 2 of construction. At the base of the frame where the concrete height of 800 mm was large enough to generate notable hydrostatic pressures during casting, steel soldiers were braced against the base side panels to provide lateral stability. Where floor anchor bolts were to be installed at the base (Appendix A), 75 mm (3") diameter holes were drilled in the side panels in order to insert twelve 75 mm (3") ABS pipes that were to be cast-in-place. Similarly, 25 mm (1") holes were drilled at the second-storey mid-column side panels to accommodate galvanized pipes. 25 mm (1") threaded rods would eventually be inserted through these pipes to help lift the specimen.

Custom-fitted corner mouldings were fabricated and attached onto the column bases and beams (where CFRP was to be wrapped during repair) as illustrated in Figure 3.6c. The curved corner moulding was designed with a radius of 50 mm to reduce the CFRP corner stress concentration and hence prevent CFRP local rupture (ISIS #4 Design Manual, 2001). Appendix A contains the moulding details as well as the fabrication sequence. Since oiling at a later time would be difficult once the steel cage was assembled, formwork pieces that were in place were oiled in preparation for casting.

3.4.2 Construction Phase 2: Preparation and Placement of Reinforcement

Preparation and placement of reinforcement involved cutting and bending longitudinal and transverse rebars to the specified dimension, installing strain gauges (see Section 3.6.1), and arranging the rebars as depicted in Figure 3.7. The steel reinforcement was assembled in the following manner. First, the base steel cage was constructed separately and placed into position. Wooden rebar spacers and rebar ribbon ties were used to keep the steel from shifting during assembly. Plastic chair spacers were

employed to elevate the longitudinal steel bars to the desired cover height. Next, the first-storey beam cage was constructed and moved into psition. The two column cages were then assembled in place. This involved individually inserting each longitudinal column rebar through the base rebar cage, column opening in the base formwork, column hoop ties, and finally the first-storey beam-column joint.

The level of steel congestion at this point was high. To alleviate obstruction and facilitate further steel placement, the inner column hoop ties within the base-column joints, and both the inner and outer column hoop ties in the beam-column joints were omitted for the time being. The important aspect to note here is the correct placement of rebar overlap between the column and beam longitudinal rebars. Once the column cages were fully assembled, the second-storey beam cage was built and carefully inserted into position, again paying close attention to the rebar overlap. Finally, the column hoops that were omitted at the base-column and beam-column joints were bent and welded into place. Bars were bent either manually using a pipe bender or by heating with a torch and subsequently bent into position with a hammer.

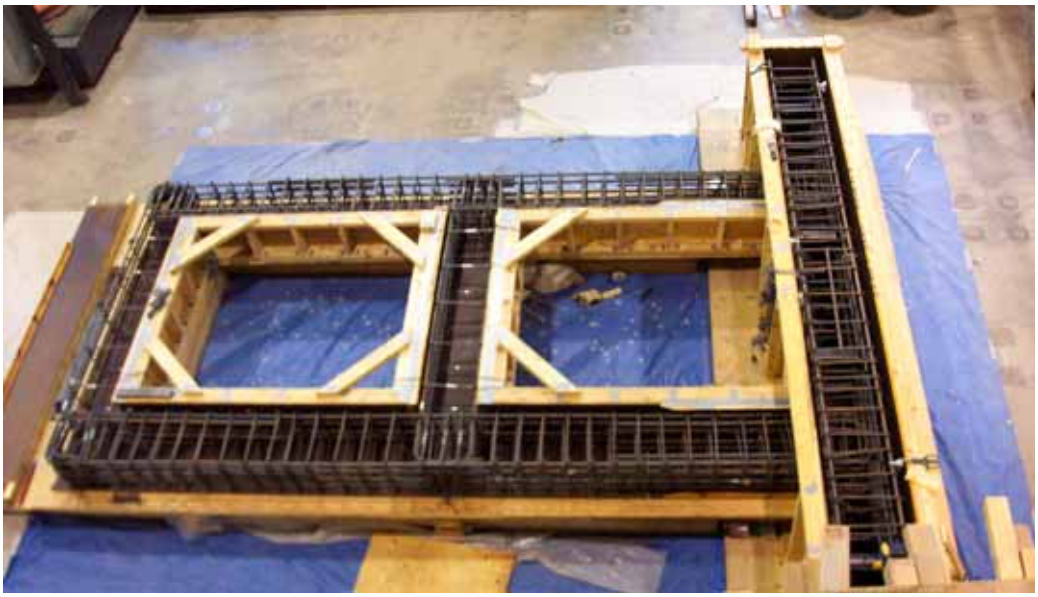

Figure 3.7 Full Steel and Partial Formwork Assembly

3.4.3 Construction Phase 3: Final Assembly of Formwork and Lateral Support System

Once all the steel work was completed, the remaining side wall panels and corner mouldings were oiled and attached. The joints were sealed with silicon. Aluminum pipes for the lifting attachment and ABS pipes for the floor anchor bolts were placed into position. Additional 50 x 100 mm (2”x4”) wooden ties were screwed laterally onto the top of the body and base formwork to provide stability during casting. As well, steel soldiers and threaded rods were anchored at the base. Figure 3.8 shows the full steel and formwork assembly prior to casting.

Figure 3.8 Full Steel and Full Formwork Assembly

3.4.4 Construction Phase 4: Concrete Casting

The fourth and final phase of construction was casting the specimen (Figure 3.9). The base and body of the frame were cast simultaneously in four and two layers respectively. A large vibrator was used as the primary means of consolidation. In addition, a small vibrator was used in areas where the frame was congested with steel

reinforcement. The concrete surface was leveled and finished with trowels. Two hours after casting, the surface was covered with wet burlap and plastic to promote moist curing. The burlap was kept wet for 10 days. In addition to the test specimen, 30 cylinders (150 mm in diameter and 300 mm in height) and four modulus of rupture moulds (152 x 152 x 508 mm) were cast to obtain standard material property data.

Figure 3.9 Casting of Test Frame

3.5 TEST SETUP

The test setup involved moving the frame into its testing position, preparing the concrete surface, and assembling the instrumentation and testing apparatus. At one month after casting, the frame was lifted from its casting position and placed into its testing position with the use of an overhead crane, a steel beam, two steel ropes, and two lifting attachments as illustrated in Figure 3.10. The steel beam was suspended from the crane where steel ropes were attached at the two ends of the beam. These ropes were

then looped around two lifting attachments that were located at the midheight of the second-storey columns of the frame. Once the frame was in position, its base was fixed to the strong floor via twelve post-tensioned anchor bolts. The concrete surface was sanded and painted with a 1:1 water to white latex paint mixture. Electronic demountable gauges (Zurich gauges) were epoxied onto the concrete surface as discussed in Section 3.6.2. The testing assembly and instrumentation layout were set up as depicted in Figure 3.11, and described in the following paragraphs and next section respectively.

The testing assembly consisted of a vertical and lateral loading system, as well an out-of-plane bracing system. Vertical column loads were applied in the following manner through four hydraulic jacks. On top of each column rested a 300 x 300 x 25 mm loading plate and on top of the plate rested a transverse steel beam. Two hydraulic jacks, each with a capacity of 450 kN, were attached to each end of the beam via threaded rods and Dywidag bars (Figure 3.12). The bottom of the hydraulic jacks were attached to the floor plates and subsequently bolted to the strong floor. The column load of 420 kN per column (210 kN per jack) was applied and held constant through out the test in a force controlled manner.

Horizontal loading was applied using a displacement controlled actuator positioned at the top storey beam centreline. This actuator had a load capacity of 1000 kN and a stroke capacity of around $\pm$ 165 mm (after accounting for the slack of the loading system). The actuator was balanced into position with a pulley system as depicted in Figure 3.13. Both the forward and reverse loading was applied to the frame. For loading consistency, a loading apparatus was fabricated to induce a compression force in the second-storey beam when either a forward or reverse cyclic was applied. This loading apparatus consisted of two 35 mm diameter rebars attached to two 254 x 254 x 25 mm HSS sections. The rebars straddled the top storey beam and were slotted through two HSS sections that rested on the north and south column outer faces (Figure 3.14). During forward loading, the actuator applied a direct lateral load to the frame and induced a compression force to the second-storey beam. During load reversal, the

actuator pulled against the HSS section on the north end, thereby pulling the two rebars. In turn the rebars pulled against the HSS section at the south end and induced a horizontal compression force to the beam. Since the actuator stroke capacity was ±100 mm, in order to accommodate larger displacement ranges during the cyclic portion of testing, three actuator spacers were fabricated. These spacers were made out of HSS 127 x 178 x 12 sections that were cut into three different lengths: 80 mm, 170 mm, and 240 mm. For instance, to achieve the largest forward stroke, the actuator was backed up completely, the 240 mm spacer was slotted between the actuator and loading apparatus, and the actuator was pushed forward.

Finally, an out-of-plane framing system consisting of four columns was implemented. The four columns, two at the north end and two at the south end, were bolted to the strong floor on the east and west sides of each concrete column (Figure 3.11). A stub beam was bolted on the top of each steel column to provide out-of-plane support in the unlikely event of total collapse in the out-of-plane direction. The four steel columns also provided supports to mount LVDTs (Section 3.6.3).

Figure 3.10 Lifting of Test Frame

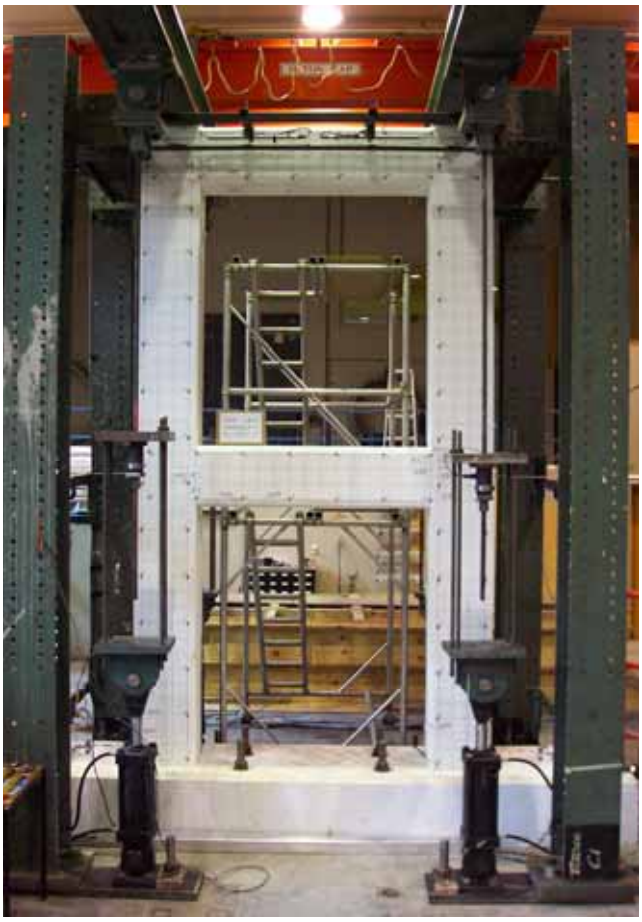

West Elevation

North East Elevation

Figure 3.11 Overall View of Test Setup

Figure 3.12 Vertical Loading System

Counter Weight

Actuator Pulley Cables

Figure 3.13 Actuator Pulley System

North View

West View

South View

Figure 3.14 Lateral Loading System

3.6 INSTRUMENTATION

The Heliotronic data acquisition system is a computer-controlled system used to record all electronic test data from the following outputs: steel and CFRP strain gauges, Zurich gauges, and LVDTs. Descriptions of these devices are discussed below.

3.6.1 Strain Gauges

Two types of strain gauges were used in this experiment: 5 mm length gauges for reinforcing steel and 60 mm length gauges for CFRP. When attached to a rebar, the gauge was able to monitor the steel deformation during testing. Readings from the strain gauges were used to correlate rebar stresses in the experiment. A total of thirty-six steel strain gauges were mounted at the locations of the beam and column flexural hinging and on the beam stirrups (Figure 3.16). Eight of these strain gauges (C1-C8) were placed on the column longitudinal rebars within the vicinity of column hinging, at approximately 60 and 360 mm away from the column-base interface. Sixteen gauges (B1-B16) were attached on the beam longitudinal rebars at the four hinge locations, at approximately 30 mm away from the beam-column interface. The remaining twelve gauges (S1-S12) were placed at midheight of the first and second-storey beam stirrups. Thirty-two strain gauges were attached to the CFRP surface (Figure 3.17). Similar to the rebar strain readings, the CFRP surface strain readings were correlated to CFRP stresses and load contributions. There were five CFRP strips equally spaced out on each of the two beams. On the west face of the beams, ten strain gauges were applied at the mid-depth, along the vertical centreline of each strip. In addition, top and bottom strain gauges were attached to several CFRP strips to record the strain profiles along the depth. Top and bottom strain gauges were located on average 50 mm from the top, and 50 mm from the bottom of the beam respectively. On the east face of the beams, ten gauges were also applied at the mid-depth.

3.6.2 Zurich Gauges

Zurich targets are small (approximately 10 mm in diameter) circular metal studs that were attached to the concrete surface and used to measure concrete surface strains. Zurich readings were only taken during Phase A of testing, because targets on the beams were removed to accommodate repair. Surface strains were recorded after each load stage by measuring the relative movement between the targets using an electronic gauge. Vertical, horizontal and diagonal surface strains were recorded between the targets. Prior to testing, eighty-eight targets were attached to the west face of the frame's concrete surface using a thin layer of super glue, followed by an epoxy coating applied around the targets' edges. Targets were arranged in a 300 mm x 300 mm grid along the columns and beams (Figure 3.18). The first set of column targets were positioned at 50 mm from the column-base interface. The beam targets were centreed about the specimen's vertical axis. All targets were situated 50 mm from the outer concrete edge, which represented the approximate location of the longitudinal reinforcement in the specimen. Furthermore, square grid lines 100 x 100 m in dimension were drawn on the west face to improve clarity in crack documentation.

3.6.3 Linear Variable Differential Transducers

Linear variable differential transducers (LVDTs) were placed at various locations on the frame to monitor lateral and vertical deflections, as well as any potential base slip and out-of-plane movement. Where possible, the LVDTs were attached at the centreline of the specimen. Seventeen LVDTs were used in total and were placed in the locations described in Table 3.7 and Figure 3.16. The top storey lateral displacement was detected by four LVDTs (WNHT, WSHT, ENHT, ESHT) located at the east and west faces of the north and south columns. Ideally, these LVDTs should be attached at the north and south column faces directly; however, the lateral load attachment was present at these locations. Lateral displacements at the first storey beam height and column base level were monitored by four LVDTs (NHM, NHB, SHM, SHB). Potentially base slip was screened

at the south end with one LVDT (BASESLIP), and out-of-plane movement was detected by two LVDTs (NHTOP, SHTOP). These two LVDTs were located on the east face of the specimen, at the top of the north and south columns. Column axial shortening and elongating was monitor by six LVDTs (NVT, NVM, NVB, SVT, SVB, SVB). These LVDTs were located on the east faces of the columns, at the top, middle and bottom of the each column.

Table 3.7 Layout of LVDTs

Horizontal LVDT	**Location on Specimen**	**Direction of LVDT**
WNHT	N column, W face, top storey beam-column joint	NS
WSHT	S column, W face, top storey beam-column joint	NS
ENHT	N column, E face, top storey beam-column joint	NS
ESHT	S column, E face, top storey beam-column joint	NS
NHM	N column face at mid height (1st storey beam)	NS
NHB	N column face at column base	NS
SHM	S column face at mid height (1st storey beam)	NS
SHB	S column face at column base	NS
NHTOP	N column, E face, top storey beam-column joint	EW
SHTOP	S column, E face, top storey beam-column joint	EW
BASESLIP	Base south end	NS
Vertical LVDT		
NVT	N column, E face, top storey beam-column joint	Up Down
NVM	N column, E face, mid height (1st storey beam)	Up Down
NVB	N column, E face, column base	Up Down
SVT	S column, E face, top storey beam-column joint	Up Down
SVM	S column, E face, mid height (1st storey beam)	Up Down
SVB	S column, E face, column base	Up Down

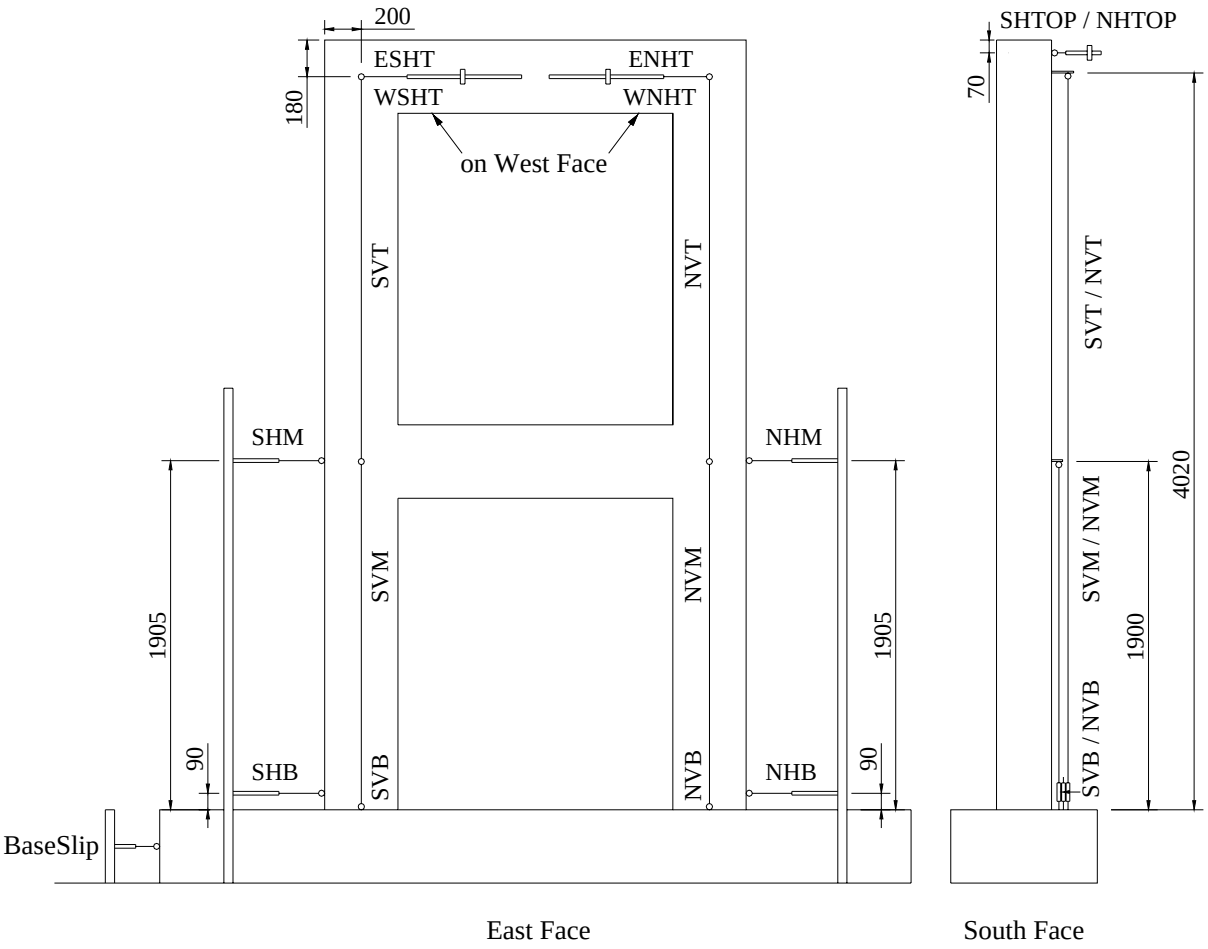

Note: SVB and NVB are located at the height of the column-base interface, and offset at 65 mm away from the column face.

All dimensions in mm

Figure 3.15 Layout of LVDTs

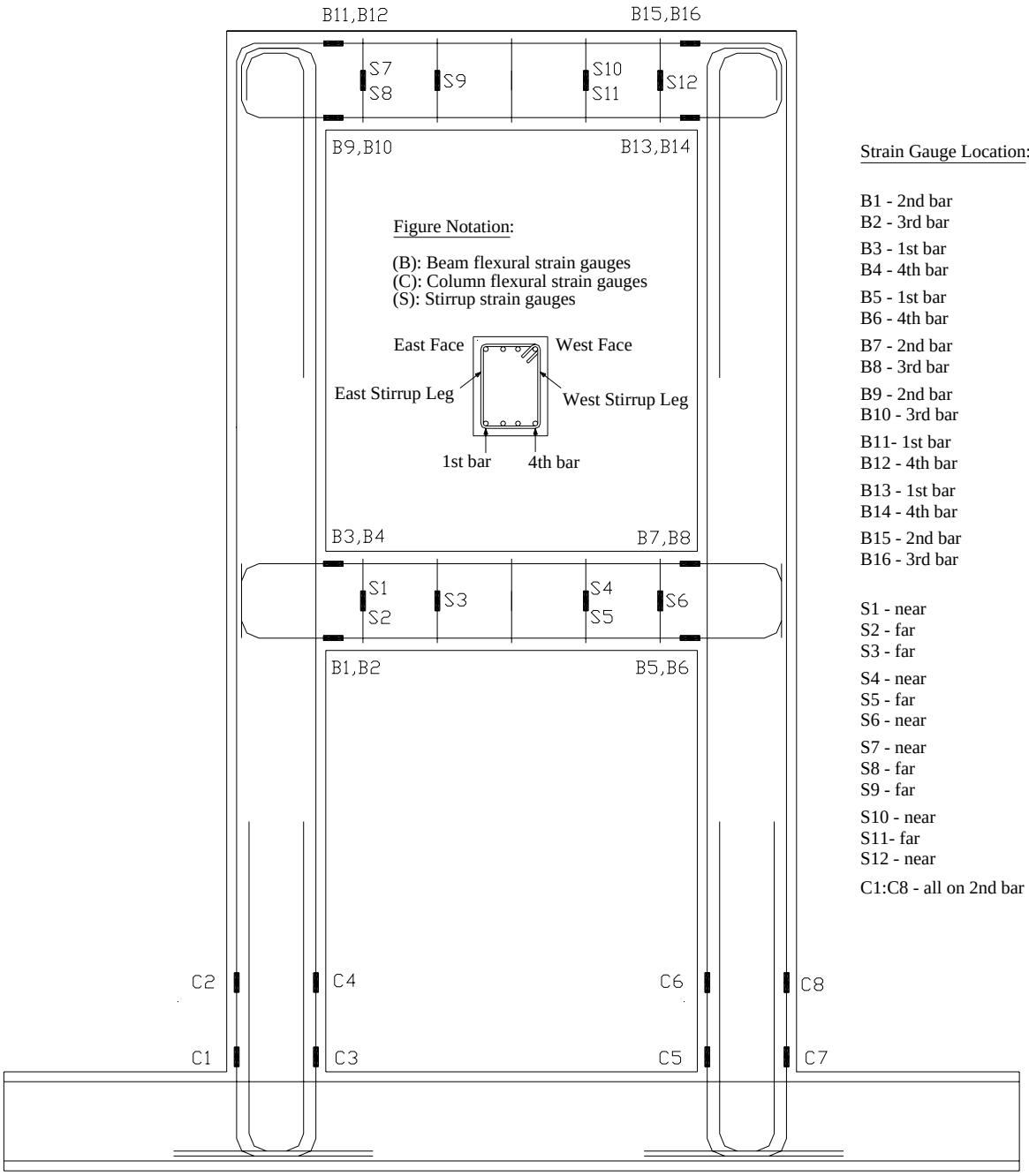

Notes:

Beam flexural strain gauges (B) were located 30 mm from the face of the column.
Column flexural strain gauges (C) were located 60 mm and 360 mm from the face of the base.
Stirrup strain gauges (S) were located at the midheight of the stirrups.

Transverse steel in the columns and base were ommited from the drawing for clarity.

Figure 3.16 Steel Strain Gauge Layout

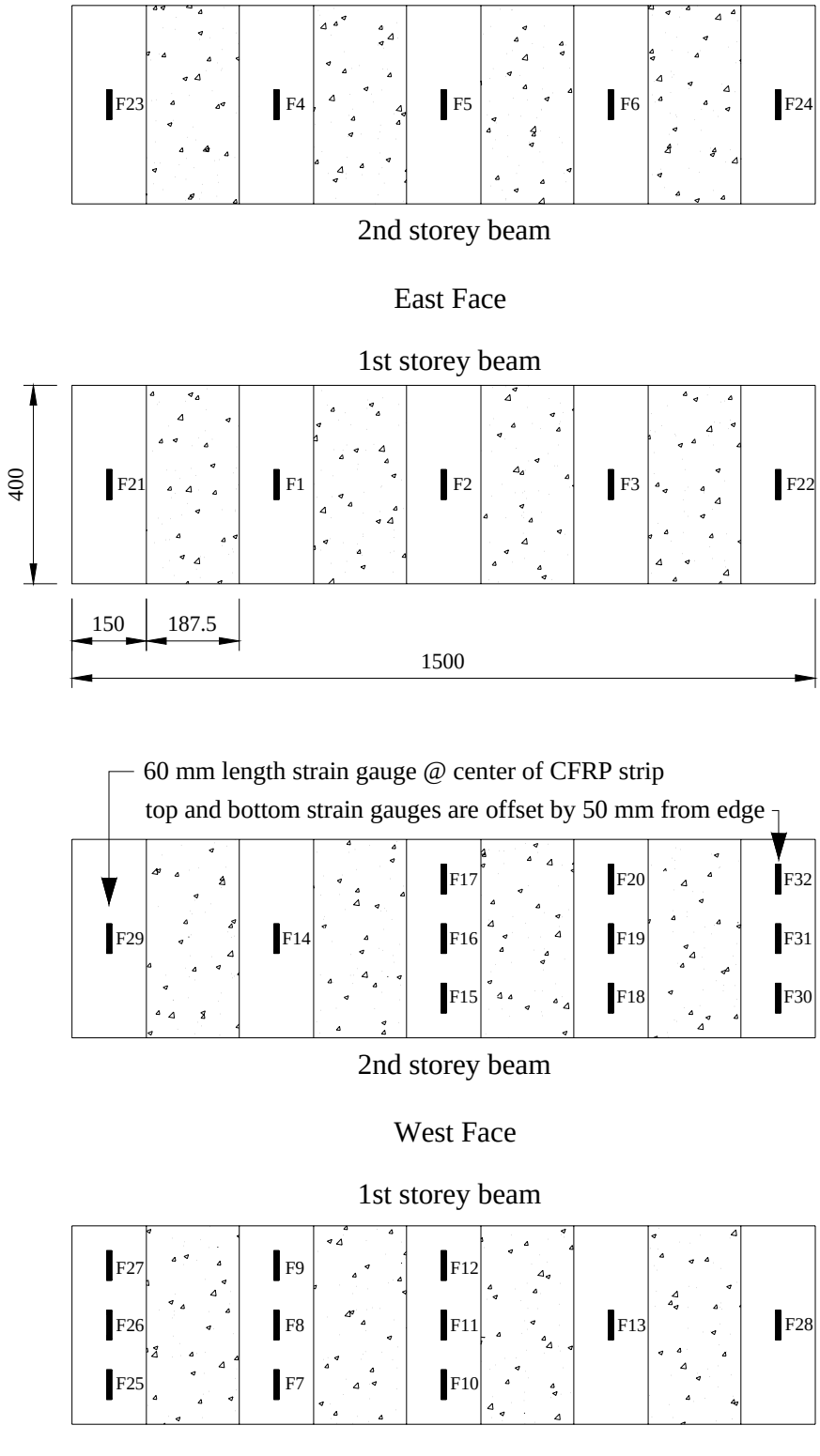

Figure 3.17 CFRP Strain Gauge Layout

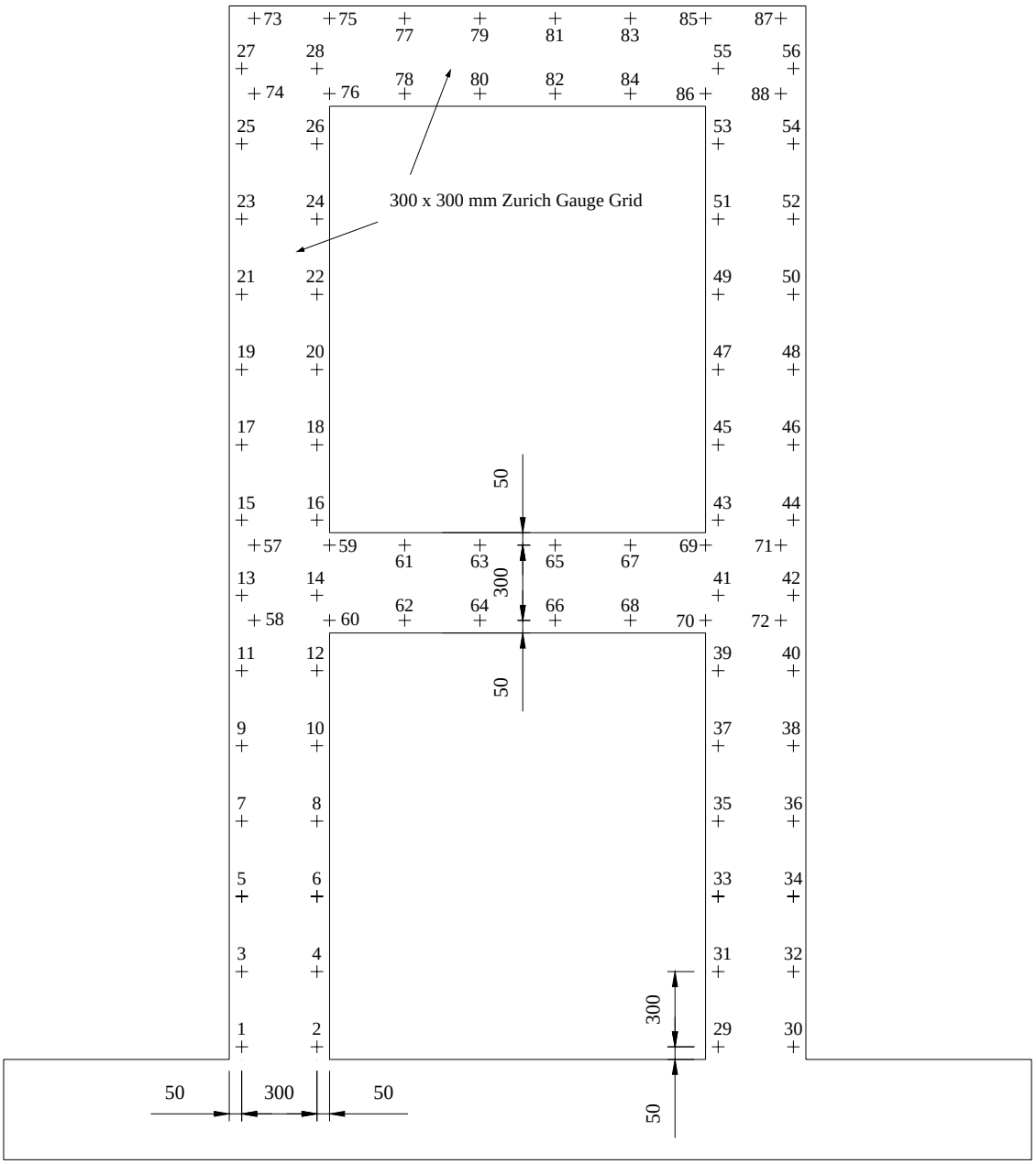

All dimensions in mm

Figure 3.18 Zurich Gauge Layout

3.7 LOADING SEQUENCE

Two phases of loading were carried out: Phase A for a single reverse cycle and Phase B for a sequence of reverse cycles at multiples of the yield displacement. In Phase A, the frame was loaded in the forward direction (forward half-cycle) until significant shear damage occurred, retracted back to zero, loaded in the reverse direction (reverse half-cycle) to the same displacement reached in the forward half-cycle, then unloaded. This phase of testing took five days to complete and twenty-six load stages to record. Repair of the beams was made in between Phase A and B as described in Section 3.8. In Phase B, twelve load cycles were performed at various increments of the yield displacement. Seven days were devoted to this phase of testing.

The testing regime commenced by applying a constant vertical load of 420 kN at the top of each column. This force-controlled load was sustained throughout the entire duration of testing (during Phase A, repair, and Phase B). The horizontal load was applied in displacement-controlled mode. Horizontal load was applied at the second-storey beam via the horizontal loading attachment as described in the Section 3.5. At early load stages, the horizontal load was held constant while data such as crack widths and Zurich readings were gathered; however, at latter load stages, the load was reduced to approximately 80% for safety. At the end of each day, the horizontal load was released, while the vertical load was held. At the beginning of each test day, the horizontal load was brought back to the original level from the previous load stage.

During the forward half-cycle of Phase A, load stages were taken at increments of 25 kN or at important changes in structural behaviour (e.g. first cracking, sudden propagation in crack width etc.). The data was collected diligently at each stage since the results were used extensively in the discussion portion of this project. During the reverse half-cycle of Phase A, a courser load increment of approximately 30 kN was adopted. Only the prominent crack widths were measured and Zurich readings were only recorded

at selected load stages for time economy. The entire loading sequence for Phase A is summarized in Table 3.8.

Table 3.8 Loading Sequence of Phase A

Load Stage	MTS Load (kN)	Zurich Reading	Comments
Phase A: Forward Half-cycle			
0	0	Y	Zurich reading was read twice prior to column loading, and once after column loading.
1	25	Y	
2	50	Y	
3	75	Y	First beam flexural crack
4	100	Y	First column flexural crack
5	125	Y	
6	150	Y	First beam shear crack
7	175	Y	
8	200	Y	
9	225	Y	
10	250	Y	
11	275	Y	First joint crack
12	300	Y	
13	325	Y	
14	331	Y	Sudden drop in load
15	335	Y	10+ mm shear crack width, 40 mm Δ
Phase A: Reversed Half-cycle			
16	0	Y	Initial position after repair
17	-30	Y	First beam flexural crack
18	-70	N	
19	-86	Y	Sudden propagation in flexural crack width
20	-110	Y	Zero displacement position & first column flexural crack
21	-140	N	First beam shear crack
22	-170	N	
23	-186	N	Sudden propagation of shear crack width
24	-200	N	
25	-265	N	4 mm shear crack width
26	-310	N	Approximately - 40 mm Δ

Note: Refer to the Chapter 4 (Results) for a detailed summary of the structural behaviour at each load stage.

Load cycles during Phase B were performed in the following sequence:

2 cycles each of	$\pm 0.75\ \Delta_y$
	$\pm 1.0\ \Delta_y$
	$\pm 2.0\ \Delta_y$
	$\pm 3.0\ \Delta_y$
4 cycles of	$\pm 4.0\ \Delta_y$

The yield displacement was determined from Phase A to be 25 mm (Chapter 4). This displacement corresponded to the approximate first yielding of the beam flexural steel of the original test specimen. Following the fourth cycle at $\pm 4.0\ \Delta_y$, the frame was pulled until the actuator stroke limit was reached. This corresponded to $-6.6\ \Delta_y$ or 160 mm. Since the actuator stroke capacity was $\pm$100 mm, and taking into account for slack displacement inherent in the horizontal loading attachment, loading spacers were changed at each half-cycle of the $\pm 4.0\ \Delta_y$ cycles in order to reach the desired displacements. At the start of each load cycle, the horizontal load was increased continuously until the desired positive displacement was reached. Depending on the stability of the structure, the load was either sustained or decreased slightly while crack lines were drawn, crack widths were measured, and photos were taken. Zurich readings were not taken during Phase B. After data recording, the load was reversed until the corresponding negative displacement was reached. Once again, data was gathered. Since the beams elongated when cracking occurred, for the pushing phase of each cycle, the displacement was read off from the top storey beam LVDTs located on the north side of the specimen (i.e. WNHT, ENHT), and vice versa.

3.8 REPAIR

After Phase A of testing, repair was carried out on the first and second-storey beams. The repair procedure involved chipping off unsound concrete, grouting the large voids, epoxy injecting the cracks, grinding off paint, smoothing out sharp corner edges, and wrapping the beams with CFRP. The lateral load was removed during repair while

the vertical load was held constant through out. Refer to Figure 3.19 to Figure 3.23 for photographs of the repair process.

Three days were devoted to chipping off loose concrete. The regions of unsound concrete were determined by knocking on the concrete surface with a metal bolt and listening to the impact sound. Unsound concrete produced an echoing tone that was different from the crisp sound produced from sound concrete. The loose concrete was chipped off with a hammer and an electric jack chisel. Five sections in total were removed. Two additional days were spent grouting the five sections that were chipped off. Hand patching was performed using a ThoRoc SP20 mortar: a shrinkage-compensated, microsilica-enhanced wet mortar suitable for hand troweling on horizontal, vertical, and overhead surfaces (refer to Appendix A). The grouting procedure was in compliance with the recommended procedure from the manufacturer's datasheet. This grout was selected for its workability and compatible strength to the existing concrete. The grout was moist cured for the minimum recommended three days.

Once the grout was cured, epoxy injection of cracks was carried out. Due to the advanced technical nature of epoxy injection, this task was performed by the Vector Construction Group: a consulting firm who specialized in reinforced concrete repair. Plastic pump tubes were first epoxied onto the crack surface. Next, an epoxy paste - KEMKO 022 SuperSEAL - was applied along the crack lines to seal up all cracks. Pressure injection was carried out via the plastic tubes using a liquid form of epoxy - KEMKO 068 LoVIS IR. This liquid epoxy cured into a rigid form that was suitable for the structural repair of cracks and delaminations in concrete. This procedure took one day to complete.

Following the epoxy injection, approximately four days were spent to prepare the concrete surface for CFRP wrapping. The plastic tubes from the injection were chipped off. The surface epoxy, rough concrete corners, and surface paint were grinded and sanded off to expose a smooth, bare, and even concrete surface. Although wooden corner mouldings were previously cast-in-place to create a curved beam corner profile, some

edges were still sharp and uneven, and required grinding. An electric stone wheel grinder was used to smoothen out the corners.

Once the beam concrete surface was smooth, dry, and free of dust, two days were spent to wrap ten strips of CFRP around the first and second-storey beams. The CFRP fabric was delivered as a roll of approximately 610 mm in width. Strips of CFRP 150 mm wide and approximately 1500 mm long were cut. 1500 mm in length gave a CFRP overlap of approximately 150 mm. The two-part epoxy resin (Tyfo® S) was used as specified in Section 3.3.3. A mechanical mixer was used to mix the two epoxy components for five minutes at a speed ranging between 400 to 600 rpm. The CRFP was first saturated with the epoxy resin on both sides with a paint roller and / or brush. As well, the concrete surface was also painted with epoxy where the strips of CFRP were to be applied. The epoxy resin was allowed 45 minutes to cure and become less viscous and slightly sticky. At this point, the CFRP was carefully wrapped around the beam, starting from the top of the beam, then working along the vertical face, bottom face, other vertical face, and finally back to the top where it overlapped itself. The thickness of the epoxy resin was not measured; however, at each stage, the paint roller was rolled against the concrete surface to squeeze out all the air bubbles and excess epoxy. This ensured a tight and smooth bond between the concrete and FRP, and between the FRP and FRP (at the overlap). The CFRP was left to cure overnight before surface strain gauges were applied.

First-storey Beam: West Elevation

First-storey Beam: East Elevation

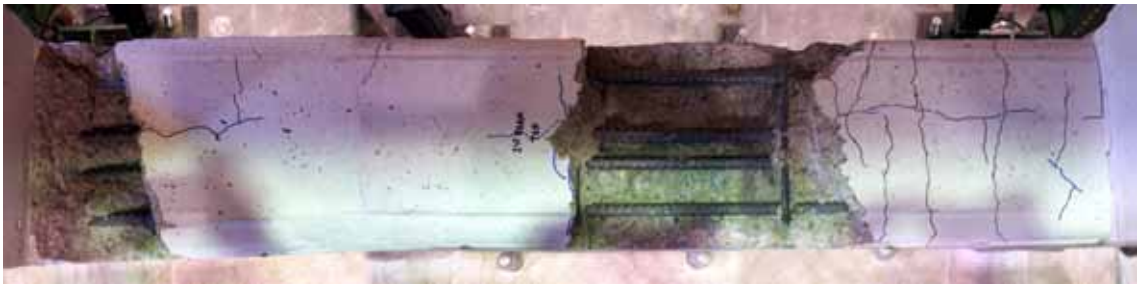

First-storey Beam: Top View

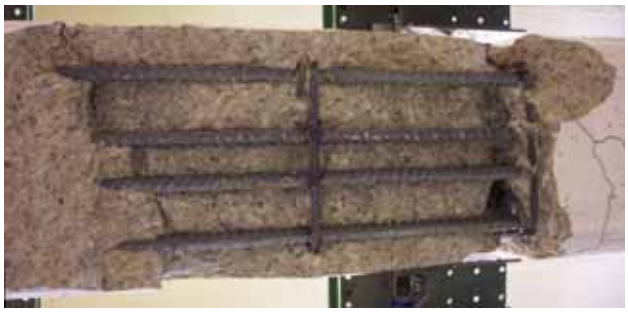

First-storey Beam: Bottom View

Second-storey Beam: South End, Top View

Second-storey Beam: East Elevation

Figure 3.19 Repair: Chipped Beams

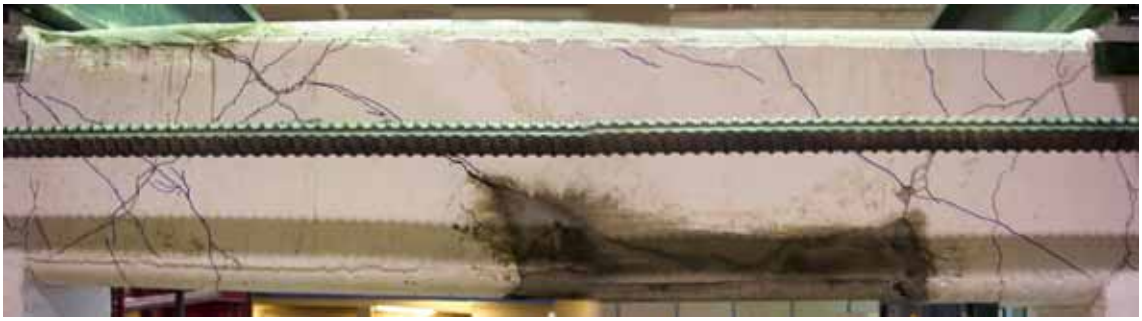

Second-storey Beam: East Elevation

First-storey Beam: West Elevation

Figure 3.20 Repair: Grouted Beams

Second-storey Beam: East Elevation

First-storey Beam: West Elevation

Figure 3.21 Repair: Epoxy Injected Beams

Second-storey Beam: East Elevation

Second-storey Beam: West Elevation

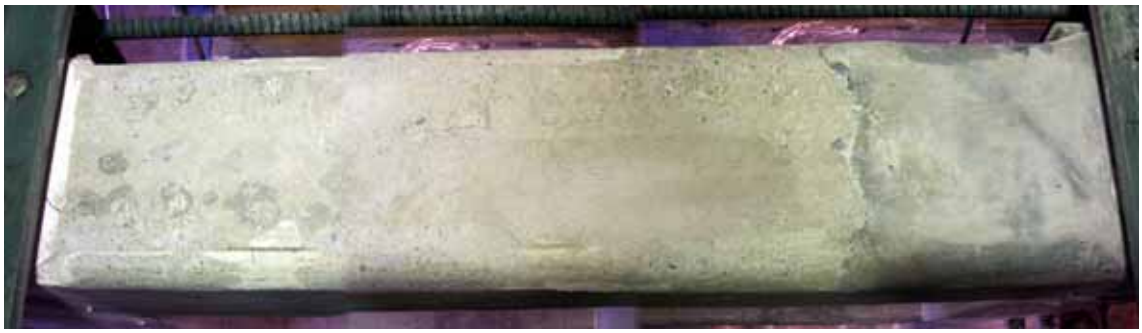

Second-storey Beam: Top View

Second-storey Beam: Bottom View

Figure 3.22a Repair: Pre-wrapped Beams (Beam2)

First-storey Beam: West Elevation

First-storey Beam: East Elevation

First-storey Beam: Top View

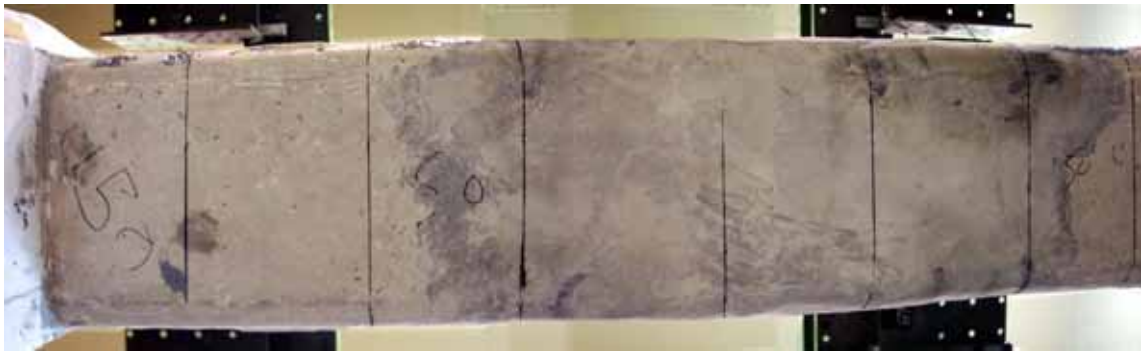

First-storey Beam: Bottom View

Figure 3.22b Repair: Pre-wrapped Beams (Beam1)

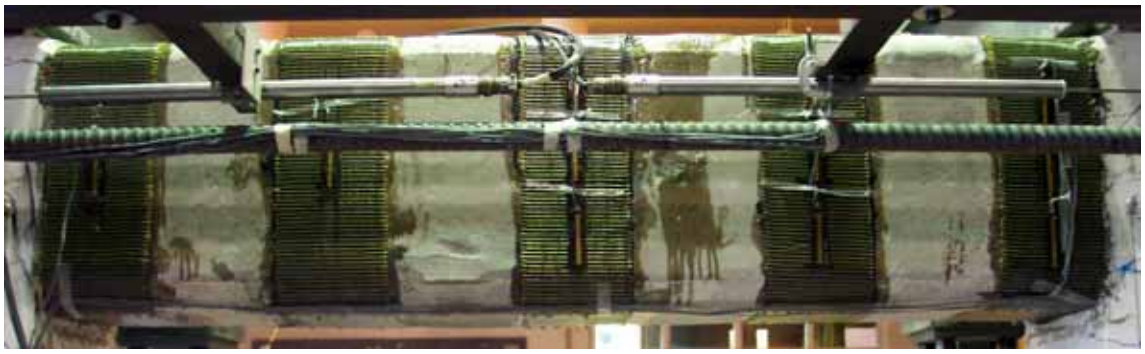

Second-storey Beam: East Elevation

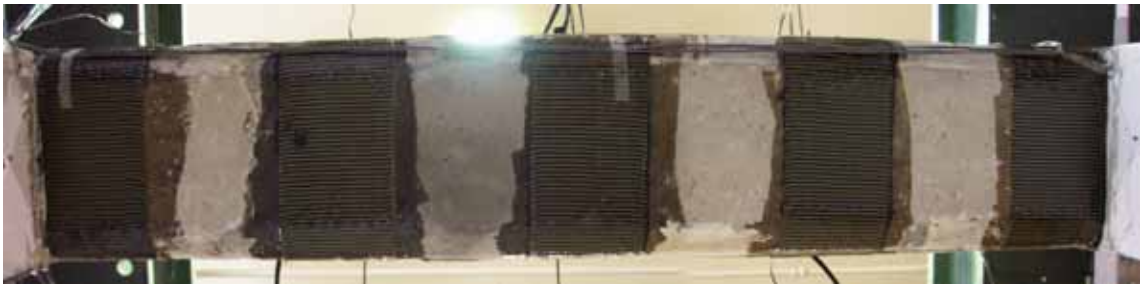

Second-storey Beam: Bottom View

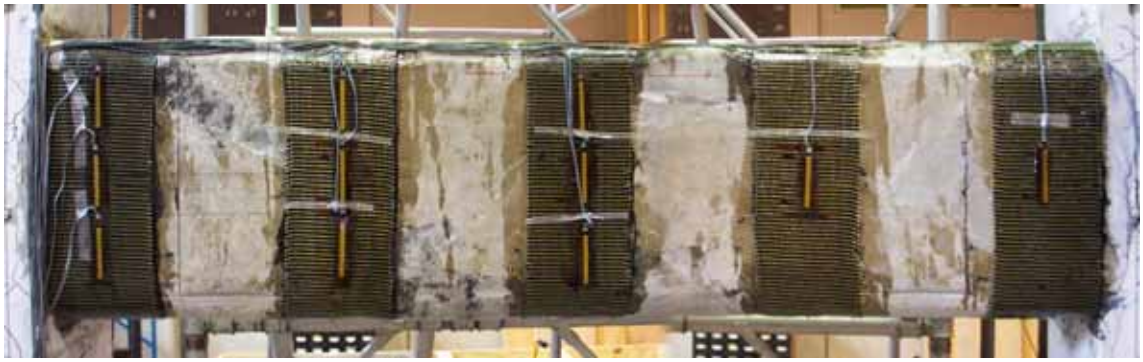

First-storey Beam: West Elevation

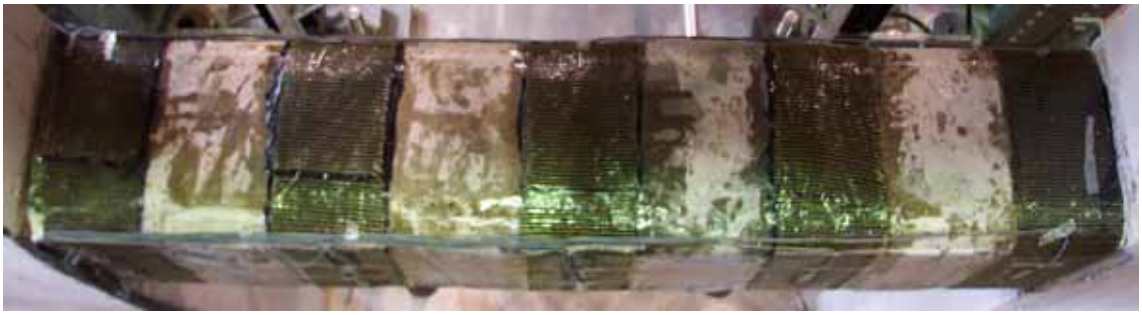

First-storey Beam: Top View

Note: The bottom and top views of both beams were similar

Figure 3.23 Repair: CFRP Wrapped Beams

Experimental Results

4.1 INTRODUCTION

This chapter summarizes in detail the experimental results and test observations. An overview of the frame orientation and testing conventions is first given, followed by a brief overview of the loading sequence and a detailed record of the test results. Documentation is made regarding the crack pattern, crack width propagation, locations of the first flexural and shear cracks, first reinforcement yield, locations of flexural hinging, and progression of CFRP debonding. Selective test photos are presented at the end of each testing phase. Graphs pertaining to the experimental results of Phase A and B are presented at the end of this chapter. This chapter focuses on the presentation of the unbiased results. Refer to Chapter 5 for the experimental discussion of all graphs.

4.1.1 Frame Orientation & Testing Conventions

To familiarize the reader with the frame orientation, a description of its layout is made with reference to the structural laboratory setting (refer to Figure 4.1). Note that some details of the test setup were excluded from this figure for clarity. The test frame was oriented in the north-south direction with its north column located near the strong wall. The actuator (not shown) was supported by the strong wall and was situated between the wall and the north column. Located on the east and west sides of the frame were four steel support columns and their accompanying steel floor plates. Four hydraulic column jacks (not shown) were mounted on top of these four floor plates and were used to apply the column vertical loads.

This chapter makes reference to the MTS actuator force and the net horizontal force. The former refers to the force generated by the actuator, while the latter refers to the actual net horizontal force exerted on the frame. This net force was calculated by taking into consideration the horizontal components of the vertical column jacks. As the

frame deformed laterally, the column forces that were being applied no longer remained vertical; therefore, the horizontal components of these column forces had to be subtracted from the actuator force in order to determine the net horizontal force. The horizontal induced forces from the column jacks were calculated at each load stage using trigonometry between the height of the column loading beam and the top storey lateral deflection. The lateral deflection was taken as the average LVDTs readings of WNHT, ENHT, WSHT, ESHT (Section 3.6.3). Unless stated otherwise, a reference made to the horizontal force refers to the net force.

Zurich targets and gridlines were drawn on the west face of the frame whereas the east face remained free of gridlines. Recall that the gridlines were 100 x 100 mm. The horizontal load indicated on the photos refers to the MTS actuator load, and not the net horizontal load. When test results are described for the beams, the following abbreviations are used:

- Beam1 referred to the lower or first-storey beam.
- Beam2 referred to the upper or second-storey beam.
- N / S / M referred to the north end, south end, or midspan of the beam, respectively.

For example, Beam1N(300) describes the location on the first-storey beam, at 300 mm away from the north beam-column interface. When a shear crack is assigned a specific location, this location refers to the distance measured from the beam-column interface to the origin of the shear crack located at the beam tensile edge.

To observe the crack pattern and to distinguish between cracks developed at various testing phases, several coloured markers were used (refer to Section 4.2.2 for an overview of the testing sequence or Section 3.7 for a detailed summary of the testing sequence). Blue was used for initial cracks caused from shrinkage and post-tensioning of the base, black for the forward half-cycle of Phase A, blue again for the reverse half-cycle of Phase A, and red for Phase B.

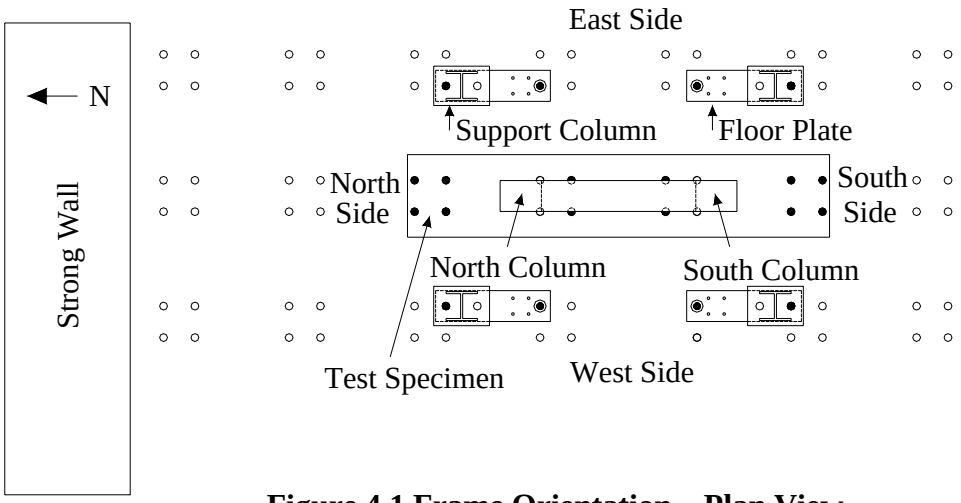

Figure 4.1 Frame Orientation – Plan View

4.2 RESULTS

4.2.1 Initial Conditions

Prior to loading, the frame was examined for cracks that may have developed from shrinkage or post-tensioning of the frame base. The frame did not exhibit any shrinkage cracks; however, post-tensioning cracks on the base were evident, particularly near the two columns where the anchor bolts were concentrated (Figure 4.2). These cracks were caused by undulations and bumps present in both the strong floor and frame base. Even though metal shims were inserted along the edge of the base to reduce the unevenness, gaps within the centre of the base were still present. The cracks were at most 0.1 mm wide and were superficial in nature. The base did not suffer any noticeable damage throughout the duration of testing, except during the last load cycle in Phase B. Even then, the base remained structurally sound.

Figure 4.2 Initial Conditions at Column Bases

4.2.2 Overview of Loading Sequence and Lateral Drift

Refer to Section 3.7 for the complete detailed loading sequence. Two phases of loading were carried out: Phase A for a single reverse cycle (i.e. forward half-cycle, and reverse half-cycle) and Phase B for a sequence of reverse load cycles at intervals of the yield displacement. The yield displacement was determined experimentally to be 25 mm. In Phase A, the frame was loaded in the forward direction (forward half-cycle) until significant shear damage took place, retracted back to zero load, loaded in the reverse direction (reverse half-cycle) to the peak displacement reached during the forward half-cycle, then unloaded. In Phase B, twelve load cycles and one reverse half-cycle were performed at various increments of the yield displacement. Table 4.1 summarizes the loading sequence and the corresponding lateral drift percentages. The lateral drift percentage was calculated as:

$$\text{Lateral Drift} = \Delta_{st} / H_{frame} * 100$$

where:

Δ_{st} = Lateral displacement (mm) at the centreline of the top storey beam taken as the average of four lateral LVDTs (WNHT, ENHT, WSHT, ESHT).

H_{frame} = Height of the column taken as the distance from the column-base interface to the centreline of the top storey beam (4000 mm).

Table 4.1a Summary of Net Horizontal Load and Lateral Drift

Load Stage	Net Horizontal Load (kN)	Avg. 2nd Storey Lat. Displ. Δ_{st} (mm)	% Lateral Drift
Phase A: Forward Half-cycle			
1	25	0.76	0.02
2	51	1.60	0.04
3	75	2.65	0.07
4	99	4.13	0.10
5	125	5.46	0.14
6	148	7.41	0.19
7	174	9.60	0.24
8	197	11.7	0.29
9	221	13.8	0.35
10	246	18.	0.46
11	272	21.7	0.54
12	295	25.5	0.64
13	320	30.0	0.75
14	325	32.3	0.81
15	327	44.7	1.12
unloading	281	42.7	1.07
	199	35.1	0.88
	107	24.8	0.62
Phase A: Reverse Half-cycle			
16	-2	10.8	0.27
17	-32	9.10	0.23
18	-69	5.56	0.14
19	-84	4.09	0.10
20	-111	1.02	0.03
21	-139	-1.78	-0.04
22	-168	-4.94	-0.12
23	-185	-7.10	-0.18
24	-197	-12.9	-0.32
25	-260	-24.6	-0.62
26	-304	-39.5	-0.99
unloading	-195	-33.5	-0.84
	-95	-23.6	-0.59
	+2	-7.43	-0.19

Note: Positive load, displacement, and drift values refer to the forward direction, and vice versa.

Table 4.1b Summary of Net Horizontal Load and Lateral Drift

Load Cycle		Net Horizontal Load (kN)	Avg. 2nd Storey Lat. Displ. Δ_{st} (mm)	% Lateral Drift
Phase B: Reverse Cyclic				
1	+0.75 Δ_y	+233	+18.8	+0.47
1	-0.75 Δ_y	-247	-19.2	-0.48
2	+0.75 Δ_y	+233	+19.3	+0.48
2	-0.75 Δ_y	-241	-19.6	-0.49
3	+1.0 Δ_y	291	+25.2	+0.63
3	-1.0 Δ_y	-298	-25.7	-0.64
4	+1.0 Δ_y	+283	+25.4	+0.64
4	-1.0 Δ_y	-289	-25.7	-0.64
5	+2.0 Δ_y	+399	+51.1	+1.28
5	-2.0 Δ_y	-395	-51.7	-1.29
6	+2.0 Δ_y	+377	+51.1	+1.28
6	-2.0 Δ_y	-384	-51.6	-1.29
7	+3.0 Δ_y	+422	+77.9	+1.95
7	-3.0 Δ_y	-424	-77.4	-1.94
8	+3.0 Δ_y	+406	+77.6	+1.94
8	-3.0 Δ_y	-414	-77.7	-1.94
9	+4.0 Δ_y	+417	+104	+2.59
9	-4.0 Δ_y	-422	-98.5	-2.46
10	+4.0 Δ_y	+403	+103	+2.58
10	-4.0 Δ_y	-412	-104	-2.61
11	+4.0 Δ_y	+397	+104	+2.60
11	-4.0 Δ_y	-403	-104	-2.59
12	+4.0 Δ_y	+377	+93.0	+2.33
12	-4.0 Δ_y	-395	-103	-2.58
13	-6.6 Δ_y	-444	-164	-4.09

Note: Positive load, displacement, and drift values refer to the forward direction, and vice versa. Δ_y was 25 mm.

4.2.3 Detailed Test History of Phase A: Forward Half-Cycle

Table 4.2 summaries the detailed observations for this portion of testing with reference to Figure 4.3 to Figure 4.9 (selective experimental photographs). All lateral LVDTs were set to zero immediately after the column loads were applied, and prior to any lateral load applications. For the forward half-cycle of Phase A, cracks were marked in black. Longitudinal steel strain gauges B4 and B5, located at the top layer of Beam1S and bottom layer of Beam1N, were damaged during construction.

The test specimen was not loaded to collapse. Damage to the specimen was critical to the point where any additional applied load or induced deflection may have caused the frame to fail or be damaged beyond a repairable point (i.e. excessive crack width). In the forward half-cycle of Phase A, the maximum lateral load applied was approximately 327 kN with a corresponding average top storey lateral displacement of 44.7 mm. The damage mode was a combined flexural-shear. Lower and upper beam flexural cracks were first observed at 75 kN, followed by a lower beam shear crack at 148 kN. At 197 kN, flexural cracks at both ends of the upper and lower beams stabilized while the lower beam shear crack widened up. In addition, several new shear cracks developed at the second-storey beam during this load stage. At approximately 295 kN, the first-storey beam longitudinal steel yielded in flexure at both ends. Stirrups at the first-storey beam yielded shortly after at 320 kN. At the most heavily damaged state, the largest shear crack at the first-storey beam reached 9 mm wide, while the largest shear crack at the second-storey beam reached 2 mm wide. Flexural cracks were at most 0.25 mm wide. The tensile steel stresses at the column base were less than half of yield throughout the forward half-cycle.

Table 4.2 Summary of Test Sequence of Phase A: Forward Half-Cycle
(Refer to Figure 4.3 to Figure 4.9)

Load Stage & Net Load (kN)		Observations
Phase A: Forward Half-cycle		
0	0	Column loads were applied. The north and south columns shortened by 0.60 mm and 0.58 mm, respectively.
1	25	No cracks were observed.
2	51	No cracks were observed.
3	75	**First beam flexural** cracks (0.05 mm wide) were observed at the flexural tensile faces at Beam1N, Beam1S, and Beam2N. At both ends of Beam1, flexural cracks at the beam-column interfaces [denoted Beam1N(0) and Beam1S(0)] were 200-250 mm long. Cracks located at BeamN1(150) and Beam1S(150) were 75-150 mm long (i.e. covered a third of the beam depth). At Beam2N(0), the single interface flexural crack at the north end was 75 mm long. Zurich target #77, located at the upper beam, was loose and re-epoxied back on. The Zurich readings for the upper beam were re-measured.
4	99	Refer to Figure 4.3. Existing beam flexural cracks each propagated by approximately 25 mm in length. The new crack lengths were 225 mm at Beam1N(0), 150 mm at Beam1N(150), 175 mm at Beam1S(150), 350 mm at Beam1S(0), and 100 mm at Beam2N(0). A new beam flexural crack developed at Beam1N(450) and was 150 mm long. Another crack, 100 mm long, developed at the Beam2S beam-column interface (denoted Beam2S(0)). The flexural crack spacing corresponded to the approximate stirrup layout in the beam (at 1/2S or 150 mm, and 1.5S or 450 mm from the beam-column interface). All beam flexural cracks were at most 0.05 mm wide. **First column flexural** cracks appeared at the **north column**, at the base on the north / tensile side). Cracks were evenly distributed and developed from the base up to 600 mm in the column height, and were spaced at approximately 150 mm (column ties were spaced at 130 mm). Crack widths ranged from 0.05 to 0.1 mm. The first column crack signified the **first** notable decrease in the structural stiffness.
5	125	New beam flexural cracks developed at Beam1N(250), Beam2N(150), and Beam2S(150). All new cracks were around 150 mm deep. Existing interface beam-column cracks were 0.1 mm wide at most, while beam flexural cracks remained at 0.05 mm. North column cracks remained stable.

6	148	Refer to Figure 4.4. **First beam shear** crack occurred at the **first-storey beam** (Beam1S(400)) and extended nearly the entire depth of the beam. This crack was 0.1 mm wide and was inclined at ~55 degrees from the horizontal. The flexural crack at Beam1N(250) propagated to 250 mm long. Beam flexural cracks and interface cracks were at most 0.15 mm and 0.2 mm wide, respectively. Two column **flexural cracks** appeared for the first time at the base of the **south column** north / tensile side. These two hairline cracks were located at 25 mm and 300 mm from the base. North column cracks remained stable.
7	174	Beam1S(400) shear crack widened to 0.15 mm, flattened to ~45 degrees from the horizontal, and extended the entire beam depth. New flexural beam cracks appeared at Beam2N(300) and Beam2S(225). North column cracks remained stable. More flexural cracks developed in the south column.
8	197	Refer to Figure 4.5. **Beam shear** cracks developed at the s**econd-storey beam** for the first time at Beam2N(300) and Beam2S(350). These cracks were 0.05 mm to 0.1 mm wide and were inclined at ~45 degrees from the horizontal. Beam-column interface cracks and flexural beam cracks were at most 0.25 mm and 0.15 mm wide, respectively.
9	221	Refer to Figure 4.6. Beam shear cracks at Beam2N(300), Beam2S(350), and Beam2S(250) nearly extended the entire depth of the beam. These cracks were 0.1 mm to 0.2 mm wide. Another shear crack developed at Beam1N(450) and was 0.1 mm wide. The shear crack at Beam1S(400) widened to 0.45 mm. **Second notable** change in structural stiffness was observed. The single beam shear crack at the first-storey beam (Beam1S(400)) widened to 0.25 mm, while the flexural cracks in the beams, interfaces, and columns remained stable.
10	246	All shear cracks widened, while flexural cracks remained stable. Shear cracks at Beam1N(450) widened to 0.45 mm, at Beam1S(400) widened to 0.65 mm, and at Beam2N(300) and Beam2S(350) both widened to 0.3 mm. Hairline longitudinal cracks fanned along the top and bottom edges of the lower beam near midspan.
11	272	Refer to Figure 4.7. **First joint crack** developed at the **first-storey north beam-column** joint. This crack was 0.05 mm wide and was inclined at around -45 degrees from the horizontal. Another joint crack, though minor, developed below the loading plate at the second-storey south beam-column joint. Shear cracks at Beam1N(300) widened to 0.6 mm, at Beam1S(400) widened to 0.8 mm, and at Beam2N(300) and Beam2S(350) both widened to 0.4 mm. More hairline longitudinal cracks fanned along the edges of Beam1 near midspan. Column cracks at both the north and south column bases reached 0.15 mm wide. Cracks extended to 1.2 m high at the north column, and 0.8 m high at the south column.

12	295	Shear cracks at Beam1N(450) widened to 1.05 mm, at Beam1S(400) widened to 1.1 mm, and at Beam2N(450) and Beam2S(350) widened to 0.5 mm. Beam-column interface cracks were 0.25 mm wide. **First flexural yielding** (tensile) of longitudinal steel occurred at both ends of the lower beam (as evident from strain gauges B3 and B6). Gauges B11 to B14 indicated that the flexural steel at both ends of Beam2 was near yield (reached 410 MPa or 92% of yield). Stirrups S4 and S12 within the crack regions of Beam1N(450) and Beam2N(450) were near yield (473 MPa and 383 MPa, respectively). Recall the stirrups yielded around 506 MPa. The stress in the column flexural steel remained below half the yield stress through out Phase A.
13	320	Shear cracks at Beam1N(450) widened to 1.8 mm, at Beam1S(400) widened to 1.6 mm, at Beam2N(300) widened to 0.7 mm, and at Beam2S(350) remained stable at 0.5 mm. **Stirrups** S4 and S12 within the crack regions of Beam1N(450) and Beam2N(450) **yielded**. Strain gauges B11, B2, and B14 also indicated **flexural yielding** at both ends of Beam2. Column cracks were noticeable in the second-storey level of the north column, at the north face. A large joint crack appeared at the second-storey north beam-column joint. This crack was inclined at around -45 degrees from the horizontal.
14	325	Refer to Figure 4.8. All shear cracks remained stable except for Beam1N(450) where the crack opened up to **4.0 mm**. The top concrete cover at the Beam1N beam-column interface was debonding.
15	327	Refer to Figure 4.9. This load stage was considered the peak load of the forward half-cycle. The shear crack at the first-storey beam propagated to **9 mm**. This shear crack was accompanied by longitudinal splitting along the bottom layer of rebar near midspan. Shear cracks at Beam1S(400) remained at 1.6 mm, at Beam2N(300) widened to 2.0 mm, and at Beam2S(350) widened to 0.8 mm. Stirrup S8 [at Beam2S(350)] **yielded** at this load stage. A load slightly higher load than 327 kN may have been achieved with further loading; however, the test frame was at risk of being damaged beyond a repairable point. The forward half-cycle of Phase A was concluded.

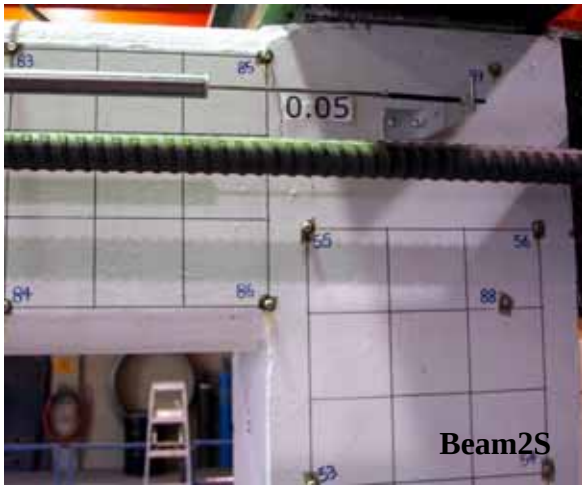

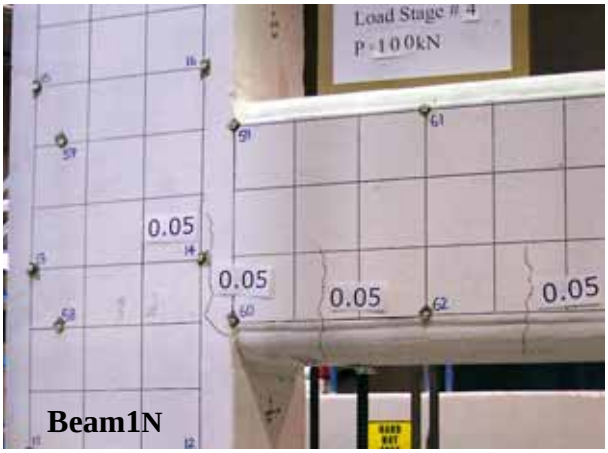

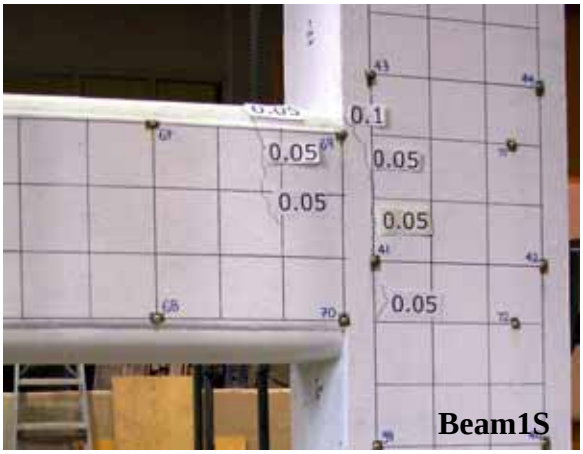

Figure 4.3 Frame at Load Stage 4

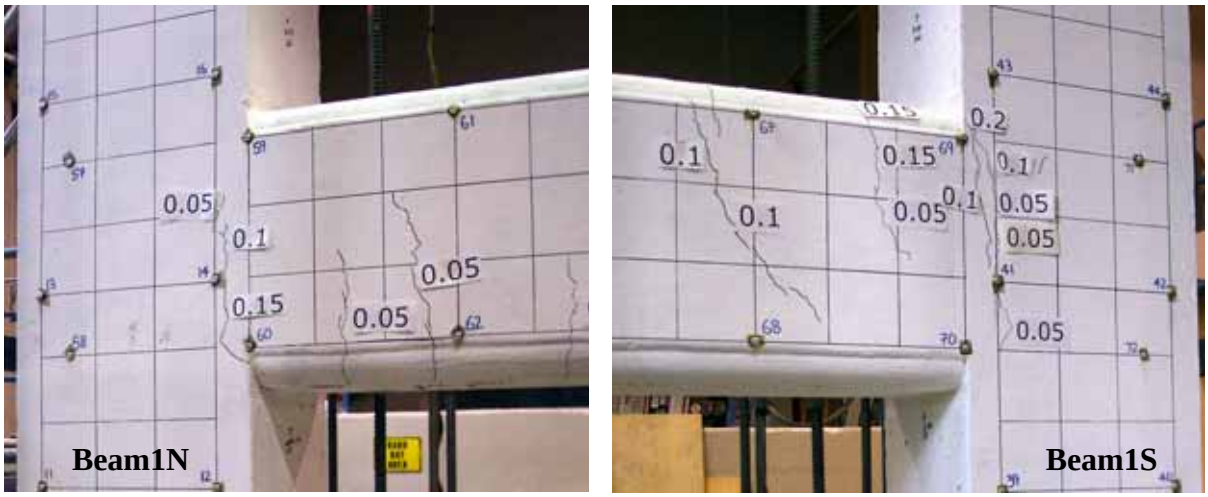

Figure 4.4 Frame at Load Stage 6

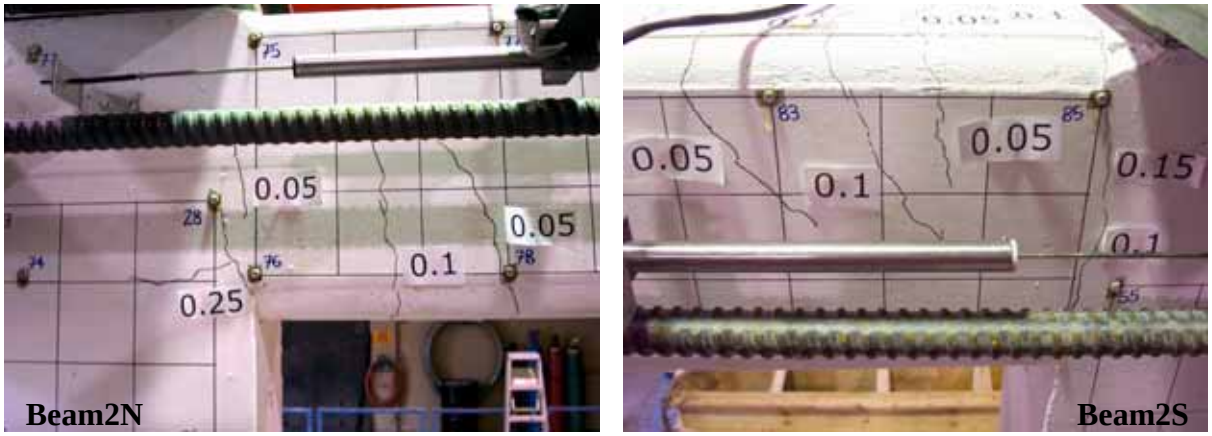

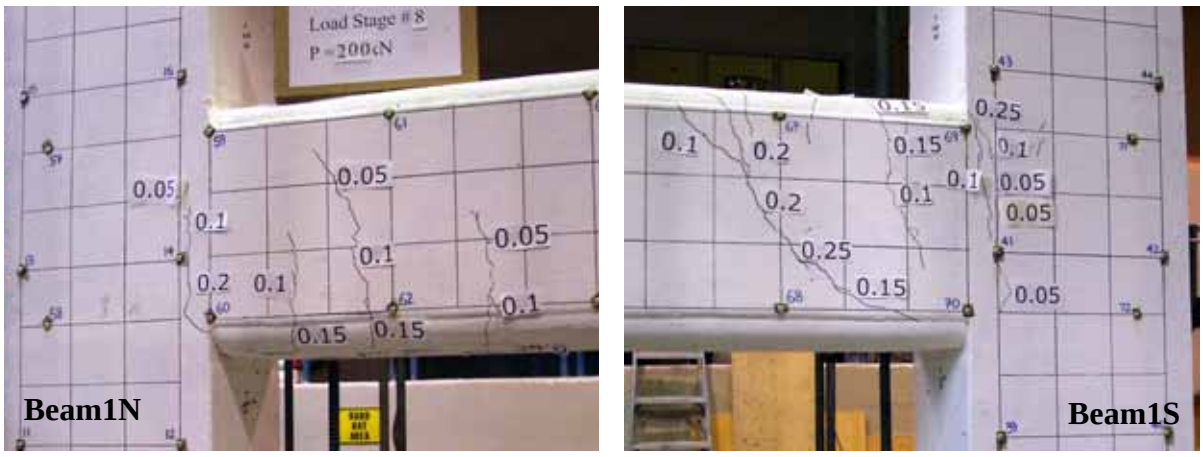

Figure 4.5a Frame at Load Stage 8

Figure 4.5b Frame at Load Stage 8

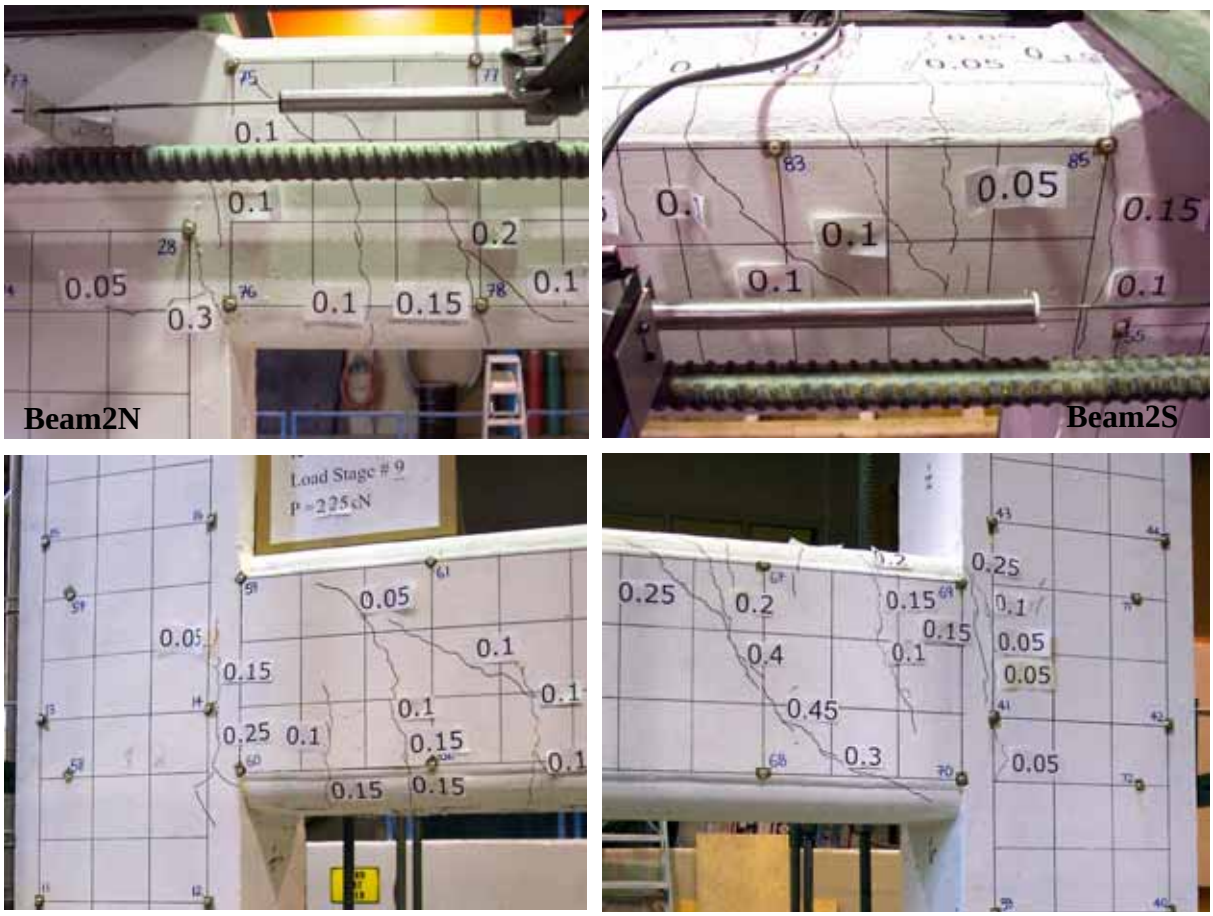

Figure 4.6 Frame at Load Stage 9

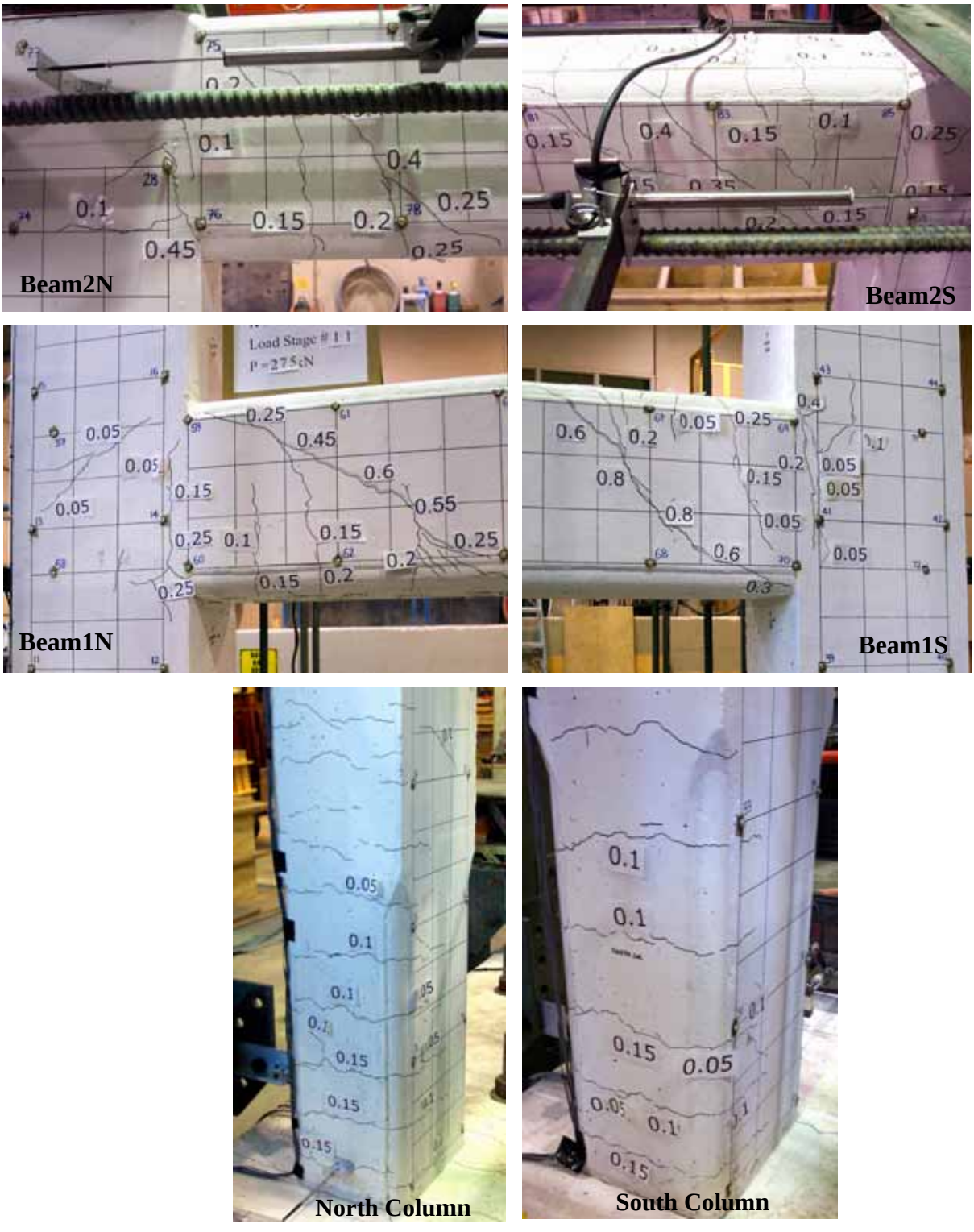

Figure 4.7 Frame at Load Stage 11

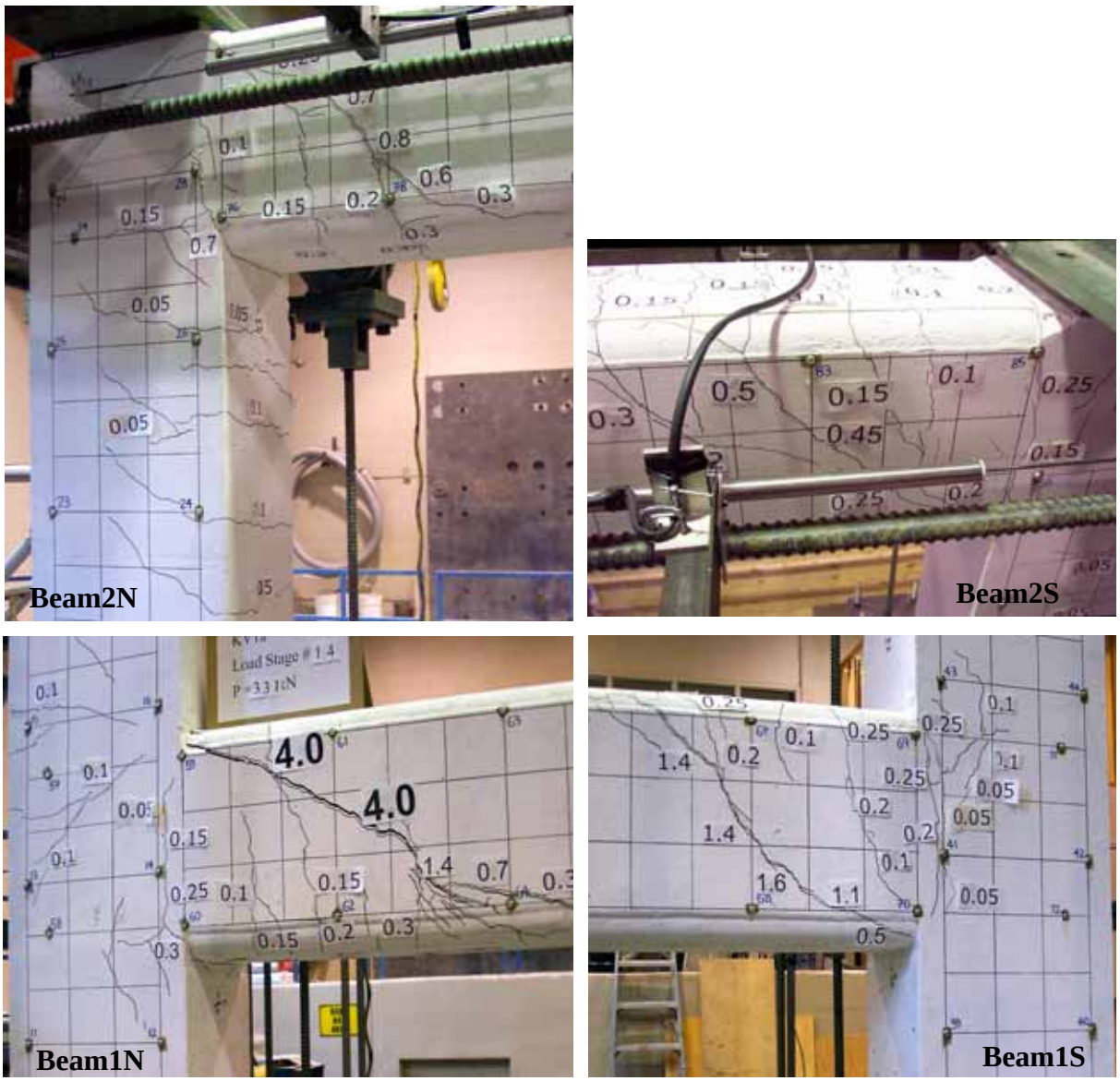

Figure 4.8 Frame at Load Stage 14

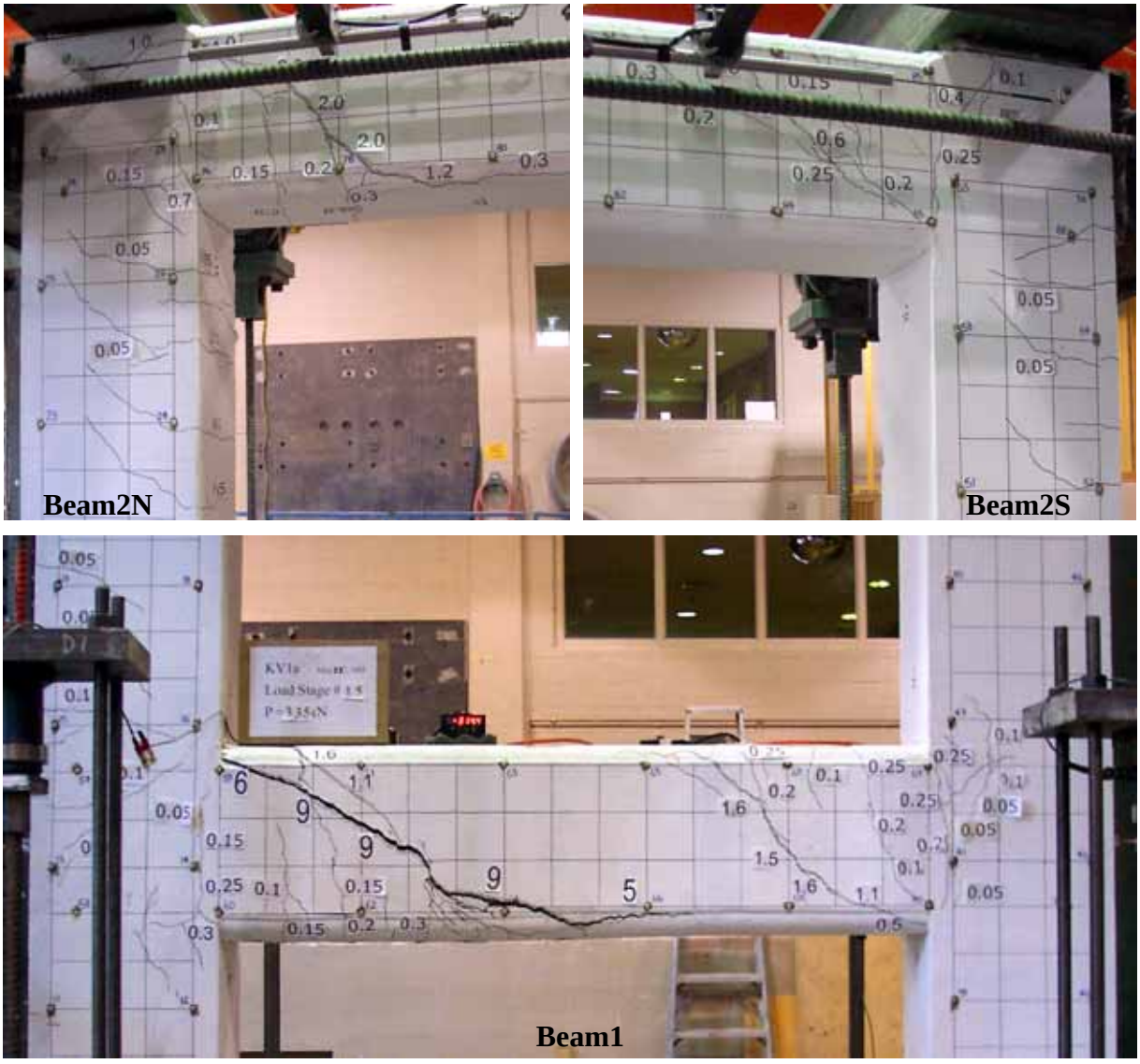

Figure 4.9a Frame at Load Stage 15

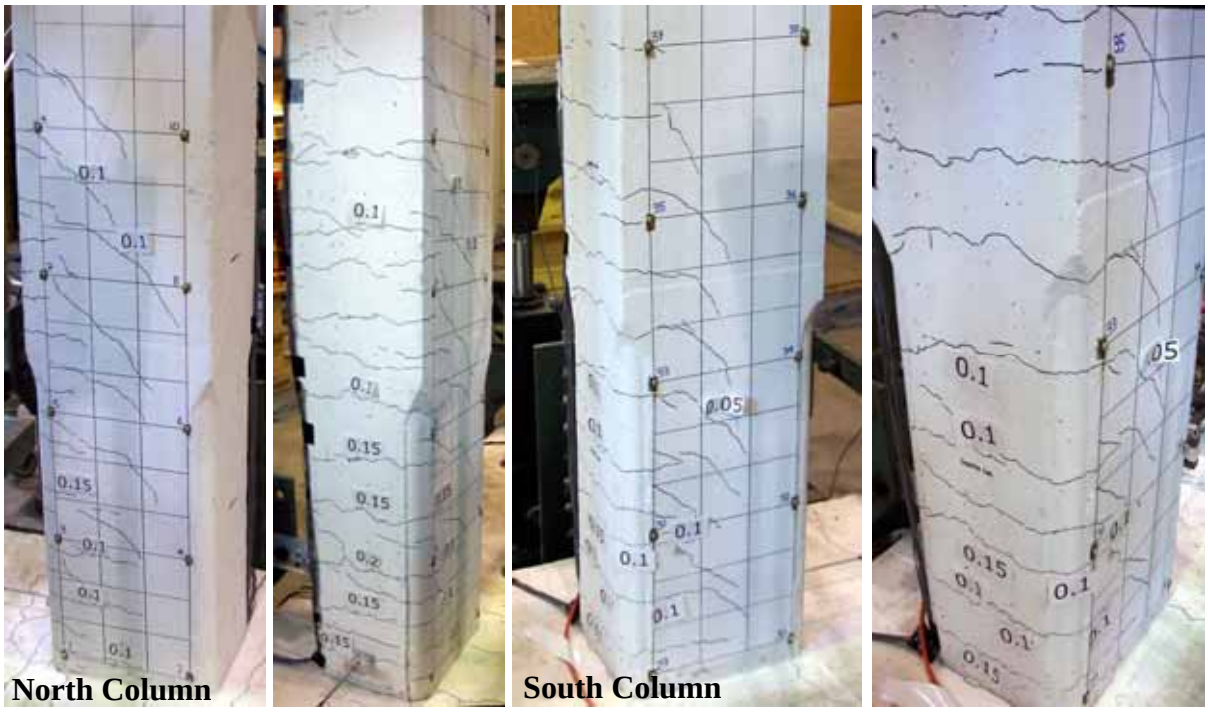

Figure 4.9b Frame at Load Stage 15

4.2.4 Detailed Test History of Phase A: Reverse Half-cycle

Table 4.3 below summarizes the detailed observations from this portion of testing. Refer to Figure 4.10 to Figure 4.15 for selected experimental photographs. For the reserve half-cycle, small cracks were of minor interest. Their propagation was still monitored, but only cracks that were of potential significance (i.e. that had the potential to cause failure) were measured for crack width. Cracks were marked with a blue marker. Upon unloading from the previous forward half-cycle, plastic steel deformation caused residual strains in the majority of the steel strain gauges. These strain readings did not return to their zero position. The following strain gauges were damaged during the forward half-cycle: S5 located at Beam1N(450), S8 located at Beam2S(150), S12 located at Beam2N(150), and B11 located at the top longitudinal steel layer of Beam2N. B4 and B5, located at the south and north ends of the lower beam, were previously damaged during construction.

The test specimen was pulled in the reverse direction to approximately the peak displacement reached during the forward half-cycle (around 40 mm). At zero horizontal load at the end of the forward half-cycle, the frame exhibited approximately 11 mm of top storey residual lateral deflection. Unlike the forward half-cycle where the damage mode was a combined flexural-shear, the frame in the reverse direction displayed damage mostly in shear. At the conclusion of the reverse half-cycle, a peak horizontal load of -304 kN was reached with an average top storey lateral displacement of -39.5 mm. Lower and upper beam flexural cracks were developed at -32 kN, while the lower beam shear cracks appeared at -84 kN. In general, the crack development was discontinuous and abrupt. Because of the numerous cracks generated from the forward half-cycle, the cracks during the reverse half-cycle were often interrupted and jagged. The sudden propagation of cracks was also a common behaviour. At -260 kN, the stirrups in the lower beam yielded. At the peak load of -304 kN, the largest shear cracks at the lower and upper beams were 7 mm and 5 mm wide, respectively. The beam flexural steel was near yield at 430 MPa (around 95% of yield). The column flexural steel stress was below half of yield. Beam and column flexural cracks were minor in comparison to the beam shear cracks. At the end of this loading phase, the lateral load was retracted and the frame was pushed forward to a displacement where the residual lateral deflection upon unloading was approximately zero.

Table 4.3 Summary of Test Sequence of Phase A: Reverse Half-cycle
(Refer to Figure 4.10 to Figure 4.15)

Load Stage & Net Load (kN)		**Observations**
Phase A: Reverse Half-cycle		
16	-2	This load stage was considered the zero horizontal load position. There was a residual top storey displacement of approximately 11 mm.
17	-32	**First beam flexural** cracks (0.05 mm wide) were observed at Beam1N(450) and Beam2N(150).

18	-69	The two existing beam flexural cracks propagated, while new flexural cracks developed at Beam1N, Beam1S, and Beam2N. Minor beam-column interface cracks appeared at both ends of the lower beam.
19	-84	Refer to Figure 4.10. Sudden propagation of beam flexural cracks occurred at Beam1N(150) and Beam1N(450). These two cracks extended the entire depth of the beam. **First beam shear** crack appeared at Beam1N(300). This crack extended a third way down the beam depth, intersected with a large shear crack from the forward half-cycle, and reappeared back at the bottom third of the beam. The discontinuous characteristic of this shear crack was typical of the shear cracks that developed during the reverse half-cycle.
20	-111	This load stage corresponded to the zero displacement position. **First column flexural** cracks were observed at the south face of the south column.
21	-139	Refer to Figure 4.11. The shear crack at Beam1N(300) widened to 1.2 mm.
22	-168	The shear crack at Beam1N(300) widened to 1.4 mm. A minor beam shear crack appeared at Beam2N(350).
23	-185	Refer to Figure 4.12. A **sudden large shear crack** (1.6 mm wide) developed at the first-storey beam at midspan (denoted Beam1M) and caused an abrupt drop in load. The crack initiated at the lower beam top edge and propagated to ¾ of the beam depth. This sudden crack signified a **notable** change in the structural stiffness. All other significant cracks were unchanged.
24	-197	Refer to Figure 4.13. The shear crack at the top of Beam1M widened to 3.0 mm. Another shear crack at Beam1M appeared, but originated from the bottom edge and was 0.3 mm wide. The south second-storey beam-column joint appeared to be moving out-of-plane in the east direction by around 5 mm. In general, the frame was twisting slightly, causing the shear cracks on the west face to be slightly wider than their counterparts on the east face.
25	-260	Refer to Figure 4.14. Shear cracks at the top and bottom of Beam1M widened to 4.0 mm and 2.5 mm, respectively. Other notable shear cracks were located at Beam2S(400) (0.4 mm wide) and at the bottom of Beam2M (0.6 mm wide). **Stirrups** S3 and S7 **yielded**. S3 was located at Beam1S(450) and S7 was situated at Beam2S(150).
26	-304	Refer to Figure 4.15. This load stage corresponded to the approximate peak displacement reached during the forward half-cycle. Shear cracks at the top and bottom edges of Beam1M widened to **7.0 mm** and 6.0 mm, respectively. The shear crack at Beam2M widened to **5.0** mm. The damage mode was classified as shear-critical. Other beam shear and flexural cracks, and column flexural cracks had little contribution to the damage mode. Stirrup S4, at Beam1N(450), yielded. Stirrup S9, at Beam2S(450), was near yield at 474 MPa. The flexural steel at both the lower and upper beams was near yield (430 MPa maximum or 96% of the yield stress), but none reached the yielding point. Column flexural steel remained below the half yield mark.

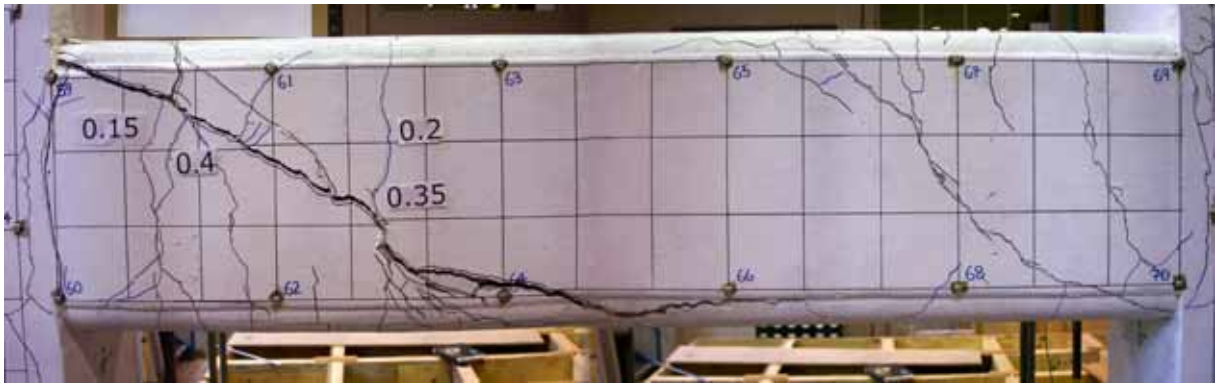

Figure 4.10 Frame at Load Stage 19

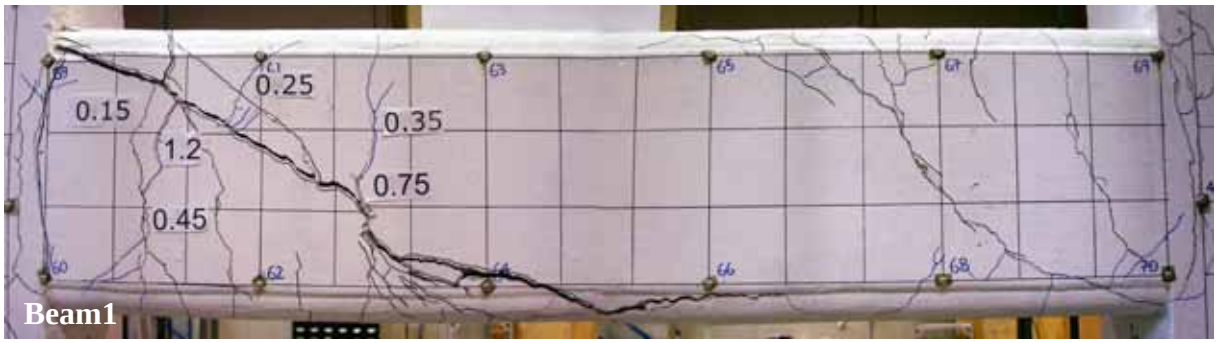

Figure 4.11 Frame at Load Stage 21

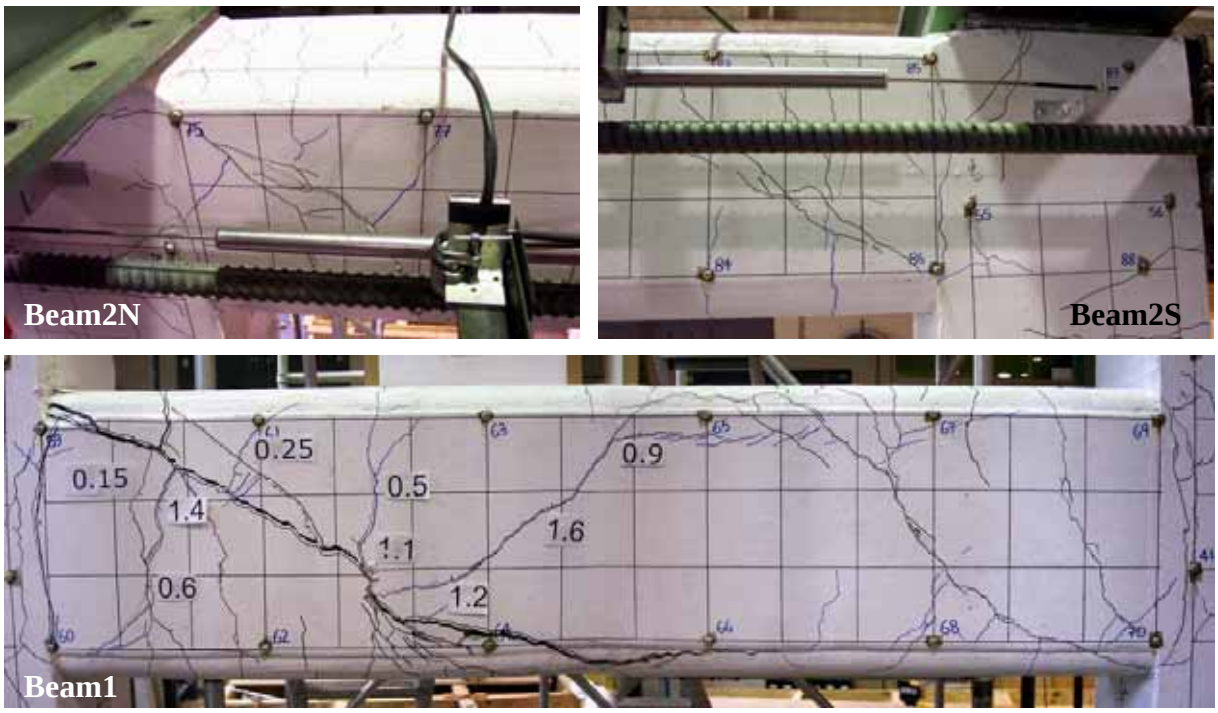

Figure 4.12 Frame at Load Stage 23

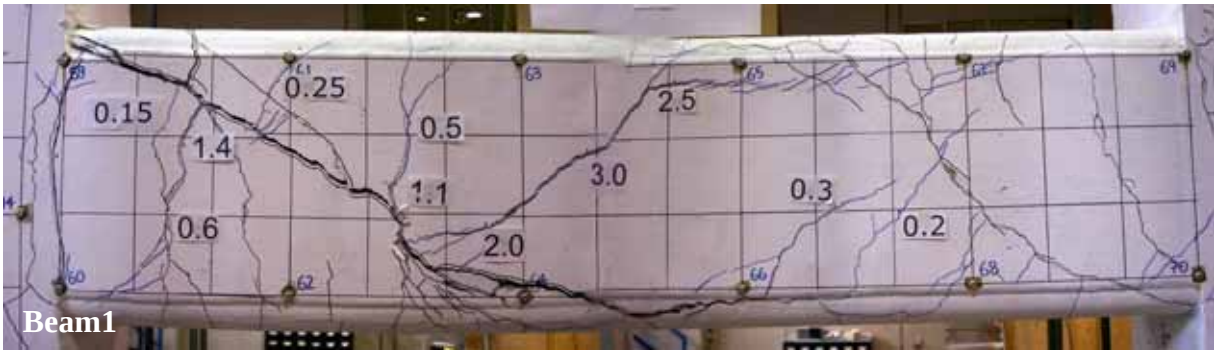

Figure 4.13 Frame at Load Stage 24

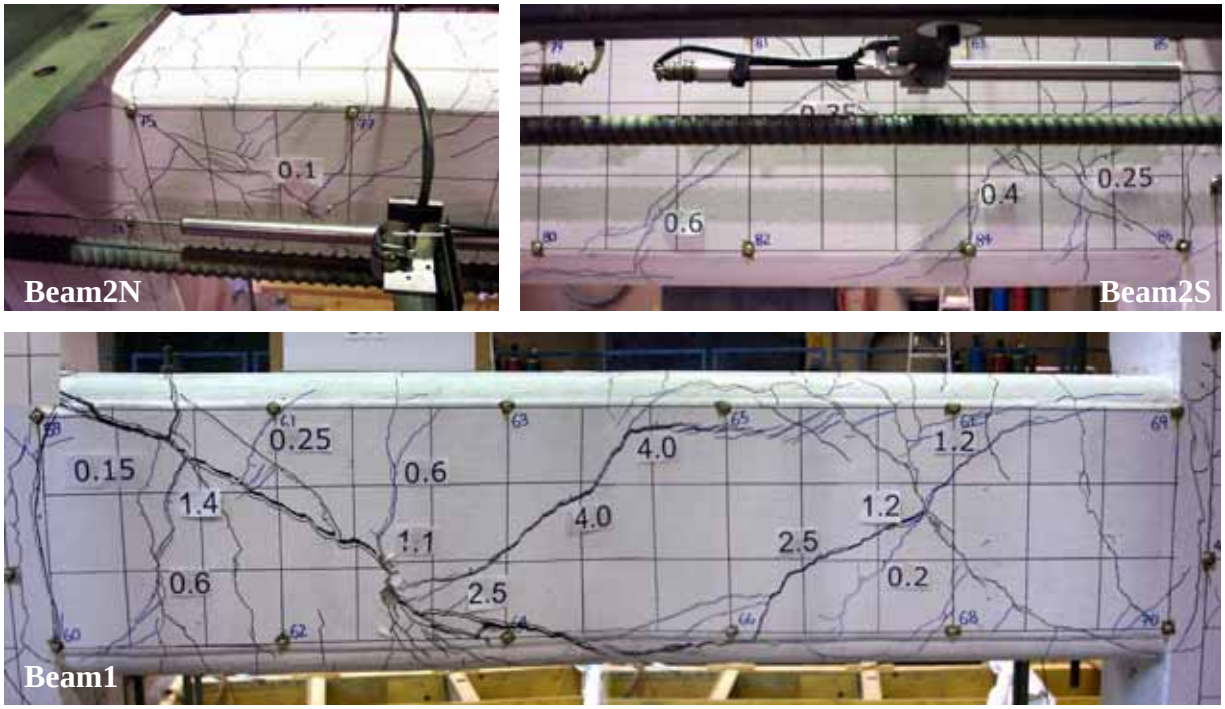

Figure 4.14 Frame at Load Stage 25

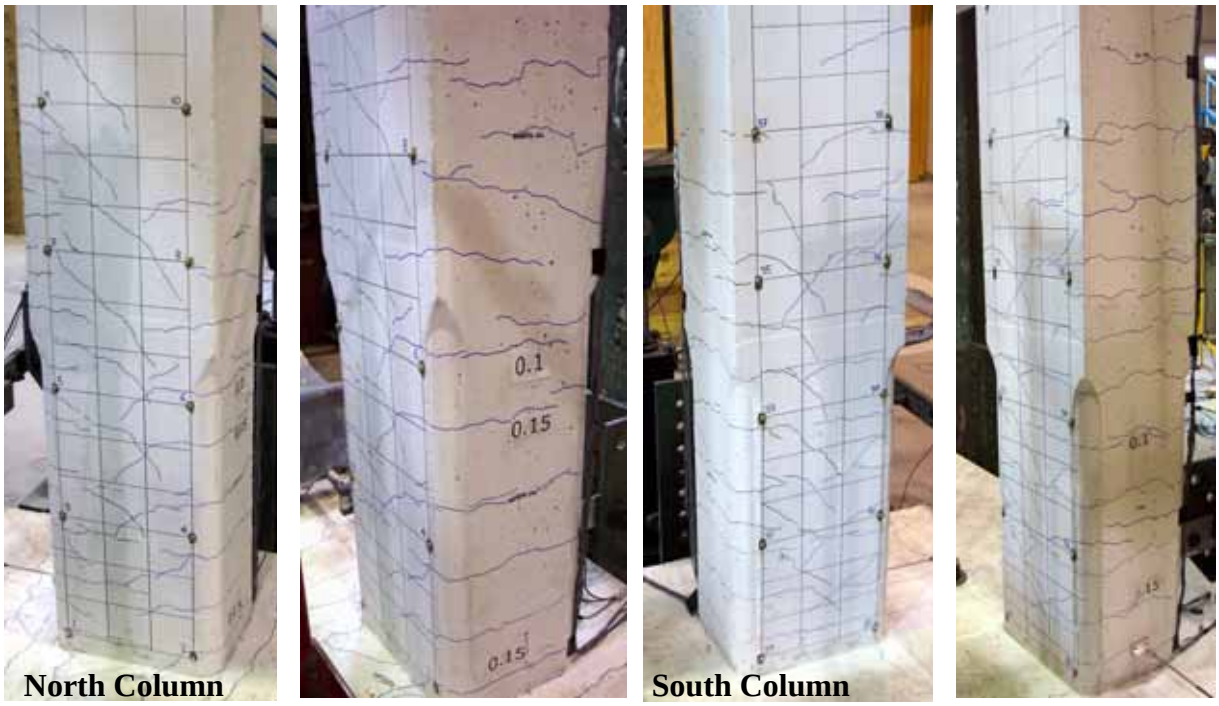

Figure 4.15a Frame at Load Stage 26

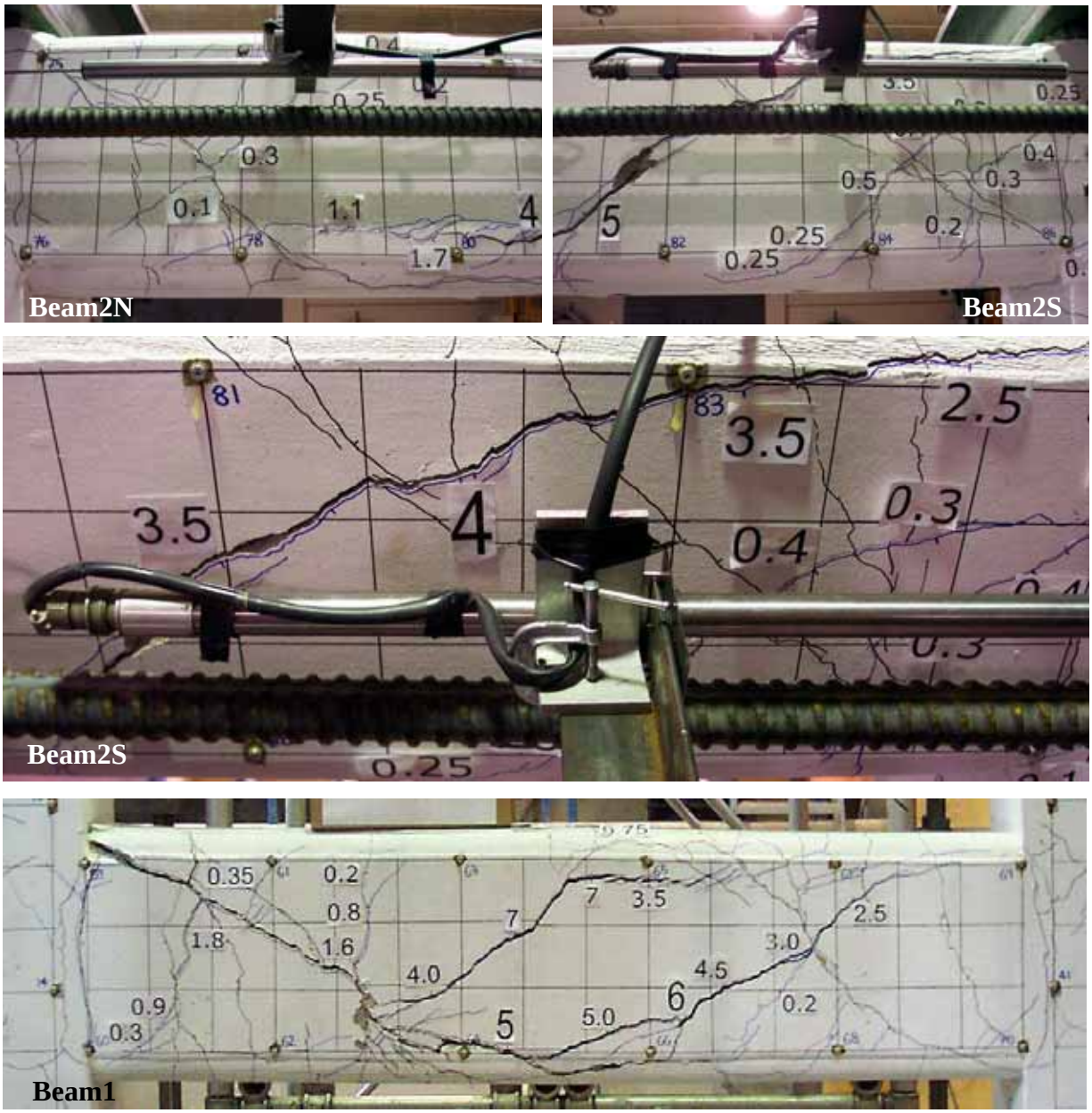

Figure 4.15b Frame at Load Stage 26

4.2.5 Detailed Test History of Phase B: Reverse Cyclic

Table 4.4 below summarizes the detailed observations from this portion of testing. Refer to Figure 4.16 to Figure 4.23 for selected experimental photographs. Similar to the reverse half-cycle of Phase A, small cracks were of minor interest in Phase B. The crack propagations were monitored; however, only significant cracks were measured. Cracks

were marked with a red marker. Because 50% of the beam length was wrapped with CFRP, the cracking pattern could not be detected where the cracks developed beneath the wrap. For the experimental photos during the first eight load cycles (Figure 4.16 to Figure 4.23), the crack widths displayed on the frame indicted simultaneously the maximum widths observed during both the forward and reverse loadings (i.e. the width signage of the forward half-cycle were not removed during the reserve half-cycle). Beyond the eighth load cycle, crack widths were displayed for each individual forward and reverse half-cycle.

Several strain gauges were malfunctioning at this stage. They included:

- S4 and S5: stirrups at Beam1N(450)
- S8: stirrup at Beam2S(150)
- S12: stirrup at Beam2N(150)
- B4: top longitudinal rebar layer at Beam1S
- B5: bottom longitudinal rebar layer at Beam1N
- B11 and B12: top longitudinal rebar layer at Beam2S
- B16: top longitudinal layer at Beam2N

In addition, C2, located at the outer longitudinal rebar layer of the south column base, was unhooked to provide an additional channel for a CFRP strain gauge. The majority of column gauges were still in good condition; residual strains were at most 270 $x10^{-6}$ at C7 (outer rebar layer of the north column base). The longitudinal beam gauges were in fair condition. Apart from the five broken gauges aforementioned, B7 (top longitudinal rebar layer at Beam1N) indicated a strain reading of 1100 $x10^{-6}$. Of the remaining nine longitudinal rebar beam gauges, B8 (top layer of Beam1N) and B15 (top layer of Beam2N) had strains as high as 350 $x10^{-6}$. The stirrup strain gauges were in poor condition. Five out of twelve gauges were already damaged. S7 [Beam2S(150)] had a strain over 5000 $x10^{-6}$, while S11 [Beam2N(450)] and S1 [Beam1S(150)] had strains around 650 $x10^{-6}$ and 500 $x10^{-6}$, respectively. These large residual strains indicated that

a great amount of plastic deformation had taken place during Phase A, and the majority of steel stirrups exhibited permanent elongation or contraction upon unloading. Because of the large plastic deformation, strain gauge results were difficult to interpret. Therefore, steel strains recorded during Phase B should be considered as general trends, rather than definitive readings.

The test frame developed a full plastic hinge failure mechanism at the end of Phase B. Hinges were formed at the four beam ends and at the two column bases. The peak lateral load reached was -444 kN, which corresponded to an average second-storey displacement of -164 mm (-6.6 Δ_y). This displacement was limited by the actuator stroke range. Collapse of the frame did not occur. Shear cracks in both beams were first observed at $\pm$0.75 Δ_y. Flexural interface cracks at all four ends of the two beams were developed shortly after at $\pm$1.0 Δ_y. At $\pm$3.0 Δ_y, shear cracks were approximately 1.5 mm wide, while flexural interface cracks were 3.5 mm wide. Flexural hinges at the beam ends were fully developed at this displacement. In addition, shear cracks were also exhibited at the second-storey beam-column joints. At $\pm$4.0 Δ_y, beam shear cracks were 2.5 mm wide, column base flexural cracks were 1.5 mm wide, and column base concrete cover was spalling. Due to excessive damage of the two concrete beams, the specimen was twisting out-of-plane. At the final load cycle (LC 13), beam shear cracks were 3.5 mm wide, while the beam interface flexural cracks reached a maximum of 6 mm. The concrete cover at the second-storey beam-column joints was partially spalled off.

When strains in the steel were monitored, the following observations were made. Even though a full plastic hinge mechanism was developed, the stirrups at the first and second-storey beams yielded. The stirrups at both ends of the lower beam (S1, S6) and at Beam2N (S11) yielded at $\pm$2.0 Δ_y, while the stirrup at Beam2S yielded at $\pm$3.0 Δ_y (S9). The longitudinal flexural steel in the lower beam yielded in tension at around $\pm$1.0 Δ_y, while the longitudinal flexural steel in the upper beam yielded in tension at around $\pm$2.0 Δ_y. The beam compression longitudinal steel remained below yield. The column steel

yielded in both tension and compression at the base when $\pm 3.0\ \Delta_y$ displacement was reached. At the end of LC 13, the longitudinal flexural steel at the column bases did not reach strain hardening.

When strains in the CFRP were examined, it was observed that the majority of CFRP strains at the lower beam exceeded the design strain limit of 4000 $x10^{-6}$ (ISIS #4 Design Manual, 2001). The majority of the strains in the upper beam remained below 4000 $x10^{-6}$ up until LC 13, when one reading (F23) exceeded this limit. For a fully wrapped beam such as this specimen, the term debonding meant that the vertical CFRP-concrete interface was breaking, but the wrap was still intact and provided shear resistance. Partial CFRP debonding was initiated at the lower beam at LC 5 ($\pm 2.0\ \Delta y$). At the $\pm 4.0\ \Delta_y$ cycles, all of the CFRP wraps at the lower beam exhibited debonding of more than 50% of their original bonded area. Partial debonding took place at the upper beam at $\pm 4.0\ \Delta_y$. From -4.0 Δy to -6.6 Δ_y, the CFRP strains increased slightly, but not at the same rate as the increase from $\pm 3.0\ \Delta_y$ to $\pm 4.0\ \Delta_y$. The maximum CFRP strain recorded was approximately 6200 $x10^{-6}$ at F13 (located at the second strip from the north end of the lower beam). In the upper beam, with the exception of one F3 (located at Beam2S), the maximum CFRP strain recorded was around 3800 $x10^{-6}$. F23 reached 4300 $x10^{-6}\ \varepsilon$ at load cycle 13. No sign of CFRP rupture was observed at any location in the beams.

Table 4.4 Summary of Test Sequence of Phase B: Reverse Cyclic
(Refer to Figure 4.16 to Figure 4.23)

Load Cycle & Net Load (kN)			Observations
Phase B: Reverse Cyclic			
1	+0.75 Δ_y	+233	**Minor shear cracks** ranging from 0.1 mm to 0.3 mm wide developed at both ends of the lower beam, while a single shear crack 0.15 mm wide appeared at Beam2S. There were no signs of flexural cracking. Most likely, the flexural cracks were hidden underneath the CFRP wrap.
1	-0.75 Δ_y	-247	Minor shear cracks developed in a similar pattern to the forward half-cycle, except the crack pattern was mirrored about the y-centreline.
2	+0.75 Δ_y	+233	Refer to Figure 4.16. The second cycle at $\pm$0.75 Δ_y did not generate any significant crack development. A few minor shear cracks developed at the four beam ends, while the existing crack widths increased by 0.05 mm. The maximum crack width was 0.35 mm. At the -0.75 Δ_y half-cycle, strain gauge B8 located at the top longitudinal steel layer of **Beam1N** indicated **steel yielding** in tension.
2	-0.75 Δ_y	-241	
3	+1.0 Δ_y	291	Hairline beam-column **interface flexural cracks** were observed at all four joints (both ends of the lower and upper beams). The shear crack pattern remained stable. Shear cracks at the lower and upper beams increased to maximum widths of 0.5 mm and 0.3 mm, respectively. At the +1.0 Δ_y half-cycle, strain gauge B3 located at the top longitudinal steel layer of **Beam1S** indicated **steel yielding** in tension. There were no gauges available at the bottom layer of Beam1N. At the -1.0 Δ_y half-cycle, strain gauges B1 and B2 located at the bottom longitudinal steel layer of **Beam1S** indicated **steel yielding** in tension. The flexural tensile steel at the second-storey beam on average had stresses around 400 MPa (89% of the yield stress).
3	-1.0 Δ_y	-298	
4	+1.0 Δ_y	+283	Refer to Figure 4.17. The second cycle at $\pm$1.0 Δ_y did not generate any significant development in the crack pattern. Shear crack widths at Beam1 increased to a maximum of 0.55 mm, while the shear cracks at the upper beam remained stable. The stress conditions in the longitudinal beam rebars were similar to load cycle 3.
4	-1.0 Δ_y	-289	
5	+2.0 Δ_y	+399	Partial **CFRP debonding** was exhibited at the lower beams. Shear crack at the lower and upper beams increased to 0.65 mm and 0.4 mm wide, respectively. At the +2.0 Δ_y half-cycle, strain gauges B13 and B14 located at the bottom longitudinal steel layer of **Beam2N** indicated **steel yielding** in tension**.** There were no gauges available at the top layer of Beam2S. At the -2.0 Δ_y cycle, strain gauges B15 and B16 located at the top longitudinal steel layer of **Beam2N** indicated **steel yielded** in tension, as did gauge B9 located at the bottom longitudinal steel of **Beam2S**.
5	-2.0 Δ_y	-395	

6	+2.0 Δ_y	+377	Refer to Figure 4.18. Shear cracks at the lower and upper beams increased to 0.7 mm and 0.5 mm wide, respectively. The interface flexural cracks at all four beam ends did not propagate; however, the crack width increased to approximately 1.5 mm wide. Old column cracks from Phase A re-opened. New column cracks were minor and scarce.
6	-2.0 Δ_y	-384	
7	+3.0 Δ_y	+422	Shear cracks at the lower and upper beams increased to 1.0 mm and 0.7 mm wide, respectively. The interface flexural cracks at Beam1N and Beam1S increased to 2.0 mm and 3.5 mm wide, respectively. Both ends of the upper beam had interface flexural cracks that were 2.5 mm wide. Several new column cracks developed, although none were of significance. The base-column interface was starting to spall.
7	-3.0 Δ_y	-424	Refer to Figure 4.19. Shear cracks at the lower beam increased to 1.4 mm wide, while shear cracks at upper beam remained stable at 0.7 mm. The interface flexural cracks at Beam1N and Beam1S were both 3.5 mm wide. The upper beam interface flexural cracks remained stable at 2.5 mm. Large **diagonal shear cracks** appeared at both the north and south second-storey beam-column joints. These cracks developed as a result of a high local stress concentration caused from both the column and lateral loads being applied at the same region. The **column base longitudinal steel yielded** in tension and compression at $\pm 3.0\ \Delta_y$.
8 8	+3.0 Δ_y -3.0 Δ_y	+406 -414	Refer to Figure 4.20. Shear cracks at both beams remained stable. With each forward and reverse loading cycle, the interface flexural cracks opened and closed. For example, during the +3.0 Δ_y half-cycle, the interface crack at Beam1S opened up to 3.5 mm wide near the top edge, and 1.6 mm wide at mid depth. During the -3.0 Δ_y half-cycle, the crack width at the top edge closed to around 1.6 mm, while the crack width near the bottom edge opened to 3.5 mm. This behaviour was characteristic of all four interface flexural cracks. All interface cracks were 3.5 mm at their widest locations. Diagonal shear cracks at the second-storey north and south beam-column joints were approximately 1.0 mm and 2.5 mm wide, respectively. At the first-storey beam ends, where regions of flexural tension were present, the flexural cracks were not only prominent at the beam-column interfaces, but now extended into the **CFRP end wraps**. These large flexural cracks were located to the left and right of the CFRP end wraps and propagated along the entire tensile face. This cracking pattern suggested that the plastic hinge length extended out to the tip of the CFRP end strip (150 mm). Recall that the regions of flexural tension alternated between the top and bottom faces depending on the direction of lateral loading. **CFRP strains** at the lower beam exceeded 4000 $x10^{-6}$.

9	+4.0 Δ_y	+417	Refer to Figure 4.21. Shear cracks at the lower and upper beams increased to 2.5 mm and 1.4 mm wide, respectively. The maximum interface flexural crack widths at both beams ranged from 3.0 mm to 4.5 mm. Flexural crack widths were only approximate at this stage, since the widths were dependent on how the cracks opened up and closed up. For instance, the crack widths were smaller where sliding occurred. The flexural cracks adjacent to the **CRFP end wraps** at both ends of the lower beam were clearly prominent. These cracks at the bottom face of Beam1N and the top face of Beam1S were 1.4 mm and 1.7 mm wide, respectively. Similar cracks at the end strips were observed at the upper beam, but to a lower degree. The diagonal shear cracks at the second-storey beam-column joints were sliding back and forth with each load cycle. The shear crack width reached 4 mm wide. **Flexural column cracks** that were 1.5 mm wide developed at the north and south column bases, and just above the first storey beam at the north face of the north column. Due to limited access, cracks at the latter location were not recorded.
9	-4.0 Δ_y	-422	Refer to Figure 4.22. Shear crack widths at the lower and upper beams were 1.8 mm and 1.0 mm wide, respectively. The flexural cracks adjacent to the **CRFP end wraps** at the Beam1 were approximately 4 mm at the top face of Beam1N, and 2.5 mm at the bottom face of Beam1S. The maximum interface flexural crack widths ranged from 2.5 mm to 4.5 mm wide. Column cracks developed in a similar pattern to the previous forward half-cycle, except the cracks were wider (0.3 mm maximum). A column flexural crack, 1.4 mm wide, developed at the south face of the second-storey south column. This crack was equivalent to the second-storey column flexural crack that was developed during the previous forward half-cycle. CFRP wraps at the lower beam exhibited debonding of more than 50% of their original area. Partial debonding took place at the upper beam.
10	+4.0 Δ_y	+403	Shear crack widths at both beams remained stable. Interface flexural cracks opened and closed as expected. Base column cracks increased to 1.7 mm, and cover spalling was exhibited at the north face of the north column base.
10	-4.0 Δ_y	-412	Shear cracks at the lower and upper beams increased to 2.5 mm and 1.2 mm wide, respectively. Cover concrete at the second-storey beam-column joints began spalling off. Column cracks remained stable; however, excessive cover spalling was present at the south face of the south column base.

11	+4.0 Δ_y	+397	The lateral loading plate was misaligned from the column face at this stage (although the misalignment went undetected until LC 12). The entire specimen slowly twisted out-of-plane as the force was being applied. The south column moved to the east, while the north column moved towards the west (the movements may be as large as 5 cm). Shear crack widths at the lower and upper beams were 2.5 mm and 1.8 mm wide, respectively. The flexural cracks adjacent to the **CRFP end wraps** were stable.
11	-4.0 Δ_y	-403	The specimen realigned itself in plane during the reverse half-cycle. All the critical crack widths in the beams and columns remained stable.
12	+4.0 Δ_y	+377	At the north end of the specimen, the lateral loading plate was off centre by approximately 25 mm. The loading plate was realigned. During the forward loading, the north column shifted to the west by 5 cm, while the south column remained in plane. A large piece of concrete cover at the south second-storey beam-column joint spalled off. Other vital signs of the specimen remained stable. All the critical crack widths in the beams and columns remained stable The **CFRP** in F13 (second strip from the north end at the lower beam) reached a maximum strain of 6400 $x10^{-6}$ ε.
12	-4.0 Δ_y	-395	No significant changes in behaviour were observed.
Intermediate Load Cycle			The original plan was to cycle the specimen at $\pm$5.0 Δ_y. However, because of the excessive out-of-plane frame movement that occurred during the previous forward loading cycle, it was deemed unsafe to push the specimen further than +4.0 Δ_y. Consequently, the specimen was pulled back as far as possible until either failure took place or the stroke limit of the actuator was reached.

13	-6.6 Δ_y	-444	Refer to Figure 4.23. Shear crack widths at the lower and upper beams were 3.5 mm and 2.5 mm wide, respectively. The flexural cracks adjacent to the **CRFP end strips** were 9 mm wide at the top face of Beam1N, 3+ mm wide at the bottom face of Beam1S, and 5+ mm wide at both the top face of Beam2N and bottom face of Beam2S. A fully plastic hinged frame was formed with hinges developed at the four beam ends and the two column bases. Collapse of the frame did not take place as the actuator stroke limit was reached. The average second-storey displacement was -164 mm (-6.6 Δ_y). The second-storey beam-column joints continued to deteriorate. At the south joint, the majority of the concrete cover at the south edge spalled off. Spalling was less significant at the north joint; however, the diagonal shear crack was prominent. Flexural column cracks at the north column base reached 2.0 mm wide. The concrete cover at the north base debonded. The cover at the south column base spalled off. At the second-storey south face of the south column, the flexural crack opened to 1.8 mm wide. The CFRP wraps at the lower beam nearly debonded completely, while the strips at upper beam were partially debonded (~30% of area). **CFRP strain** gauge F23, located at the end of Beam2S, was the only gauge to record strain in excess of the 4000 $x10^{-6}$ design limit (4300 $x10^{-6}$ ε was recorded).

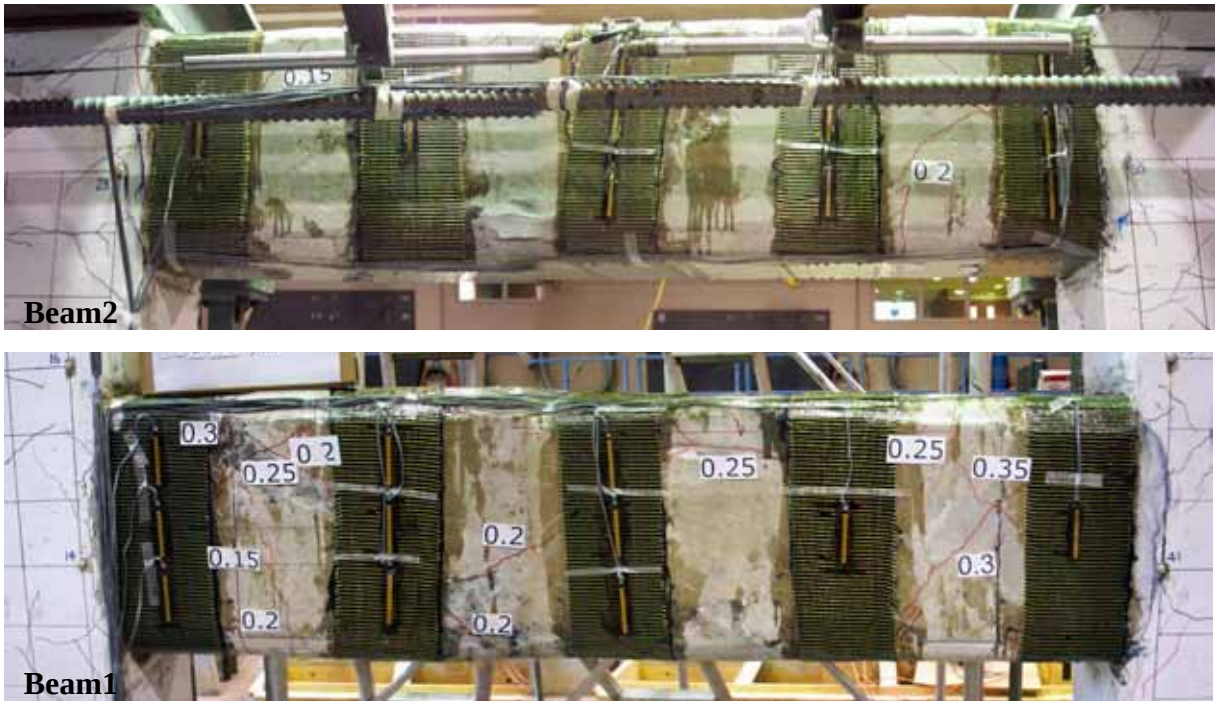

Figure 4.16 Frame at Load Cycle 2 (-0.75 Δ_y)

Figure 4.17 Frame at Load Cycle 4 (-1.0 Δ_y)

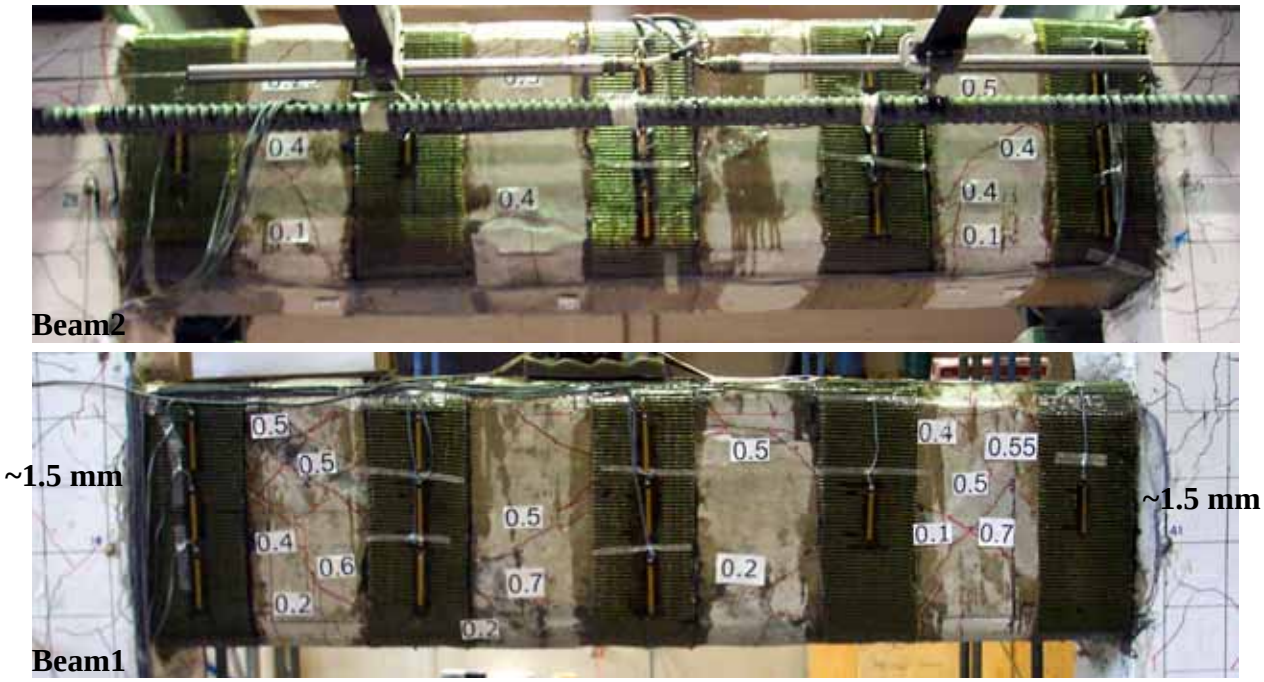

Figure 4.18 Frame at Load Cycle 6 (-2.0 Δ_y)

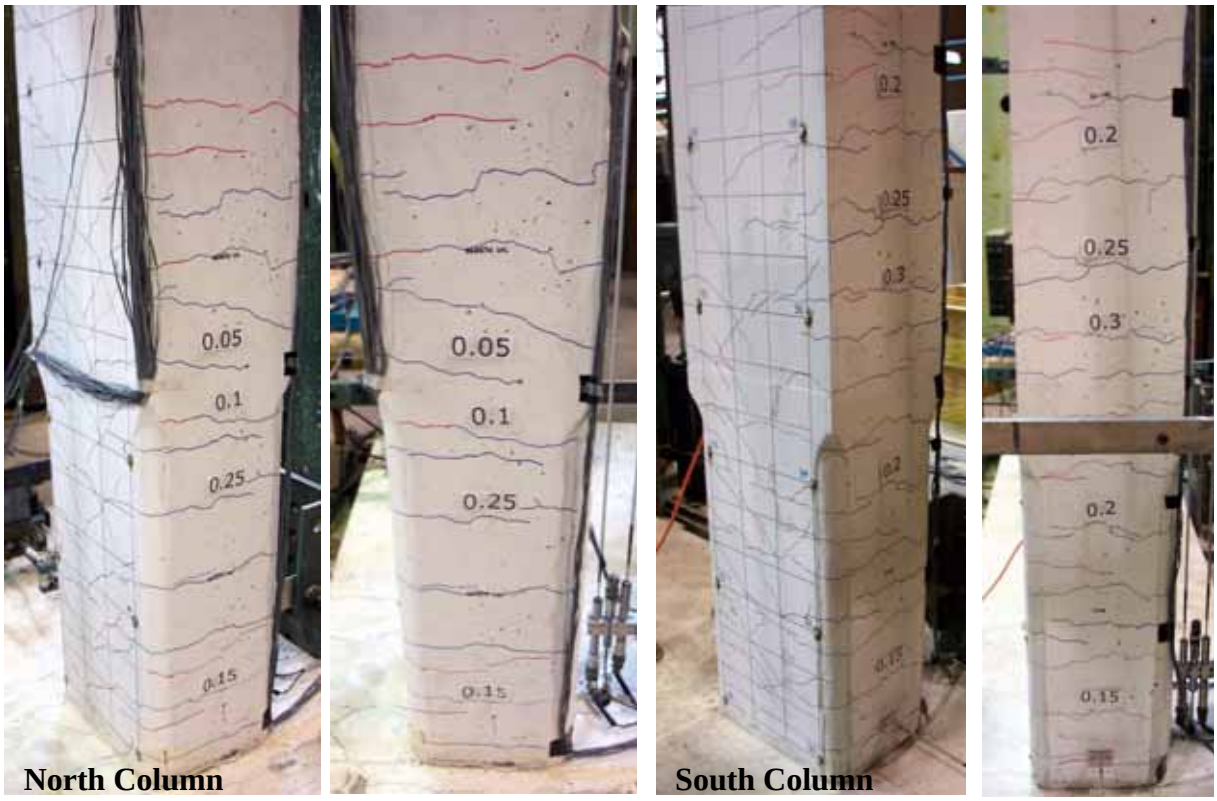

Figure 4.19 Frame at Load Cycle 7 (-3.0 Δ_y)

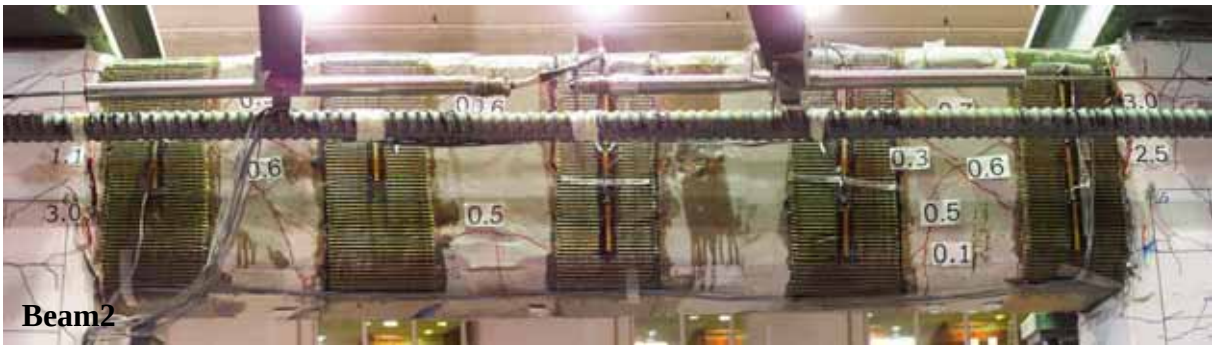

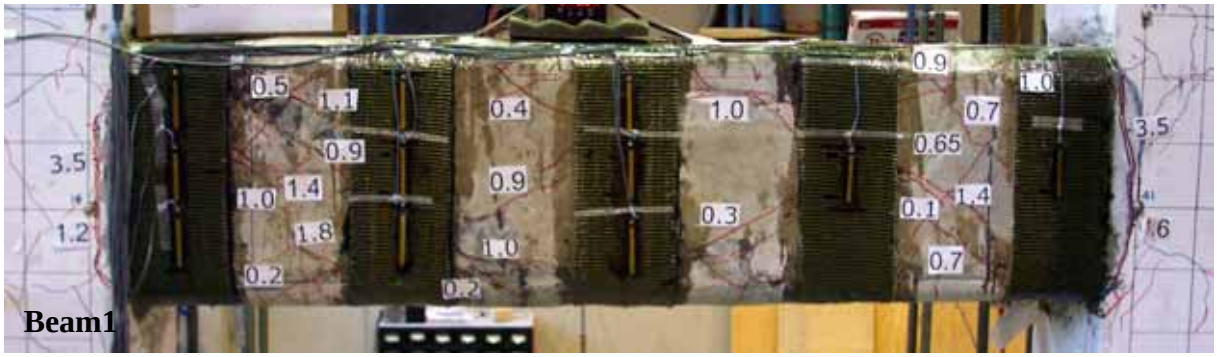

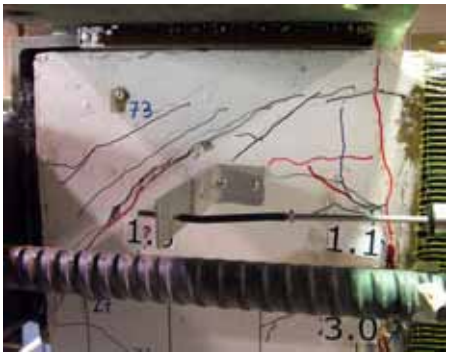

Second-Storey Beam-Column Joint (North)

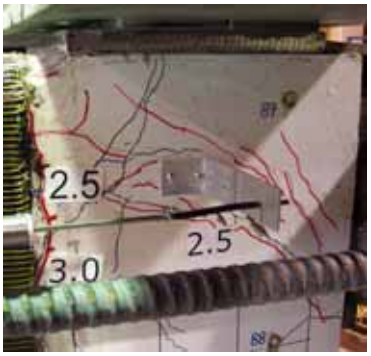

Second-Storey Beam-Column Joint (South)

Beam1N Top Face

Figure 4.20 Frame at Load Cycle 8 (-3.0 Δ_y)

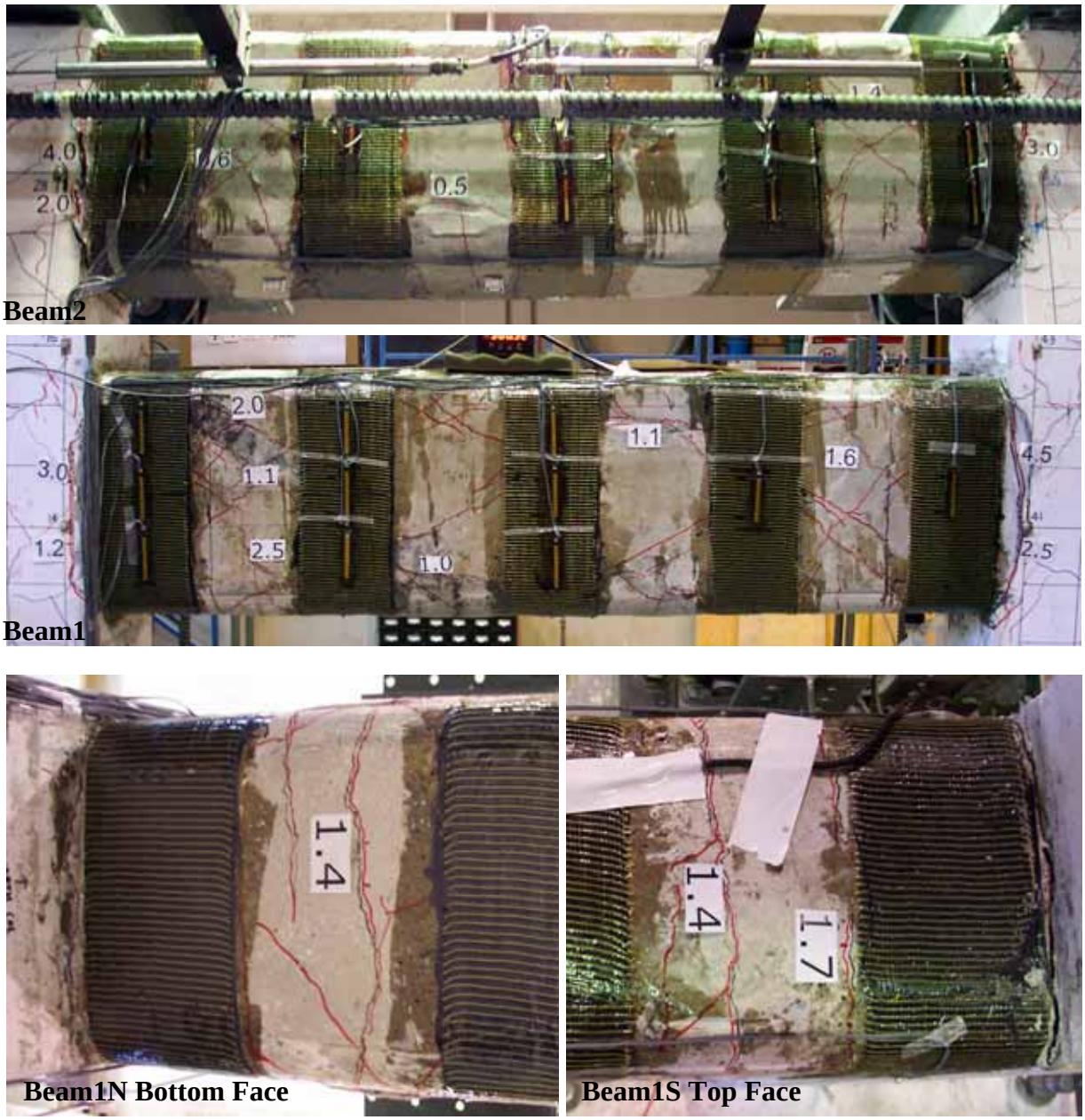

Figure 4.21a Frame at Load Cycle 9 (+4.0 Δ_y)

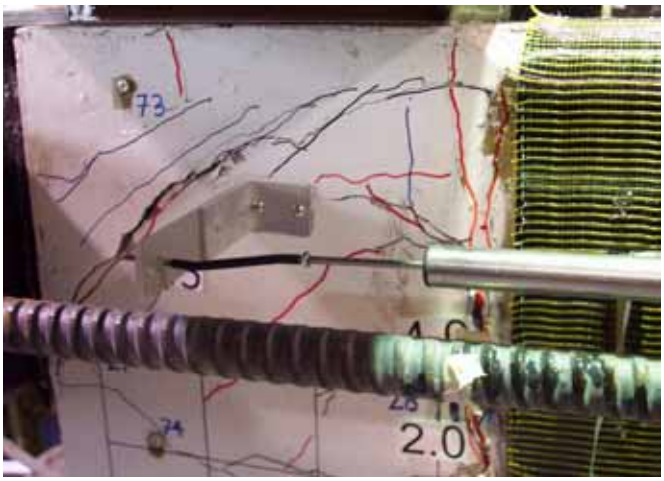

Second-Storey Beam-Column Joint (North)

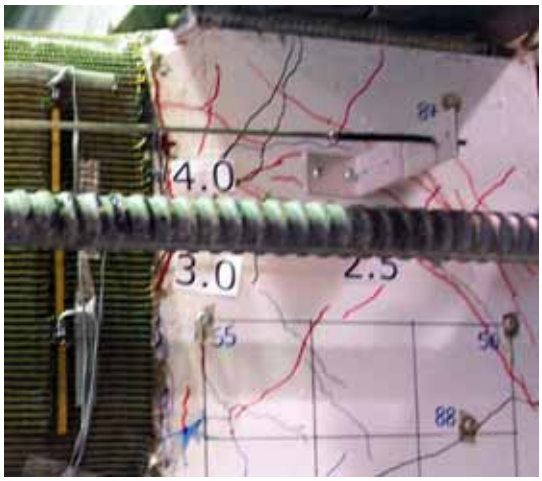

Second-Storey Beam-Column Joint (North)

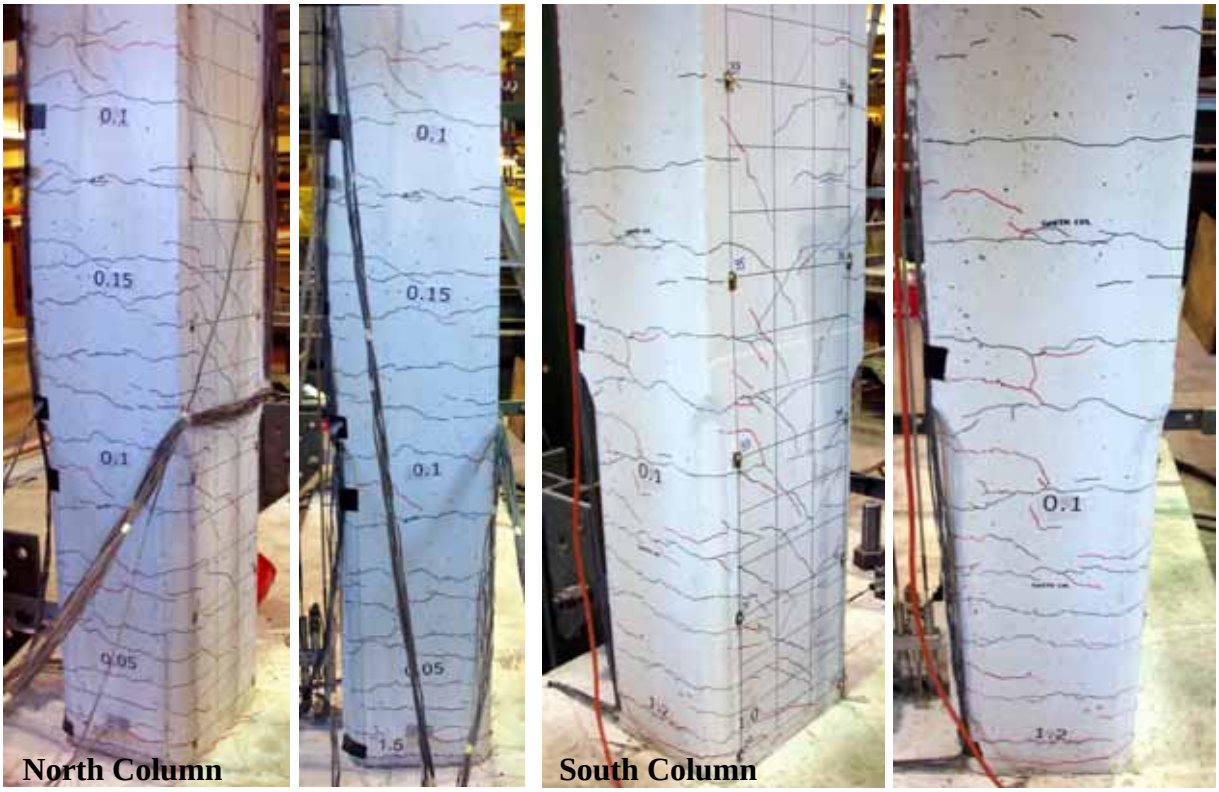

Figure 4.21b Frame at Load Cycle 9 (+4.0 Δ_y)

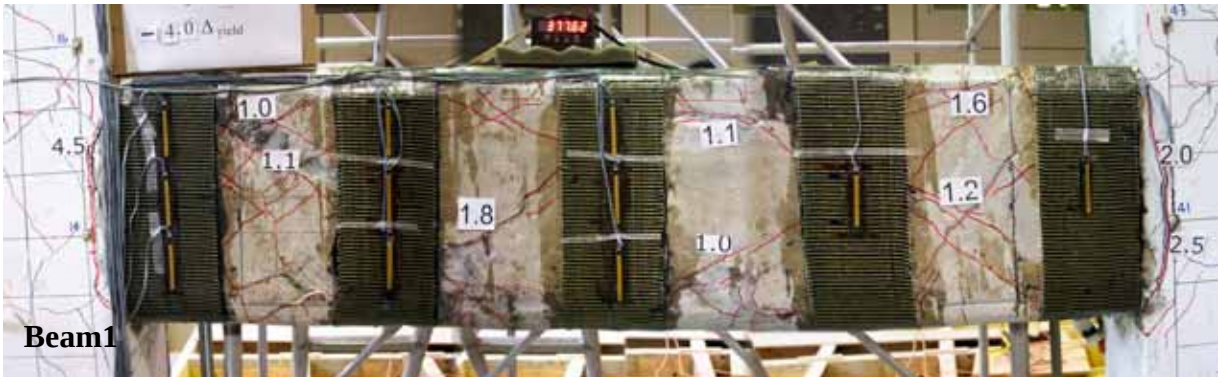

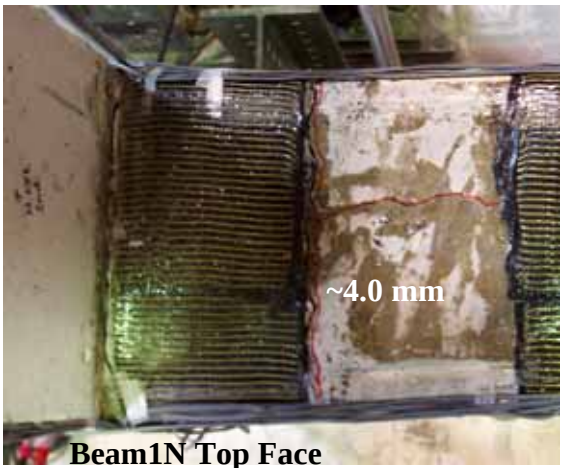

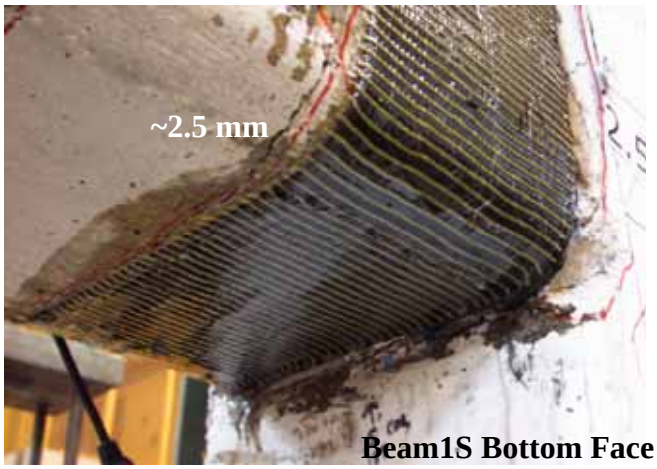

Figure 4.22a Frame at Load Cycle 9 (-4.0 Δ_y)

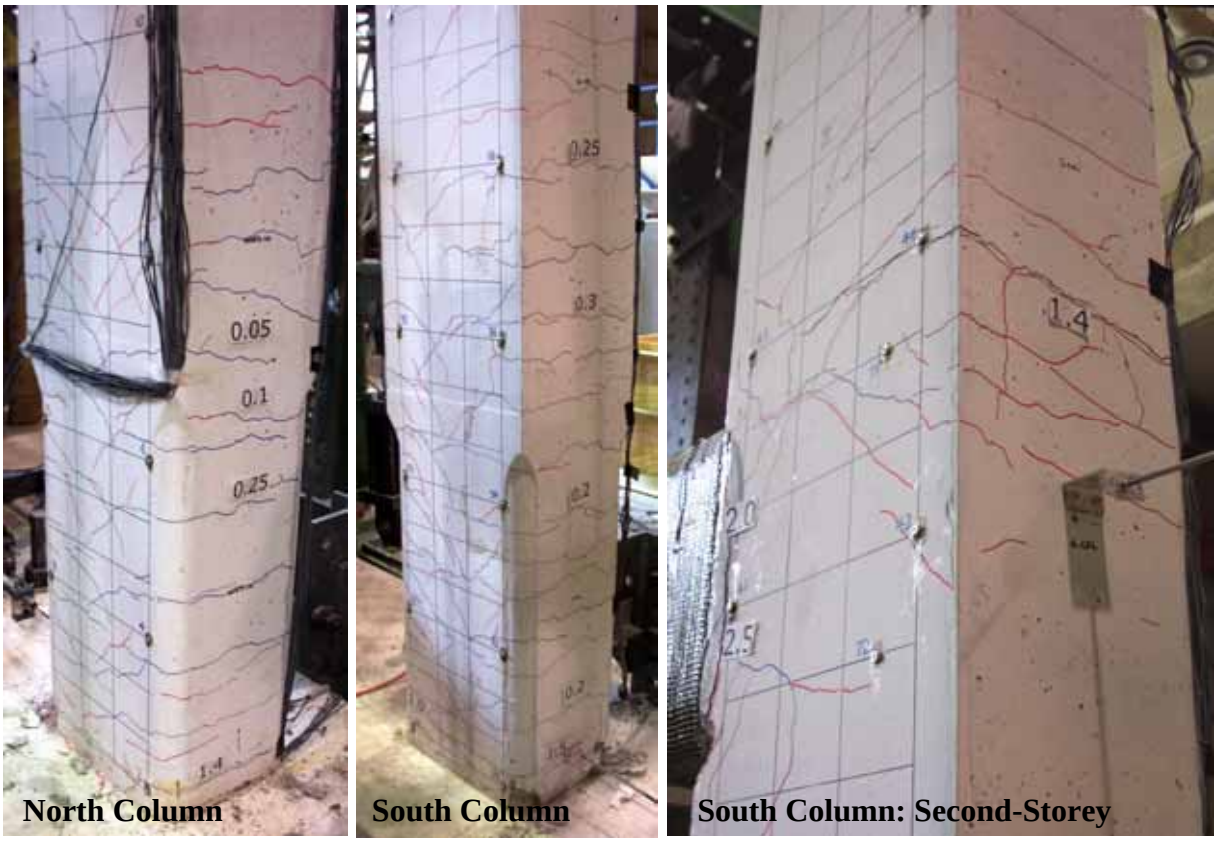

Figure 4.22b Frame at Load Cycle 9 (-4.0 Δ_y)

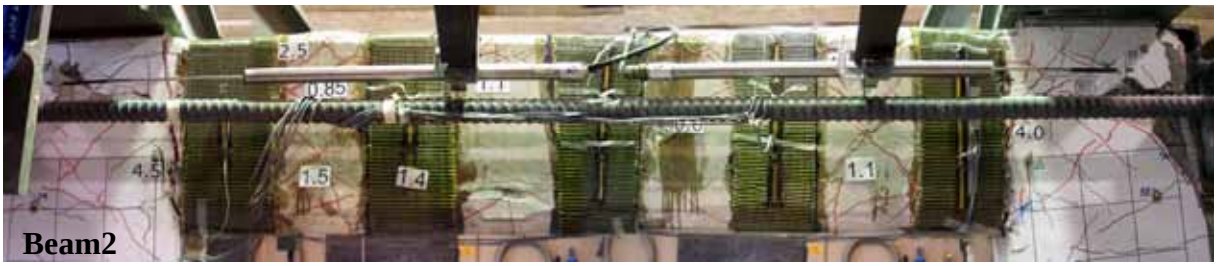

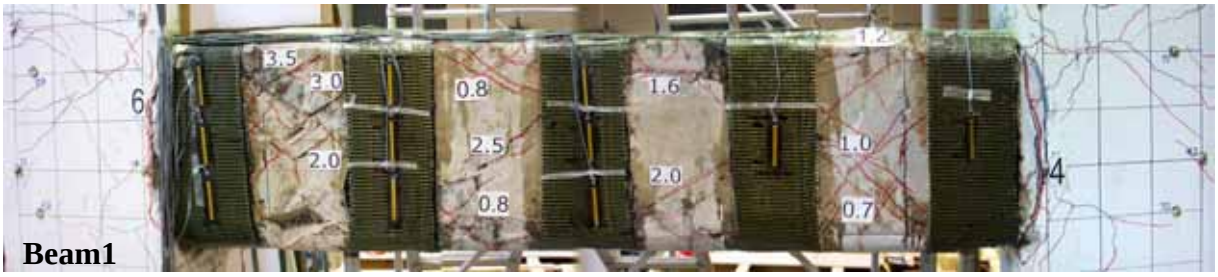

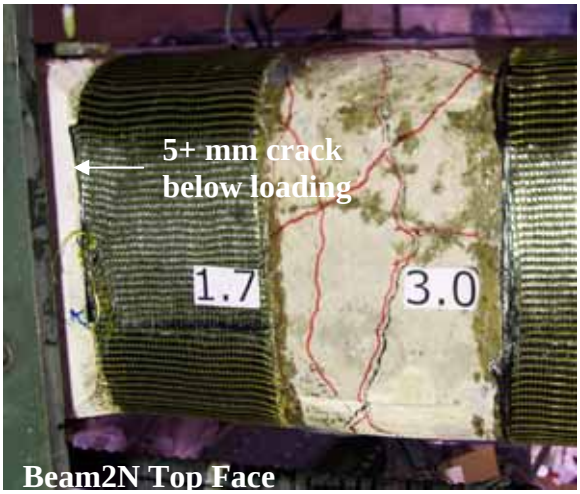

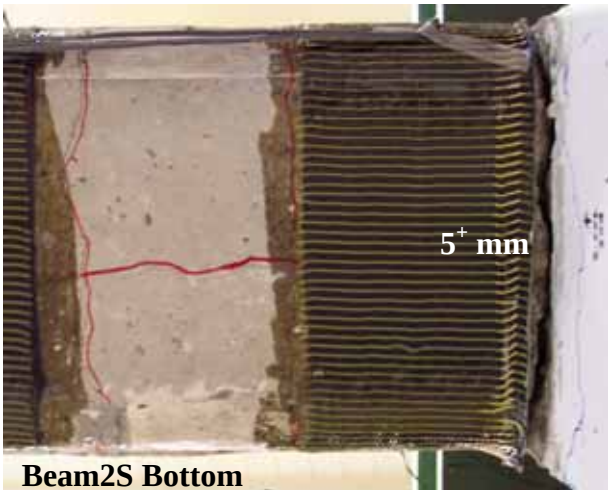

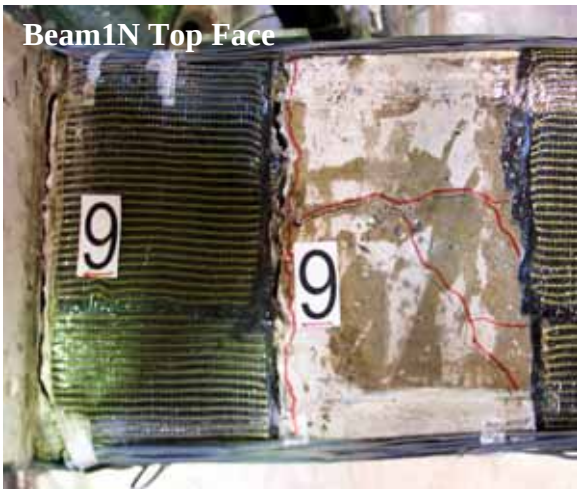

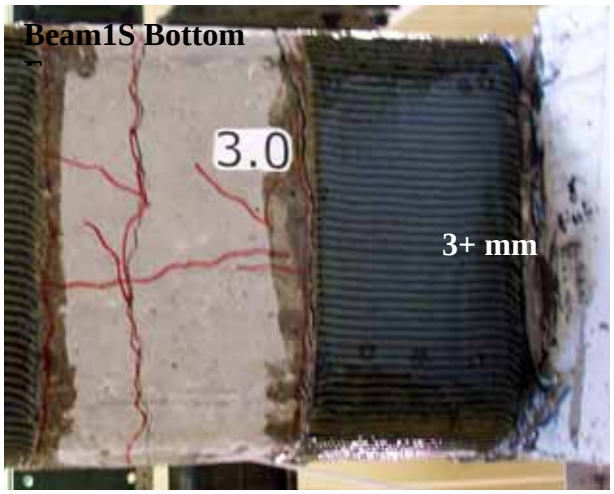

Figure 4.23a Frame at Load Cycle 13 (-6.6 Δ_y)

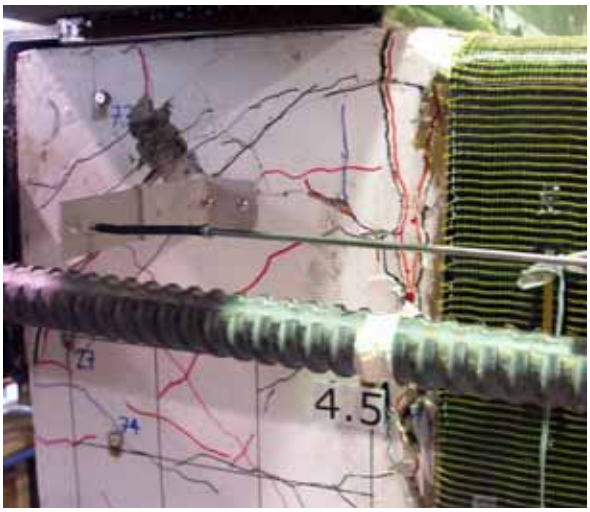

Second-Storey Beam-Column Joint (North)

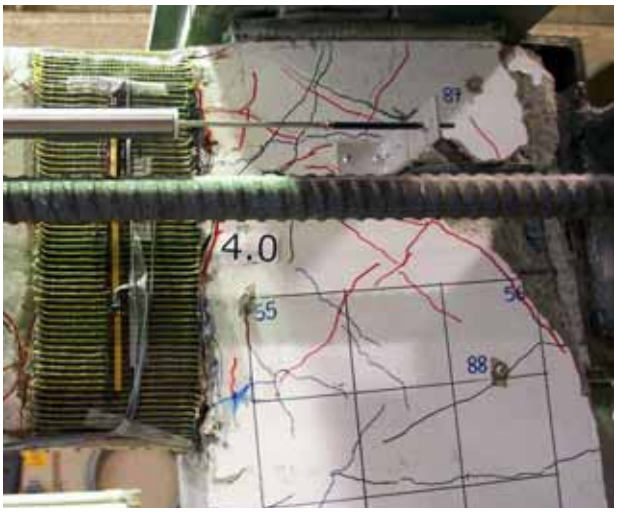

Second-Storey Beam-Column Joint (South)

North Column Top Elevation

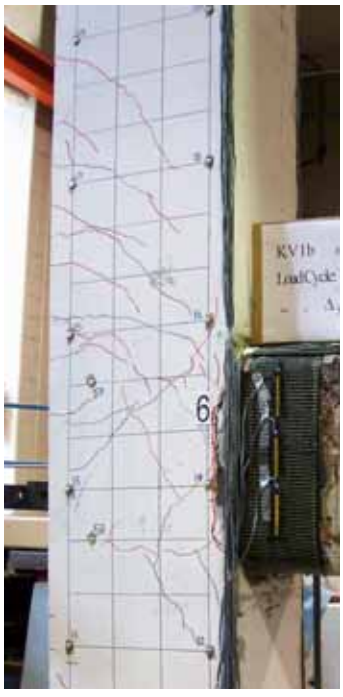

Mid Elevation

Bottom Element

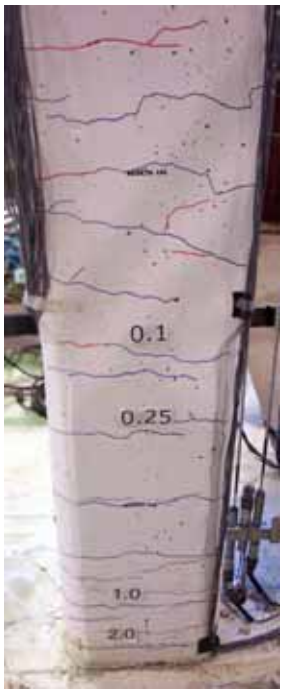

Side Elevation

Figure 4.23b Frame at Load Cycle 13 (-6.6 Δ_y)

South Column
Top Elevation

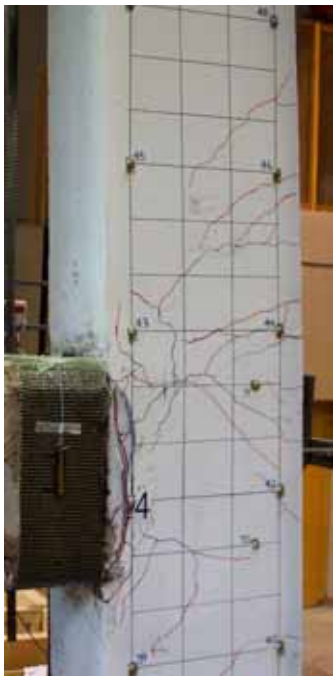

Mid Elevation

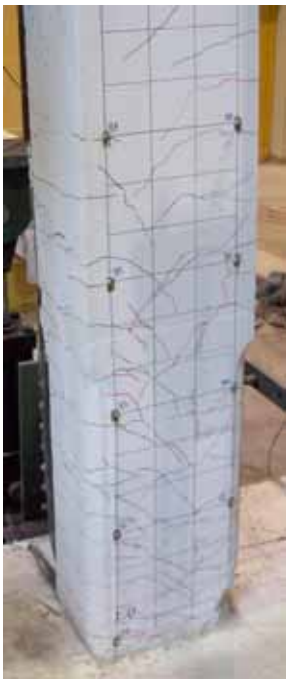

Bottom Elevation

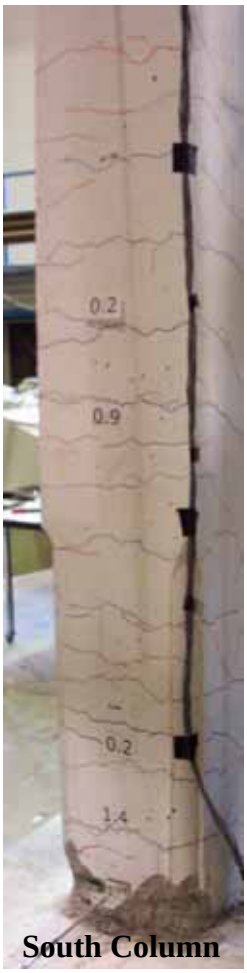

South Column

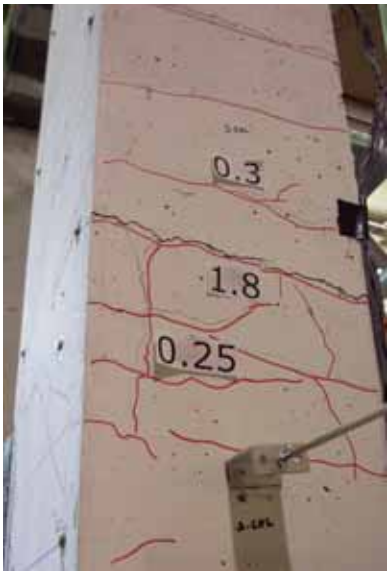

South Column:
Second-Storey

Figure 4.23c Frame at Load Cycle 13 (-6.6 Δ_y)

4.2.6 Zurich Readings

The horizontal, vertical, and shear surface strains were calculated along the first and second-storey beams via Zurich gauge readings. Figure 4.24 illustrates the layout of the Zurich grids, the target numbering, and the grid numbering. There were seven grids on each beam; each grid was sized at approximately 300 mm x 300 mm. The surface strains were calculated for each grid and results are presented in the next section (4.2.7).

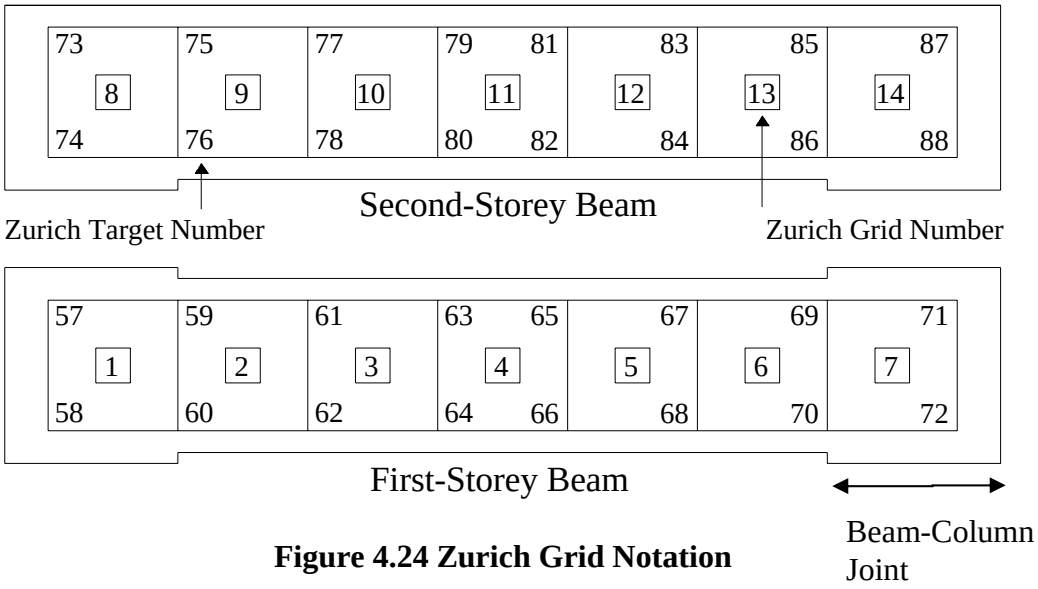

Figure 4.24 Zurich Grid Notation

4.2.7 Graphs of Specimen Response: Phase A

This section presents the graphs of the specimen response from Phase A of testing. Only the graphs and descriptions of how the source data was processed are included. Refer to Chapter 5 for a full discussion of these graphs. Figure 4.25 illustrates the lateral load versus average second-storey displacement response. The displacement was taken as the average of the four second-storey LVDTs located at both ends of the second-storey beam (WNHT, WSHT, ENHT, ESHT). In this figure, the important load stages were pointed out where the structural stiffness changed. Table 4.5 summarizes these specific load stages, as well as other load stages where important events took place. Figure 4.26 illustrates the lateral load versus longitudinal tensile steel strain for the first-storey beam.

All gauges at the first-storey beam were plotted except for B4 and B5 which were non-functional. The compressive steel strain was not plotted for clarity. The top half of Figure 4.26 indicates the tensile strains recorded during the forward half-cycle, while the bottom half indicates the tensile strains measured during the reverse half-cycle. Recall that the tensile yield strain for the No. 20 longitudinal steel was 2250 $x10^{-6}$. Refer to Appendix C for the graphs that illustrate the complete strain cycle (i.e. where compression plots were also included). Figure 4.27 is equivalent to Figure 4.26, except that the longitudinal tensile strain of the second-storey beam is of interest. Figure 4.28 is a bar graph that shows the peak tensile strain reached by each stirrup during the forward half-cycle. Recall that the tensile yield strain for the US No.3 transverse steel was 2410 $x10^{-6}$ ε. Similarly Figure 4.29 illustrates the peak tensile strain reached by the stirrups during the reverse half-cycle. Several strain gauges were non-functioning after the forward loading and are shaded white in the plot. Refer to Appendix C for the figures that illustrate the net lateral load versus stirrup strain.

Figure 4.30 illustrates the lateral load versus first-storey beam elongation. The elongation was taken as the difference between the two lateral LVDTs located at the north and south ends of the first-storey beam (NHM, SHM). Similarly Figure 4.31 illustrates the net lateral load versus second-storey beam elongation. The elongation was taken as the difference between the four lateral LVDTs located at the north and south ends of the second-storey beam (WNHT, WSHT, ENHT, ESHT).

Figure 4.32 illustrates the lateral load versus north column axial deformation. The zero point for the column deformation was taken after the column vertical loads were applied. The top, middle, and bottom column deformations were recorded with LVDTs NVT, NVM, and NVB, respectively. To account for any possible base uplift, the lateral load was plotted against the north column net axial deformation (Figure 4.33). This net deformation was taken as the difference between LVDTs NVT and NVB. Equivalent to the north column, Figure 4.34 and Figure 4.35 illustrate the lateral load versus column

deformations for the south column. Corresponding LVDTs at the south column were SVT, SVM, and SVB.

Figure 4.36 to Figure 4.42 illustrate the surface strains for both beams as calculated from the Zurich measurements. The upper and lower halves of these graphs displayed results for the forward and reverse half-cycles, respectively. Because some the data points near the end of the forward half-cycle were omitted, the plots were discontinuous between the latter stages of the forward half-cycle and the first stage of the reverse half-cycle. The + and – in the legend indicated the forward and reverse directions of loading, respectively.

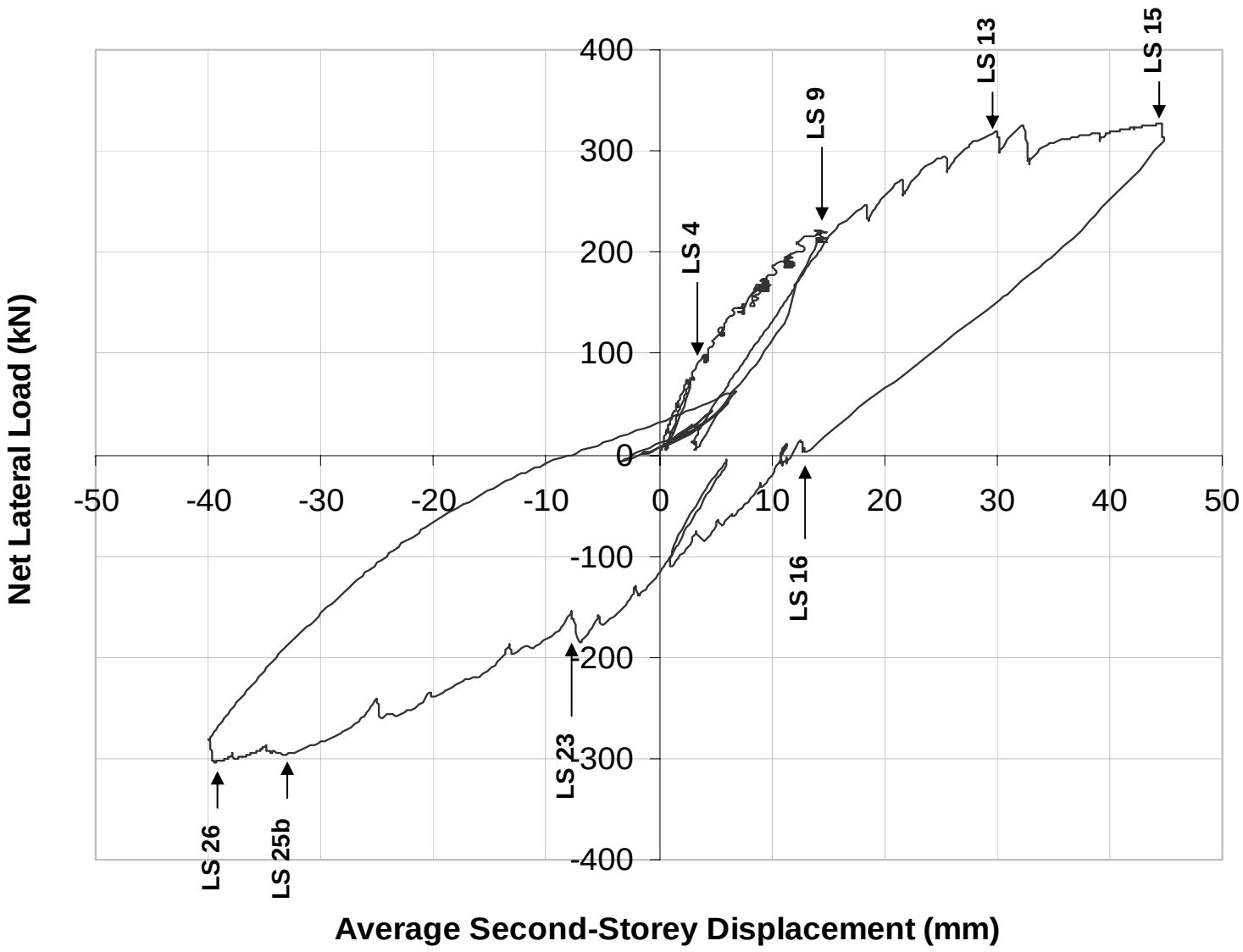

Figure 4.25 Lateral Load vs. Second-Storey Displacement (Phase A)

Table 4.5 Key Load Stages (Phase A)

Load Stage	Load (kN)	Avg. 2nd Storey Lat. Displ. (mm)	Comment
Forward Half-cycle			
0	0	0	Initial condition
3	75	2.65	First lower beam flexural crack
4	99	4.13	First north column flexural crack
5	125	5.46	First lower beam shear crack First south column flexural crack
8	197	11.7	First upper beam shear crack
9	221	13.8	Change in structural stiffness
12	295	25.5	Lower beam flexural yielding (B3, B6)
13	320	30.0	Upper beam flexural yielding (B11, B2, B14) Shear yielding in upper (S12) and lower (S4) beams
14	325	32.3	Lower beam shear crack was 4.0 mm wide
15	327	44.7	Shear yielding in upper (S8) beam Lower beam shear crack was 9.0 mm wide Upper beam shear crack was 2.0 mm wide
Reverse Half-cycle			
16	-2	10.78	Initial condition
17	-32	9.10	First lower beam flexural crack
19	-84	4.09	First lower beam shear crack
20	-111	1.02	First south column flexural crack
22	-168	-4.98	First upper beam shear crack
23	-185	-7.10	Sudden large lower beam shear crack
25	-260	-24.6	Shear yielding in upper (S7) and lower (S3) beams
25b	-295	-33.6	Intermediate reading
26	-304	-39.5	Shear yielding in lower (S4) beam Lower beam shear crack was 7.0 mm wide Upper beam shear crack was 5.0 mm wide
	-2	-7.43	Final condition

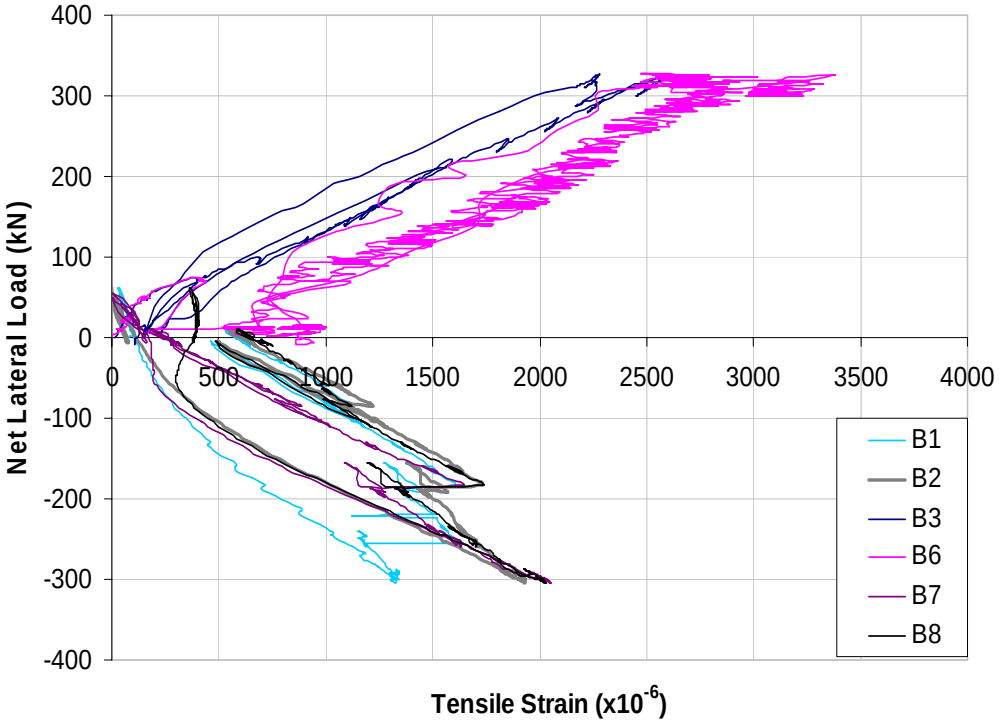

Figure 4.26 Lateral Load vs. Longitudinal Tensile Steel Strain: First-Storey Beam (Phase A)

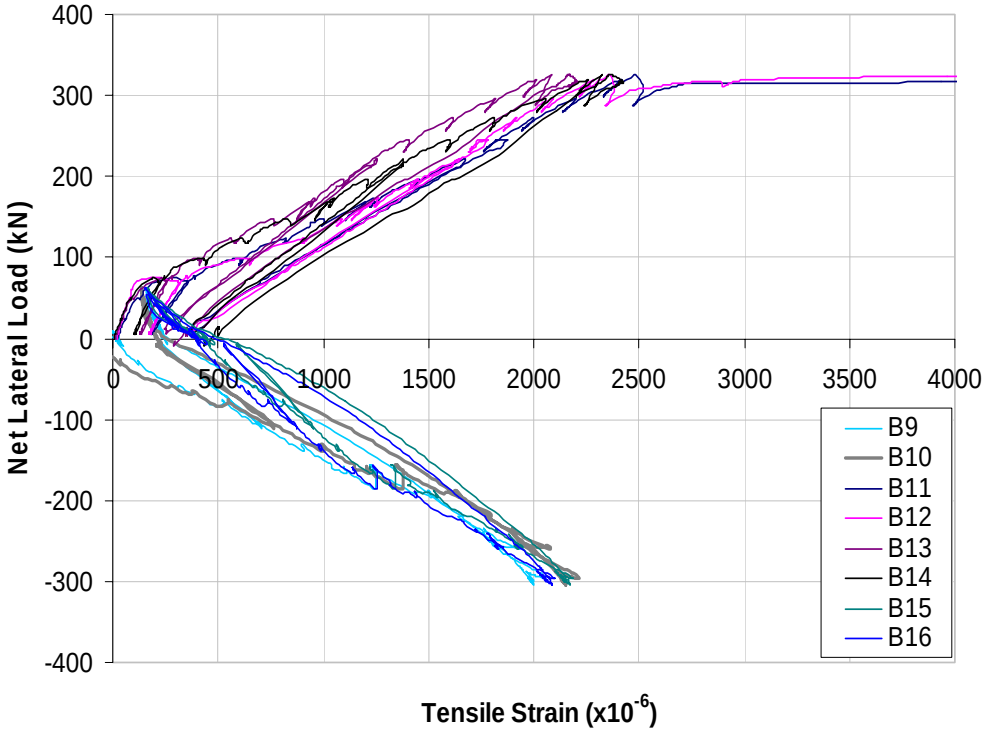

Figure 4.27 Lateral Load vs. Longitudinal Tensile Steel Strain: Second-Storey Beam (Phase A)

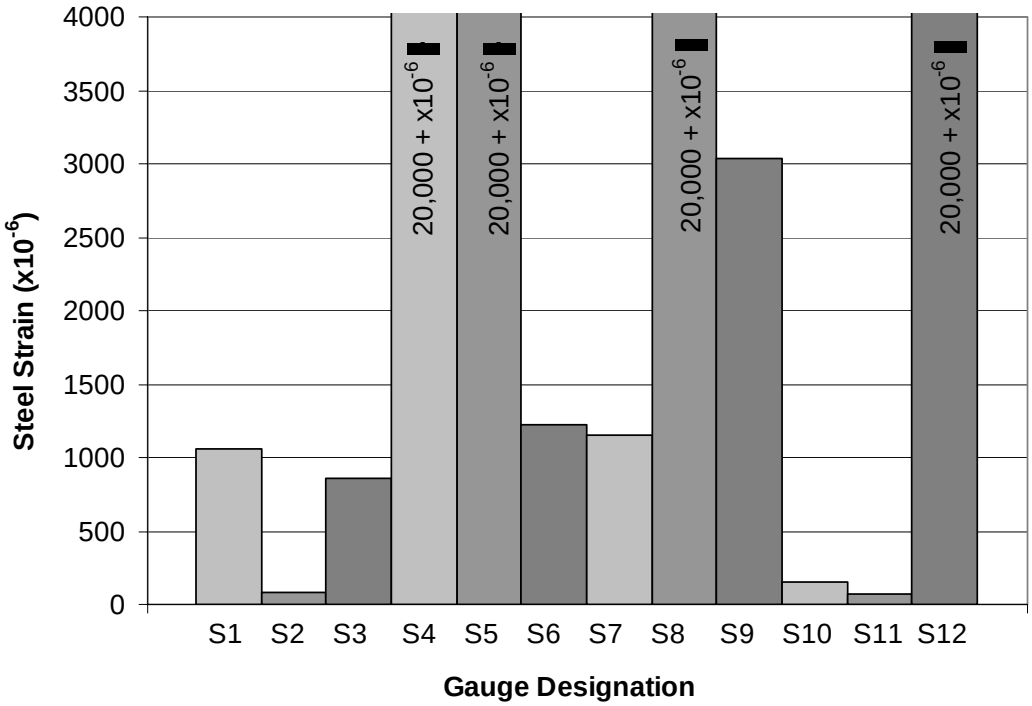

Figure 4.28 Maximum Stirrup Steel Strain: Forward Half-cycle (Phase A)

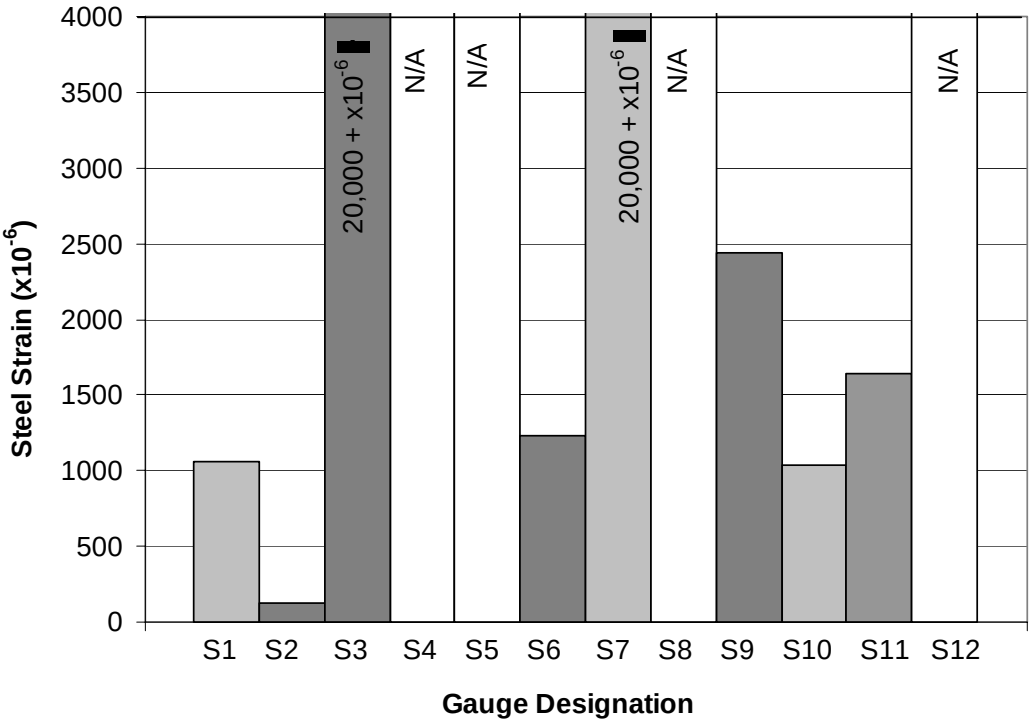

Figure 4.29 Maximum Stirrup Steel Strain: Reverse Half-cycle (Phase A)

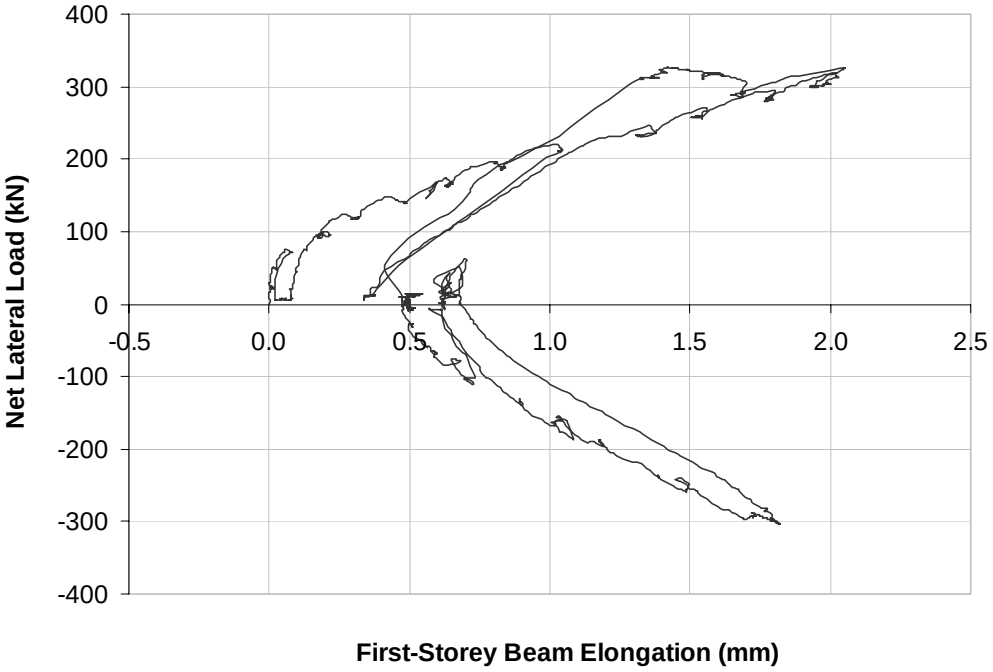

Figure 4.30 Lateral Load vs. First-Storey Beam Elongation (Phase A)

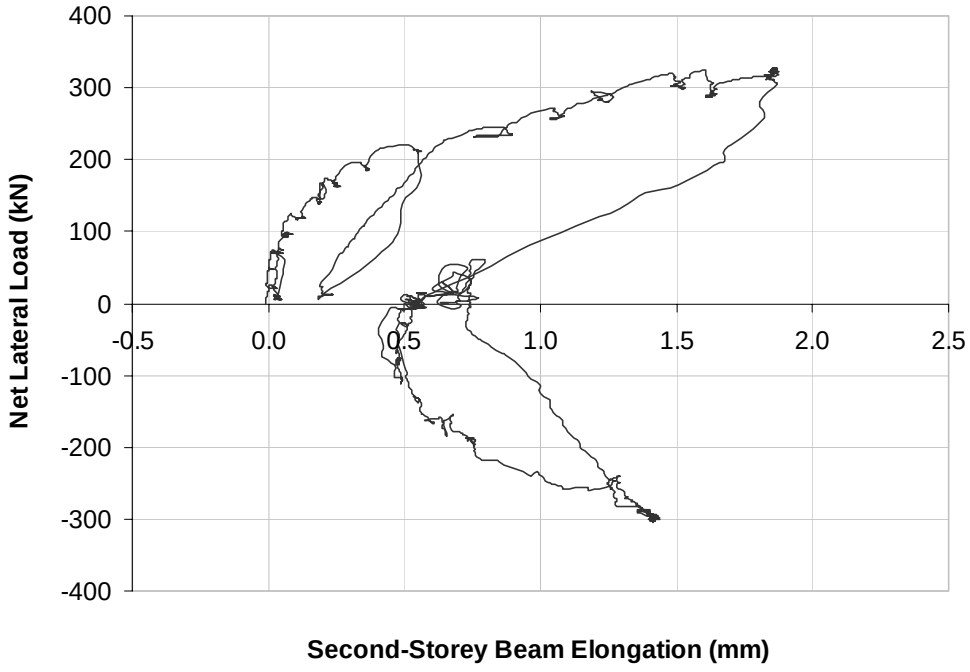

Figure 4.31 Lateral Load vs. Second-Storey Beam Elongation (Phase A)

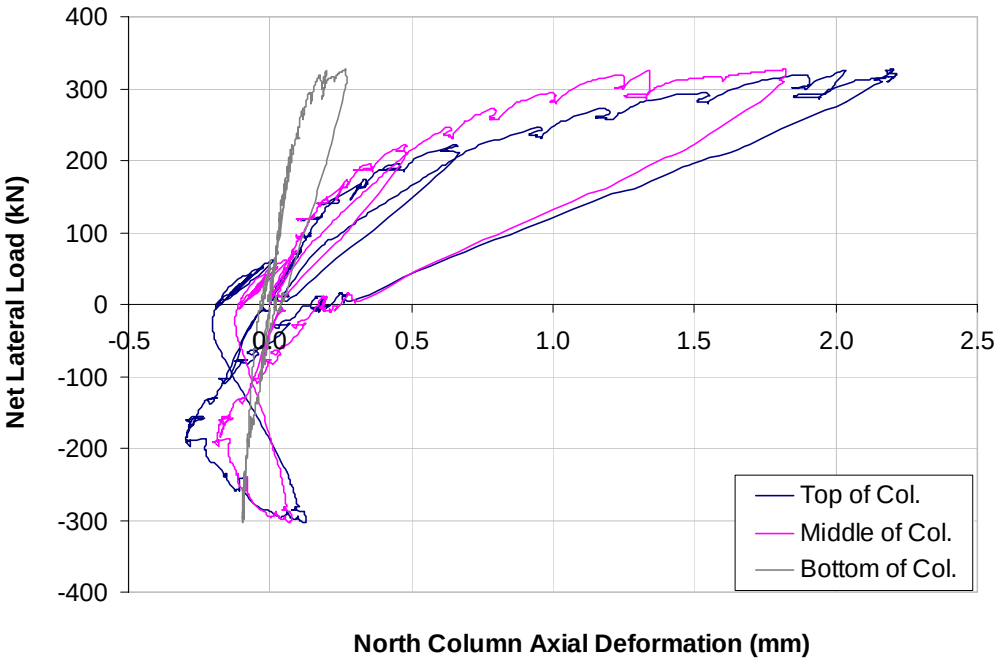

Figure 4.32 Lateral Load vs. North Column Axial Deformation (Phase A)

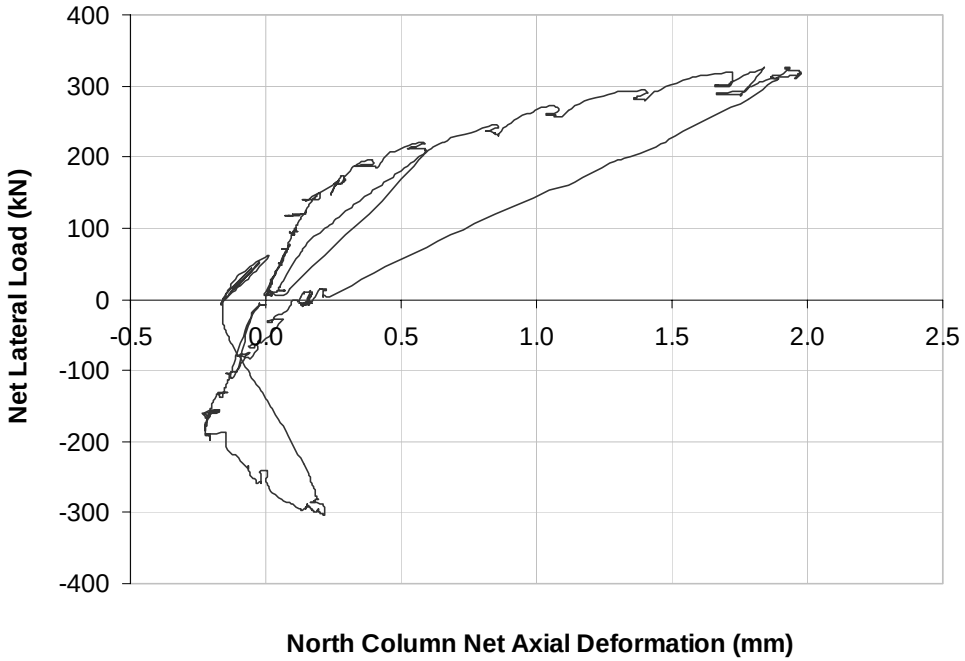

Figure 4.33 Lateral Load vs. North Column Net Axial Deformation (Phase A)

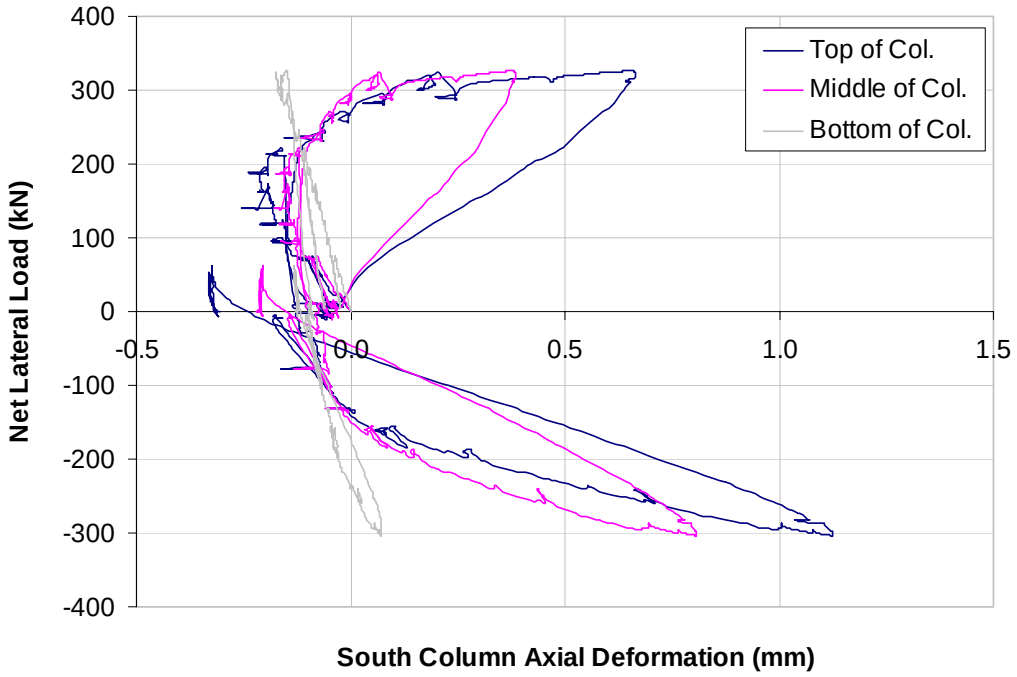

Figure 4.34 Lateral Load vs. South Column Axial Deformation

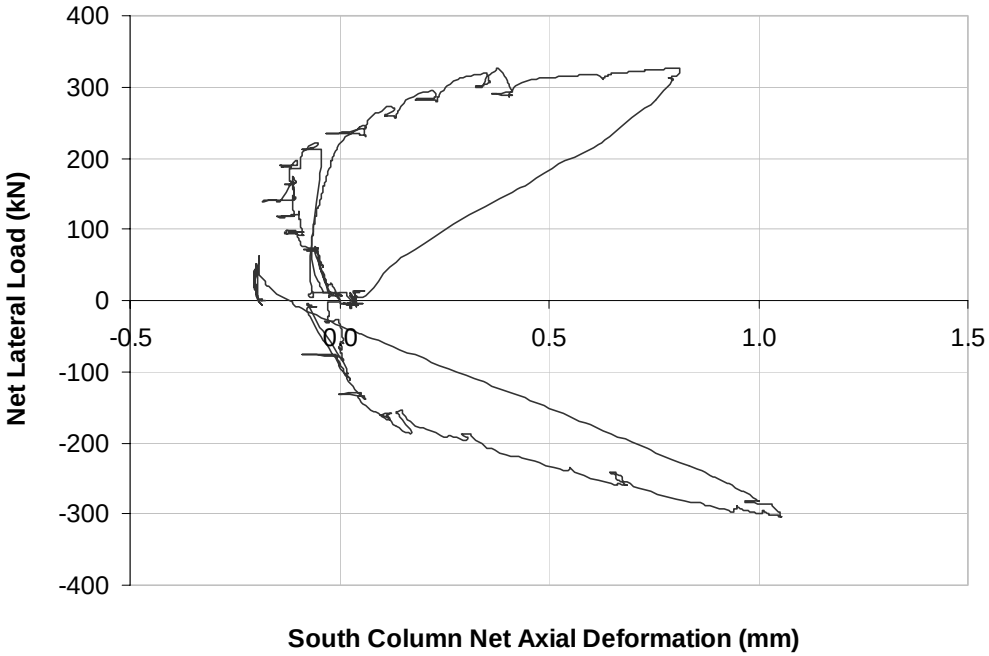

Figure 4.35 Lateral Load vs. South Column Net Axial Deformation

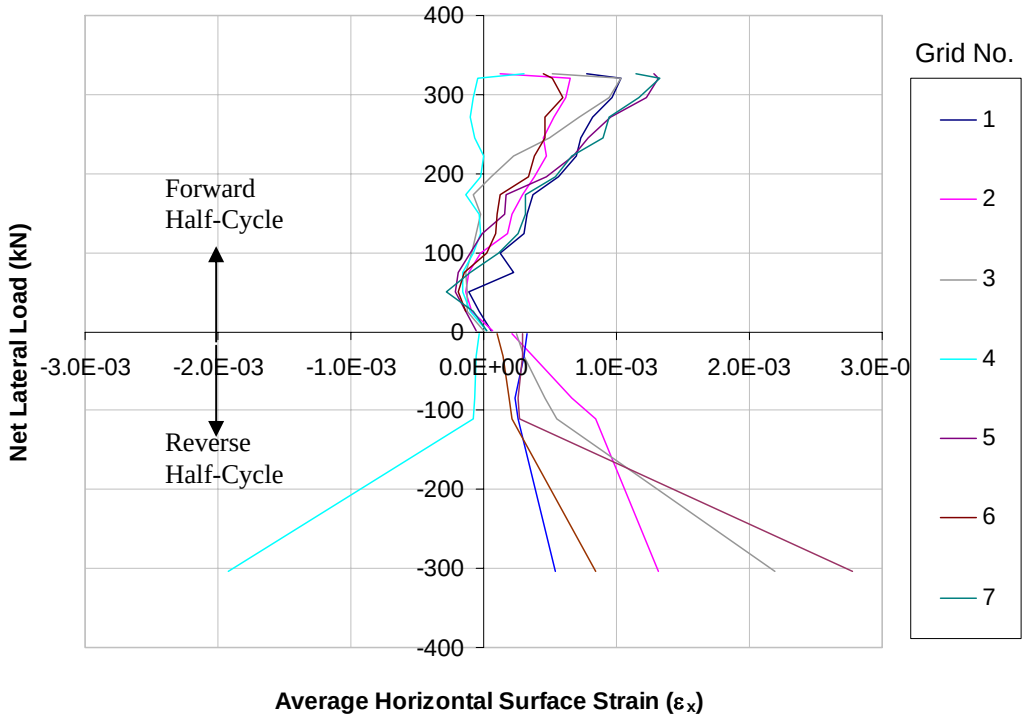

Figure 4.36 Lateral Load vs. Horizontal Surface Strain: First-Storey Beam

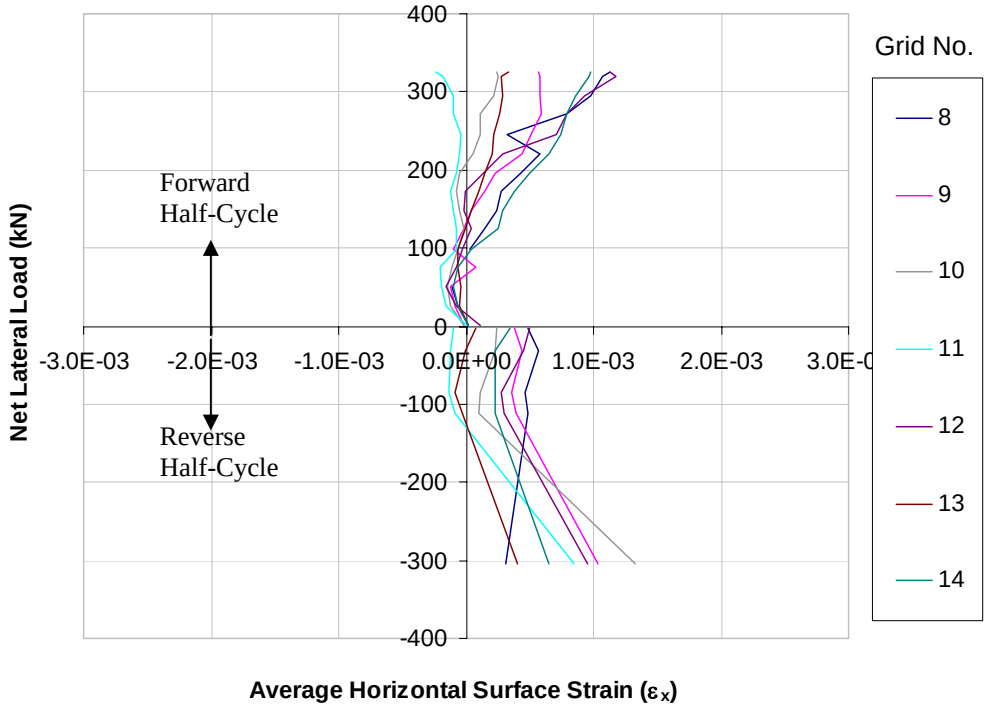

Figure 4.37 Lateral Load vs. Horizontal Surface Strain: Second-Storey Beam

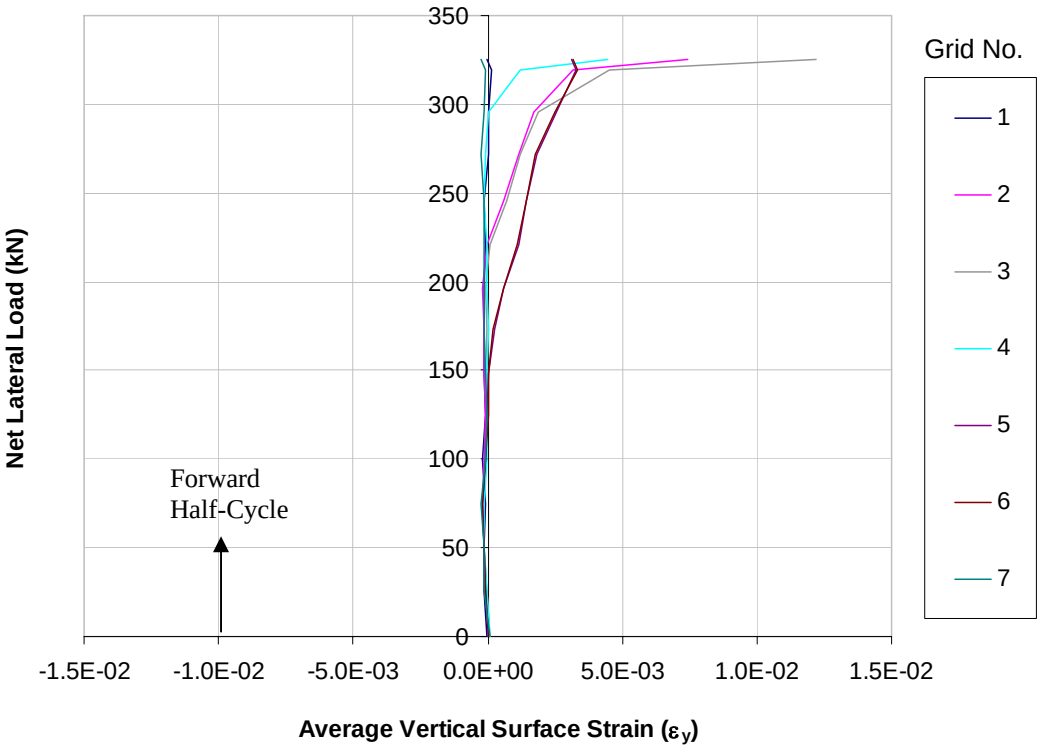

Figure 4.38 Lateral Load vs. Vertical Surface Strain: First-Storey Beam

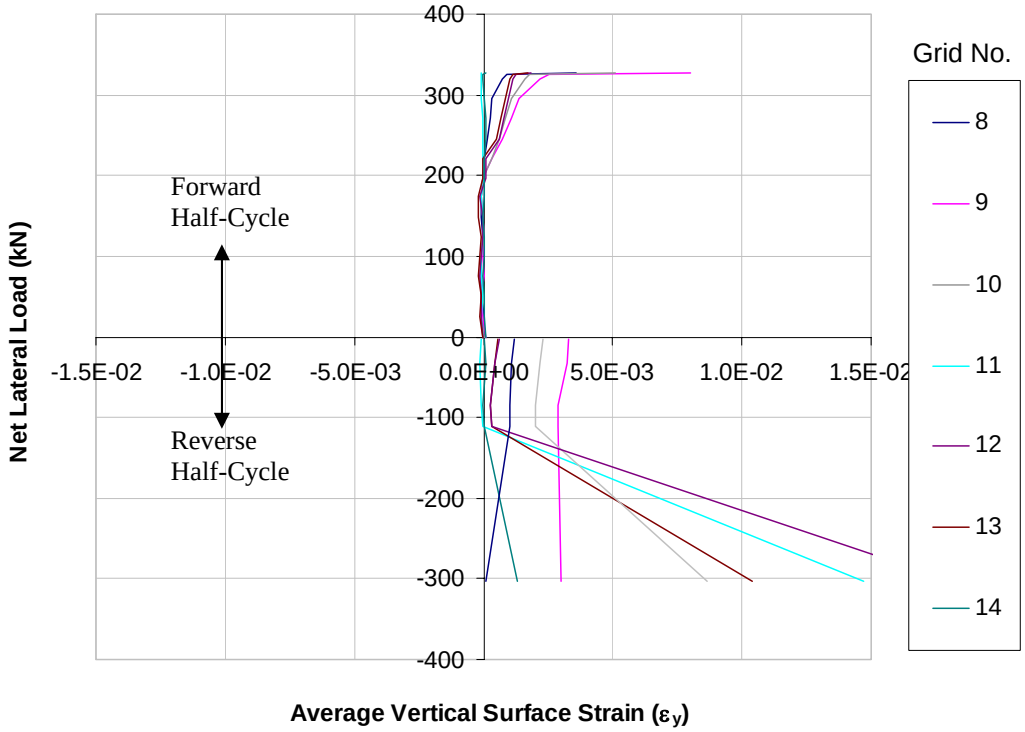

Figure 4.39 Lateral Load vs. Vertical Surface Strain: Second-Storey Beam

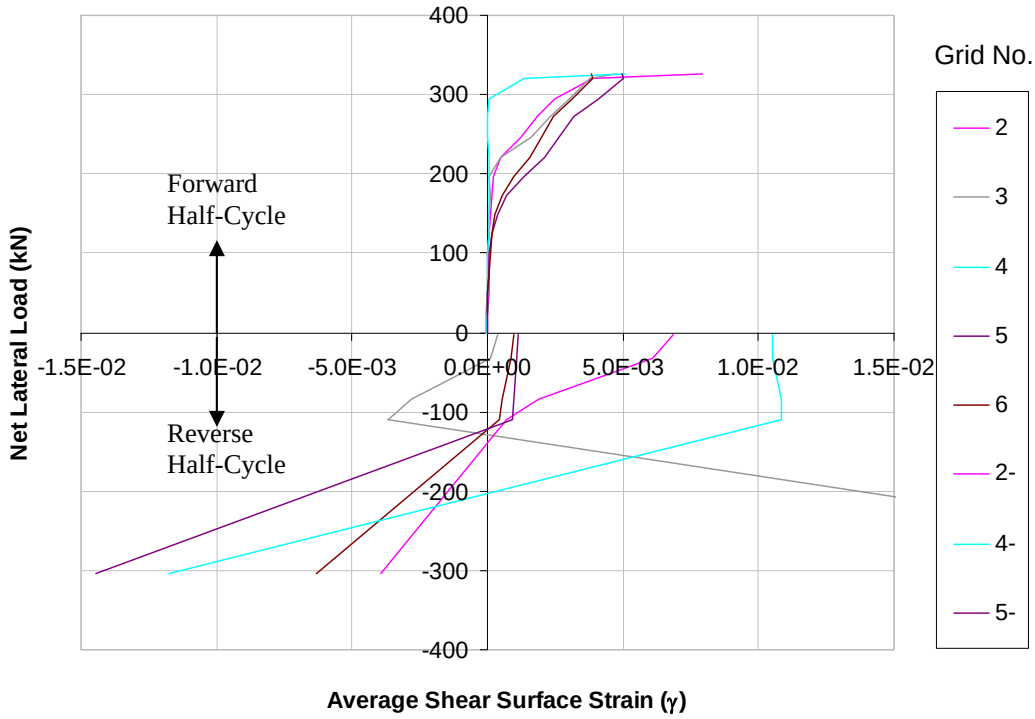

Figure 4.40 Lateral Load vs. Shear Surface Strain: First-Storey Beam

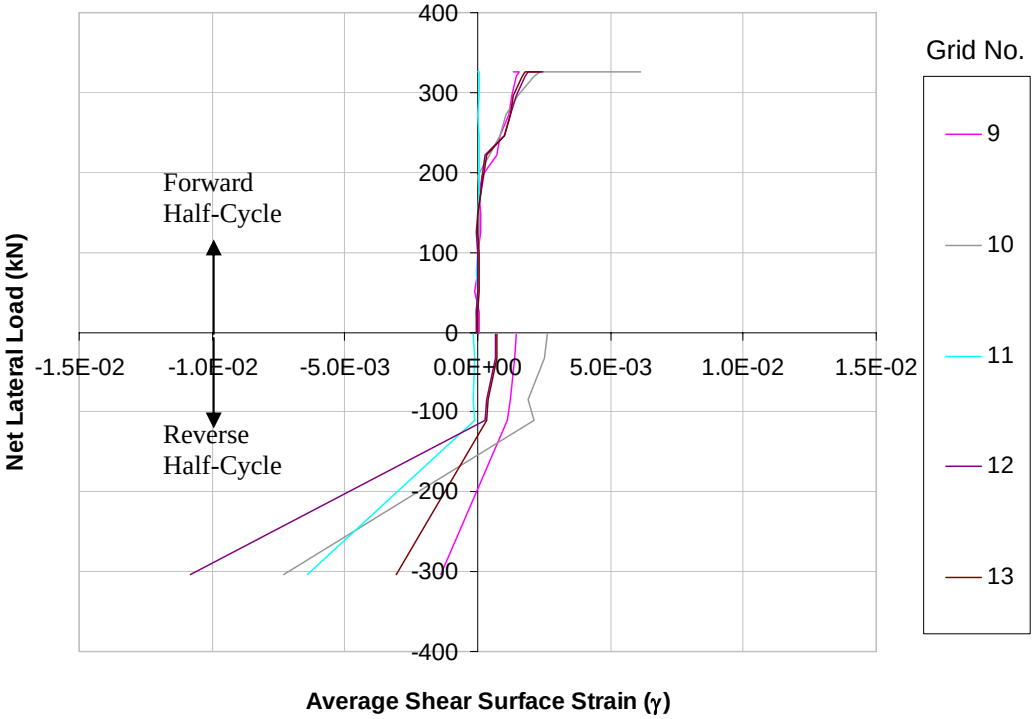

Figure 4.41 Lateral Load vs. Shear Surface Strain: Second-Storey Beam

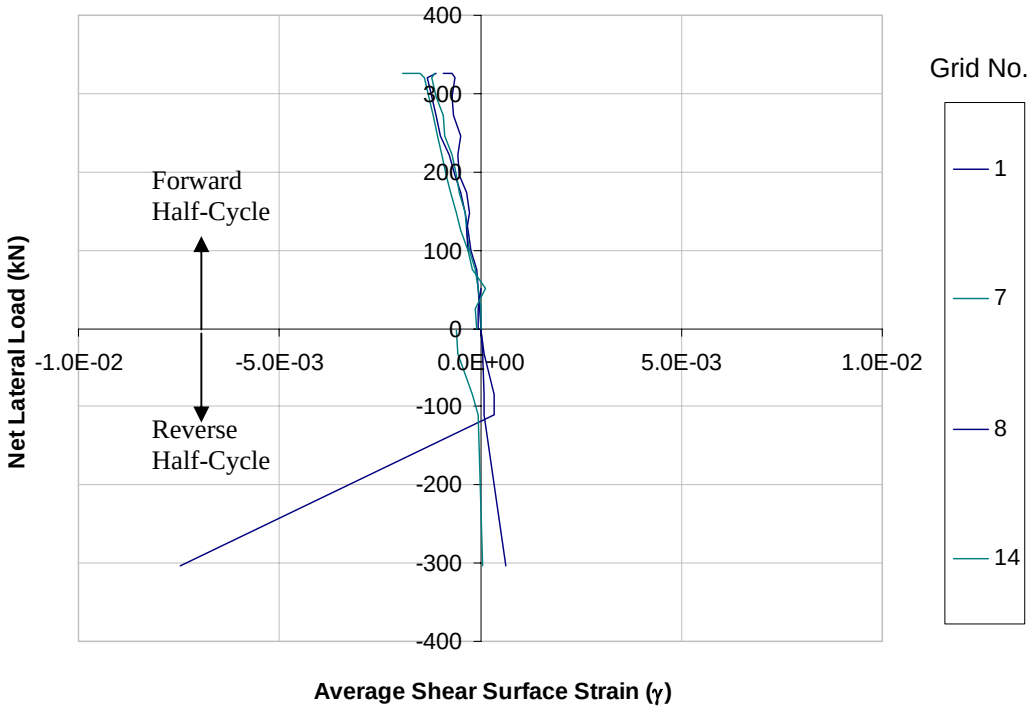

Figure 4.42 Lateral Load vs. Shear Surface Strain: Beam-Column Joints (Phase A)

4.2.8 Graphs of Experimental Response: Phase B

This section presents the graphs of the specimen response from Phase B of testing. Only the graphs and descriptions of how the source data was processed are included. Refer to Chapter 5 for a full discussion of these graphs. Figure 4.43 illustrates the lateral load versus second-storey displacement for Phase B of the experiment. The set of LVDTs used to record the displacement was the same as those used for Figure 4.25. Table 4.6 summarizes the characteristics of the cyclic response of this specimen. Figure 4.44 and Figure 4.45 show the average CFRP stress level with respect to the forward and reverse load cycles. The average stress was taken from the five CFRP wraps located along the length of each beam. The set of graphs presented in Figure 4.46 contains similar information to the graphs presented in Figure 4.44 and Figure 4.45, except the shear stresses are plotted for all five strips located at each beam. The numbering of the wraps started at the north end of the beam and progressed to the south end of the beam (refer to Figure 3.17). Wrap 1 was placed at the north end of the beam, flushed against the north beam-column interface. Wrap 2 was located at approximately d_v (310 mm) away from the north beam-column interface. Wrap 3 was located at the beam midspan. Wrap 4 was located at around d_v away from the south beam-column interface, and Wrap 5 was placed flushed against the south beam-column interface. Figure 4.47 and Figure 4.48 illustrate the CFRP stress distribution for a given wrap at the top, mid-depth, and bottom locations. There are ten graphs in each figure; each graph represent the strain for one of the ten wraps present (five wraps per beam). Figure 4.47 and Figure 4.48 present the findings for the forward and reverse cycles, respectively.

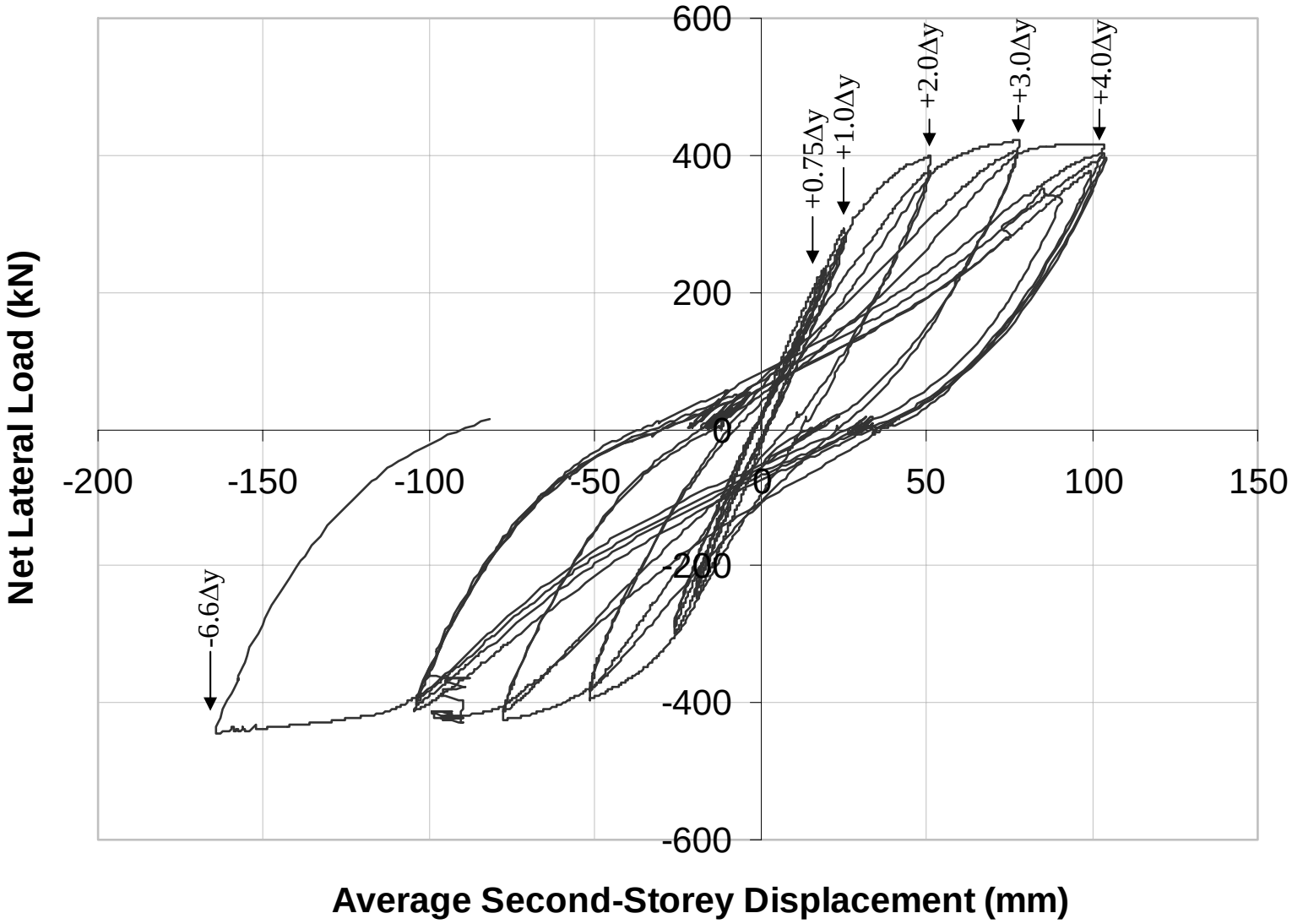

Figure 4.43 Lateral Load vs. Second-Storey Displacement (Phase B)

Table 4.6 Cyclic Response of Test Specimen

	Phase A	**Phase B**	
V_{peak}	327 kN	444 kN	
δ_y	11 mm	24 mm	
δ_{max}	44 mm	164 mm	
* $\mu_\Delta = \delta_{max} / \delta_y$	~ 4.0	> 6.8	
V_{peak} increase	~ 1.4 x original		
δ_{max} increase	> 3.7 x original		
μ_Δ increase	> 1.7 x original		
Energy. Dissipation	> 5.7 x original		
Initial Lateral Stiffness (kN / mm of top storey displacement)			
0 to 99 kN: 99 to 221 kN:	24.2 kN/mm 12.6 kN/mm	15.2 kN/mm 10.9 kN/mm	
Subsequent Initial Lateral Stiffness (kN / mm of top storey displacement)			
LC 1,2	$\pm$0.75 Δ_y	~12.5 kN/mm	100%
LC 3, 4	$\pm$1.0 Δ_y	~12.5 kN/mm	100%
LC 5	$\pm$2.0 Δ_y	10.2 kN/mm	82%
LC 6	$\pm$2.0 Δ_y	6.3 kN/mm	50%
LC 7	$\pm$3.0 Δ_y	~6.3 kN/mm	50%
LC 8	$\pm$3.0 Δ_y	4.4 kN/mm	35%
LC 9	$\pm$4.0 Δ_y	~4.4 kN/mm	35%
LC 10, 11, 12	$\pm$4.0 Δ_y	3.1 kN/mm	25%
LC 13	-6.6 Δ_y	~3.1 kN/mm	25%

Note: * Refer to Appendix B for the derivation of the displacement ductility (μ_Δ).

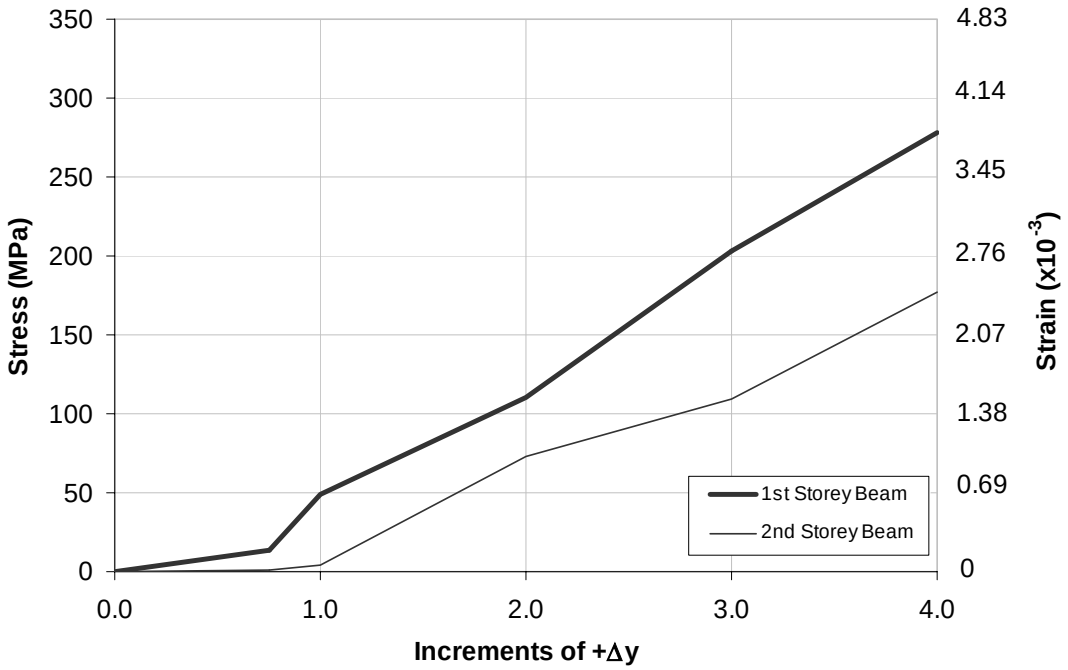

Figure 4.44 Average CFRP stress and strain at the Forward Load Cycles of Phase B

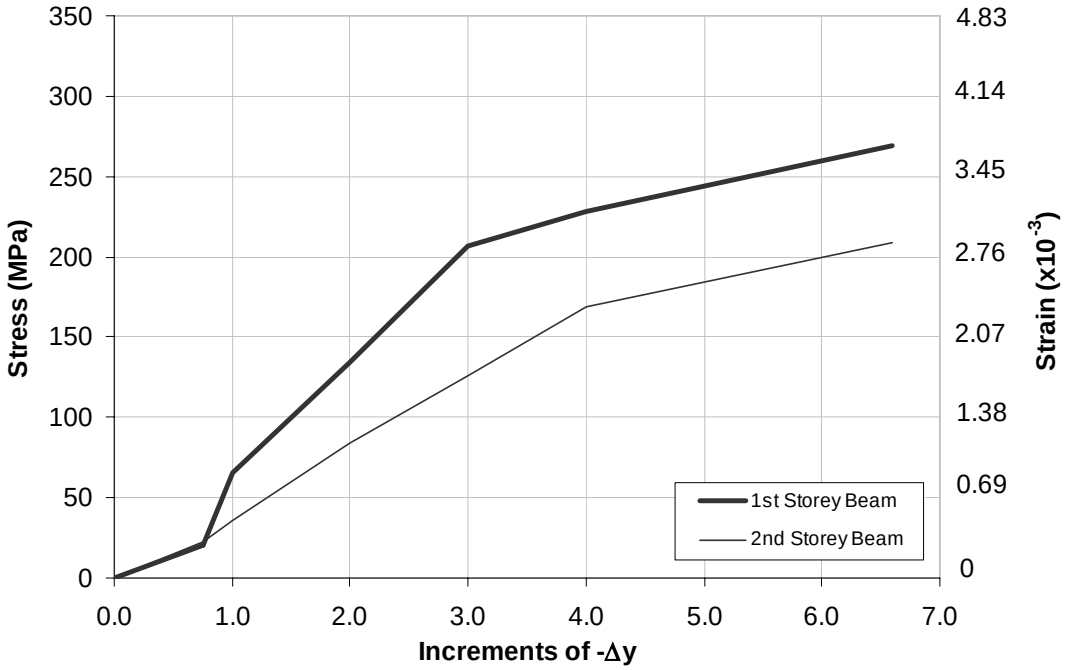

Figure 4.45 Average CFRP Stress and strain at the Reverse Load Cycles of Phase B

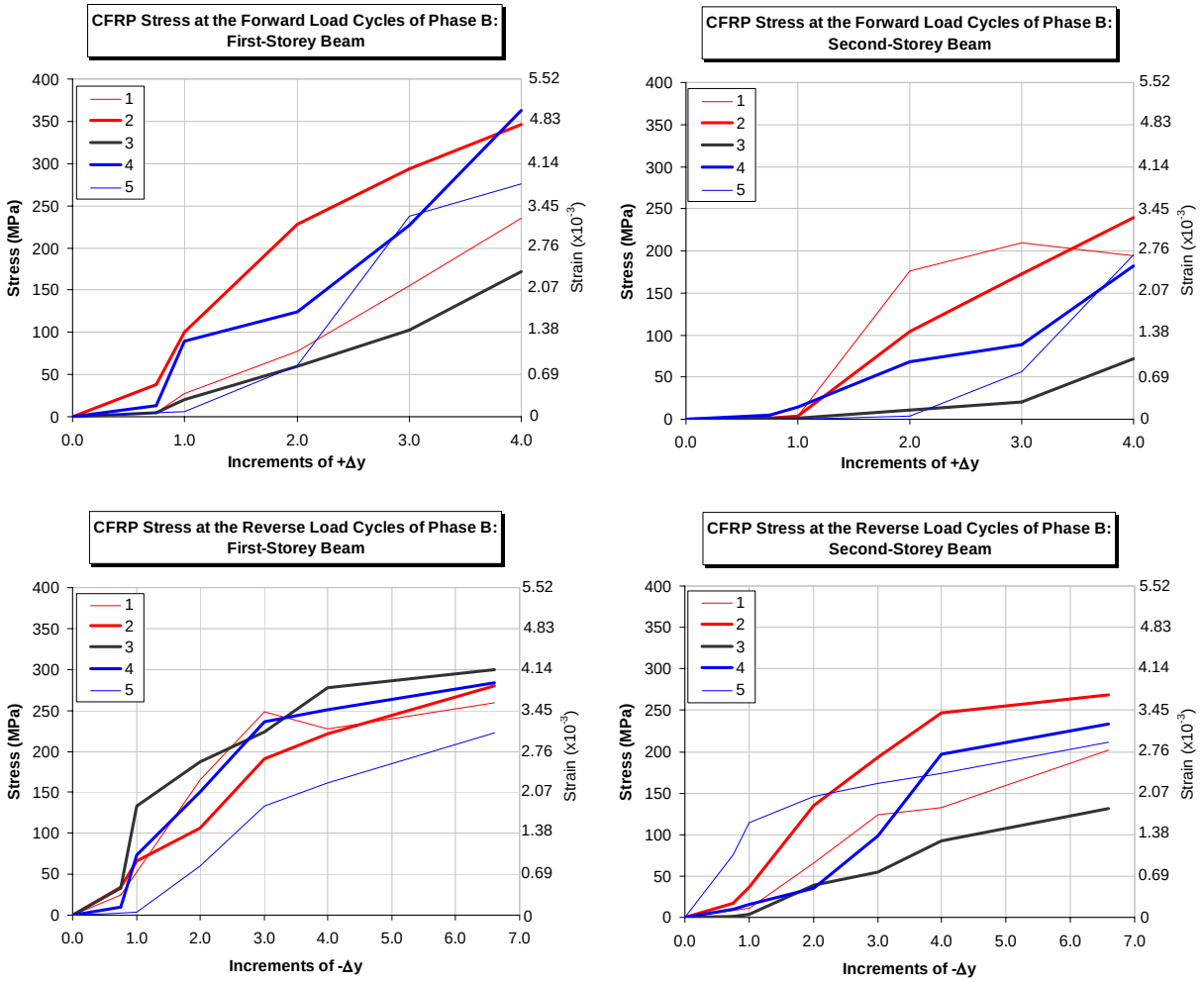

Figure 4.46 CFRP Stress at the Forward and Reverse Load Cycles of Phase B: First and Second-Storey Beams

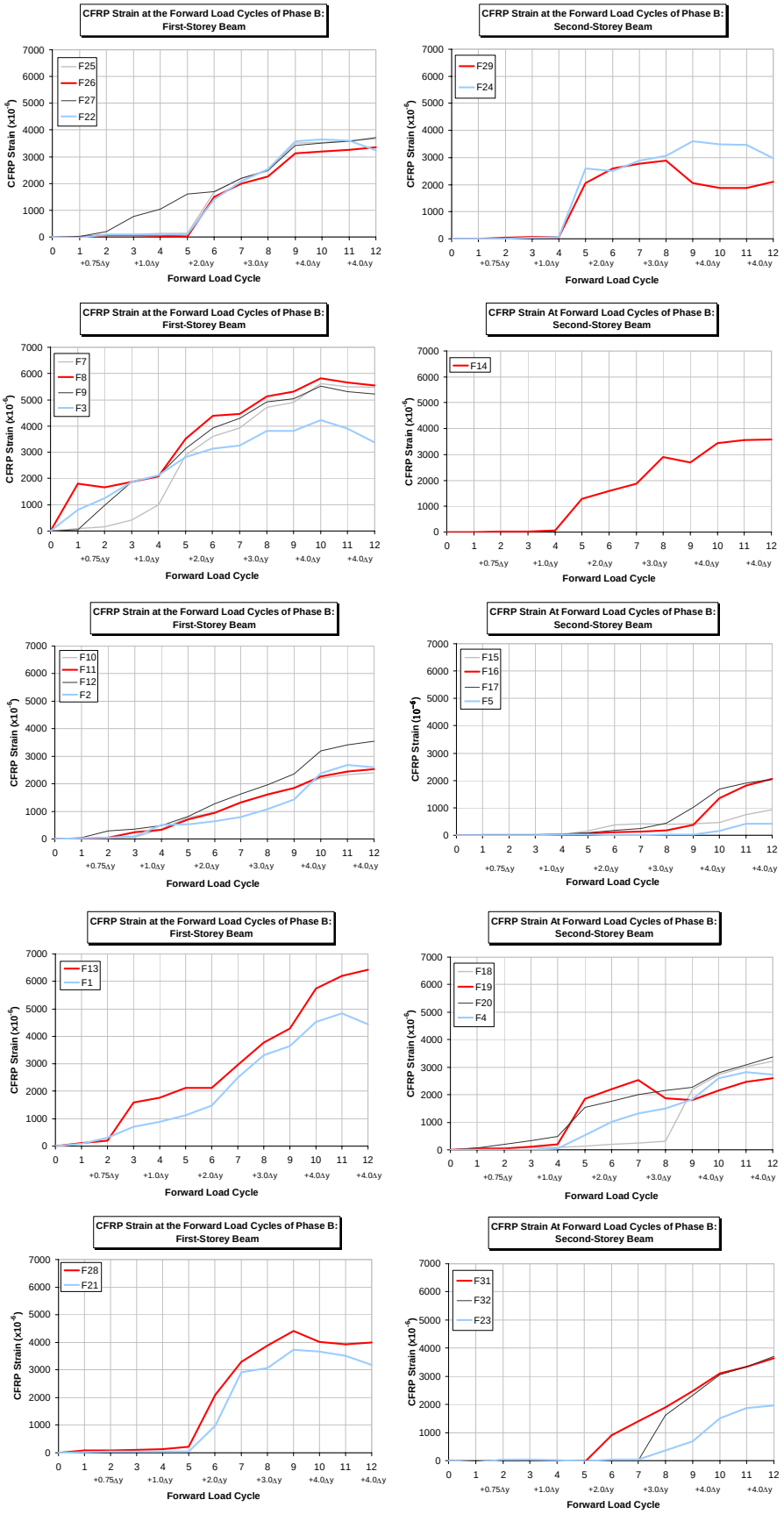

Figure 4.47 CFRP Strain Profiles of the Beams: Forward Cycles of Phase B

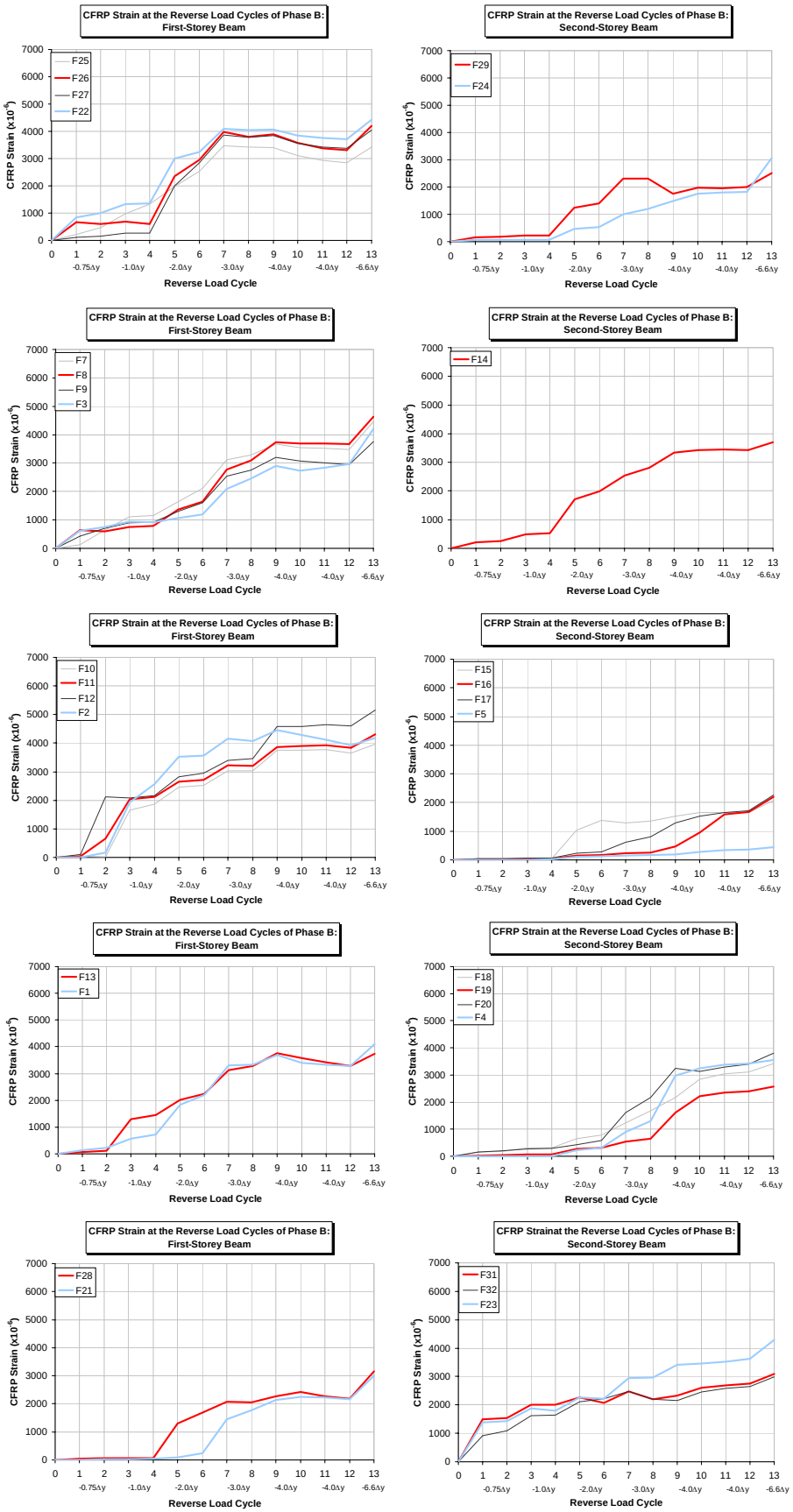

Figure 4.48 CFRP Strain Profiles of the Beams: Reverse Cycles of Phase B

Discussion of Experimental Results

5.1 INTRODUCTION

This chapter discusses the experimental results with regards to the overall frame behaviour and failure modes. Analyses were made on readings from LVDTs, steel and CFRP strain gauges, and Zurich surface strain gauges. In Phase A, the focus was on the following topics with emphasis of the discussion on the forward half-cycle of the loading:

- Progression of the failure mechanism through examining the load versus second-storey displacement plot, and load versus steel strain plots.
- Axial deformation of the beams and columns with respect to the lateral load.
- Estimation of the shear failure load (V_f) in the first-storey beam.
- Horizontal, vertical, and shear surface strains of the beams.

In Phase B of the experimental discussion, the focus was on the following topics:

- Reverse cyclic response of the repaired frame (e.g. peak lateral load, maximum deflection, ductility, energy dissipation, pinching), and improvements due to CFRP retrofitting on the shear strength and failure mode of the repaired frame.
- Evaluation of the observed CFRP debonding strain, peak strain, and comparison to the strain limits suggested by ISIS Canada (ISIS #4 Design Manual, 2001).
- Assessment of the CFRP strain profile along the depth of the beam.
- Estimation of the shear force (V_f), concrete shear strength (V_c), and total shear capacity (V_r).

5.2 LIMITATIONS & SOURCES OF ERROR

This experiment generated a large amount of data such that a wide range of discussion topics were possible; however, due to time constraint, the scope of this discussion was limited to the topics aforementioned in the Section 5.1. To estimate the

shear capacity of the beam before and after CFRP wrapping, hand calculations were performed using logical assumptions and experimental observations. The results from these calculations were reasonable, but coarse in nature. More refined solutions using rigorous analysis was beyond the scope of this thesis. Some sources of errors were incurred when the Zurich, steel strain gauge, and CFRP strain gauge readings were taken. In addition, inherent errors were present in the instrumentation set-up. The errors in the Zurich reading, steel and CFRP strain gauge readings, and instrumentation set-up are discussed below

The surface strain readings from the Zurich gauges were sensitive to local cracking and cover spalling. For example, when a crack suddenly propagated, the horizontal, vertical, and diagonal surface strain readings at this location increased significantly. In addition, when the frame exhibited rapid deterioration (i.e. during the latter load stages of the forward and reverse half-cycles of Phase A), the Zurich readings became more scattered and less reliable. At large crack locations, the surface deformation exceeded the range of the Zurich gauge and produced erroneous results. During the forward half-cycle, the Zurich readings at the last two load stages (15 and 16) were deemed unreliable and were discarded from the plots. For the reverse half-cycle, Zurich data points were scarce; no readings were taken between -111 kN and the last load stage at -304 kN. The strains between these two loads were linearly interpolated. In general, the surface strain readings taken during the forward half-cycle were more reliable than the readings taken during the reverse half-cycle. For grid number eight on the upper north beam-column joint, only one diagonal (XY_{-45}) was recorded accurately due to access limitation. The shear strain calculated for this grid was only based on a single reading, rather than an average reading. Surface strains were not recorded in Phase B.

The steel strain gauges were located at key positions, but the readings only represented the strains at these specific positions. For instance, if a singular shear crack intersected a stirrup strain gauge, then the recorded strain would indicate a high shear

stress at this localized position; however, this high localized stress does not necessarily indicate that other parts of the same stirrup were highly stressed as well. On the other hand, if a shear crack did not intersect a strain gauge, then the strain increase may not have been detected adequately. In general, where cracks were well distributed, the strain indicated by the gauge was a more realistic representation of the strain at that region. Once the steel had yielded, the gauges exhibited residual strains that made future stress-strain correlations difficult to assess. For this reason, the steel strain gauge readings were more reliable for the forward half-cycle of Phase A. Readings during the reverse half-cycle of Phase A and during all cycles of Phase B should be taken as general trends, rather than definitive values.

CFRP strain gauges were mounted on both sides of every wrap. Some wraps had gauges at the top, mid-depth and bottom of the beam, while others only had gauges at the mid-depth. As a result, the accuracy of the data was variable, even though the strains were fairly evenly distributed along the depth of the beams (Section 5.4.4).

The LVDTs were mounted in such a manner that errors would be minimized; the LVDTs were positioned along the centreline of the members, leveled and mounted to a sturdy base. Unfortunately, once excessive deformation or out-of-plane movement was present in the frame, the LVDT alignment was off. For example, LVDT ENHT recorded the horizontal displacement at the north top storey beam-column joint; however, the joint not only displaced horizontally, but also vertically due to column axial deformation and joint rotation. Overall, these errors were considered small and did not affect the general behavioural trends of the frame behaviour.

5.3 PHASE A: DISCUSSION

5.3.1 Lateral Load versus Second-Storey Displacement

The damage mode observed during the forward half-cycle was interpreted as a combined flexural-shear, while the damage mode during the reverse half-cycle was primarily shear (Refer to Figure 4.25 and Table 4.5). Several key events took place during the loading cycle that affected the structural stiffness of the frame. In general, the events that had significant changes to the structural stiffness involved either notable shear cracking, or yielding of the longitudinal and transverse beam reinforcement. The stiffness of the frame response was linearized between these key data points as illustrated in Figure 5.1 and described in Table 5.1 and Table 5.2. During the forward half-cycle, the initial lateral stiffness of 24 kN/mm was relatively constant until the first set of north column flexural cracks were developed at 99 kN (Pt. 1 on Figure 5.1). Prior to the first north column cracking, the lower beam developed flexural cracks at 75 kN, but these cracks did not have a notable impact on the structural stiffness at this load stage. Between 99 kN and 221 kN (Pt. 2), the stiffness decreased to 12.6 kN/mm. Load stage 2 at 221 kN occurred shortly after the lower and upper beams exhibited shear cracks (at 125 kN and 197 kN, respectively). In addition, the south column developed flexural cracks at 125 kN. Between 221 kN and 320 kN (Pt. 3), the stiffness decreased further to 6.1 kN/mm. By 320 kN, the upper and lower beam flexure and shear steel had yielded. From 320 kN to 327 kN (Pt. 4), the stiffness was near zero at about 0.5 kN/mm. The unloading stiffness was -9.6 kN/mm.

For the reverse half-cycle, the lateral stiffness was governed mainly by a sudden large shear crack that developed at -185 kN. Between 0 kN (Pt. 6) to -185 kN (Pt. 7), the structural stiffness was -9.4 kN/mm. Prior to -185 kN, the lower beam developed flexural and shear cracks in the reverse direction at -69 kN and -84 kN, respectively. The south column exhibited flexural cracks at -111 kN, and the upper beam exhibited shear cracks at -168 kN. Between -185 kN to -295 kN (Pt. 8), the stiffness decreased to -4.2 kN/mm. By -295 kN, the stirrups in the both beams had yielded. Between -295 kN and

-304 kN (Pt. 9), the stiffness further decreased to -1.5 kN/mm. The unloading stiffness was 8.6 kN/mm.

It is important to point out that the peak lateral load of 327 kN was reached at 44.8 mm (average top storey lateral displacement) during the last stage of the forward half-cycle. Collapse, as conventionally defined, did not take place. The first-storey beam was heavily damaged in shear but the structural integrity of the frame was still intact. Since repair of the beams was to take place, the loading was stopped to prevent any catastrophic beam failure. The peak load of the frame may have been slightly higher than 327 kN had the loading continued; however, judging by the 10+ mm shear crack width, the limit of the frame was nearly reached. The lateral load was not expected to increase significantly, if any.

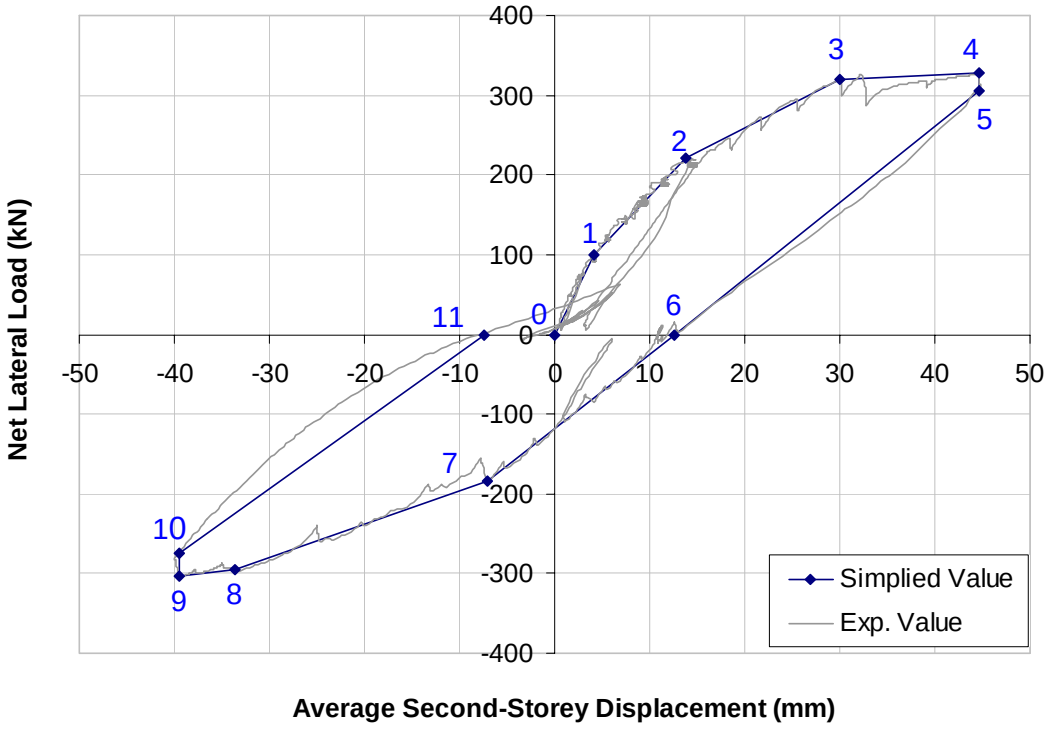

Figure 5.1 Lateral Load vs. Second-Storey Displacement

Table 5.1 Key Load Stages (Phase A)

Graph Point	Load (kN)	Load Stage	Avg. 2nd Storey Lat. Displ. (mm)	Comment
Forward Half-cycle				
0	0	0	0	Initial condition
1	99	4	4.13	First north column flexural crack
2	221	9	13.83	Change in structural stiffness shortly after shear cracks in upper and lower beams. South column cracked at 148 kN.
3	320	13	30.0	Lower beam flexural yielding (B3, B6) at 295 kN Upper beam flexural yielding (B11, B2, B14) Shear yielding in upper (S12) and lower (S4) beams
4	327	15	44.7	Final forward load stage
5	305		44.7	Intermediate reading
Reverse Half-cycle				
6	-2	16	10.78	Initial condition
7	-185	23	-7.10	Sudden large lower beam shear crack
8	-295		-33.7	Intermediate reading
9	-304	26	-39.5	Shear yielding in lower beam (S4) Lower beam shear crack was 7.0 mm wide Upper beam shear crack was 5.0 mm wide
10	-274		-39.5	Intermediate reading
11	-2		-7.43	Final condition

Table 5.2 Lateral Stiffness of the Frame (Phase A)

Graph Point	Stiffness (kN/mm)
Forward Half-cycle	
0-1	24.0
1-2	12.6
2-3	6.1
3-4	0.5
5-6	-9.6
Reverse Half-cycle	
6-7	-9.4
7-8	-4.2
8-9	-1.5
10-11	8.6

5.3.2 Lateral Load versus Beam Longitudinal and Transverse Steel Strain

Figures 4.26 and 4.27 indicated that towards the latter load stages of the forward half-cycle, all of the tensile longitudinal steel yielded (recall the yield strain for the No. 20 rebar was 2250 $x10^{-6}$). A closer inspection of these two figures reveals that the lower beam yielded in flexural just shortly before the upper beam. In addition, the north and south ends of both beams appeared to have yielded at similar instances. The south end of the lower beam may have yielded slightly earlier that the north end, but in the upper beam, this difference was unnoticeable. During the reverse half-cycle, none of the tensile longitudinal steel bars yielded. The strains reached 95% of the yielding. Figures 4.28 and 4.29 indicated that several stirrups yielded during both the forward and reverse loadings. During the forward half-cycle, five out of twelve stirrups yielded. These stirrups were located at regions of major shear cracks. During the reverse half-cycle, three out of eight working strain gauges indicated steel yielding. Although three strain gauges were damaged from the forward half-cycle, it was highly probable that the stirrups associated with these non-functional gauges also yielded during the reverse half-cycle. The observations from these four figures concluded that the damage mode during the forward half-cycle was combined flexural-shear, as evident by yielding of both the longitudinal and transverse steel. During the reverse half-cycle, the frame was damaged predominately in shear since only the transverse steel yielded.

5.3.3 Lateral Load versus Beam Elongation

In general, as the lateral load and lateral frame deformation increased, the beam's elongation increased (refer to Figure 4.30 and Figure 4.31). During the forward half-cycle, the elongation was caused initially by flexural cracking, but was dominated by shear cracking at the latter load stages. Prior to the first flexural beam cracking at 75 kN, the initial rate of beam elongation was negligible. From 75 kN to around 221 kN, the beam elongated at a steady rate that was caused by both flexural and shear cracks. After

221 kN, when the flexural cracks stabilized while the shear cracks continued to propagate, the shear cracks governed the rate of beam elongation. The shear deformation had a greater effect on the beam elongation as evident by the higher rate of beam elongation after 221 kN. This higher rate corresponded to a general decrease in the overall structural stiffness of the frame (Section 5.3.1 and Figure 5.1). During the last forward load stage at 327 kN, the maximum beam elongation in the first and second-storey beams were 2.06 mm and 1.87 mm, respectively. The corresponding maximum average lateral second-storey deformation was 44.8 mm.

When the lateral load was retracted to zero after the forward half-cycle, both beams exhibited a residual elongation of approximately 0.48 mm. As the lateral load increased during the reverse half-cycle, the beams elongated once again. Similar to the forward half-cycle, the beams initially exhibited little or no elongation. As the flexural and shear cracks developed, the rate of elongation increased. Once the flexural cracks stabilized and shear cracks continued to propagate, the rate of elongation further increased. This second increase in the rate of beam elongation occurred at -185 kN when a sudden large shear crack (1.6 mm wide) developed in the lower beam. The overall frame structural stiffness also decreased at this load stage. At the last reverse load stage at -304 kN, the peak average lateral second-storey deformation was 39.9 mm, and the first and second-storey beams elongated by 1.82 mm and 1.44 mm, respectively. Since the first-storey beam was already significantly damaged in shear during the forward half-cycle, its shear capacity was much lower during the reverse half-cycle. As a result, the lower beam deteriorated at a faster rate than the upper beam during the reverse loading stages as evident in the experimental results; recall that during the forward half-cycle, the peak beam elongation difference between the two beams was 0.19 mm (2.06 mm minus 1.87 mm), while the difference during the reverse half-cycle was 0.38 mm. The peak beam elongation was lower in the reverse half-cycle because the overall lateral frame deformation was slightly lower. When unloaded, both beams exhibited a residual elongation of approximately 0.7 mm. The first-storey beam exhibited a larger elongation

than the second-storey beam during both the forward and reverse half-cycles. Since the second-storey beam had a higher induced axial compressive force from the lateral point load, the upper beam's shear capacity was higher. As a result, shear deformation and cracking was not as significant in the second-storey beam, and the elongation was lower.

5.3.4 Lateral Load versus Column Net Axial Deformation (Contraction and Elongation)

After the vertical axial load of 420 kN was applied to each column, the top and bottom of the north column displaced downwards by 0.68 mm and 0.08 mm, respectively (refer to Appendix C.5). Recall that the displacement at the bottom of the column was measured against the column-base interface, while the top column displacement was measured 200 mm below the top of the frame (Figure 3.15). These displacements were equivalent to a net column contraction of 0.60 mm. The top and bottom of the south column displaced downwards by 0.75 mm and 0.17 mm, respectively, or equivalent to a net column contraction of 0.58 mm (refer to Appendix C.5). The middle and bottom of the each column displaced in a similar trend to the top of that column, but at lower magnitudes. The lateral load versus south column net axial deformation indicated that the middle displacement was roughly 70% of the top, and the bottom displacement was less than 10% of the top (refer to Figures 4.34 and 4.35). These estimates concluded that the majority of the column axial deformation occurred between the base and the first-storey beam, while the deformation was minimal between the first and second-storey beams. Greater deformation occurred between the base and first-storey beam because the frame was designed with a stiff base support such that the greatest column moment was attracted at the base. As a result, the greatest amount of column damage occurred at the base. The discussion henceforward is based on the net column axial deformation.

In general, when the forward lateral load was applied, the north column elongated throughout the loading duration, while the south column initially shortened but eventually

elongated once notable flexural cracking developed in the columns (refer to Figures 4.33 and 4.35). The experimental results indicated that column deformation was affected more by the flexural crack than by the applied column axial load. In addition, the degree of shear cracking in the beams was a good indicator of the degree of flexural cracking in the columns. The lateral load versus net column axial deformation relations are described below for both the north and south columns.

During the forward loading, the rate of elongation and axial stiffness of the north column was affected by several key events: first north column flexural crack at 99 kN, first south column flexural crack and first lower beam shear crack at 148 kN, and the first upper beam shear crack at 197 kN. From the start of loading to 150 kN (around the south column flexural and lower beam shear crack), the initial column axial stiffness was approximately 920 kN/mm. From 150 kN to 200 kN (around the first upper beam shear crack), the stiffness decreased significantly to 230 kN/mm. After 200 kN, the stiffness decreased to 100 kN/mm until the end of the forward loading. The maximum net column elongation was 1.97 mm. When unloaded, the residual elongation was 0.15 mm.

During the forward loading, the rate of elongation and axial stiffness of the south column was also affected by the column flexural crack. Initially, from the start of loading to 150 kN (first south column flexural crack and first lower beam shear crack), the column axial stiffness was approximately -1400 kN/mm (negative for shortening). From 150 kN to 200 kN (around the first upper beam shear crack), the axial deformation remained stable (i.e. stiffness was very high). After both columns and beams exhibited large cracking, instead of shortening, the south column started to elongate with further loading. Flexural cracks in the south column caused the column to elongate and override the initial shortening caused by the applied column axial load. Figure 4.35 indicates that at around 225 kN, the south column started to elongate. A close examination of Figure 4.34 reveals that the top column displacement is still negative at 225 kN; however the relative displacement between the top and bottom of the column suggests that the column has started to elongate. From 200 kN to the near peak load of 320 kN (corresponding to

0.37 mm of elongation), the stiffness was 400 kN/mm. After this point, the column continued to elongate with minimal load increase until the forward loading was concluded. Figure 4.34 suggests that the column elongation took place predominately between the first and second-storey beams. The maximum net column elongation exhibited was 0.81 mm. Note: the south column net axial deformation at the peak load was greater than the top column displacement. The net deformation took into account the displacement at the bottom of the column, which was negative at the peak load. When unloaded, there was a residual elongation of 0.03 mm.

During the reserve half-cycle, the behaviour of the columns was similar to the forward half-cycle. When the reverse lateral load was applied, the south column elongated throughout the reverse loading, while the north column shortened but elongated towards the end. Once again, the axial stiffness for both columns was affected by several key events. They included the first south column flexural crack at -111 kN and the sudden development of a large shear crack at the lower beam at -187 kN. For the south column, the initial stiffness was around 2000 kN/mm up to a lateral load of -110 kN (around the first south column flexural crack). From -110 kN to -185 kN (approximate point of the sudden lower beam shear crack), the stiffness decreased to 480 kN/mm. After this point, the stiffness decreased to 140 kN/mm until the end of the reverse loading. The maximum net column elongation exhibited was around 1.05 mm. When unloaded, there was a residual shortening of 0.13 mm. For the north column, the initial shortening stiffness was -600 kN/mm up to a lateral load of -190 kN (approximate point of the sudden lower beam shear crack). From -190 kN onwards, the column elongated with a stiffness of 280 kN/mm until the end of the reverse loading. The maximum net column elongation exhibited was around 0.22 mm. When unloaded, there was a residual shortening of 0.15 mm.

The behaviour of the columns suggested that the column deformation was affected by both the column flexural crack and the applied column axial load. Around half way through the loading, the elongation caused by flexural cracks override the initial

shortening caused by the applied axial load. In general, for the column located towards the near end of the lateral loading point (i.e. column that elongated throughout), its stiffness was first governed by the first column flexural crack, then by the first south column flexural crack. For the column located on the far end of the lateral loading point, it contracted initially until notable column flexural and beam shear cracks were developed. Once excessive cracking took place (at -187 kN of lateral load), the column elongated. The maximum elongation reached by the north column during the forward half-cycle was 1.97 mm, while the maximum elongation reached by the south column during the reverse half-cycle was 1.05 mm. The north column exhibited a larger elongation because the peak lateral load and frame displacement was greater during the forward half-cycle. Table 5.3 summarizes the column stiffness during the forward and reverse half-cycles of Phase A.

Table 5.3 Summary of Column Axial Stiffness (Phase A)

Data Point (kN, mm)	**North Column Stiffness (kN/mm)**	**Data Point (kN, mm)**	**South Column Stiffness (kN/mm)**
Forward Half-cycle: Phase A			
Initial to 138 kN, 0.15 mm	920	Initial to 150 kN, -0.11 mm	-1400
138 kN, 0.15 mm to 194 kN, 0.39 mm	230	150 kN, -0.11 mm to 210 kN, 0.09 mm	~ 3000
194 kN, 0.39 mm to 323 kN, 1.68 mm	100	210 kN, 0.09 mm to Final	400
323 kN, 1.68 mm to Final	~ 0		
Reverse Half-cycle: Phase A			
Initial to 189 kN, -0.21 mm	-600	Initial to 113 kN, 0.02 mm	2000
189 kN, -0.21 mm to Final	280	113 kN, 0.02 mm to 185 kN, 0.17 mm	480
		113 kN, 0.02 mm to Final	140

Note: Positive and negative stiffness values refer to column elongation and contraction, respectively.

5.3.5 Estimation of V_f in the First-Storey Beam

The peak shear force in the first-storey beam was estimated using the CSA A23.3 2004 code (the detailed calculations are provided in Appendix B). Results from Chapter 4 determined that at a net lateral load of 325 kN, the large shear crack in the first-storey beam was 4.0 mm wide (recall the peak lateral load was 327 kN), the stirrups and flexural steel at both ends of the beams had yielded, and the first-storey beam elongated to a maximum of 2.0 mm. Because the two columns were fixed at the base, they restricted the beam from elongating. As such, the beam elongation caused approximately 40 kN of induced compressive force in the beam (Appendix B). Assuming yielding of the stirrups and an axial force of -40 kN, the shear capacity was calculated to be 202 kN (V_c = 98.8 kN, V_s = 103 kN). The predicted result according to code was a good estimation because this result correlated well to several experimental observations. For example, the predicted shear failure angle θ of 35.9 degrees was agreeable with the measured failure angle (between 32-35 degrees, see Figures 4.14 and 4.15). The predicted force in the longitudinal flexural reinforcement at d_v (310 mm) away from the beam-column interface was 88% of yield; at 30 mm away from the interface where the moment was slightly greater, strain gauges indicated that flexural yielding took place. In addition, several calculations were performed with axial compression loads ranging from 0 to 100 kN and it was concluded that the shear capacity and failure angle of the beam was not sensitive to the magnitude of the axial compression force. Overall, the calculated beam shear failure load of 202 kN in the first-storey beam was a good estimation.

It was difficult to correlate the actual beam shear failure load to the lateral applied load because the frame was an indeterminate structure; however, if the ends of the beam were assumed to reach M_y (the flexural steel at the beam ends just reached yield), the corresponding V_f would be 211 kN (similar to CSA A23.3 2004 code).

5.3.6 Lateral Load versus Horizontal Strain in Beams

The axial deformation of the beams was monitored on a local level with horizontal Zurich surface strain readings (ε_x) recorded along the length of the beam. Recall that the beam-column joints were also monitored. In general, horizontal strain values followed a similar trend to the global beam elongation; as the lateral load increased, the horizontal strain increased (refer to Figure 4.36 to Figure 4.37). The local strains indicated that the joints tended to elongate the most, while the midspan of the beam elongated the least. This behaviour made sense since flexural and shear cracks were concentrated mainly at the ends of the beams, while the point of contra-flexure was located at the center. Globally, the initial rate of beam elongation was negligible prior to first beam cracking (before 75 kN); however, on a local level, the ε_x data indicated that the beams actually contracted slightly during the first three load stages (up to 75 kN). After first flexural cracking, the beams elongated as expected. At 51 kN of lateral load, the peak negative horizontal strains were exhibited: -0.18×10^{-3} and -0.12×10^{-3} for the first and second-storey beams, respectively. These strains were equivalent to an axial contraction of approximately 0.37 mm and 0.26 mm. At 320 kN, the average ε_x values per grid were $+0.83 \times 10^{-3}$ and $+0.59 \times 10^{-3}$ for the first and second-storey beams, respectively. These strains were equivalent to an axial elongation of approximately 1.75 mm and 1.24 mm. The LVDT readings at this load level indicated a global beam elongation of 2.02 mm and 1.48 mm at the lower and upper beams, respectively. Both sets of data were comparable. Upon unloading, there was an average residual strain of 0.24×10^{-3} per gird for both beams, which was equivalent to a residual elongation of approximately 0.5 mm (similar to the global response).

During the reverse half-cycle, the lateral load versus horizontal strain exhibited similar trends to the forward half-cycle. As the load increased, the horizontal strains increased. The second-storey beam displayed horizontal strain levels that were similar to the forward half-cycle while the first-storey beam had greater horizontal strains. Since

the first-storey beam was already heavily damaged from the forward half-cycle, its shear strength was lower. Consequently, greater shear damage took place which resulted in a larger lateral strain. The lateral strains in the lower beam were more scattered because the beam further deteriorated. Zurich grid number four (at the midspan of the lower beam) indicated contraction at the last load stage. This erroneous data point may have been caused by the cover spalling at midspan.

5.3.7 Lateral Load versus Vertical Strain in Beams

The vertical surface strain of the beams was monitored along the entire length via Zurich surface strain gauges. Intuitively, the vertical strain should be negligible until shear cracks were developed. Flexural cracks should not influence the vertical strain. This hypothesis was proven correct in the experiment (refer to Figure 4.38 to Figure 4.39). During the forward half-cycle, the ε_y values in both beams were near zero until the first shear cracks developed. At the lower beam, the first shear crack occurred at the south end at 148 kN. At this load stage, the vertical strains in grids five and six increased (these two grids corresponded to the south end of the lower beam – see Figure 4.24). At the upper beam, several shear cracks developed just after 200 kN. The vertical strain in the upper beam increased correspondingly at around this load stage. The vertical strain in the beam-column joints for both beams remained low as there were no major joint cracks. Near the peak load in the forward half-cycle, the vertical strain at both beams increased rapidly as the beam shear cracks widened. At 320 kN, the average ε_y at the upper and lower beams were approximately 0.15×10^{-3} and 0.25×10^{-3}, respectively. As expected, the ε_y at the lower beam was greater because shear cracks were larger here.

For the reverse half-cycle, it was difficult to assess the trend as data points were limited. For the upper beam, there was a residual vertical strain of around 0.2×10^{-3}. The ε_y remained relatively stable probably until the first shear crack developed in the upper beam (predicted to be around 250 kN). The exact point when the ε_y increased was

unknown due to a lack of data. For the lower beam, the data was very scattered and unreliable because of the deterioration exhibited during the forward half-cycle. The plot was not represented and no discussion was made for this set of data.

5.3.8 Lateral Load versus Shear Strain in Beams

A positive shear strain was defined such that the potential cracks were aligned from the top left to bottom right position, and vice versa (see Appendix B). In general, the shear strains were positive in the forward cycle, and negative in the reverse cycle. The lateral load versus shear strain relationship was dependant on the shear crack development. During the forward half-cycle, shear strains remained negligible at the lower beam until 148 kN of lateral load was reached (197 kN at the upper beam) (Refer to Figure 4.40 to Figure 4.42). These loads corresponded to the approximate development of the first shear cracks at the respective beams. From the point of first shear cracking onwards, with the exception of the shear strains at the joint region and beam midspan, the shear strains increased in a positive manner at a steady rate until 320 kN. At 320 kN, the shear crack widths opened rapidly and caused the shear strains to increase significantly. Shear strains at the lower and upper beams were around 4.8 $x10^{-3}$ and 2.3 $x10^{-3}$, respectively. Higher shear strains at the lower beam indicated greater shear damage as evident in the experiment. As explained in Section 5.3.3, the upper beam had a higher shear capacity because of the higher induced compressive force. After this load stage, the shear strains exceeded the range of the Zurich gauge. With regards to the shear strains at the joints and beam midspan, shear strains at the beam-column joints were slightly negative, which indicated cracking in the counter-clockwise direction as evident in the experimental photos (Figures 4.7 and 4.8). At the beam midspan, the shear strain was negligible during the majority of the forward half-cycle. When shear cracks were developed at the midspan during the last few load stages, the shear strains increased accordingly.

During the reverse half-cycle, the lateral load versus shear strain relationship was difficult to assess due to missing data point (i.e. no reading between 111 kN and 304 kN), and scattered data as a result of beam deterioration (particularly in the lower beam). In general, as the load increased, the shear strain remained unchanged until shear cracks developed. Once shear cracks developed, the shear strains decreased (recall the shear crack were now inclined in the negative direction). Grid number three near the lower beam midspan did not follow the general trend of the other shear strains. The strain here increased rapidly instead of decrease. It was uncertain whether this was an error caused by excessive deformation, or if the positive strain was in fact realistic. At grid three, the large shear crack that developed during the reverse loading intersected with a large shear crack that was generated during the forward loading. Shear strains in both the first and second-storey beam column joints remained stable as shear cracking was minor here. Grid number eight, corresponding to the upper north beam-column joint, indicated shear strains up to -7.5×10^{-3}; however, this was probably wrong because shear cracking at this region was minor, and the mistake may have been caused by a measurement error. Recall that the shear strain for grid number eight was based on a single reading rather than an average (Section 5.2).

5.4 PHASE B: DISCUSSION

5.4.1 Reverse Cyclic Response of the Repaired Frame

The repaired frame performed very well when subjected to the sequence of reverse cyclic loading (Refer to Figure 4.43 and Table 4.6). The repaired performance was much more suitable for earthquake design than the original frame. Great improvements were exhibited in all aspects of the response: increase in the peak lateral load, maximum deformation, and displacement ductility. In addition, the failure mode changed from brittle flexural-shear failure to ductile flexure.

The displacement ductility is a measure of the plastic deformation before collapse. This parameter is defined easily in the case of an elasto-plastic behaviour; however, in reinforced concrete structures where such a characteristic is usually absent, there is no universal definition for ductility. Paulay and Priestley (1992) determine the ductility by approximating the material response curve with a bilinear curve. A secant stiffness line is drawn from the origin and intersects the curve at the first section tensile yielding point. A yield plateau line is then drawn; the yield displacement is taken at the intersection point of these two lines. This method is reasonable, but is limited to structures where sectional yielding took place. Sheikh and Khoury (1993) propose constructing a tangent stiffness line instead of a secant stiffness line. The yield displacement corresponds to the point on this tangent line where the peak load is reached. The maximum displacement corresponds to the post-peak position where the load has declined by more than 20% of the peak load. The method suggested by Sheikh and Khoury (1993) is used to calculate the ductility for this test frame (Appendix B). Since failure did not take place in the specimen, the maximum displacement is taken at the end of loading.

The specific improvements of the repaired frame were as follow. The peak lateral load increased by a factor of around 1.4 to 444 kN, the displacement ductility improved from approximately 4.0 to at least 6.8 or an increase by a factor of at least 1.7, the maximum displacement increased by a factor of at least 3.7, while the energy dissipation increased by a factor of at least 5.7. Note: if the displacement ductility was calculated using the method proposed by Paulay and Priestley (1992), the ductility for Phase A and B would be 1.6 and 4.7 or an increase in 3.0 times. Recall that for Phase A, although failure of the frame did not take place, the frame exhibited large beam shear cracks that suggested failure was near. Therefore, the ductility and maximum displacement reported were very close to the actual value. Contrary, for Phase B, the peak load and displacement were reached at the end of the last load cycle (LC 13) where the test was stopped not by the limitation of the frame, but by the limitation of the actuator stroke capacity. Therefore, the maximum displacement and ductility were inconclusive; the

values reported were the lower limits. At the peak lateral displacement in Phase B, full plastic hinges were formed at the four ends of the beams and at the column bases. The steel in the column base had yielded but did not reach strain hardening. If further loading was continued, the peak load was expected to increase slightly when strain hardening was reached at the base, while the displacement and ductility was expected to increase as the frame yielded further. The connections were intact and concrete failure due to excessive deformation was unlikely since the most failure prone portions of the frame (i.e. the beams) were wrapped with CFRP.

The hysteresis generated by this frame was typical of a ductile reinforced concrete frame. The structural stiffness decreased with each subsequent cycle after $\pm 1.0\ \Delta_y$. The cycles at $\pm 0.75\ \Delta_y$ and $\pm 1.0\ \Delta_y$ did not deteriorate the frame's stiffness because cracks were still minimal. If the stiffness at $\pm 1.0\ \Delta_y$ (12.5 kN/mm) was assigned the control value (i.e. 100%), the frame's lateral stiffness decreased to 82% during the first cycle at $\pm 2.0\ \Delta_y$, to 50% during the second cycle at $\pm 2.0\ \Delta_y$, to 35% during the second cycle at $\pm 3.0\ \Delta_y$, and to 25% at the $\pm 4.0\ \Delta_y$ cycles. This gradual decrease in structural stiffness was evident by the pinching exhibited in Figure 4.43. As the frame was cycled further, the specimen was losing its energy dissipation capacity.

The initial lateral stiffness of the original frame in Phase A was 24.0 kN/mm when the stiffness was measured from the origin to 99 kN, and 12.6 N/mm when measured from 99 kN to 221 kN. At around 99 kN, the first north column flexural cracking occurred, while at 221 kN, the first shear cracks in the upper and lower beams developed. After repair, the initial stiffness was 15.2 kN/mm when measured from the origin to 99 kN, and 10.9 kN/mm when measured from 99 kN to 221 kN. Since the columns were not repaired, a decrease in the structural stiffness caused by deterioration of the north column was observed (15.2 kN/mm or 37% decrease from Phase A). On the other hand, when the stiffness depended more on the beam shear cracks, the repaired stiffness from 99 kN to 221 kN only decreased to 10.9 kN/mm or 13% reduction from the

original. Taking into account that the joints were not repaired and further reduction in column stiffness was present, a stiffness decrease of 13% from 99 kN to 221 kN suggests that the beams were repaired very well in terms of epoxy injection and CFRP wrap.

5.4.2 Distribution of CFRP Stress Along the Length of the Beam

The following observations were drawn from Figures 4.44 and 4.45. The rate of CFRP stress increase was related to the rate of lateral load increase in the frame. The CFRP stress increased at a steady rate up to around $\pm 3.0\ \Delta_y$ and $\pm 4.0\ \Delta_y$, but the reate declined slightly from this point forward. Correspondingly, the lateral load increased at a steady rate up to a displacement of $\pm 3.0\ \Delta_y$. At this displacement, over 90% of the peak load had been attained, and the loading rate declined. The peak forward and reverse average CFRP stresses at the lower beam were 279 MPa and 269 MPa, respectively. The peak forward and reverse average CFRP stresses at the upper beam were 177 MPa and 209 MPa, respectively. For both the forward and reverse cycles of loading, the average shear stresses at the lower beam were greater than those at the upper beam. This correlated with the experimental results where the lower beam exhibited more shear cracks.

When the distribution of CFRP stresses was examined along the length of the beam (Figure 4.46), the following general observations were made. For a given beam at a specific load cycle, the distribution of the stress along the beam was variable. The highest and lowest stresses at different parts of the beam varied by a factor of more than three (i.e. at the upper beam during the $+4.0\ \Delta_y$ cycle). From statics, the shear force should be relatively constant along the length of the beam, but these scattered results indicated that the stresses in the CFRP wraps were not constant throughout. Typically, Wrap 2 and 4 located at approximately d_v away from either beam-column interface exhibited the highest shear stress levels. Wrap 1 and 5 located at the beam ends had lower shear stresses, while Wrap 3 located at the midspan had similar stresses to the end

wraps. This general observation suggested that the shear stress was greatest at approximately d_v away from the support. In theory, d_v is the approximate distance from the support where the full shear is first developed. At the midspan, the moment was the lowest. Moment and shear interaction suggests that the shear stress here be lower than at d_v away from the support, which was observed in the experiment. At the ends of the beams, the shear was not fully developed as some of the force was taken directly by the joint.

5.4.3 CFRP Debonding Strain, Peak Strain, and Strain Limits Suggested by ISIS #4 Design Manual (2001)

Experimental observations suggested that partial debonding took place at several wraps at the lower beam during load cycle 5 ($\pm$2.0 Δ_y), and at the upper beam during load cycles 9 through 12 ($\pm$4.0 Δ_y). Figures 4.47 and Figure 4.48 indicate that when partial debonding occurred (i.e. at the lower beam during load cycle 5, and at the upper beam during load cycles 9 through 12), the maximum CFRP strains reached was around 3000 $x10^{-6}$. It was difficult to quantify the degree of debonding since the beam was fully wrapped; however, physical examination of the CFRP wraps concluded that for the wraps that exhibited partial debonding at the load stages mentioned above, approximately 10-15% of their bonded area was broken. Duing load cycle 9 ($\pm$4.0 Δ_y) at the lower beam, experimental inspection revealed that more than 50% of the bonded area for each wrap was broken. The CFRP strains recorded in the lower beam were on average 4000 $x10^{-6}$. Had the wrap not been properly anchored, they would have likely ripped off. At load cycle 13 (-6.6 Δ_y), further debonding took place at the upper beam; the majority of strains recorded here ranged between 3000 and 4000 $x10^{-6}$. Recall that CFRP strain was recorded at the vertical centreline of the wrap (i.e. where the gauges were installed). The variation of strain along the width of each wrap was unknown. Taking this limitation into consideration, it was concluded that the CFRP-concrete interface exhibited partial

debonding when the CFRP strain at the wrap vertical centreline reached approximately 3000 $x10^{-6}$, while more than 50% of the debonded area was broken when approximately 4000 $x10^{-6}$ was reached.

ISIS Canada recommends a strain limit of 4000 $x10^{-6}$ when calculating the shear contribution of CFRP for fully wrapped beams (ISIS #4 Design Manual, 2001). They suggest that above this strain limit, the aggregate interlock of the concrete is lost due to widening of the crack. As indicated by Figures 4.47 and 4.48, the majority of the strains recorded in the lower beam were in excess of 4000 $x10^{-6}$, but all of the wraps remained intact. This experimental finding indicated that the strain limit placed by ISIS is conservative. In addition, for the type and layout of the CFRP used, the ISIS design manual suggests a rupture strain limit of 5500 $x10^{-6}$ (ISIS #4 Design Manual, 2001). The maximum CFRP strain recorded in this experiment was 6430 $x10^{-6}$, while several other gauges recorded strains close to 6000 $x10^{-6}$. All of the CFRP wraps were fully intact at the end of the experiment. Again, the ISIS design manual recommendation is conservative. It is interesting to note that for the given beam cross-section, the manual suggests a debonding strain limit of 3800 $x10^{-6}$ if the beam is assumed wrapped in a U-shape, and a strain limit of 3300 $x10^{-6}$ if the beam is wrapped only at the vertical sides. These two debonding strain limits were similar to the experimentally observed strains. The design manual does not have a debonding strain recommendation for fully wrapped beams.

5.4.4 CFRP strain profile along the depth of the beam

The CFRP strain profile along the depth of the beam was of interest before and after debonding took place (Refer to Figure 4.47 and Figure 4.48). To assess the strain profile before debonding, the distribution of the strain along the depth was examined for cases where the strains were less than 3000 $x10^{-6}$ (approximate strain when debonding initiated – Section 5.4.3). For the first-storey beam, load cycles up 4 or $\pm 1.0\ \Delta_y$ were

relevant. For the second-storey beam, load cycles up to around 8 or $\pm 3.0\ \Delta_y$ were relevant. To assess the strain profile after debonding, cases where the strains were in excess of 3000 $x10^{-6}$ were relevant. This range applied to load cycles 5 and up for the lower beam, and load cycles 9 and up for the upper beam.

Prior to debonding, it was difficult to make a clear conclusion regarding the strain profile because the strain was sensitive to local shear cracking. The strains appeared scattered in the upper beam, but in the lower beam, the profile appeared to be fairly evenly distributed along the depth. For example, in the lower beam during both the forward and reverse loading directions of load cycle 4, around half of the CFRP wraps had similar strains along the beam depth. For the upper beam, the erratic strain profiles were most likely governed by local strain concentrations caused by excessive lateral frame deformation.

After debonding had initiated, the shear strains at the top, mid-depth, and bottom of the wrap started to converge. The strain profiles for the majority of the wraps were relatively constant at several strain levels. This finding suggests that for a fully wrapped configuration, the strains were fully developed up to the top and bottom edges of the beam. Even though there were no strain gauges located at beam edges, it was hypothesized that the strains indicated by the top and bottom gauges (located 50 mm away from the edges) extended to the edges. This constant CFRP strain profile after debonding had taken place was in contrast to the typical concrete or stirrup shear strain where the strain was greatest near the mid-depth, and zero at the top and bottom edges.

5.4.5 Estimation of V_f, V_c, and V_r in the First-Storey Beam

The total shear resistance Vr is equal to the summation of the concrete shear strength (V_c), transverse steel strength (V_s), and CFRP strength (V_{frp}):

$$V_r = V_c + V_s + V_{frp}$$

The peak shear force in the first-storey beam was estimated at $\pm 3.0\ \Delta_y$ using hand calculations and experimental observations (Refer to the calculations in Appendix B and Figure 5.2). This specific load cycle was chosen because it was reasoned that the beam shear force was close to its peak here and the concrete shear force was also at its maximum. At this load cycle, the regions of plastic hinging at both ends of the first-storey beam were well defined, the lateral load was at 90% of the peak load, and the stirrups had yielded. The plastic hinge region was estimated to be at least 150 mm long and extended from the beam-column interface (i.e. M_y was reached at 150 mm). This region was evident by the 3.5 mm wide flexural crack at the interface, and 2 mm wide flexural crack immediately adjacent to the 150 mm wide CFRP wrap. At $\pm 2.0\ \Delta_y$, the flexural steel at the beam-column interface had yielded; however, the plastic hinge region was unknown (less than 150 mm). Since the estimation of the shear force was very sensitive to the location where M_y was assumed, a poorly defined hinge region would produce an inaccurate V_c, while an overly conservative estimation would yield a very low V_c. At $\pm 4.0\ \Delta_y$, the plastic hinge region was clearly observed (at least 150 mm). Without a dependable estimate of a hinge region greater than 150 mm, V_c estimated at $\pm 3.0\ \Delta_y$ would yield a higher strength (since V_{frp} increased from $\pm 3.0\ \Delta_y$ to $\pm 4.0\ \Delta_y$, while V_s remained constant, and M_y was assumed at the hinge tip).

To calculate the shear force V_f, the tip of the plastic hinge region at 150 mm away from the beam-column support was assumed to reach the yield moment M_y. The flexural steel had yielded as evident by the large flexural crack width, but it was uncertain if strain hardening was reached. The stirrups had yielded, but did not reach strain hardening because the CFRP wrap provided vertical confinement that limited the increase in the stirrup strain. With an estimated induced compressive force of 40 kN (from Phase A), M_y and V_f were calculated as shown in Appendix B. The estimated M_y and V_f values were 159 kNm and 264 kN, respectively. Using the average stress of the CFRP wraps along the lower beam, and taking an average of the stresses between the forward and

reverse cycles, V_{frp} was estimated to be 83.4 kN (σ_{frp} = 200 MPa). The peak V_c calculated was 77.6 kN in Phase B, which was slightly lower than the V_c obtained in Phase A at failure (98.8 kN).

It is important to illustrate the sensitivity of the plastic hinge region on the V_f calculation. The moment at 150 mm away from the beam-column interface was assumed conservatively to reach M_y. If the plastic hinge region extended to 400 mm away from the interface (i.e. the height of the beam according to St. Vernant's Principle) and M_y was assumed here, V_f would equal 453 kN and V_c would equal 267 kN. The concrete shear strength would increase as a result of the confining pressures of the CFRP, but even so, a concrete shear strength of 267 kN appears to be unrealistic. The actual concrete shear strength (V_c) lay between 77.6 kN and 267 kN, with the former strength reported confidently as the lower limit.

The ultimate shear resistance of the repaired beam was also estimated by assuming yielding of the stirrup, rupture of the CFRP (12.1 $x10^{-3}$ mm/mm), and conservatively neglecting the V_c contribution. At a strain level of 12.1 $x10^{-3}$, large shear cracks in the beam significantly reduce the concrete shear strength. Even though the CFRP-concrete interface will break prior to rupture, the CFRP can still carry the load because of its fully wrapped configuration. The total shear resistance was estimated to be 414 kN. **Error! Reference source not found.** illustrate various shear strengths versus CFRP strain. The dotted lines represent rough estimates of the behaviour. The three points shown were the V_{frp}, V_s, and V_c values calculated at +3.0 Δ_y.

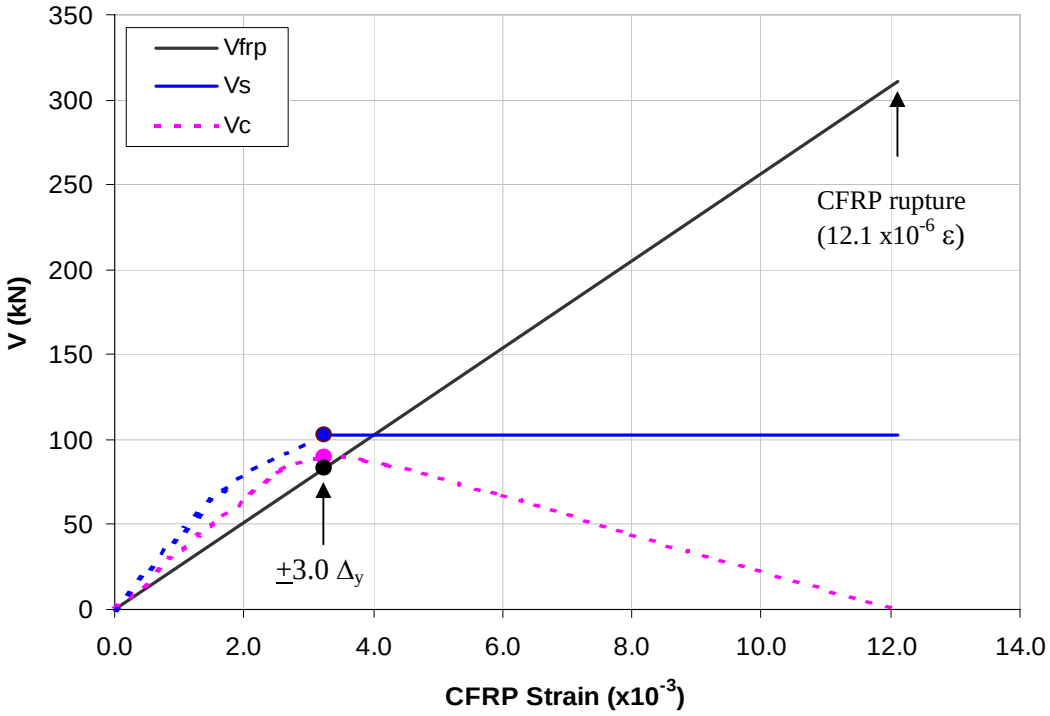

Figure 5.2 Shear Strength (V_c, V_s, V_{frp}) vs. CFRP Strain

Finite Element Analysis

6.1 INTRODUCTION

To augment the experimental work, analytical modelling was performed on the test specimen using VecTor2, a nonlinear finite element (FE) software developed at the University of Toronto. The modelling procedures and analytical results are discussed in this chapter. Specifically, the subsections contain descriptions of the modelling technique (Section 6.2), details of the parametric study and of the analytical response of the test specimen (Section 6.3), and results of all FE analyses (Section 6.4). Section 6.5 includes a discussion of the parametric study results and a comparison between the analytical versus experimental responses. Conclusions and recommendations are given in. Refer to Appendix D for all of the VecTor2 input files.

6.2 VecTor2 MODELLING

The FE mesh was built using the program FormWorks, a pre-processor to VecTor2. In general, the frame was modelled in its entirety using rectangular elements to represent concrete, truss elements to represent ductile steel and externally bonded CFRP, and link elements to represent the bond characteristics at the CFRP-concrete interface. Refer to the FormWorks manual by Wong and Vecchio (2002) for a detailed summary of the program functionality and material library. Two versions of the model were implemented in this study: one with link elements to study the behaviour of the CFRP-concrete interface bond, and one without link elements where perfect bond was assumed. In addition, for both models, elements such as damaged and repaired concrete, CFRP trusses, and links were activated and deactivated depending on the analysis requirement. Section 6.3 summarizes the characteristics of all the models. The current section focuses on the various aspects of the FE mesh and modelling procedures. The FE mesh is presented in Figure 6.1 below.

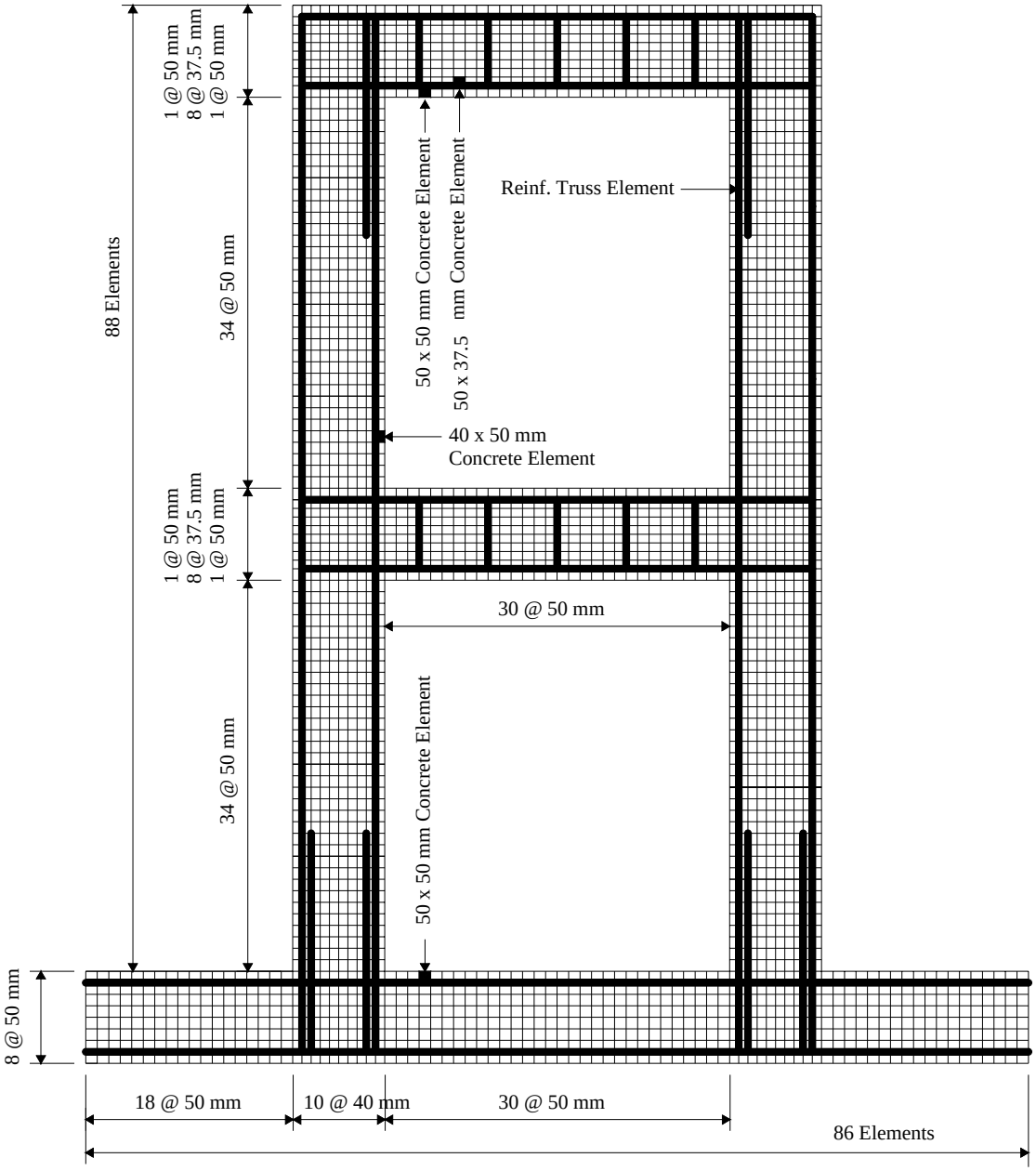

Note: Refer to Figures 3.2 and 3.3 for the frame dimensions. CFRP and link elements are not shown in this figure for clarity.

Figure 6.1 Finite Element Mesh

6.2.1 Support Conditions

In the experimental setup, the concrete frame base was post-tensioned onto the strong floor to provide a fixed support via twelve floor bolts. There were six sets of bolts (two bolts per set) located along the base (see Appendix A). Each bolt was stressed to approximately 35.5 kN (8000 lbs) or 71 kN (16000 lbs) per two bolts. These post-tensioning forces were accounted for in the FE modelling by applying six 71 kN downwards forces at the bolt locations. The base of the frame was supported to the floor in such a manner that when the base pushed downwards against the strong floor (i.e. from compression caused by the column), the floor would prevent any base deformation. On the other hand, when the base deflected upwards away from the floor (i.e. from column uplift), except for the restraint provided by the aforementioned post-tensioned bolts, the base was free to deform otherwise. The most accurate method to model the described support condition would be to provide vertical restraint at the base where compression occurred and no restraint where tension occurred. Unfortunately, such a method meant the support conditions would have to be changed in between each forward and reverse half-cycle. This procedure would be error prone and inefficient.

The methodology used provided restraints to selected nodes along the base (refer to Figure 6.2). Specifically, pinned supports were provided to nodes that were within a distance of d_v (flexural depth of the base) from the left and right of each bolt. The flexural depth was selected as the rough distance within the left and right of each point load where the base remained rigid (i.e. where uplift was restricted). In total, 62 nodes along the base were restrained from X and Y movement. Nodes at the base were spaced apart at 40 mm underneath the two columns, and 50 mm elsewhere. Experimental results indicated that the base did not slide during testing, which justified the pinned support condition in the modelling. In addition, the base stayed in tact with little damage and with minimal uplift during testing.

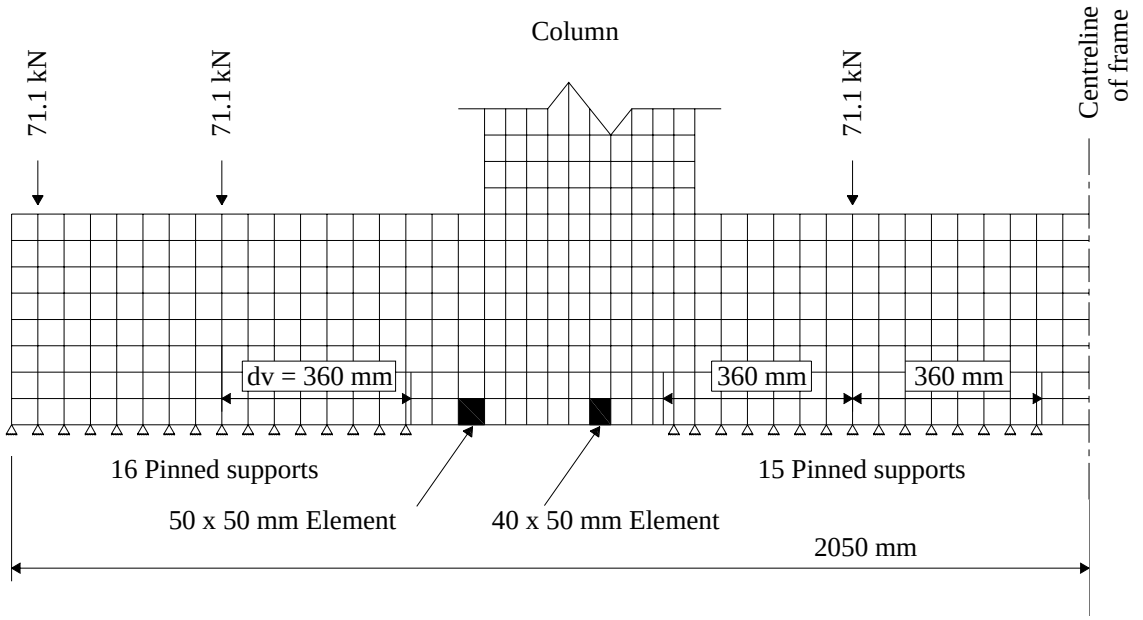

Figure 6.2 Base Support Conditions

6.2.2 Concrete Elements

Plane stress rectangular elements were used to model both reinforced and plain concrete. Rectangular elements were chosen over quadrilateral elements for the majority of the analyses as the latter type has not been well tested at this stage of the software development. 3648 concrete elements were used at most; 600 of these elements represented the repaired concrete (if present). The sizes of the concrete elements were chosen to coincide with the centrelines of the member steel reinforcement depths. Elements were 50 mm x 50 mm to coincide with the 50 mm centreline reinforcement depth at the base and beams, and 50 mm x 40 mm to coincide with the 40 mm reinforcement depth at the columns. Within the rectangular element type, well-distributed transverse reinforcement was modelled as smeared reinforcement. Six different concrete types were used with varying reinforcement ratios and thicknesses (refer to Table 6.1). Concrete Types 1 and 2 were assigned to the typical reinforced base and column sections, respectively. Their unreinforced cover counterparts were assigned to Types 3 and 5. The beam modelling was a special case. Because the beam stirrups were scarcely sparsely at 300 mm, and since the precise stresses and strains of the stirrups

were of interest, they were modelled using discrete truss elements instead of smeared reinforcement (see Section 6.2.3). As a result, the typical beam section was equivalent to a plain concrete element type (Type 3). To account for the rounded off beam cover where CFRP was wrapped, Type 4 was introduced with a reduced thickness of 225 mm. In addition, upon repair, the CFRP wrap provided some out-of-plane confinement to the beam section. The confinement was addressed with Type 6 at the top and bottom edges of the beam where CFRP out of plain confinement pressures were though to be effective. Confinement caused by the closed stirrups and ties were ignored since the equivalent out-of-plane reinforcement ratios present were negligible. Figure 6.3 below illustrates the material assignment locations.

Table 6.1 Concrete Element Type

Concrete Type	Location	Thickness (mm)	Reinforcement		
			Size	Direction	Ratio
1	Base	800	No. 10	90°	0.429 %
2	Column	300	No. 10	0°	1.018 %
3	Beam / Column (plain)	300	-	-	-
4	Beam cover	225	-	-	-
5	Base (plain)	800	-	-	-
6	Beam (w/ FRP confinement)	225	CFRP	Out-of-plane	2.0%

Note: Refer to Chapter 3 for the material properties of the steel and concrete.

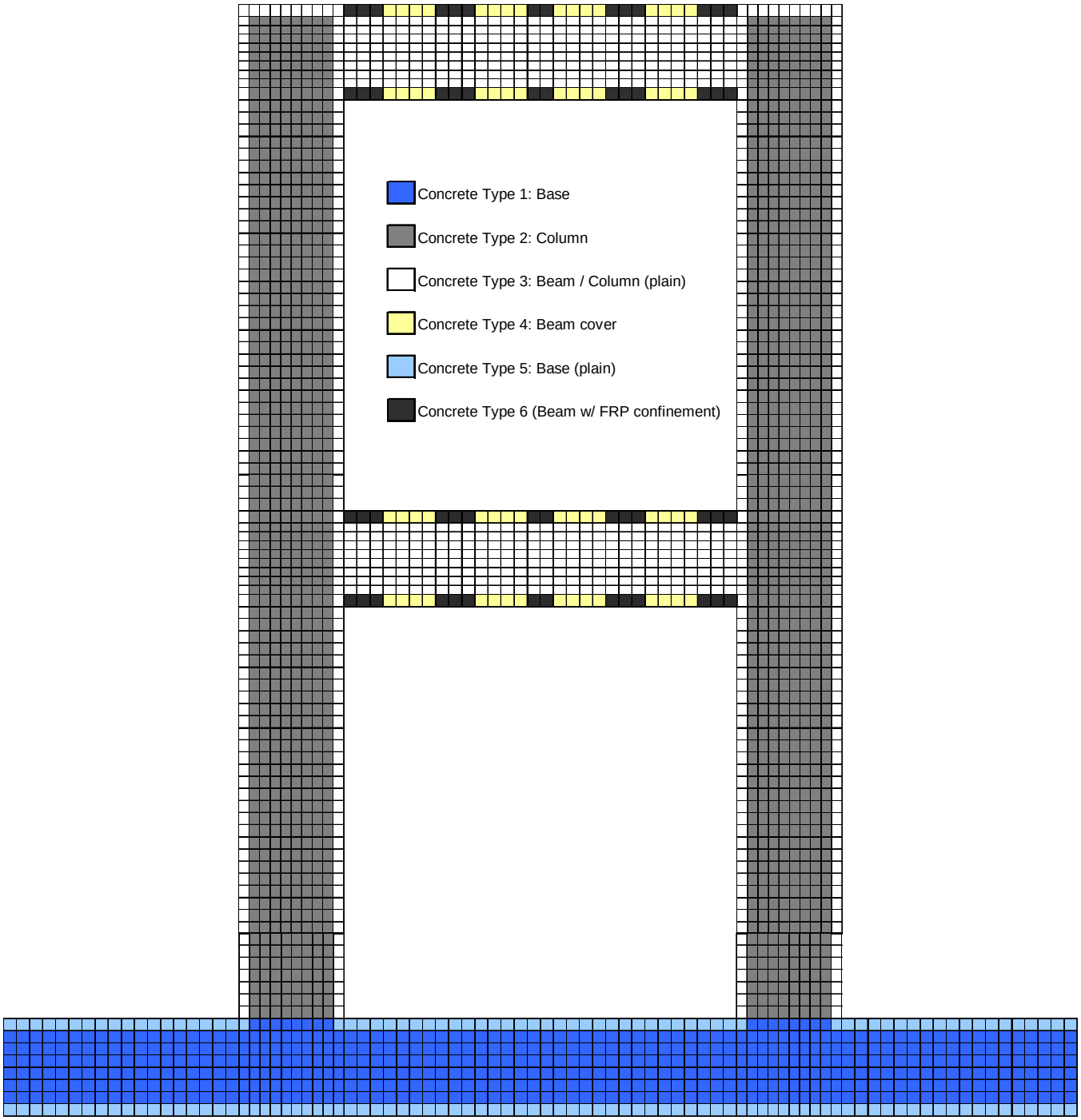

Note: Concrete Type 6 (Beam w/ CFRP confinement) was only implemented when models were repaired with CFRP wrap.

Figure 6.3 Concrete Material Assignment

6.2.3 Reinforcement Elements

Ductile steel reinforcement and CFRP wrap were modelled using discrete truss elements. Truss elements were two-noded elements with a uniform cross-sectional area. Each node had two degrees of freedom (X and Y), giving each element a total of four degrees of freedom. Ductile steel reinforcement included longitudinal rebars in the base, beams, and columns, and transverse reinforcement (stirrup and CFRP wrap) in the beams. The length of each truss element was either 40 mm or 50 mm depending on the nodal geometry. Recall that the nodal geometry was governed by the concrete element geometry. A total of 1318 truss elements were used; 938 of these truss elements were used for the reinforcing steel, and 380 for the CFRP wrap. Figure 6.4 and Figure 6.5 illustrate the steel material assignment and CFRP modelling layout, respectively. Table 6.2 summarizes the steel element type.

The longitudinal rebars and stirrups were designed to reach full yield experimentally by using adequate development lengths or hooks. Where hooks were present, the hooks themselves were not modelled. These hooks were simulated by assuming a perfect bond at the end of the rebar. Where straight development lengths were present, the rebar was also assumed fully bonded; however, to take into account the gradual decreasing steel stress that occurred towards the rebar end, the steel area was decreased in an approximate proportion to the decreasing steel stress level. In the FE modelling, the first half of the rebar development length had a gradual decreasing cross-sectional area, while the second half of the development length was omitted (refer to Figure 6.4). For example, the development length for a No. 20 rebar was conservatively taken as 800 mm. The first 200 mm of the development length closest to the mid length of the rebar was assumed fully developed with 100% of the cross-sectional steel area, the next 50 mm was assigned 75% of the total cross-sectional area, the next 100 mm was assigned 50%, and the next 50 mm was assigned 25%. The last 400 mm was excluded from the FE modelling. An alternative method to account for the development length would be to use bond elements with varying confinement pressures along the length;

however, this method would be more computationally demanding. The experimental results indicated that rebar slippage was not a concern.

The CFRP wraps were 150 mm wide, and spaced at 187.5 mm. Since the nodes along the beams were spaced at 50 mm and because the CFRP truss locations was constrained by the predefined grid, the exact location of the CFRP could not be modelled. The largest discrepancy between the modelled versus actual CFRP location was 25 mm, which was an acceptable error. The CFRP strip was modelled with either three or four lines of truss elements (Figure 6.5). Where three lines of truss elements were present, each line was given 1/3 of the total area. Where four lines of truss elements were present, each of the two interior lines was given 1/3 of the total area, while the exterior two lines were assigned 1/6 of the total area. The modelling of the bond between the CFRP and concrete surface is discussed in Section 6.2.4. Eight different reinforcement types were used with varying reinforcement areas and material properties (refer to Table 6.2). Reinforcement Type 1 was assigned to the base longitudinal rebars. Type 2 was allocated to the beam and column longitudinal steel. Types 3 through 5 took into account the rebar development length as previously discussed. Type 6 was assigned to the beam stirrups. Types 7 and 8 corresponded to 1/6 and 1/3 of a single CFRP strip, respectively. Figure 6.4 illustrates the CFRP truss bar placement and assignment.

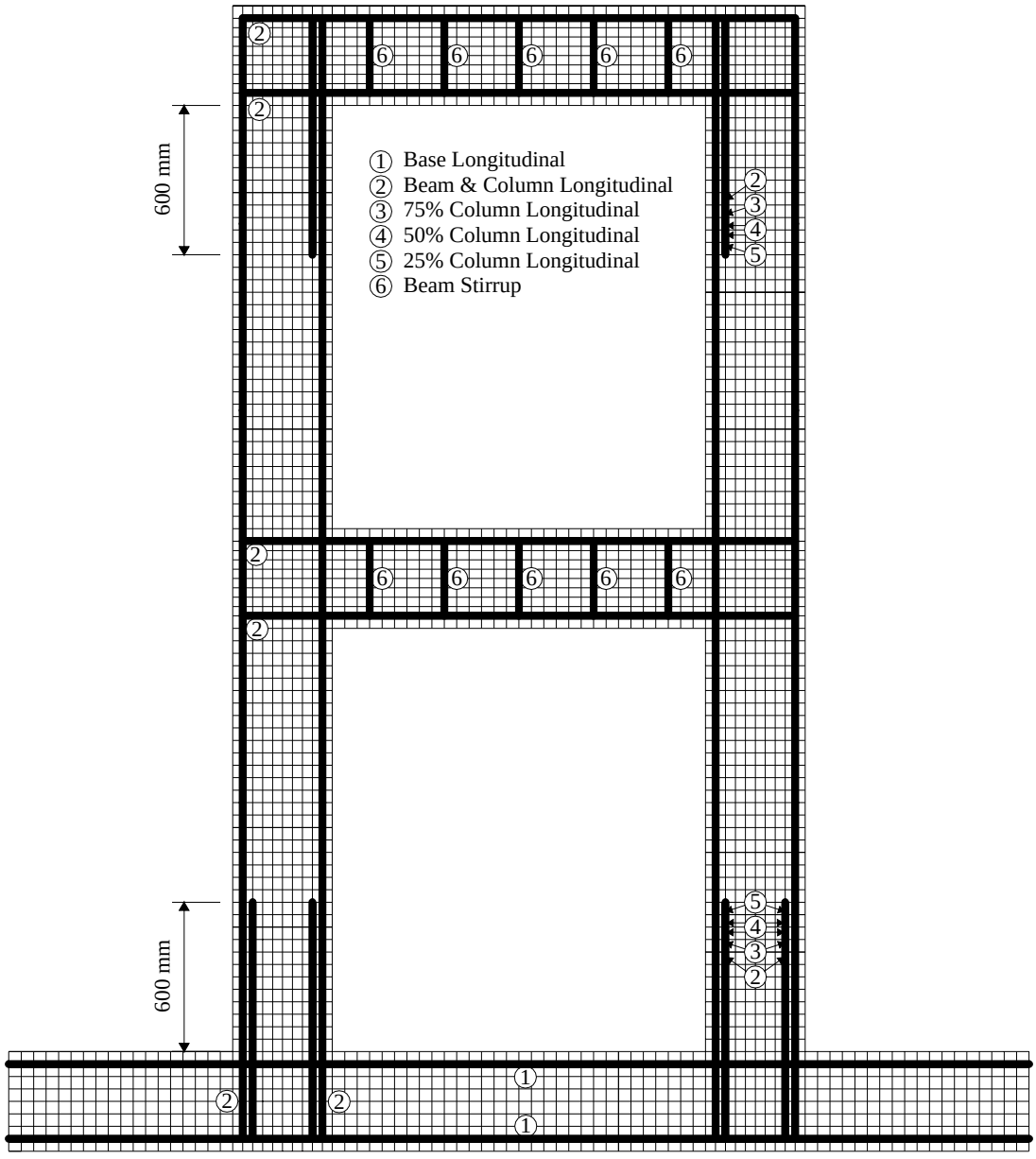

Figure 6.4 Steel Material Assignment

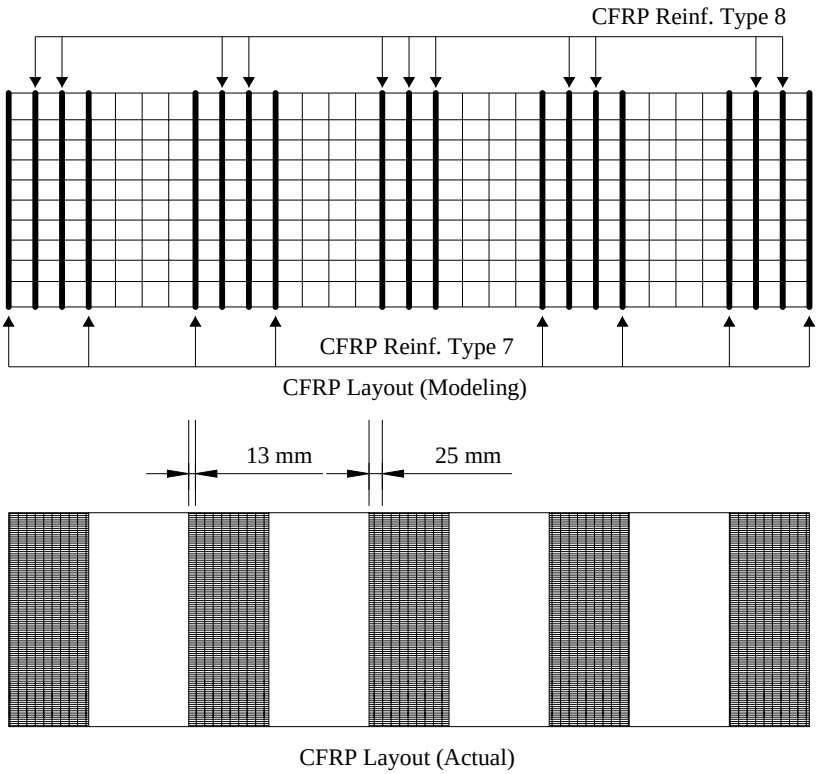

Figure 6.5 CFRP Modelling Layout

Table 6.2 Reinforcement (Ductile Steel) Element Type

Reinforcement Type	Location	Size
1	Base Longitudinal	8 No. 20
2	Beam & Column Longitudinal	4 No. 20
3	75% of Column Longitudinal	3 No. 20
4	50% of Column Longitudinal	2 No. 20
5	25% of Column Longitudinal	1 No. 20
6	Beam Stirrup	1 US #3
7	Beam CFRP	1/6 of a single strip
8	Beam CFRP	1/3 of a single strip

Note: Refer to Chapter 3 for the steel and CFRP material properties.

6.2.4 Link Elements

The interface between the CFRP and concrete surface was modelled using bond elements. In the FE mesh, the bond elements were situated between the CFRP trusses and the concrete elements. There are two types of bond elements available in VecTor2: link and contact. A link element is a two-noded, non-dimensional element, while a contact element is a four-noded, linear dimension element. For this thesis, the link elements were chosen over contact elements because the former type was less computationally intensive, easier to implement, and worked reasonably well in the past for FRP modelling (Wong, 2001). The most influential aspect of the CFRP interface modelling was the choice of a suitable bond stress-slip relationship. The correlation between bond stress and slip was dependent not only on the type of CFRP used, but also on the type of epoxy. For the specific type of CFPR and epoxy used in this study, Sato and Vecchio (2003) proposed a bilinear bond stress-slip relationship that was defined in relationship to the fracture energy G_f (the area under the stress-slip plot in N/mm). For a concrete strength of 43 MPa, the ultimate bond shear stress was 4.37 MPa and this corresponded to a slip of 0.038 mm. At a slip limit of 0.201 mm, the stress was zero. The bilinear bond stress-slip relationship is shown in Figure 6.6.

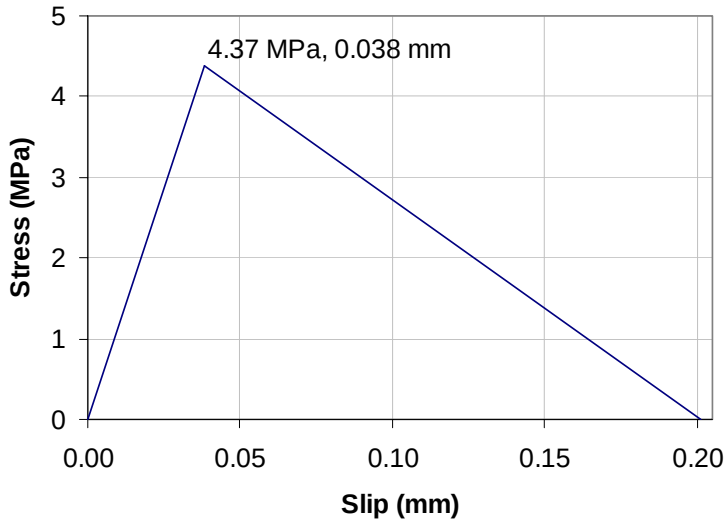

Figure 6.6 Bond Stress vs. Slip Model for CFRP

Three bond types were used with varying bonded surface area (refer to Table 6.3). The surface area was calculated according to the tributary area of the CRFP wrap around the bond element (Wong and Vecchio, 2001). Type 1 was the special case of the beam corner, where the CFRP was assumed to achieve near perfect bond from the fully wrapped configuration. An arbitrarily high shear strength of 10 MPa was assigned to Type 1. Types 2 and 3 were assigned to the bonded areas that corresponded to the CFRP reinforcement Types 6 and 7, respectively (1/6 and 1/3 of the strip area).

Table 6.3 Bond Element Type

Bond Type	Location	Bonded Surface Area (mm^2)	U1 (MPa)	U2 (MPa)	U3 (MPa)	S1 (mm)	S2 (mm)	S3 (mm)
1	Beam corner	2000	10	0.1	0	0.038	0.2	0.201
2	Reinf. Type 7	2000	4.37	0.1	0	0.038	0.2	0.201
3	Reinf. Type 8	1000	4.37	0.1	0	0.038	0.2	0.201

Note: U1, U2, U3, S1, S2, and S3 were points on the bond stress-slip curve.

6.2.5 Loading Conditions & Procedures

In the experiment, a vertical column load of 420 kN was applied uniformly to the top of each column via a loading plate. In the FE modelling, nine nodes situated at the top of each column were each assigned 46.6 kN of vertical downward force that was held throughout the analysis (refer to Figure 6.7). The lateral load was applied at the mid-depth of the second-storey beam at the pushing end. For instance, during the forward direction of testing (frame moving towards the south direction), the displacement was applied to the north end of the beam, and vice versa. The interchanging of loading nodes at each forward and reverse half cycle was necessary to avoid tearing of the concrete element. This procedure meant that prior to each load reversal, the results were examined to locate the last stage of compressive loading. At this load stage, the load and job files were modified accordingly. The displacement was maintained at 1 mm displacement

increments through out the analyses. For the parametric study in Section 6.3.1, a monotonic load type was used. For all other analyses (i.e. analytical response of the experiment), a reverse cyclic load type was assigned.

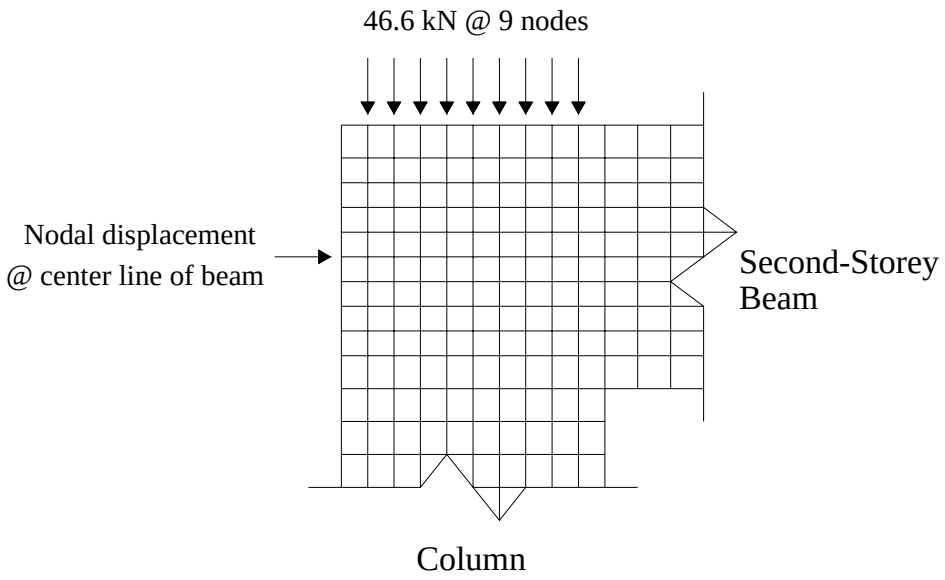

Figure 6.7 Column and Lateral Loadings

6.2.6 Concrete, Reinforcement, and Bond Analytical Models

Table 6.4 summarizes the material properties for the concrete elements, reinforcement elements, bond elements, and the corresponding analytical model(s) chosen for each material property. Analytical models with and without asterisks beside their names indicated whether they were the default or non-default options in VecTor 2, respectively. Refer to the FormWorks manual by Wong and Vecchio (2002) for a description of all the analytical models. For several material properties, there existed multiple analytical models, but no definitive first choice. These properties were concrete crack width check, reinforcement dowel action, and concrete bond model. These properties were examined in a parametric study in Section 6.3.1.

Typically, the default analytical models were chosen unless there was a valid justification to select an alternative model. For the concrete compression pre-peak

response, the Popovics High Strength model was chosen over the default Hognestad Parabola to reflect the relatively high concrete strength used in the specimen (f'c of 43 MPa). The Popovics High Strength model was better suited to capture the pre-peak response of high strength concrete. For the concrete compression post-peak response, the Montoya 2003 was the most recently developed model and was chosen over the default Modified Park-Kent model.

The effects of concrete tension softening was particularly important in lightly reinforced regions exhibiting brittle failure modes. This property affected the load-deformation response and ductility of the member. The bilinear model was chosen over the linear model for better accuracy in representing the post-peak tensile stress-strain curve.

The hysteretic response of concrete played an important role to the strength and ductility of the reinforced concrete structures subjected to cyclic or reverse cyclic loading. The Palermo 2002 (with decay) was the most recently developed model for the hysteretic response of concrete; however, this model gave unstable results that caused the analyses to terminate prematurely. It was uncertain if the instability was caused by errors in the Palermo model, the nature of the frame, or incompatibilities with various updates of other analytical models used. The default nonlinear with plastic offsets model was selected instead.

Table 6.4 Analytical Models Used in the FE Analyses

Material Property	Analytical Model
Concrete Compression Pre-Peak Response	Popovics (HSC) *
Concrete Compression Post-Peak Response	Montoya 2003 *
Concrete Compression Softening Model	Vecchio 1992-A (e1/e2-Form)
Concrete Tension Stiffening Model	Bentz 2003
Concrete Tension Softening	Bilinear *
Concrete Tension Splitting	Not considered
Concrete Confinement Strength	Kupfer / Richart Model
Concrete Lateral Expansion	Variable - Kupfer
Concrete Cracking Criterion	Mohr-Coulomb (Stress)
Concrete Crack Slip Check	Vecchio-Collins 1986
Concrete Crack Width Check	Agg./5 Max Crack Width 5 mm Crack Width * Stability Check Omitted *
Concrete Creep and Relaxation:	Not Available
Concrete Hysteretic Response	Nonlinear w/ Plastic Offsets
Reinforcement Hysteretic Response	Seckin Model (Bauschinger)
Reinforcement Dowel Action	Tassios Model (Crack Slip) Tassios Model (Strength) * Not Considered *
Reinforcement Buckling	Asatsu Model
Concrete Bond	Eligehausen Model Perfect Bond *

Note: * Non-default model

6.3 SUMMARY OF FINITE ELEMENT ANALYSIS

Three series of finite element analyses were carried out. In Series 1 and 2, monotonic push-over analyses were performed on the frame (with and without CFRP) as part of the parametric study (Section 6.3.1). In Series 3, reverse cyclic analyses were carried out to predict the experimental results of Phase A and Phase B (Section 6.3.2). The models used in all three series were essentially the same; the variations occurred when CFRP was modelled (CFRP elements were added), or when the CFRP-concrete interface bond was of interest (link elements were added). In Series 1, the models consisted of a base model and a revised version where 380 CFRP truss elements were implemented directly onto the beam (i.e. without the use of link elements). In Series 2

where the interface bond was studied, the set of models utilized CFRP truss elements with 418 corresponding link elements and 418 additional nodes. The models in Series 3 were extracted from those in Series 1 and 2. The only modifications were changes in the load files to accommodate the reverse cyclic loading sequences, and the addition of 600 rectangular elements to account for the repaired concrete beams present in Model 3c. Table 6.5 summarizes the models included in the three series and the number of elements used for each type of element. There were seventeen models in total. Each model had at least one unique characteristic from the rest. For example, a different reinforcement dowel action or another crack width option was used. Table 6.6 distinguishes the different characteristics of each model.

Table 6.5 Summary of Modelling Series and No. of Elements Used

Element Type	**No. of Elements**					
	Series 1		**Series 2**	**Series 3**		
	Base: *1a, 1b, 1c, 1d, 1j, 1k*	w/ CFRP (no link) *1e, 1f, 1g,1h, 1i*	w/ CFRP (and link) *2a, 2b, 2c*	*3a*	*3b*	*3c*
Concrete	3048	3048	3048	3048	3048	3648
Steel Reinforcement	938	938	938	938	938	938
CFRP Reinforcement	-	380	380	-	380	380
Link	-	-	418	-	-	-
No. of Nodes	3357	3357	3775	3357	3357	3357

Note: Series 1 and 2 were for the monotonic analyses (parametric study). Series 3 was for the reverse cyclic analyses (analytical response of the experiment).

Table 6.6 Summary of Model Characteristics

Name	Reinforcement Dowel Action	Crack Width Check	CFRP present	Link present	Other
1a	1	Agg./5	N	N	
1b	2	5 mm width	N	N	
1c	0	5 mm Width	N	N	
1d	1	Agg./5	N	N	Quadrilateral concrete elements were used
1e	1	Agg./5	Y	N	
1f	2	5 mm width	Y	N	
1g	0	5 mm width	Y	N	
1h	1	5 mm width	Y	N	
1i	1	Omitted	Y	N	
1j	1	5 mm width	N	N	
1k	1	Omitted	N	N	
Models with CFRP and link elements					
2a	1	5 mm width	Y	Y	CFRP and link elements were deactivated
2b	1	5 mm width	Y	Y	Perfect bond model
2c	1	5 mm width	Y	Y	Bond Stress-slip relationship in Figure 6.6
Reversed Cyclic Models					
3a	1	5 mm width	N	N	Phase A only - Same model as 1j.
3b	1	5 mm width	Y	N	Phase B only - Same model as 1h
3c	1	5 mm width	Y	N	Phase A (w/ deactivated repaired conc. And CFRP) Phase B (w/ activated repaired conc. and CFRP)

Reinforcement Dowel Action:
0. Not considered. 1. Tassios Crack Slip Model. 2. Tassios Strength Model

6.3.1 Parametric Study

A parametric study was carried out to examine the sensitivity of various material properties and modelling procedures on the analytical response of the shear-critical test frame. Knowledge from this study was used to assess the FE program VecTor2, and to serve as a guideline in modelling and selecting the material properties for the analytical response of the experiment (Section 6.3.2). To reiterate, Table 6.4 summarized the material properties and their corresponding analytical models available. Where there was more than one model listed for a specific category, these models were examined in the parametric study through monotonic push-over analyses. Table 6.5 sorted out the three series of models; series 1 and 2 were of interest in the parametric study. Table 6.6 distinguished the modelling differences between all of the analyses. Figure 6.8 illustrates the parameters in this study and the corresponding models.

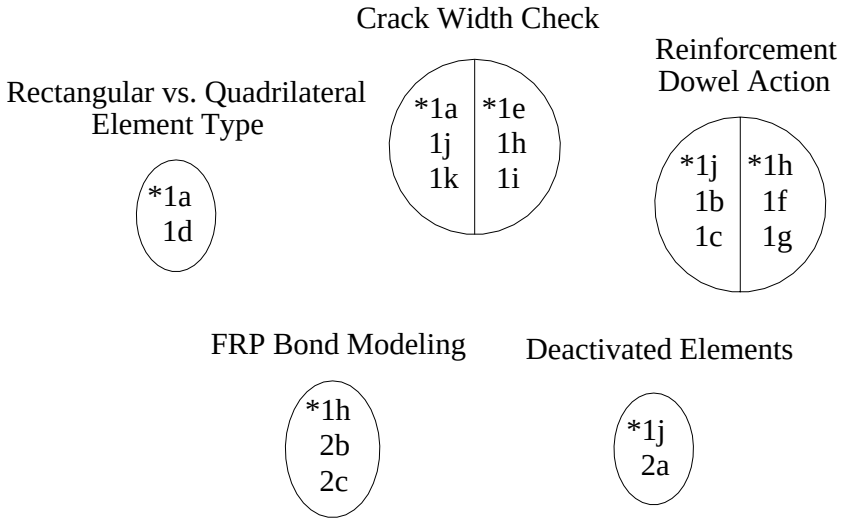

Note: * refers to the control model for each parameter

Figure 6.8 Summary of Parametric Parameters

This following is a list of parameters in question, and a brief description of the corresponding models.

Rectangular vs. Quadrilateral Element Type (1a, 1d)

The influence of using either rectangular or quadrilateral concrete elements was of interest. Both rectangular and quadrilateral elements have four nodes each, and a total of eight nodal degrees of freedom. The nodes in a rectangular element must be oriented such that its edges are parallel to the X and Y axes, whereas the nodes in a quadrilateral element may assume any orientation and shape in the X, Y coordinate system. As such, the quadrilateral element is able to account for non-linear secondary geometry effects, but is numerically more demanding and less stable. Also, the quadrilateral element type has not been rigorously tested in the past.

Crack Width Check (1a, 1j, 1k, 1e, 1h, 1i)

The effects of crack width check were examined through three options: aggregate / 5 (equivalent to 2 mm for this frame), 5 mm crack width, and omitted. The crack width options were tested for both the bare and CFRP wrapped frames. The crack width check places a limit on the average compressive stresses that can be developed when the crack width exceeds a specified limit. The width criterion is particularly influential to the ductility of lightly reinforced shear-critical elements.

Reinforcement Dowel Action (1j, 1b, 1c, 1h, 1f, 1g)

The effects of dowel action on shear critical and flexural critical structures were of interest. Three dowel action options were considered: Tassios Crack Slip model, Tassios Strength model, and dowel action not considered. These options were scrutinized for cases without CFRP wrap (1j, 1b, 1c) and cases with CFRP wrap (1h, 1f, 1g). From previous experience, the Tassios Crack Slip model worked well for shear critical structures; however, when the Tassios Strength model was used instead, the structures exhibited much higher capacities and changed the failure mode from shear to flexure.

For the case of flexural critical structures where the Tassios Crack Slip model was implemented, the structures at times exhibited premature interface shear failure (may be a numerical instability problem). The Tassios Strength model was recently developed (December 2004) to fix the interface shearing problem.

FRP Bond Modelling (1h, 2b, 2c)

Of interest was the effect of bond modelling on the response of CFRP truss elements. Three options were considered: without the use of link elements (1h), with the use of link elements assuming a perfect bond option (2b), and with the use of link elements assuming the bond stress-slip relationship depicted in Figure 6.6 (2c). The results for 1h and 2b should be identical since both considered the CFRP to be perfectly bonded to the concrete surface. Model 2c should have a lower capacity than the other two models since a real bond surface will typically have a lower capacity than a perfectly bonded surface.

Deactivated Elements (1j, 2a)

In theory, if a structure was analyzed using two models that were modelled exactly the same, except one model had additional deactivated elements, both models should give identical results. The effect of deactivated elements (if any) was studied. Model 2a, with deactivated CFRP truss and link elements was compared to its equivalent model (1j) without deactivated elements.

6.3.2 Analytical Response of the Experiment

The experimental results of Phase A and B were predicted analytically using three models of the frame (3a, 3b, 3c) that were subjected to the prescribed reverse cyclic sequences of the experiment. All three models used rectangular elements, the Tassios Crack Slip reinforcement dowel action, and 5 mm crack width check. Refer to Section 6.5.1 for the parameter selection. Model 3a predicted the response of the bare frame (i.e.

without CFRP) during the forward and reserve half cycles of Phase A. Model 3b predicted the reverse cyclic response during Phase B assuming Phase A of testing did not take place. In other words, the undamaged frame was wrapped with CFRP at the start of the analysis. Model 3b used perfectly bonded CFRP strips (without link elements). Finally, Model 3c predicted the frame's response in accordance with the testing regime. Phase A of the test was analyzed with the deactivated repaired concrete and CFRP wrap elements. After completion of Phase A and before the start of Phase B, the old set of concrete beam elements was deactivated, while the repaired concrete and CFRP truss elements were activated. Model 3c also used perfectly bonded CFRP strips (without link elements). Model 3b was compared with Model 3c to determine whether Phase A of the experiment had a great impact on the analytical response after repair. Furthermore, Model 3b provided a means to check against the results of 3c in case some strange results were produced.

6.4 RESULTS

Section 6.4.1 presents the results of the parametric study, while Section 6.4.2 presents the results of the analytical predictions of the experiment.

6.4.1 Results: Parametric Study

Figure 6.9 through Figure 6.13 illustrate the results of the parametric study. Table 6.7 through Table 6.11 summarize the peak loads and describes the failure modes.

Rectangular vs. Quadrilateral Element Type

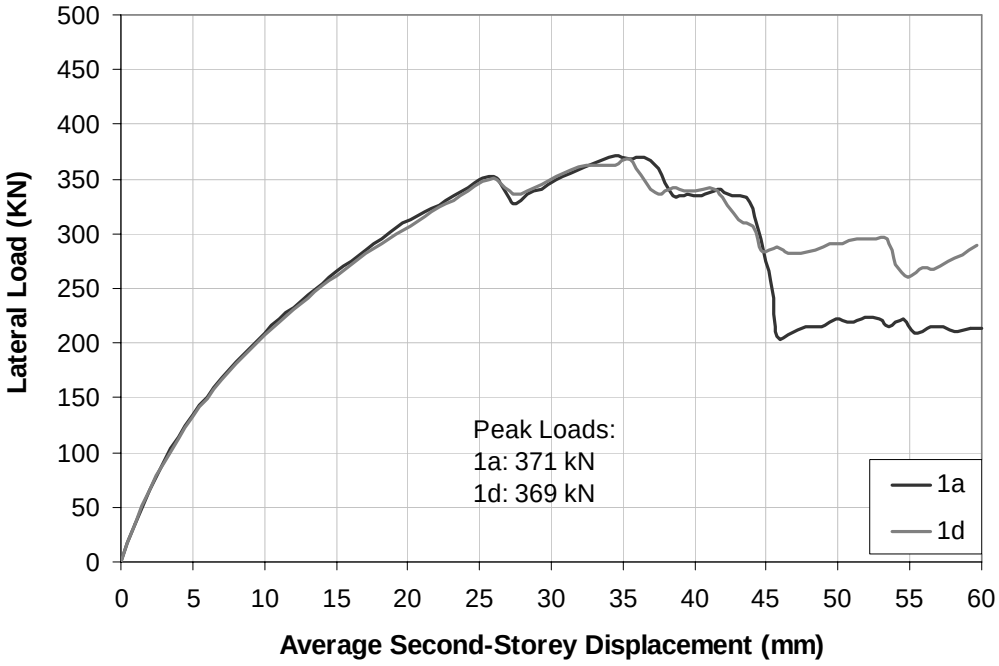

Figure 6.9 Parametric Study: Rectangular vs. Quadrilateral Element Type

Table 6.7 Parametric Study: Rectangular vs. Quadrilateral Element Type

	Model	Peak Load (kN)	Concrete Element Type	Failure Mode
No CFRP	1a	371	Rectangular	Shear failure at south end of lower beam, then north end of upper beam.
	1d	369	Quadrilateral	Same as 1a.

Crack Width Check

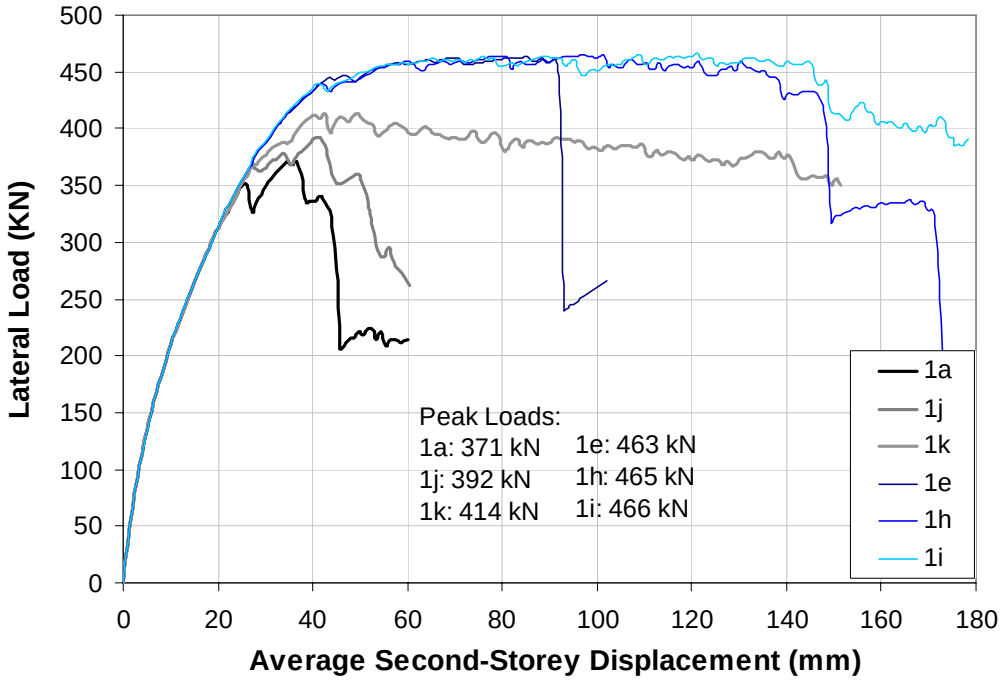

Figure 6.10 Parametric Study: Crack Width Check

Table 6.8 Parametric Study: Crack Width Check

	Model	Peak Load (kN)	Crack Width Check	Failure Mode
No CFRP	1a	371	Agg./5	Shear failure at south end of lower beam, then north end of upper beam
	1j	392	5 mm width	Similar to 1a, expect failure was not as abrupt
	1k	414	Omitted	Tension splitting along the longitudinal rebars at the lower beam and then at upper beam. Beams bulged like a stub column.
With CFRP	1e	463	Agg./5	Flexural hinging at both ends of both beams, and both column bases. Excessive deformation caused shear propagation at the four beam ends. Frame eventually failed from interface shear at north end of upper beam.
	1h	465	5 mm width	Same as 1e, except shear failure took place at south end of lower beam.
	1i	466	Omitted	Same as 1e, except final failure mode was compression failure at the loading point.

Reinforcement Dowel Action

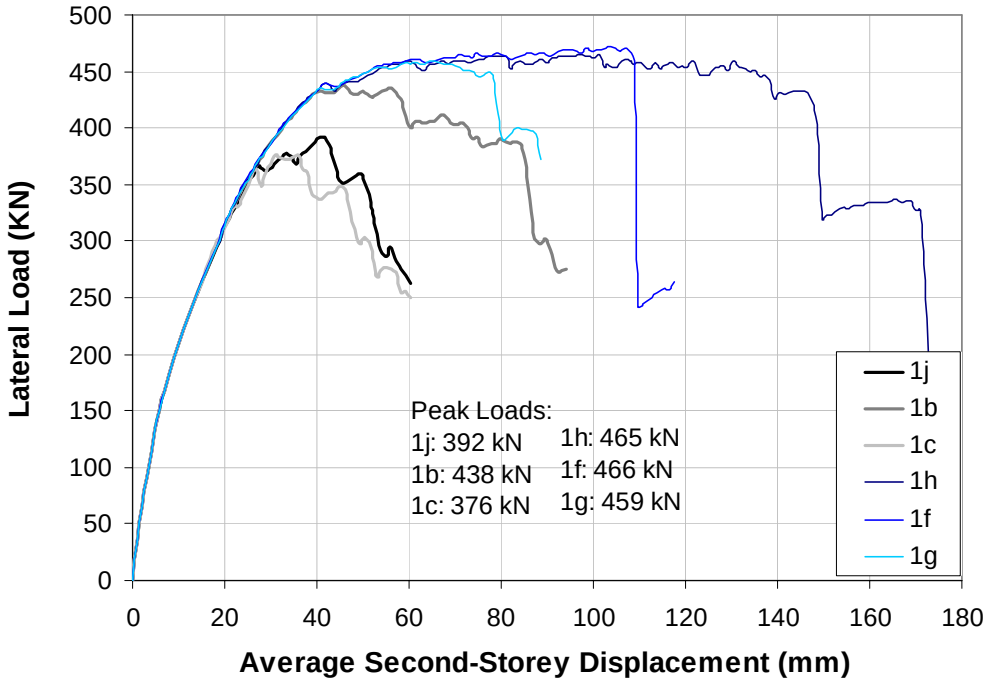

Figure 6.11 Parametric Study: Reinforcement Dowel Action

Table 6.9 Parametric Study: Reinforcement Dowel Action

	Model	Peak Load (kN)	Reinforcement Dowel Option	Failure Mode
No CFRP	1j	392	1	Shear failure at south end of lower beam, then at north end of lower beam.
	1b	438	2	Combined flexural hinging and tension splitting at lower beam, then shear-flexural failure at north end of lower beam.
	1c	376	0	Shear failure at south end of lower beam, then simultaneous shear failure at north ends of lower and upper beams.
With CFRP	1h	465	1	Flexural hinging at both ends of both beams, and both column bases. Excessive deformation caused shear propagation at the four beam ends. Finally shear failure took place at south end of lower beam.
	1f	466	2	Same as 1h, except the frame failed from interface shear at north end of upper beam.
	1g	459	0	Flexural hinging at both ends of both beams, and both column bases. Frame failed in shear at south end of lower beam and at north end of upper beam. The analysis terminated (unstable) at 86 mm.

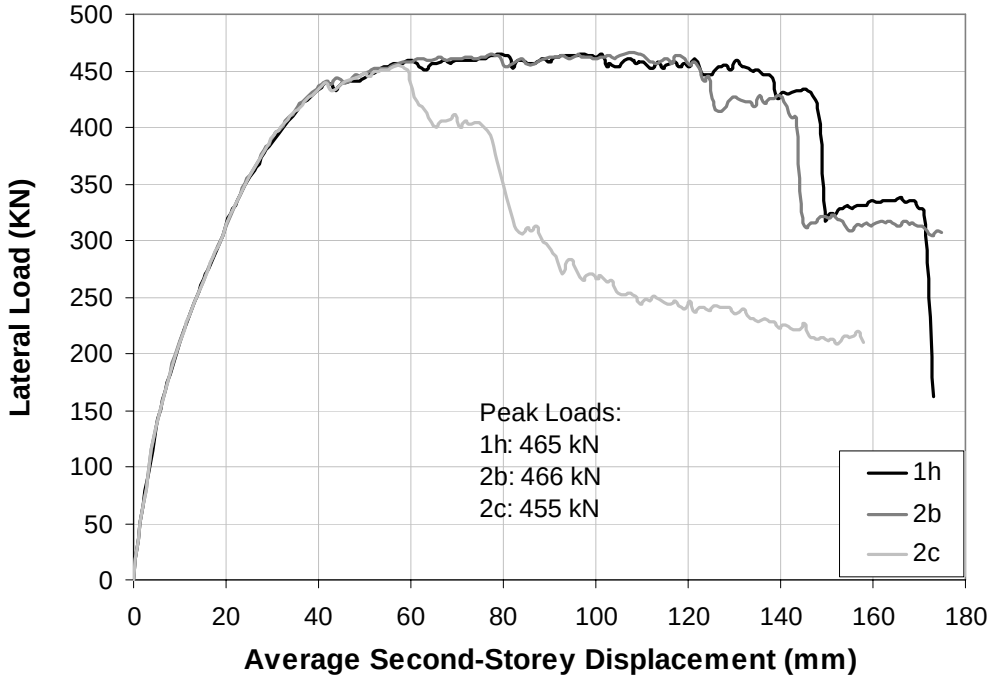

Figure 6.12 Parametric Study: FRP Bond Modelling

Table 6.10 Parametric Study: FRP Bond Modelling

	Model	Peak Load (kN)	FRP Bond	Failure Mode
With CFRP	1h	465	Prefect Bond (no link)	Flexural hinging at both ends of both beams, and both column bases. Excessive deformation caused shear propagation at the four beam ends. Finally shear failure took place at south end of lower beam.
	2b	466	Perfect Bond (link present)	Same as 1h.
	2c	455	Eligehausen	Combined tension splitting and flexural yielding at both beams. Gradually shear failure took place at north end of upper beam.

Deactivated Elements

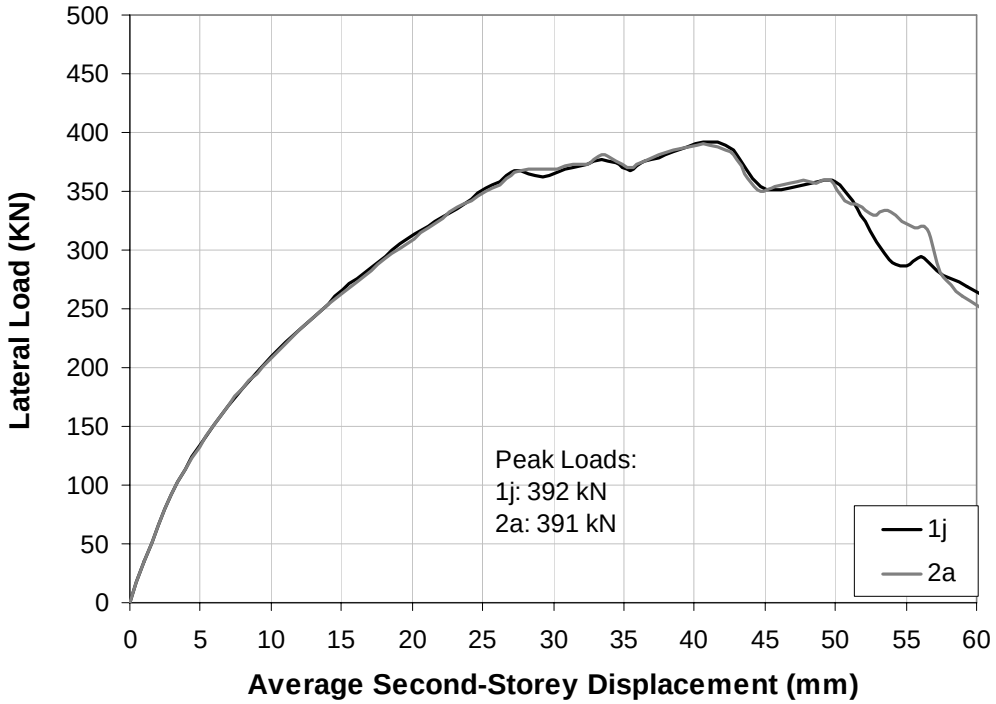

Figure 6.13 Parametric Study: Deactivated Elements

Table 6.11 Parametric Study: Deactivated Elements

	Model	Peak Load (kN)	Deactivated Elements	Failure Mode
No CFRP	1j	392	No	Shear failure at south end of lower beam, then at north end of upper beam.
	2a	391	Yes	Same as 1j.

6.4.2 Results: Analytical Response of the Experiment

The following tables and figures pertain to the analytical results of Model 3a (Phase A): Table 6.12 to Table 6.14, and Figure 6.14 to Figure 6.22. Table 6.12 summarizes the key load stages in Phase A of the analytical model. Figure 6.14 and Figure 6.15 illustrate the lateral load versus second-storey displacement for both the analytical and experimental responses. Figure 6.16 and Figure 6.17 illustrate the cracking pattern for both the analytical and experimental results at +32 mm and +40 mm of top storey displacement, respectively. The former and latter displacements correlated to load stages 14 and 15 of the forward-half-cycle, respectively. Figure 6.18 illustrates the crack pattern for -40 mm, which is equivalent to load stage 26 of the reverse half-cycle. Figure 6.19 through Figure 6.22, and Table 6.13 Beam Elongation and Residual Deformation and Table 6.14 Column Deformation and Residual Deformation summarize the beam elongation and column deformation.

The following tables and figures pertain to the analytical results of Model 3b: Table 6.15, and Figure 6.23 to Figure 6.26. Table 6.15 summarizes the lateral displacement and peak lateral loads for Model 3b, 3c, and the experiment. Only Phase B of the results for Model 3c and the experiment were presented; comparisons for Phase A of the test are presented in Figure 6.14. Figure 6.23 and Figure 6.24 present the lateral load versus second-storey displacement for the two analytical models, while Figure 6.25 superimposes the results of Model 3b on top of the experimental result. Figure 6.26 shows the predicted and experimental beam crack pattern during load cycle 7 (+3.0 Δ_y).

Table 6.12 Key Load Stages of the Analytical Results (Model 3a)

Load (kN)	Avg. 2nd Storey Lat. Displ. (mm)	Comment
Forward Half-cycle		
0	0	Initial condition
66	2.0	First lower beam hairline flexural crack
91	3.0	First upper beam hairline flexural crack
114	4.0	First north column hairline flexural crack
134	5.0	First south column hairline flexural crack
151	6.0	First lower beam shear crack (1.0 mm wide)
210	10.0	First upper beam shear crack (1.0 mm wide)
335	23.2	Shear yielding in both ends of the lower beam. Flexural steel stress at the lower beam south end was 400 MPa. Lower beam shear crack was 2 mm wide. Longitudinal tension splitting crack was 2-3 mm wide.
366	30.3	Lower beam flexural yielding at south end
373	32.4	Shear yielding at both ends of the upper beam. Lower beam shear crack was 3.5 mm wide at the south end, and 1.5 mm wide at the north end. Lower beam top longitudinal tension splitting cracks at the top and bottom were 5.9 mm, and 1.5 to 3 mm wide, respectively. Upper beam shear cracks were ~1.0 mm wide at the both ends. Upper beam top longitudinal tension splitting cracks at the top and bottom were 1.1 mm, and 1.4 mm wide, respectively.
378	33.4	Upper beam flexural stress at the north end, at cracked locations, reached yield but the average stress did not reach yield.
392	40.6	Lower beam shear crack was 4.5 mm wide at the south end, and 2.5 mm wide at the north end. Lower beam top and bottom longitudinal tension splitting cracks were ~8 mm wide. Upper beam shear cracks were 1.5 mm at the both ends. Upper beam top longitudinal tension splitting cracks at the top and bottom were 2.5 mm, and 4 mm wide, respectively.
Reverse Half-cycle		
Generally, the crack pattern prior to failure was difficult to assess because it was difficult to distinguish between old and new cracks from Augustus (post-processor). At the peak top storey lateral displacement of -40 mm, with the exception of the 3.5 mm wide shear crack located at the north end of the upper beam, all other shear cracks were less than 2 mm wide. Longitudinal splitting cracks were present at the top and bottom rebar layers of both beams, and were nearly 10 mm wide at all four locations.		
-307	-26.5	Stirrups in both beams yielded. Flexural steel stress was less than 300 MPa.
-335	-40.6	Flexural steel stress reached a maximum of around 365 MPa.

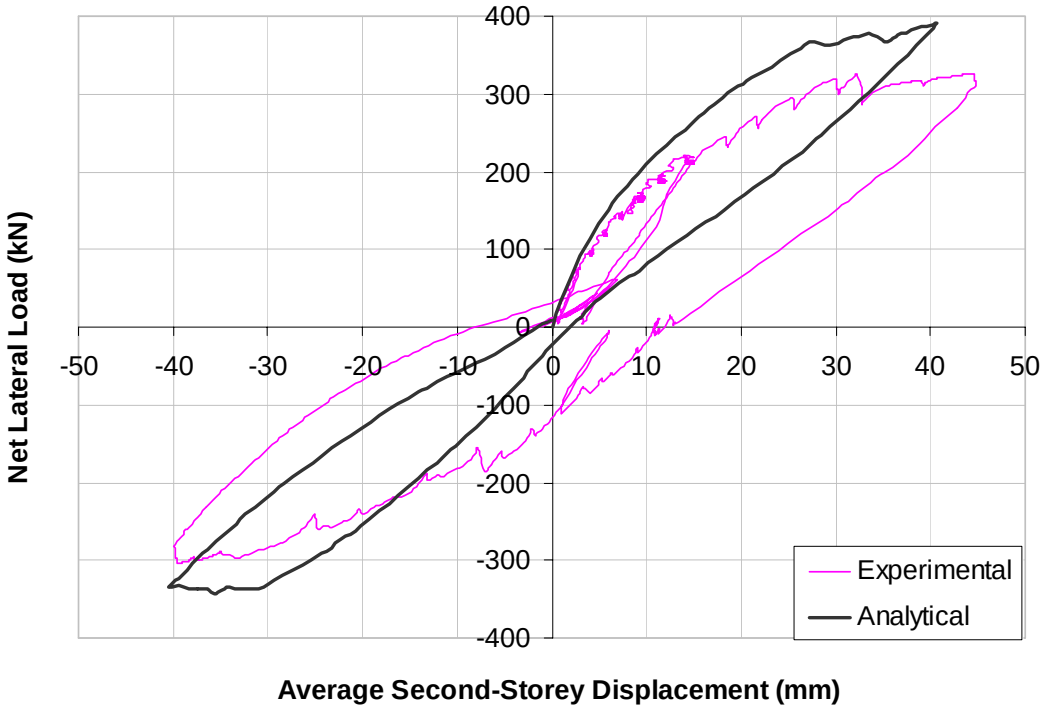

Figure 6.14 Phase A: Lateral Load vs. Second-Storey Displacement (Experimental vs. Analytical Results - Model 3a)

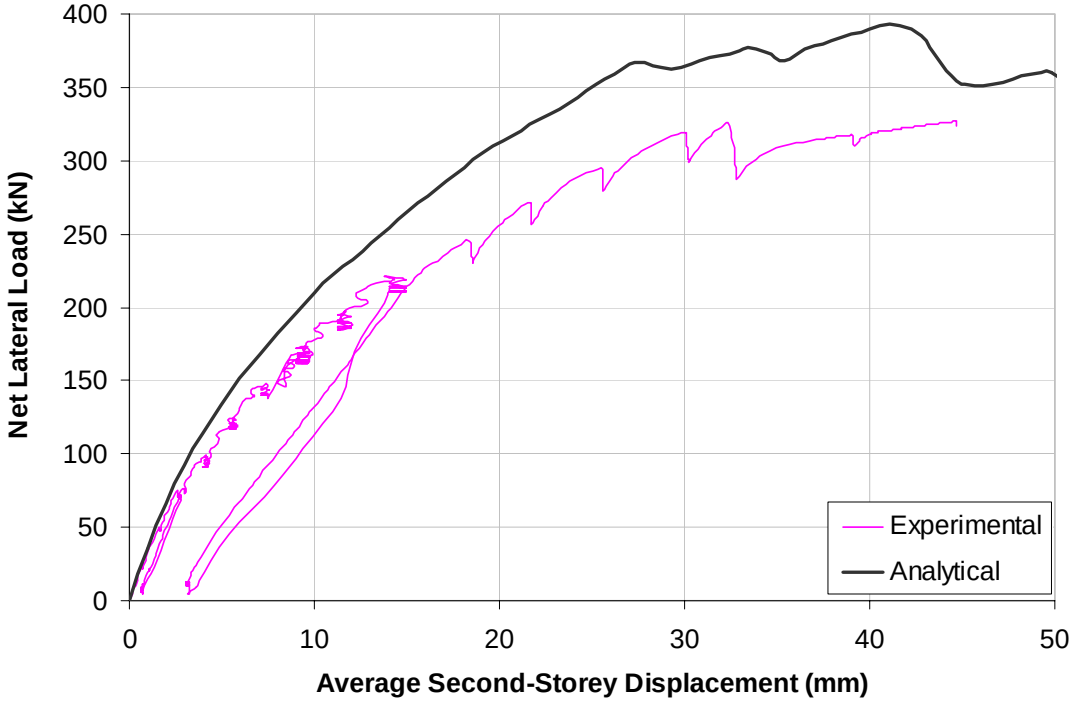

Figure 6.15 Phase A Forward Half-Cycle: Lateral Load vs. Second-Storey Displacement (Experimental vs. Analytical Results - Model 3a)

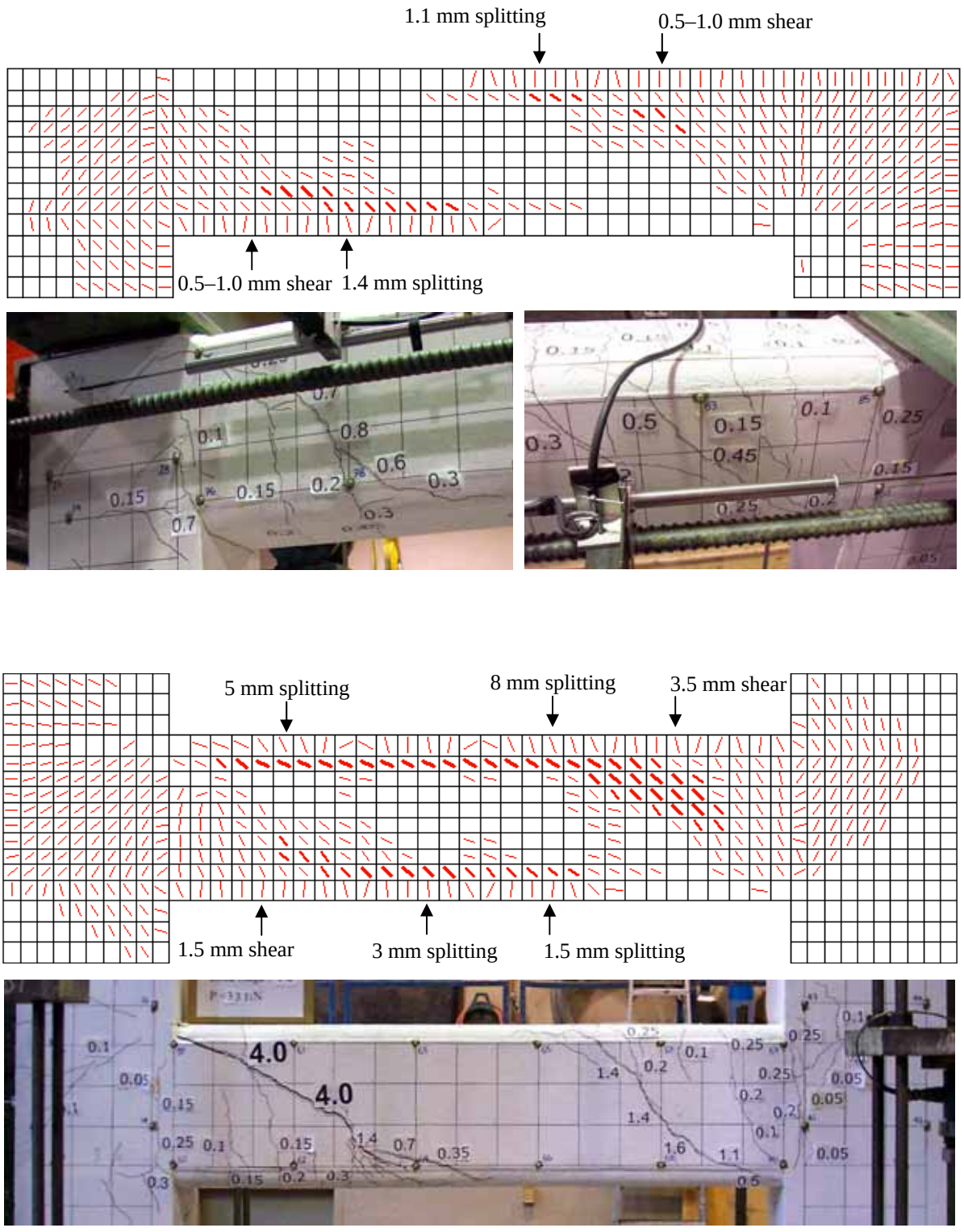

Figure 6.16 Beam Crack Pattern at +32 mm of Top Storey Deflection

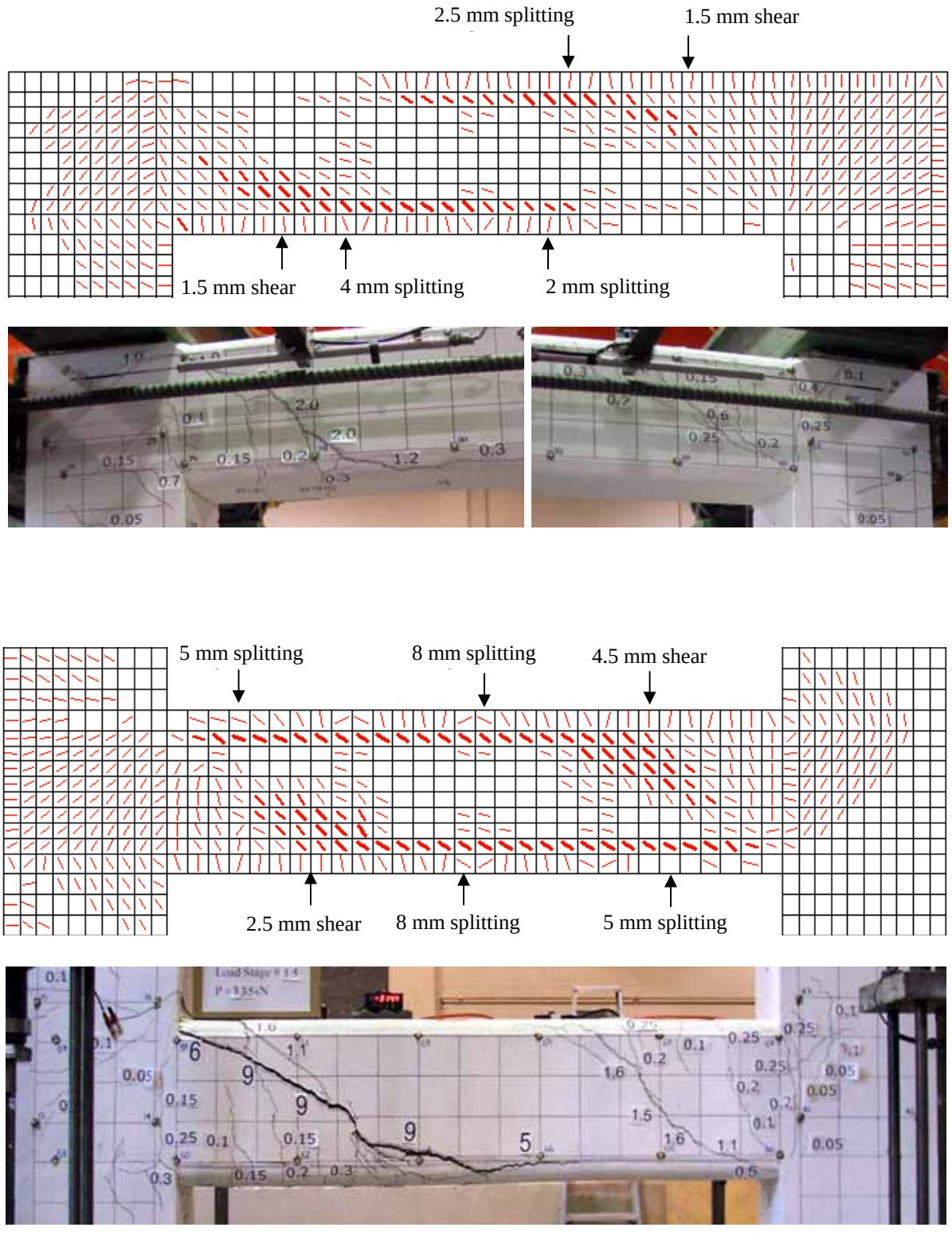

Figure 6.17 Beam Crack Pattern at +40 mm of Top Storey Deflection

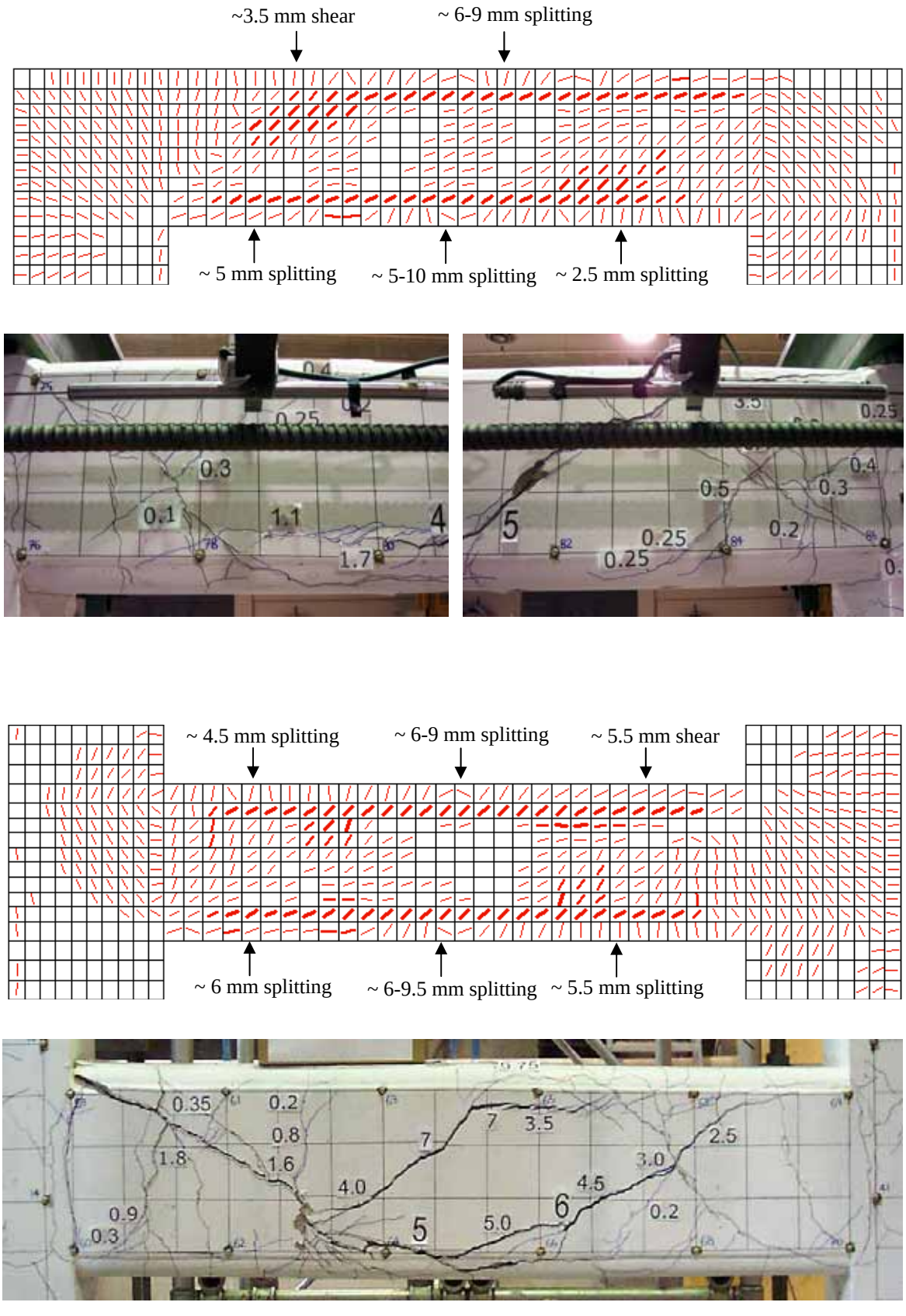

Figure 6.18 Beam Crack Pattern at -40 mm of Top Storey Deflection

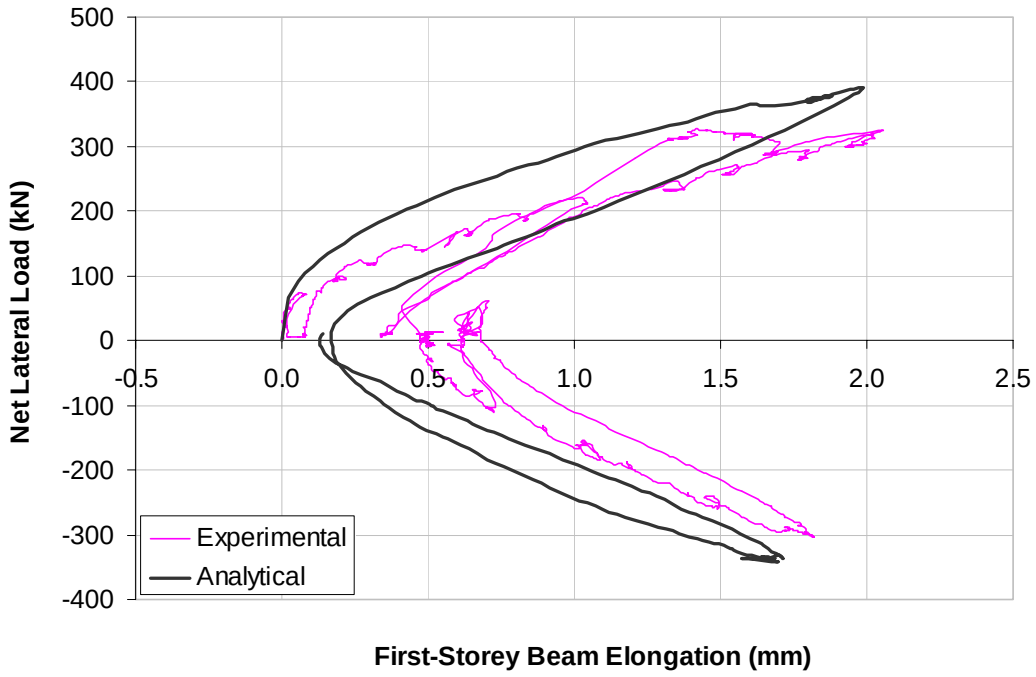

Figure 6.19 Lateral Load vs. First-Storey Beam Elongation (Experimental vs. Analytical Results)

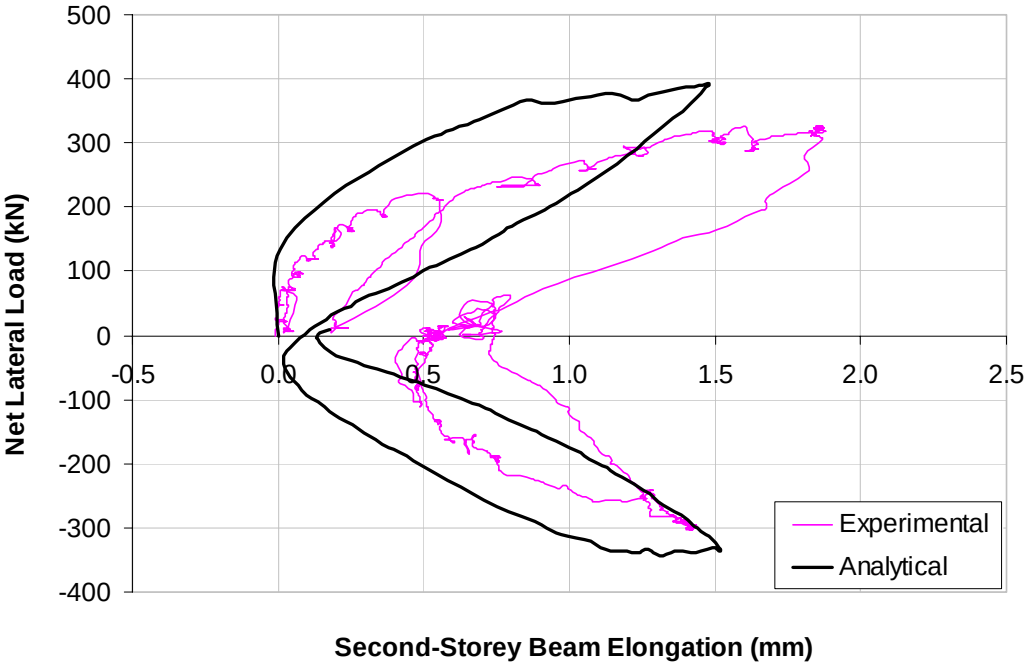

Figure 6.20 Lateral Load vs. Second-Storey Beam Elongation (Experimental vs. Analytical Results)

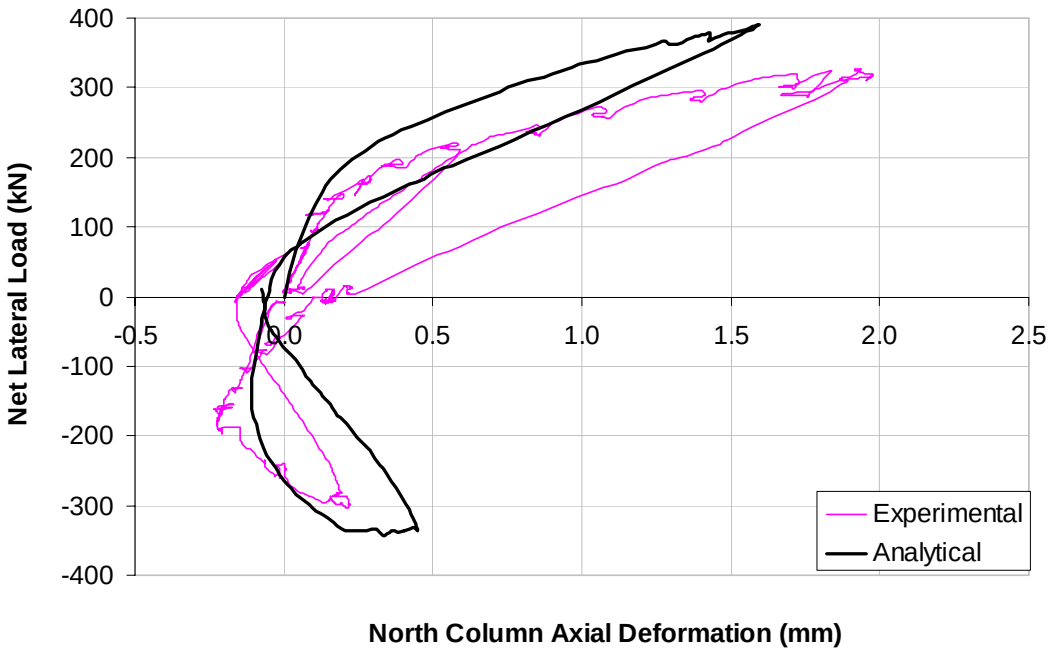

Figure 6.21 Lateral Load vs. North Column Net Axial Deformation (Experimental vs. Analytical Results)

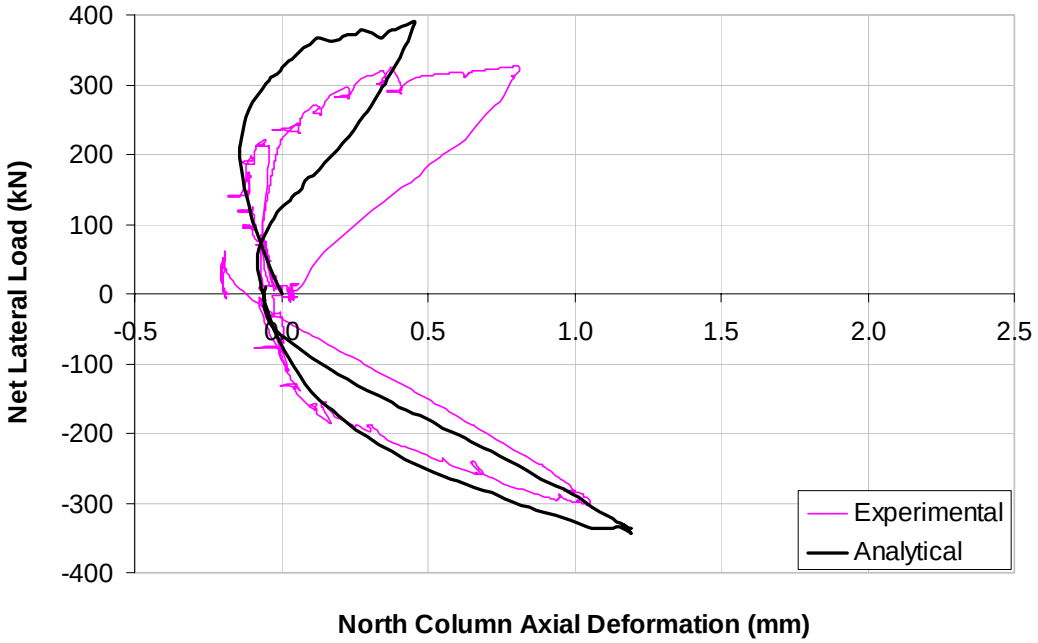

Figure 6.22 Lateral Load vs. South Column Net Axial Deformation (Experimental vs. Analytical Results)

Table 6.13 Beam Elongation and Residual Deformation

	First-storey beam		**Second-storey beam**	
	Forward Half-cycle	Reverse Half-cycle	Forward Half-cycle	Reverse Half-cycle
Peak Elongation (mm)				
Experimental	2.06	1.82	1.87	1.44
Analytical	1.99	1.72	1.48	1.50
% Difference	3.4%	3.9%	21%	5.3%
Residual Deformation (mm)				
Experimental	0.48	0.68	0.52	0.74
Analytical	0.17	0.13	0.02	0.13

Table 6.14 Column Deformation and Residual Deformation

	North Column		**South Column**	
	Forward Half-cycle	Reverse Half-cycle	Forward Half-cycle	Reverse Half-cycle
Peak Elongation (mm)				
Experimental	1.97	0.22	0.81	1.05
Analytical	1.59	0.45	0.46	1.19
% Difference	19%	51%	43%	12%
Residual Deformation (mm)				
Experimental	0.15	-0.15	0.03	-0.13
Analytical	-0.05	-0.07	-0.06	-0.06

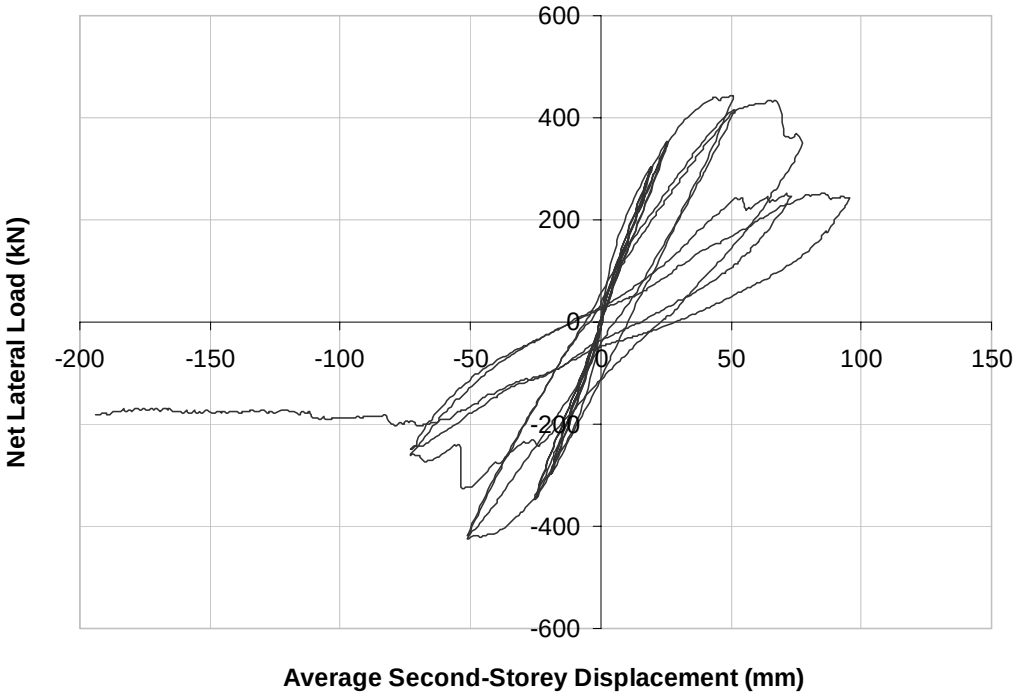

Figure 6.23 Lateral Load vs. Second-Storey Displacement of Model 3b (Phase B)

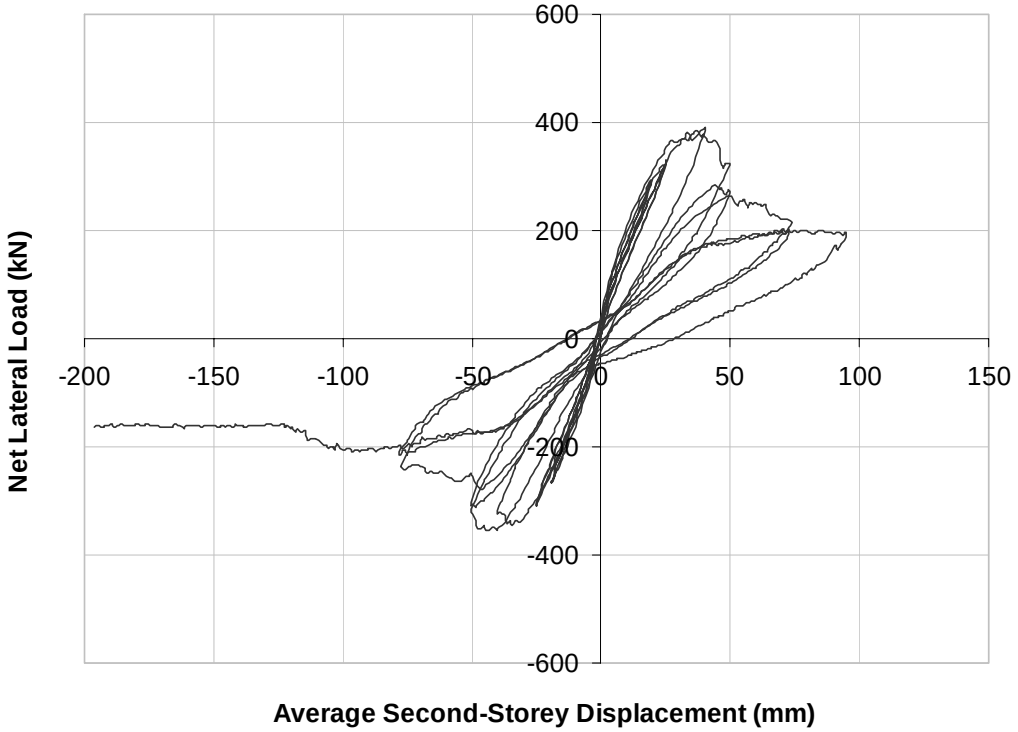

Figure 6.24 Lateral Load vs. Second-Storey Displacement of Model 3c (Phase B)

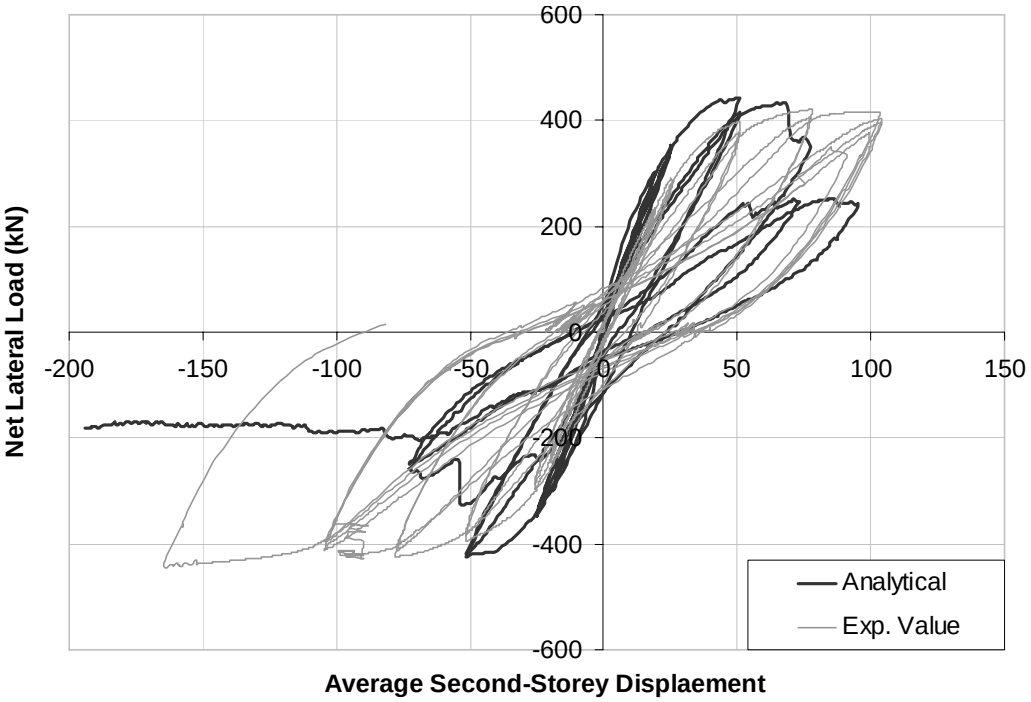

Figure 6.25 Lateral Load vs. Second-Storey Displacement: Model 3b vs. Experimental (Phase B)

Table 6.15 Lateral Displacement and Peak Lateral Loads (Model 3b, 3c, Experimental)

Load Cycle	Lat Displ. (mm)	Exp.	Model 3b	Model 3c	Model 3b / Exp. Load	Model 3c / Exp. Load
		Lateral Force (kN)				
1	+0.75 Δ_y	233	304	294	30%	26%
	-0.75 Δ_y	-247	-298	-268	21%	8%
2	+0.75 Δ_y	233	299	288	28%	23%
	-0.75 Δ_y	-241	-298	-265	23%	10%
3	+1.0 Δ_y	291	353	328	21%	13%
	-1.0 Δ_y	-298	-349	-310	17%	4%
4	+1.0 Δ_y	283	347	330	23%	17%
	-1.0 Δ_y	-289	-347	-309	20%	7%
5	+2.0 Δ_y	399	**443**	**384**	11%	-4%
	-2.0 Δ_y	-395	-424	-350	7%	-11%
6	+2.0 Δ_y	377	416	285	10%	-24%
	-2.0 Δ_y	-384	-418	-310	9%	-19%
7	+3.0 Δ_y	422	433	265	3%	-37%
	-3.0 Δ_y	-424	-323	-276	-24%	-35%
8	+3.0 Δ_y	406	247	196	-39%	-52%
	-3.0 Δ_y	-414	-249	-214	-40%	-48%
9	+4.0 Δ_y	417	253	197	-39%	-53%
	-4.0 Δ_y	-422	-203	-210	-52%	-50%
10	+4.0 Δ_y	403	-	-	-	-
	-4.0 Δ_y	-412	-	-	-	-
11	+4.0 Δ_y	397	-	-	-	-
	-4.0 Δ_y	-403	-	-	-	-
12	+4.0 Δ_y	377	-	-	-	-
	-4.0 Δ_y	-395	-	-	-	-
13	-6.6 Δ_y	**-444**	-	-	-	-

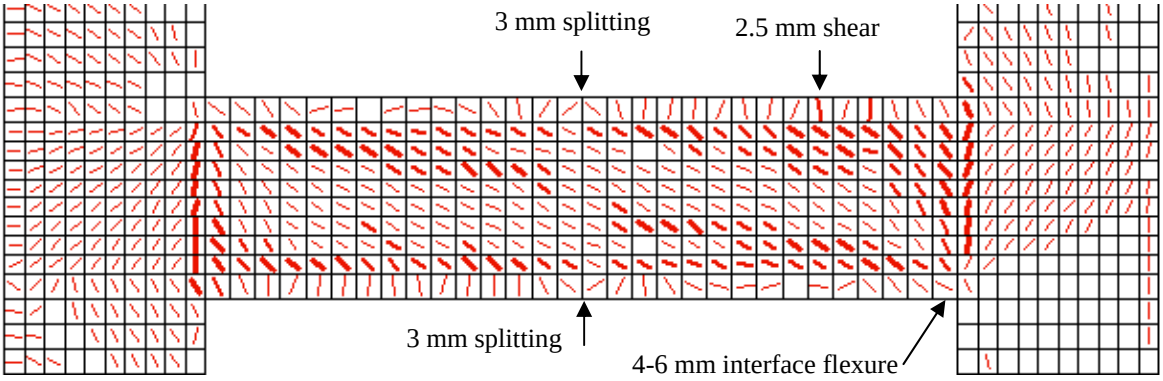

First-Storey Beam prior to Shear Failure at 53.6 mm (Analytical)

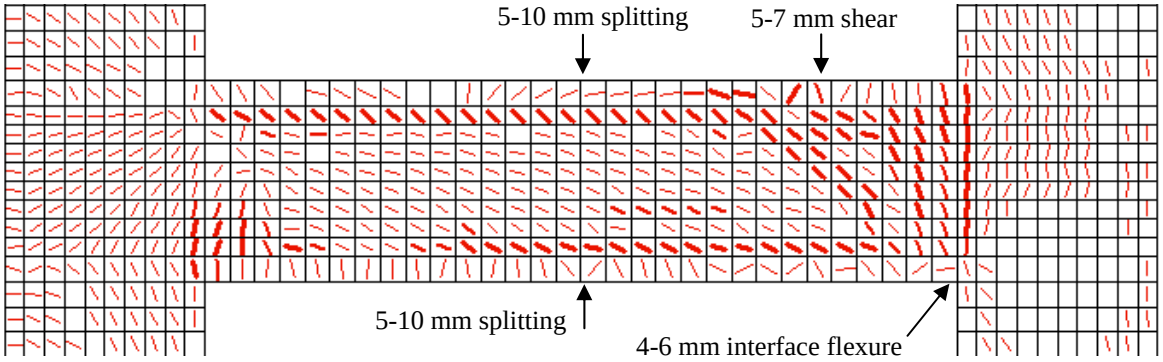

First-Storey Beam just after Shear Failure at 56.1 mm (Analytical)

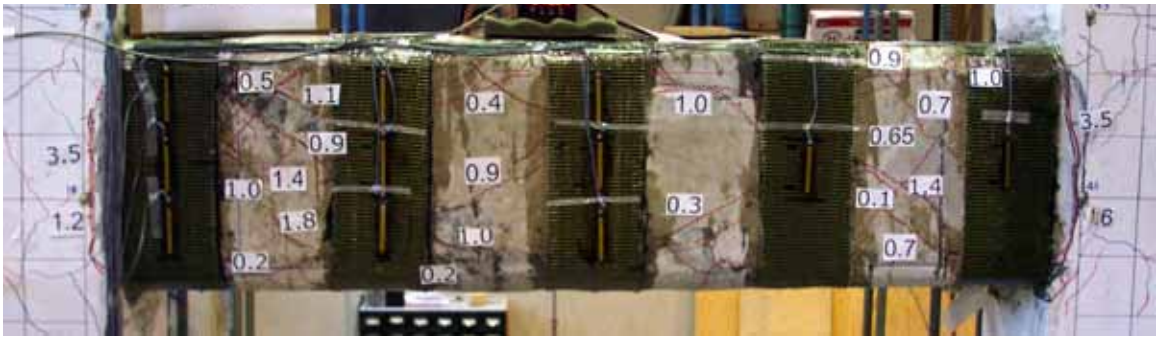

First-Storey Beam (Experimental)

Figure 6.26 Crack Pattern at Load Cycle 7: +3.0 Δ_y

6.5 DISCUSSION

Discussion of the analytical results was divided into two sections. Section 6.5.1 assesses the results of the parametric study with regards to the various analytical modelling parameters and modelling techniques. Section 6.5.2 compares the results of the analytical and experimental responses Section (Section 6.5.2.1), as well as results between Model 3b and 3c (Section 6.5.2.4). Conclusions for the parametric study and analytical-experimental comparison are given in Sections 6.5.1.6 and 6.5.2.5, respectively.

6.5.1 Parametric Study (Refer to the figures and tables in Section 6.4.1.)

6.5.1.1 Rectangular vs. Quadrilateral Element Type (1a, 1d)

For the shear critical frame case, modelling the concrete element with either a rectangular or quadrilateral element type produced very similar results. Secondary geometry effect does not appear to be a factor. Both models produced similar lateral load versus displacement plots. Since the rectangular element type was more rigorously tested in the past, numerically less demanding and more stable, it was preferred over the quadrilateral element type. Note: the secondary geometry effects were not tested for Phase B of testing where the displacement was four times greater.

6.5.1.2 Crack Width Check (1a, 1j, 1k, 1e, 1h, 1i)

For the shear critical cases (1a, 1j, 1k), options Agg./5 (equivalent to 2mm) and 5 mm crack width check had agreeable results, while the option with the crack width check omitted produced erroneous results. Model 1k, with the crack width check turned off, overestimated the peak load and produced an unrealistic failure mode: bulging of the beams. Models 1a and 1j exhibited shear failure at the first and second-storey beams, which was expected according to the specimen design. Model 1a had an abrupt shear failure, while 1j had a more subtle shear failure. Models 1a and 1j reached peak loads of 371 kN and 392 kN, respectively. A greater ductility and higher peak load for 1j was

expected since a higher crack width limit allowed for greater element rotation and a higher average compressive stress limit. Based on the analytical results, there was no clear preference between the Agg./5 and 5 mm crack width options. Both models produced logical and realistic results. From experience, the 5 mm width option usually produced more reliable results. For this reason, the 5 mm crack width option was preferred in shear-critical cases.

For the CFRP wrapped or flexural critical cases (1e, 1h, 1i), the failure modes between the three crack width options were very different from one another. All models exhibited yield plateaus to varying degrees. Flexural hinging was exhibited at both ends of both beams, and both column bases. While all three models had similar peak loads of around 465 kN, 1e (Agg./5) failed prematurely in interface shear at the north end of the upper beam, 1h (5mm) eventually failed in shear at the south end of the lower beam, and 1i (check omitted) had an erroneous local compression failure at the loading point. For flexural critical frame cases, the 5 mm crack width check produced the most accurate outcome.

6.5.1.3 Reinforcement Dowel Action (1j, 1b, 1c, 1h, 1f, 1g)

For the moment critical cases (1h, 1f, 1g), the Tassios Strength model (1f) produced an erroneous premature interface shear failure, while the analysis was unstable when dowel action was omitted (1g). The Tassios Crack Slip model (1h) was stable and produced a realistic shear failure in the lower beam. For the shear critical cases (1j, 1b, 1c), the Tassios Strength model (1b) changed the failure mode from shear to flexure. Modelling the specimen without dowel action (1c) produced similar results to the Tassios Crack Slip model (1a); however, 1c had a slightly lower peak load. Including the Tassios Crack Slip model produced the best result. For both the shear critical and moment critical frames, the default reinforcement dowel action (Tassios Crack Slip model) gave the most accurate results.

6.5.1.4 FRP Bond Modelling (1h, 2b, 2c)

The CFRP wrap was assumed perfectly bonded in Models 1h and 2b. For 1h, the perfect bond was inherent in the FE modelling when the CFRP wrap was attached directly to the same node as the concrete element. For 2b, the perfect bond option was selected when link elements were used. Both models gave very similar results in terms of failure load, failure mode, and load versus displacement response. In contrast, Model 2c failed prematurely even though this model was, in theory, the most accurate in terms of mimicking the true bond behaviour (the estimated bond stress-slip behaviour was implemented from Figure 6.6). When the results were examined closely for the models with link elements (2b, 2b), the CFRP strips behaved incorrectly. The output indicated a reasonable slip value; however, the stress level would be close to zero. In addition, the bond stress-strain values varied depending upon the size of the displacement increment used. Further study is required on the CFRP bond modelling. At this stage of the software development, modelling the CFRP wrap without link elements was the most reliable procedure.

6.5.1.5 Deactivated Elements (1j, 2a)

In theory, models with and without deactivated elements (assuming everything else was same) should produce identical results. Although the two load versus displacement plots do not lie perfectly on top of one another, their responses were very similar up to approximately 50 mm of displacement (peak load occurred at 40 mm). Numerical convergence variability caused the minor discrepancies between the two lateral load versus displacement responses. This finding concluded that where deactivated elements are used (3c of the analytical predictions), the results do not vary signifcantly from cases where deactivated elements are not used.

6.5.1.6 Conclusions and Limitations of Parametric Study

Several conclusions were drawn from the parametric study. Rectangular elements and quadrilateral elements produced similar results; however, rectangular elements were preferred over quadrilateral elements for the analytical advantages of the former type. The peak load and failure mode of the specimen was sensitive to the crack width check. A crack width check of 5 mm yielded the most accurate result for the flexural-critical case, while the default option Agg./5 (or 2 mm) and 5 mm both gave logical results for the shear-critical case. The latter option was preferred from experience. The Tassios Crack Slip reinforcement dowel action option was most accurate for both shear and flexural-critical cases. The most reliable method to model the bond between the CFRP and concrete surface was to assume a perfect bond without the use of link elements. The inclusion of link elements produced erroneous bond stress-strain results. When deactivated elements were included in the analysis, the post-peak response did not vary significantly. These findings served as a guideline to the modelling procedure and parameter selection in Section 6.3.2.

The majority of the observations were based mainly on the load versus displacement responses and the crack patterns as depicted from the post-processor program Augustus. A stringent examination of the material stresses and strains was beyond the scope of this thesis. Regarding the preference between rectangular and quadrilateral elements, the comparison was only performed for the shear-critical case. For the flexural-critical case, second-order geometry effect may be important. However, since there were many other parameters that were variable, the rectangular element type was chosen for all cases in order to reduce one variable and reduce the chances of analytical instability that may be caused by the quadrilateral element type.

6.5.2 Analytical versus Experimental Results

The analytical and experimental results were compared for both Phase A and Phase B of the experiment. Emphasis was placed on Phase A where comparisons were made on the lateral load versus second-storey displacement response, failure mode, crack pattern, beam elongation, and column deformation. In Phase B of the experiment, comparisons were made on the reverse cyclic hysteresis response, ductility, regions of failure, and shear contribution of the CFRP. Phase A and Phase B of the comparisons are presented in Sections 6.5.2.1 and 6.5.2.2, respectively.

6.5.2.1 Phase A: Analytical versus Experimental Results

In general, the FE program predicted a slightly greater peak load and higher initial stiffness than the experimental results. The damage modes were similar. Experimentally, the frame was damaged in the beams by a combined flexural-shear mechanism, whereas in the analysis, the beams were damaged in shear, flexure, and longitudinal splitting along the top and bottom reinforcement layers. When unloaded, the analytical model exhibited greater pinching (i.e. greater loss in the structural loading and unloading stiffness). This characteristic affected the shape of the lateral load versus displacement response, as well as the residual deformations in the beams and columns. The beam elongation and column deformation were predicted fairly accurately and the crack pattern was generally agreeable. The specific aspects of each behaviour are discussed below.

6.5.2.1.1 Lateral Load versus Second-Storey Displacement

During the forward half-cycle, the initial stiffness of the predicted frame was around 10-15% greater than the experimental response (Refer to Figure 6.14 and Figure 6.15). At around 30 mm of top storey displacement, the lateral load began to level off for both the analytical and experimental cases. The predicted peak forward load of 392 kN was 20% greater than the experimental peak load; however, both peak loads were reached

at around 40 mm of the top storey displacement. During the reverse half-cycle, the predicted stiffness was once again greater than the actual response. It was difficult to compare the analytical and experimental stiffness because this characteristic was dependant on several factors such as the failure mode and the residual deformation incurred during the forward half-cycle. At around -30 mm of top storey displacement, the frame's lateral load started to level off. The predicted reverse lateral peak load of 343 kN was 13% greater than the experimental peak load. Both peak loads occurred at around -40 mm.

When the frame was unloaded during both the forward and reverse half-cycles, the analytical model predicted greater pinching in the lateral load versus displacement curve. The greater pinching in the FE analysis may be attributed to the ability of the cracks to realign and close up in FE analysis, whereas in reality, the shear cracks were still prominent when unloaded. These large gaps produced a greater overall residual deformation in the frame. In addition, both ends of the upper and lower beams yielded in flexure during the experiment, but the analysis only predicted flexural yielding at the south end of the lower beam, and north end of the upper beam (see Section 6.5.2.1.2). The greater degree of flexural yielding in the experiment contributed to a higher residual displacement when unloaded.

6.5.2.1.2 Damage Mode

The frame was designed based on a weak beam-strong column system, specifically the beams were designed to be shear-critical. As such, the frame was expected to fail in shear in the beams. During the forward half-cycle, the lateral point load at the second-storey beam induced a higher compressive force in the south column than in the north column. A greater axial force attracted higher moments to the south column, and in turn, higher moments were generated at the south ends of the two beams. For the given loading conditions, shear was constant along the beam length. Taking into

account a greater moment at the south end of the beam, the constant shear force along the beam length, and the moment-shear interaction, the shear-critical region should be located at approximately d_v (310 mm) away from the north beam-column interface. When the failure mode was assessed by examining the stress in the steel reinforcement, more importance was given to the average stress over the stress at a crack location. The average stress gave a better indication of the overall member behavior rather than the local behaviour; however, the stress at a crack was also considered.

During the forward half-cycle, the analysis showed that the first-storey beam was critical in flexural-shear at the south end; the major shear cracks were located at approximate d_v away from the beam-column interface. Sequentially, the stirrups at the lower beam first yielded at both ends of the beams (Refer to Table 6.12). Towards failure, the south end of the beam exhibited greater shear yielding. Shortly after the stirrups have yielded, the flexural steel at the south end yielded. The flexural steel at the north end reached a maximum average stress of 390 MPa (87% of yield). The analysis indicated that the second-storey beam was also critical in shear, but at the north end. Once again, the stirrups yielded before the longitudinal flexural steel. Stirrups yielded at both ends of the beams, but the stirrups at the north end exhibiting greater yielding. The average stress of the flexural steel at the north end reached 425 MPa (95% of yield), while the south end reached 382 MPa (85% of yield). Although the average stress at the north end did not indicate flexural yielding, at a crack location, the analysis did indicate local flexural yielding. Note: a reinforcement response that considers local yielding in the steel hysteresis would improve the analytical response.

In the experiment during the forward half-cycle, both ends of the first and second-storey beams yielded in flexure before they yielded in shear (recall this sequence was switched in the analysis). In contrast to the analytical results where only one end of each beam yielded in flexure, the experimental results indicated that the flexural steel at both ends of both beams yielded at nearly at the same time. This observation concluded that the moments were fairly symmetric in the beams. Since the shear was constant along the

length of the beam, there was no favourable end that the flexural-shear damage would take place. Both the upper and lower beams exhibited flexural-shear damage at the south end.

During the reverse half-cycle, both experimental and analytical results indicated stirrup yielding. The flexural steel in the experiment reached around 95% of yield, while the average flexural steel in the analysis reached 80% of yield.

6.5.2.1.3 Crack Pattern

Generally, the analytical results gave good predictions of the sequence and locations of the first shear and flexural cracks (Refer to Figure 6.16 to Figure 6.18. and Table 6.12). To be consistent with the experimental procedure, the first cracking point was defined at the instance when the crack widths first reached at least 0.05 mm (what the human eye could detect). Experimentally, the sequence of first cracking was as follows: lower beam flexure, north column flexure, lower beam shear, south column flexure, and upper beam shear. All of these events occurred before 200 kN of lateral load and 12 mm of top storey displacement. Analytically, the sequence of first cracking was as follows: lower beam flexure, upper beam flexure, north column flexure, south column flexure, lower beam shear, and upper beam shear. At the latter cracking stage, the lateral load and top storey displacement reached 210 kN and 10 mm, respectively. For the initial stages of the forward half-cycle, both sets of crack observations were relatively compatible.

For the forward half-cycle at the upper beam at 32 mm, the shear cracks widths and inclination angles were agreeable for both the analytical and experimental cases. The angle of inclination was between 35 to 45 degrees from the horizontal, while the shear crack widths were 1 mm at most. While a minor longitudinal tension splitting crack (0.3 mm wide maximum) was observed experimentally at the bottom rebar layer, the analysis indicated large splitting cracks along the top and bottom rebar layers (1.4 mm wide). At 40 mm, the shear crack widths in both cases increased to around 2 mm wide.

Experimentally, the shear cracks were concentrated more at the north end, which was also the case in the analytical crack pattern. The higher cluster of shear cracks at the north end agreed with the greater degree of stirrup yielding at this region as previously mentioned in the Section 6.5.2.1.2. Intuitively, beam shear cracks should be more critical at the south end of the second-storey beam because greater moment should be exhibited here. Local effects from the lateral point load my have governed the critical damage location. While the experimental result showed that the bottom longitudinal splitting crack increased to 1.2 mm wide, the analysis predicted large longitudinal splitting cracks along both the top and bottom rebar layers that were 4 mm and 2.5 mm wide, respectively.

For the forward half-cycle at the lower beam at 32 mm, the experimental results showed a large 4 mm wide shear crack at the north end, while the largest shear crack at the south end was 1.6 mm wide. The analytical results indicated shear crack widths of 1.5 mm wide at the north end and 3.5 mm wide at the south end. The size of the shear cracks and angle of inclination were compatible for both cases, except the large shear crack location was switched. As stated in the Section 6.5.2.1.2, with regards to the flexural and stirrup steel stresses, the lower beam was shear-critical at the north end experimentally, while the south end was shear-critical analytically. Similar to the upper beam, a minor longitudinal tension splitting crack (0.7 mm wide at most) was observed experimentally at the bottom layer, but the analysis indicated very large splitting cracks along the top and bottom rebar layers (8+ mm wide at the top and 3+ mm wide at the bottom). At +40 mm, the shear crack width at the south end reached 9 mm wide in the experiment. The largest shear crack analytically was around 4.5 mm wide at the north end. The bottom longitudinal splitting crack in the test reached 5 mm wide, while splitting was not present in the top layer. In contrast, both the top and bottom longitudinal splitting cracks in the analysis were 8 mm wide.

For the reverse half-cycle, the crack pattern predicted by the analysis was generally poor. In the analysis, the longitudinal tension splitting was the predominant cracking pattern. The splitting cracks were present at the top and bottom rebar layers of

both beams, and were nearly 10 mm wide at all four locations. On the other hand, shear cracks were minor in comparison. With exception of the 3.5 mm wide shear crack located at the north end of the upper beam, all other shear cracks were less than 2 mm wide. In contrast, the experiment indicated large shear cracks that were 7 mm wide in the lower beam and 5 mm wide in the upper beam. These cracks were inclined in the opposite direction to those developed during the forward loading. At both beams, longitudinal tension splitting was present at the bottom rebar layer. These cracks were around 1.7 mm wide at the upper beam and 5 mm wide at the lower beam.

6.5.2.1.4 Beam Elongation

The analytical response of the beam elongation was compatible to the experiment result (Refer to Figure 6.19 and Figure 6.20, and Table 6.13). The initial elongation was negligible prior to first beam shear cracking. The elongation was caused initially by flexure cracks, but was governed by shear cracks at latter load stages. For the first-storey beam peak elongations, the analytical and experimental results were within 5% of each other. Considering that the first-storey beam deteriorated greatly after forward and reverse half-cycles, this second-order predication was excellent. As discussed previously, when unloaded, the cracks in the FE analysis realigned themselves while crack widths were still prominent in the experiment. As a result, the residual beam elongations were higher in the experiment. For the second-storey beam, the peak elongation prediction for the reverse half-cycle was good, but the prediction for the forward half-cycle was average. Because the second-storey beam exhibited greater lateral deflection, joint rotation, and column deformation, the beam elongation was more difficult to predict analytically and more prone to error when measured experimentally. Therefore, a greater discrepancy in the percentage difference was reasonable. In addition, the vertical and lateral loading plates may have affected the joint rotations; these plates were not modelled analytically.

6.5.2.1.5 Column Deformation

The analytical response of the column deformation was compatible with the experimental results (Refer to Figure 6.21 and Figure 6.22, and Table 6.14). Similar to the experiment, the column deformation in the analysis was governed by several key load stages. During the forward half-cycle, the north column stiffness decreased when the north and south columns were cracked in flexure at 134 kN. The stiffness was further reduced once the upper beam cracked in shear at 210 kN. During the reverse half-cycle, the north column initially contracted, but eventually elongated once major cracks were developed in the columns and beams. Analytically, the north column peak elongation was 1.59 mm or 19% lower than the experimental elongation during the forward loading, and 0.22 mm or 51% higher during the reverse loading. The latter error was greater because the north column contracted and elongated during the forward loading, which made the deformation more difficult to predict. In addition, the margin of error was smaller because a much lower net overall elongation was present.

The analytical prediction of the south column deformation was also governed by several key load stages. Like the experiment, during the forward half-cycle, the south column contracted initially until flexural cracks were developed in the south column. The deformation was stable until around 200 kN when it began to elongate (when notable cracks were developed in both columns and beam). During the reverse half-cycle, the south column elongated as expected, and at a similar rate to the experimental result. The analytical south column peak elongation was 43% lower than the experimental elongation during the forward loading, and 12% higher during the reverse loading.

The columns in the analysis exhibited lower residual deformation when unloaded. The explanation was similar to the beam residual elongation; the cracks in the FE analysis were realigned better when unloaded.

6.5.2.2 Phase B: Analytical versus Experimental Results

In general, neither Model 3b nor 3c produced acceptable results for Phase B of the experiment. Both models indicated premature shear failure rather than the ductile response observed during testing. Recall that Model 3b predicted the reverse cyclic response of Phase B with Phase A ignored, while 3c predicted the frame's response in accordance with the full testing regime. Between 3b and 3c, the former produced a slightly more accurate response. The problems associated with the premature shear failure were not resolved; more research is required on this topic. Moreover, the current version of Augustus 4.5.3 (VecTor2 post-processor) does not display the newly activated elements (i.e. in Phase B of Model 3c). Therefore, the crack pattern and crack widths of Model 3c were not assessable. No definite conclusions can be made regarding the analytical results; however, they are presented and compared with the experimental results. Section 6.5.2.3 compares the results of Model 3b to the experiment, and Section compares the results of Model 3b and 3c.

6.5.2.3 Model 3b versus Experimental Results

The analytical response of the frame predicted premature shear failure rather than the ductile response observed in the experiment (Figure 6.25). Similar to Phase A of the analytical response, the initial stiffness of the predicted frame in Phase B was higher than the actual stiffness. A larger initial analytical stiffness produced higher peak loads during the first six loading cycles (Table 6.15); however, the ultimate predicted load by the FE analysis was within 1 kN of the experimental peak load. The maximum analytical peak lateral load was reached at approximately +50 mm of top lateral displacement (+2.0 Δ_y), but this load was only sustained for an additional 4 mm. In contrast, the peak load was sustained for more than 100 mm in the experiment. At around +53.6 mm during the +3.0 Δ_y forward cycle of the analysis, the frame failed abruptly in shear at the first-storey beam. The lateral load-displacement response quickly deteriorated after this shear failure.

By the end of load cycle 7 ($\pm$3.0 Δ_y), both the upper and lower beams had failed in shear. By the $\pm$4.0 Δ_y cycles, the lateral load sustained was only half of the peak load reached previously. In addition, the analysis also produced higher forward than reverse loading resistance, while the experimental loads were similar for either direction of loading.

When the analytically predicted crack pattern was compared to the actual crack pattern, the following observations were made. Just prior to the initial shear failure that occurred at 53.6 mm, the first-storey beam crack pattern for the analytical and experimental results were comparable. Most notably, both patterns indicated large flexural interface cracking at both ends of the lower beam. The distribution and propagation lengths of the shear cracks for both cases were similar. The experiment indicated shear cracks as wide as 1.8 mm, while the predicted shear cracks were as wide as 2.5 mm. The main deficiency of the analysis was its prediction of 3 mm wide longitudinal tensile splitting cracks along both the top and bottom rebar layers. In contrast, longitudinal splitting cracks did not develop in the experiment. Recall that this error was also a problem in Phase A (Section 6.5.2.1.3). Apart from the erroneous longitudinal cracks, the predicted crack pattern was reasonable prior to shear failure. Shortly after 53.6 mm at 56.1 mm, the first-storey beam failed abruptly in shear at the south end. The experimental frame was fully intact throughout Phase B. The predicted crack pattern indicated shear cracks as wide as 7 mm. In addition, the longitudinal splitting cracks increased to 10 mm wide, but the flexural interface crack widths remained stable. The predicted shear failure was located immediately adjacent to the end CFRP wrap. The large shear crack initiated from the top of the beam, and extended downwards at 45 degrees to the fourth line of concrete element from the north beam-column interface (refer to Figure 6.26). CFRP truss bars present at the first three lines of rectangular elements prevented the shear crack from propagating any further. During the -3.0 Δ_y portion of load cycle 7, the north ends of both the upper and lower beams failed in shear in a similar manner to the first shear failure.

When the stresses in the steel and CFRP were examined, the following observations were made. Prior to the sudden shear failure, the analytical response seemed reasonable and agreed with the experiment. Like the experiment, the beams hinged in flexure, while the stirrups yielded. Initially, at $\pm 1.0\ \Delta_y$, the flexural steel at the lower beam yielded. The stirrup stress was around 450-500 MPa at this stage. By $\pm 2.0\ \Delta_y$, flexural steel at the upper beam and stirrups at both beams yielded. The flexural steel in the lower beam started to strain harden. Prior to the shear failure during $+3.0\ \Delta_y$, the stirrups remained at the yield stress, and the CFRP stresses at the upper and lower beams were around 250 MPa ($\sim 4000 \times 10^{-6}\ \varepsilon$) and 450 MPa ($\sim 6000 \times 10^{-6}\ \varepsilon$), respectively. The predicted CFRP strain was slightly higher, but was still within a reasonable range. After shear failure, the analysis was erroneous. One possible source of error is the implementation of perfectly bonded CFRP. Even though the wraps remained intact because of the fully wrapped configuration, the CFRP-concrete interface broke to various degrees.

6.5.2.4 Model 3b versus 3c

Model 3c predicted a peak load of 384 kN, which was 13% lower than 3b. As well, the peak load was sustained for a shorter displacement before shear failure in the first-storey beam occurred. A possible source of error may lie in the concrete hysteretic model. The most recently developed model, Palermo 2002 (with decay), terminated prematurely prior to the peak load. The hysteretic model chosen was the nonlinear with plastic offset. As indicated from the analytical results, the single cycle during Phase A had a significant impact on the response of Model 3c during Phase B. In addition, Table 6.15 indicates that for both 3c and 3c, the forward peak loads were greater than the reverse peak loads. Finally, Figure 6.11 in Section 6.4.1 indicates that for the monotonic response of Model 3b (i.e. monotonic response of 1h), this analysis without the cyclic

loading correlated very well with the experiment. The peak load was sustained until around 145 mm of top-storey lateral displacement.

6.5.2.5 Conclusions and Recommendations

For Phase A of testing, the analysis gave good predictions of the experiment. The damage mode for the experiment was flexural-shear, while the damage mode for the analysis was flexural-shear, with longitudinal tension splitting. The initial stiffness of the predicted frame was around 10-15% greater than the experimental response. A forward peak load of 392 kN was 20% greater than the experiment, while a reverse peak load of 343 kN was 13% greater than the experiment. The analysis indicated greater pinching in the lateral load versus displacement curve. The sequence and locations of the first shear and flexural cracks were compatible. The predicted crack pattern was good except for an overestimation of the longitudinal tension splitting crack width. The beam elongation and column deformations were predicted well, given that they are second order behaviour.

For Phase B of testing, neither Model 3b nor 3c produced acceptable results. Both models indicated premature shear failure rather than the ductile response observed during testing. Between 3b and 3c, the former gave a slightly more accurate response. Model 3b was compared with the experiment and the following conclusions were made. Model 3b predicted a peak lateral load of 443 kN, which was only 1 kN less than the experimental peak load; however this load was sustained for less than 5 mm before sudden shear failure occurred in the first-storey beam. Prior to the shear failure at 53.6 mm, the analysis indicated beam flexural hinging and stirrup yielding (same as the experiment). As well, with exception of the erroneous longitudinal splitting cracks, the predicated crack pattern was compatible with the observed crack pattern. However, after the shear failure, the cracking pattern was erroneous.

Further research is required in the reverse cyclic analytical response of the frame. Specifically, the CFRP bond modelling needs to be revised and the concrete hysteretic behaviour model needs to be refined.

Conclusions and Recommendations

7.1 EXPERIMENT

In Phase A of the experiment, the test frame was loaded laterally for one full cycle. The frame was damaged in combined flexural-shear in the first-storey beam during the forward half-cycle, and in shear during the reverse half-cycle. The peak lateral load achieved in the forward half-cycle was 327 kN; this load produced an shear force in the first-storey beam of approximately 202 kN. The concrete shear resistance was estimated to be 98.8 kN. The peak lateral load achieved in the reserve half-cycle was 304 kN.

In Phase B of the experiment, the CFRP repaired frame was subjected to a series of reserve load cycles that increased in increments of the yield displacement as determined in Phase A. The damage mode changed from shear to flexure after repair. The frame developed a full hinge failure mechanism at the four beam ends and two column bases. The peak lateral load increased by a factor of around 1.4 to 444 kN, the displacement ductility improved from approximately 4.0 to at least 6.8 or an increase by a factor of at least 1.7, the maximum displacement increased by a factor of at least 3.7, while the energy dissipation increased by a factor of at least 5.7. Recall that the frame had the capacity to deform further in Phase B such that the improved behavioural values reported were the lower limits. The CFRP stress along the length of the beam was variable, but the maximum stress was located at approximately d_v (310 mm) away from the beam-column interface. The stress distribution along the depth of the fully wrapped CFRP strips was inconclusive prior to debonding, but was evenly distributed after debonding. Partial debonding initiated at around a strain of 3000 $x10^{-6}$ in the CFRP wrap. When approximately 4000 $x10^{-6}$ was reached, more than 50% of the bonded area was broken. ISIS Canada recommended a strain limit of 4000 $x10^{-6}$ when calculating the shear contribution of CFRP for fully wrapped beams. This limit was found to be conservative since a majority of the wraps in the lower beam exceeded this limit while the beam

remained fully intact. In addition, the manual suggested a rupture strain limit of 5700 $x10^{-6}$. The maximum strain recorded in this experiment was 6430 $x10^{-6}$, while several other gauges recorded strains close to 6000 $x10^{-6}$. None of the wraps ruptured during the experiment, which suggested that the ISIS manual recommendation was once again conservative. The maximum shear force sustained in the beam was calculated conservatively to be 264 kN. Of this resistance, the CFRP contributed to approximately 71 kN, and the repaired concrete contributed roughly 90 kN.

For future experimental work, it is recommended that the flexural capacity of the beams be increased in-order to achieve shear rupture in the CFRP wrap. The flexural capacity of the beam was limited in this experiment by the largest rebar size that could fit in the beam section without encountering rebar hook or development length problems. The author suggests that anchorage at the joint region be achieved by welded end plates. This procedure not only allows for larger sized rebars to be used, but also simplifies the construction greatly.

7.2 VecTor2

The parametric study concluded that the analytical response of the frame was sensitive to several parameters: crack width check, reinforcement dowel action, and CFRP bond modeling. For the first two parameters, a 5 mm crack width check and the Tassios crack slip dowel action performed the best, while for the CFRP bond modeling, the use of link elements to model the CFRP-concrete bond interface gave erroneous stress-slip results.

When the test frame was analyzed according to the experimental testing sequence, the FE analysis gave good predictions of the frame's response during Phase A of the experiment, but yielded poor results during Phase B. In Phase A of the experiment, the analysis correlated well to the experiment in terms of the damage mode, crack pattern, beam elongation, and column deformation. The predicted stiffness and peak load were

10-20% higher, but were still within reason. In Phase B, the analyses indicated premature shear failure rather than the ductile response observed during testing. Prior to the sudden analytical shear failure at the first-storey beam, the analysis indicated beam flexural hinging and stirrup yielding (same as the experiment), and a peak load within 1 kN of the experiment. As well, with exception of the erroneous longitudinal splitting cracks, the predicated crack pattern was compatible with the observed crack pattern. After the premature shear failure, the hysteretic response, crack pattern, and material stresses were incorrect.

Further research is required in the reverse cyclic analysis of the frame. Specifically, the CFRP bond modeling needs to be revised and the concrete hysteretic behaviour model needs to be refined.

REFERENCES

ASTM C39/C39M-94
Standard Test Method for Compression Strength of Cylindrical Concrete Specimens.

ASTM C78-94
Standard Test Method for Flexural Strength of Concrete (Using Simple Beam with Third-Point Loading)

ASTM D3039/ D 3039 M
Standard Test Method for Tensile Properties of Polymer Matrix Composite Materials

Celebi, M., and Penzien, J. 1973. Experimental investigation into the seismic behavior of critical regions of reinforced concrete components as influenced by moment and shear. *UCB/EERC Report 73-04*, Earthquake Engineering Center, University of California, Berkeley.

Clough, R.W., and Gidwani, J. 1976. Reinforced concrete frame 2: testing and analytical correlation. *UCB/EERC Report 76-15*, Earthquake Engineering Center, University of California, Berkeley.

Collins, M.P., 1978. Towards a Rational Theory for RC Members in Shear. *ASCE*. 104, 4: 649-666.

Cranston, W.B. 1965. Tests on reinforced frames 1: Pinned portal frames. *Technical Report, Cement and Association, TRA/392*, London.

Cement Association of Canada (CAC), *Concrete Design Handbook (A23.3-04) Draft*, Ottawa: CAC, 2004.

ISIS Canada. 2001. *Design Manual #4: Strengthening Reinforced Concrete Structures with Externally-Bonded Fibre Reinforced Polymers.*

Ghobarah, A., Aziz, T.S., and Biddah, A. 1996. Seismic rehabilitation of reinforced concrete beam-column connections. *Earthquake Spectra*. 12, 4: 761-780.

Kachlakev, D., and McCurry, D.D. 2000. Behavior of full-scale reinforced concrete beams retrofitted for shear and flexural with FRP laminates. Composites Part B: Engineering. 31, 6-7: 445-452.

Lee, H.S., and Woo, S.W. 2002. Seismic performance of a 3-story RC frame in a low-seismicity region. *Engineering Structures*. 24: 719-734.

National Information Service for Earthquake Engineering (NISEE). Modified Dec. 9, 1997. Earthquake Damage Distribution. Internet. <http://nisee.berkeley.edu/kobe/damage.html>. Accessed Nov. 14, 2005.

Ozden, S., Akguzel, U., and Ozturan, T. 2003. Seismic retrofit of R/C frames with CFRP overlays. *Earth and Environmental Science*, NATO Science Series. 29.

Paulay, T., and Priestley, M. J. N. *Seismic Design of Reinforced Concrete and Mansonry Buildings*, New York: Wiley, 1992.

Sato, Y. and Vecchio, F.J. 2003. Tension Stiffening and Crack Formation in RC Members with FRP Sheets. *ASCE Journal of Structural Engineering*. 129, 6: 717-724.

Sheikh, S.A., DeRose, D., and Mardukhi, J. 2002. Retrofitting of concrete structures for shear and flexure with fibre-reinforced polymers. *ACI Structural Journal*. 99-S47: 451-459.

Sheikh, S.A., and Khoury, S. S. 1993. Confinement of Concrete Columns with Stubs. *ACI Structural Journal*. 90-S44: 414-431.

Vecchio, F.J., and Balopoulou, S. 1990. On the nonlinear behaviour of reinforced concrete frames. *Canadian Journal of Civil Engineering*. 17, 5: 698-704.

Vecchio, F.J., and Collins, M.P. 1986. The Modified Compression Field Theory for Reinforced Concrete Elements Subjected to Shear. *ACI Journal*. 83, 2: 219-231.

Vecchio, F.J., and Emara, M.B. 1992. Shear deformations in reinforced concrete frames. *ACI Structural Journal*. 89, 1: 46-56.

Wong, P. S., and Vecchio, F.J. 2002. *VecTor2 and Formworks User's Manual.*

Wong, R. S. Y. 2001. *Towards Modelling of Reinforced Concrete Members with Externally-Bonded Fibre Reinforced Polymer (FRP) Composites.* M.A.Sc. Thesis, University of Toronto, Canada.

APPENDIX A

Material Stress-Strain Curves
Material Datasheet (from Manufacturer)
AutoCAD Drawings

A.1 Material Stress Strain Curves

A.2 Material Datasheet (from Manufacturer)

A.3 AutoCAD Drawings

A.1 Material Stress Strain Curves

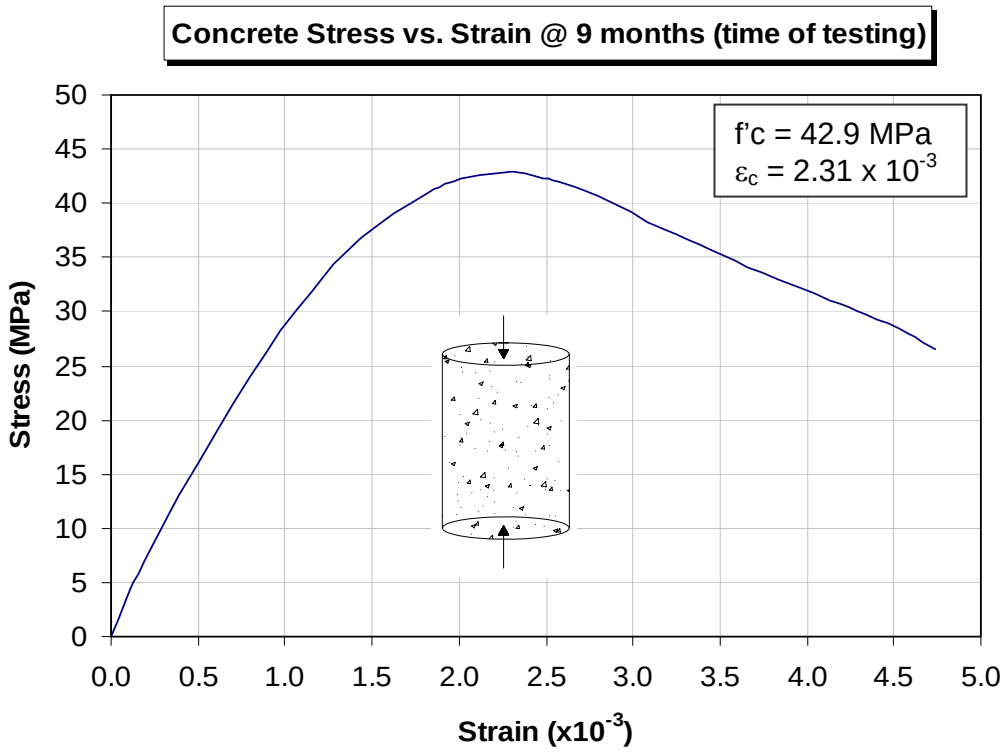

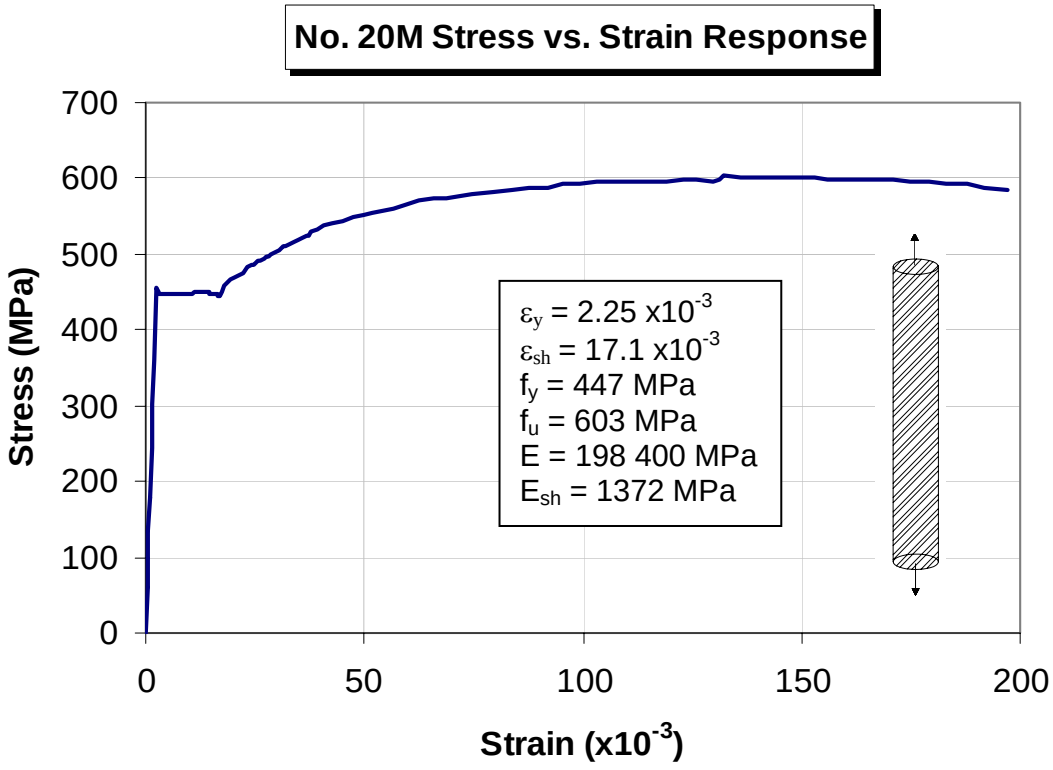

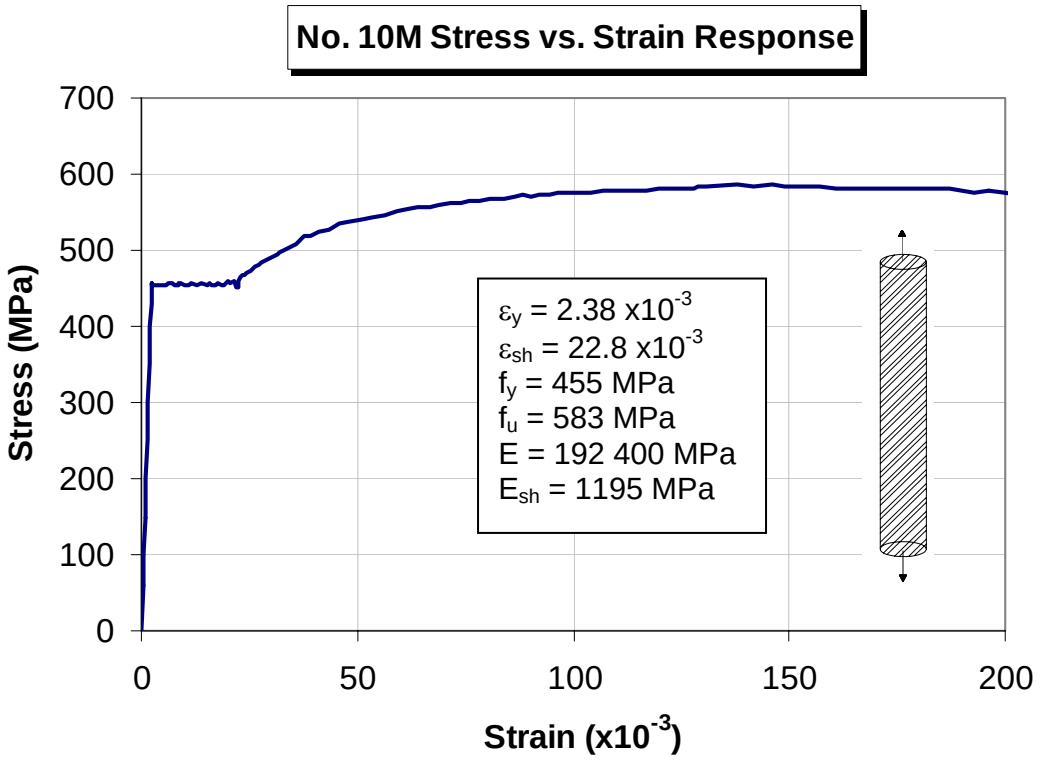
No. 10M Stress vs. Strain Response
Stress (MPa)
Strain (x10-3)
0
100
200
300
400
500
600
700
0
50
100
150
200
εy = 2.38 x10-3
εsh = 22.8 x10-3
fy = 455 MPa
fu = 583 MPa
E = 192 400 MPa
Esh = 1195 MPa

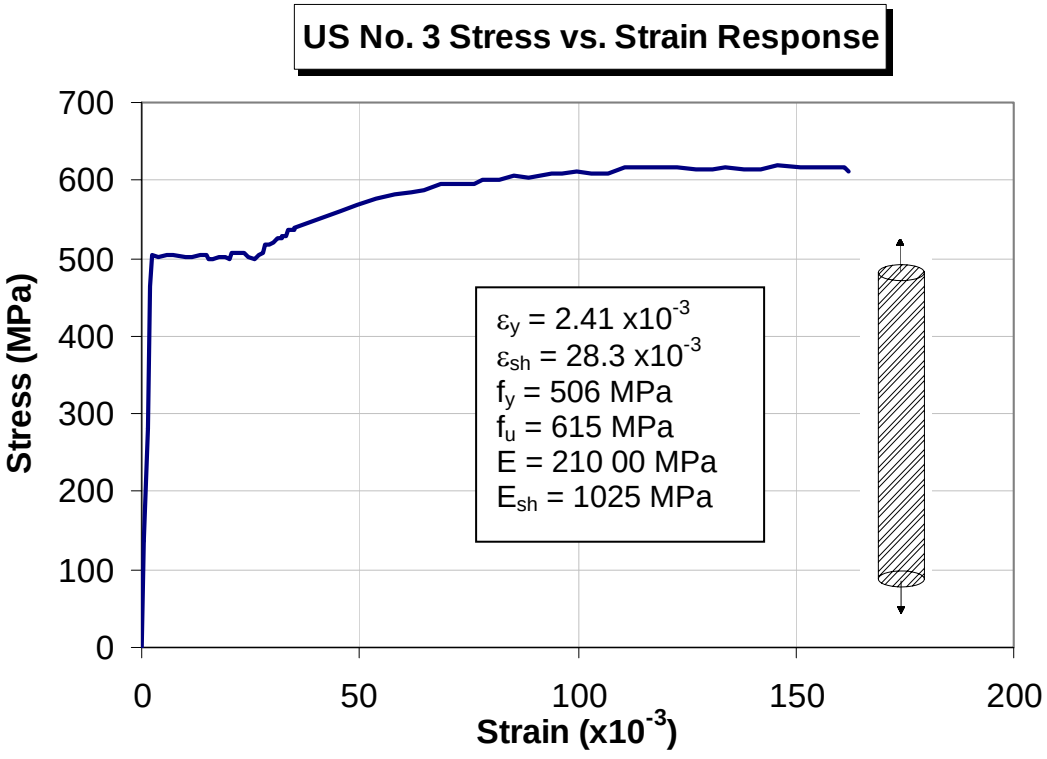
US No. 3 Stress vs. Strain Response
Stress (MPa)
Strain (x10-3)
0
100
200
300
400
500
600
700
0
50
100
150
200
εy = 2.41 x10-3
εsh = 28.3 x10-3
fy = 506 MPa
fu = 615 MPa
E = 210 00 MPa
Esh = 1025 MPa

degussa.

Construction Chemicals

SP20 SPRAY MORTAR

Fiber-reinforced wet spray mortar for below- and above-grade applications

PRODUCT DATA

3 03370 **Specially Placed Concrete**

Description

SP20 Spray Mortar is a shrinkage-compensated, microsilica-enhanced wet spray mortar. This versatile structural-repair mortar can be spray applied or hand troweled on horizontal, vertical, and overhead surfaces. A version of SP20 is available containing a corrosion inhibitor.

Yield

0.48 ft^3 per 55 lb bag
(0.014 m^3 per 25 kg)

Packaging

55 lb (25 kg) bags

Shelf Life

1 year when properly stored

Storage

Store and transport in unopened containers at 60 to 80° F (16 to 27° C) in clean, dry conditions. High temperatures or humidity will reduce the shelf life.

Features / Benefits

Features	Benefits
• ANSI / NSF 61 approved	Suitable for use with potable water
• Shrinkage compensated	Reduces drying shrinkage; reduces stress at bond lines
• Low permeability	Protection against chloride attack
• Can be sprayed for increased productivity	Minimizes labor costs
• Resists hydrogen sulfide attack to pH 3.0	Suitable below grade

Where to Use

APPLICATION

- Structural concrete repairs
- Bridges
- Parking structures
- Tunnel linings
- Seawalls
- Water and wastewater structures

LOCATION

- Vertical, overhead, and horizontal
- Interior or exterior
- Above and below grade

SUBSTRATE

- Concrete

How to Apply

Surface Preparation

1. The substrate must be structurally sound and fully cured. Remove all unsound concrete and roughen the surface to a minimum 1/4" (6 mm) profile.
2. Saw cut the perimeter of the area being patched to a minimum depth of 3/8" (10 mm).
3. Remove all laitance, oil, grease, curing compounds, and other contaminants that could prevent adequate bond.
4. The concrete substrate should be in a saturated surface-dry (SSD) condition (without standing water) just before application.

REINFORCING STEEL

1. Remove all oxidation and scale from the exposed reinforcing steel in accordance with ICRI Technical Guideline No. 03730 "Guide for Surface Preparation for the Repair of Deteriorated Concrete Resulting from Reinforcing Steel Corrosion."
2. For additional protection from future corrosion, coat the prepared reinforcing steel with Zincrich Rebar Primer or install Corr-Stops® CM.

ThoRoc®

Technical Data

Composition

SP20 Spray Mortar is a proprietary blend of cement, graded aggregate, shrinkage-compensating agents, microsilica, additives, and fibers.

Test Data

The following results were obtained with a water / powder ratio of 3.7 qts/55 lb bag (3.5 L/25 kg) bag at 73° F (22° C).

PROPERTY	RESULTS	TEST METHODS
Fresh wet density, lb/ft³ (kg/m³)	130 (2,082)	ASTM C 138
Set time, hrs		ASTM C 191
Initial	2	
Final	2.5	
Working time, min	45	
Drying shrinkage, % (µstrain)		ASTM C 157
1" (25 mm) prisms	0.04 (400)	
1" (25 mm) prisms (modified[1])	0.09 (900)	
Coefficient of thermal expansion, in/in/° F (in/in/° C)	6.0×10^{-6} (10.8×10^{-6})	CRD C 39
Modulus of elasticity, psi (GPa)	4.7×10^{6} (32)	ASTM C 469
Freeze/thaw resistance, % RDM, at 300 cycles	99	ASTM C 666
Slant shear bond strength, psi (MPa)		ASTM C 882 (modified[2])
7 days	1,750 (3.8)	
8 days	2,250 (4.5)	
Splitting tensile strength, psi (MPa)		ASTM C 496
7 days	550 (3.8)	
28 days	650 (4.5)	
Flexural strength, psi (MPa)		ASTM C 348
7 days	1,000 (7)	
28 days	1,500 (10)	
Compressive strength, psi (MPa), 2" (51 mm) cubes		ASTM C 109
1 day	3,000 (21)	
7 days	6,000 (41)	
28 days	7,500 (52)	
Compressive strength, psi (MPa), 3 by 6" (76 by 152 mm) cylinders		ASTM C 39
7 days	6,500 (45)	
28 days	8,000 (55)	

[1]According to ICRI Guideline No. 03733 (air cured).

[2]No bonding agent used; mortar scrubbed into substrate

All application and performance values are typical for the material, but may vary with test methods, conditions, and configurations.

Mixing

1. Add 3.7 qts (3.5 L) of clean water to the mixing container for each bag of SP20 Spray Mortar.

2. Add the powder to the water while continuously mixing with a slow speed (400 – 600 rpm) drill and paddle in a mortar mixer or similar forced-action mixer.

3. Mix for 3 – 5 minutes until fully homogeneous.

4. Additional water may be added up to a maximum water content of 4 qts (3.8 L) per bag of SP20 Spray Mortar.

Application

1. The minimum recommended application thickness is 3/8" (10 mm). Recommended maximum wet spray build is 4" (102 mm) per lift on vertical applications and 1" (25 mm) on overhead applications.

2. The recommended maximum hand troweling build is 3" (76 mm) per lift on vertical surfaces and 1" (25 mm) on overhead surfaces.

3. Build up thicker sections in layers, although these can sometimes be applied in a single application, depending upon the actual configuration of the repair area and the volume of exposed reinforcing steel.

4. For horizontal applications, the product can be extended with 3/8" (10 mm) clean, non-ASR-reactive aggregate. For repairs 2 – 4" (51 – 102 mm) in thickness, add up to 15 lbs (7 kg) of aggregate per bag of SP20 Spray Mortar. For repairs greater than 4" (102 mm) in thickness, add 15 – 30 lbs (7 – 14 kg) of aggregate per bag.

HAND APPLICATION

1. Using a stiff-bristled brush, scrub a coat of SP20 Spray Mortar into the SSD substrate.

2. While the scrub coat is still damp, apply the mixed mortar onto the prepared substrate by gloved hand or trowel, ensuring proper consolidation of the mortar and compaction around reinforcing steel.

3. If the mortar sags during application, remove it and reapply at a reduced thickness.

4. When multiple lifts are required, rake the surface before final set to provide a roughened profile for the subsequent lift.

SPRAY APPLICATION

1. Wet spray equipment must be capable of mixing, pumping, and applying SP20 Spray Mortar within the recommended water addition range. Spray velocity must be sufficient to ensure proper compaction.

2. Depending on the actual configuration of the repair area and the volume of exposed reinforcing steel, applications can be made in either single or multiple lifts. The practical thickness attainable on site will depend on the orientation of the substrate, the skill of the nozzle operator, and the shape of the repair area. If multiple lifts are used, lightly rake the surface after initial set and before applying subsequent lifts.

Curing

1. Proper curing is extremely important. For peak performance of the repair, cure immediately after finishing in accordance with good concrete practices (refer to ACI 308).

2. An ASTM C 309-compliant water-based curing compound may be used in place of moist curing. Apply the curing compound when the surface cannot be marred by the application process.

Clean Up

Clean hands and skin immediately with soap and water. Clean tools and equipment immediately after use with water. Cured material must be removed mechanically.

For Best Performance

- Minimum ambient, surface, and material temperature is 40° F (4° C) and rising.
- Do not mix longer than 5 minutes.
- Minimum application thickness is 3/8" (10 mm).
- Do not use aggregate extensions for vertical and overhead repairs.
- Make certain the most current versions of product data sheet and MSDS are being used; call Customer Service (1-800-433-9517) to verify the most current version.
- Proper application is the responsibility of the user. Field visits by Degussa personnel are for the purpose of making technical recommendations only and not for supervising or providing quality control on the jobsite.

Health and Safety

SP20 SPRAY MORTAR

Caution

SP20 Spray Mortar contains crystalline silica, Portland cement, calcium oxide, and amorphous silica.

Risks

Product is alkaline on contact with water and may cause injury to skin or eyes. Ingestion or inhalation of dust may cause irritation. Contains free respirable quartz, which has been listed as a suspected human carcinogen by NTP and IARC. Repeated or prolonged overexposure to free respirable quartz may cause silicosis or other serious and delayed lung injury.

Precautions

KEEP OUT OF THE REACH OF CHILDREN. Prevent contact with skin and eyes. Prevent inhalation of dust. DO NOT take internally. Use only with adequate ventilation. Use impervious gloves, eye protection and if the TLV is exceeded or used in a poorly ventilated area, use NIOSH/MSHA approved respiratory protection in accordance with applicable federal, state and local regulations.

First Aid

In case of eye contact, flush thoroughly with water for at least 15 minutes. SEEK IMMEDIATE MEDICAL ATTENTION. In case of skin contact, wash affected areas with soap and water. If irritation persists, SEEK MEDICAL ATTENTION. Remove and wash contaminated clothing. If inhalation causes physical discomfort, remove to fresh air. If discomfort persists or any breathing difficulty occurs or if swallowed, SEEK IMMEDIATE MEDICAL ATTENTION.

Refer to Material Safety Data Sheet (MSDS) for further information.

Proposition 65

This product contains material listed by the state of California as known to cause cancer, birth defects, or other reproductive harm.

VOC Content

0 lbs/gal or 0 g/L

For medical emergencies only, call ChemTrec (1-800-424-9300).

Degussa Building Systems

889 Valley Park Drive
Shakopee, MN, 55379

www.degussabuildingsystems.com

Customer Service 800-433-9517
Technical Service 800-243-6739

For professional use only. Not for sale to or use by the general public.

Form No. 1019008 9/03 (Replaces 1/02)
Printed on recycled paper including 10% post-consumer fiber.

A.3 AutoCAD Drawings

(all dimensions in mm)

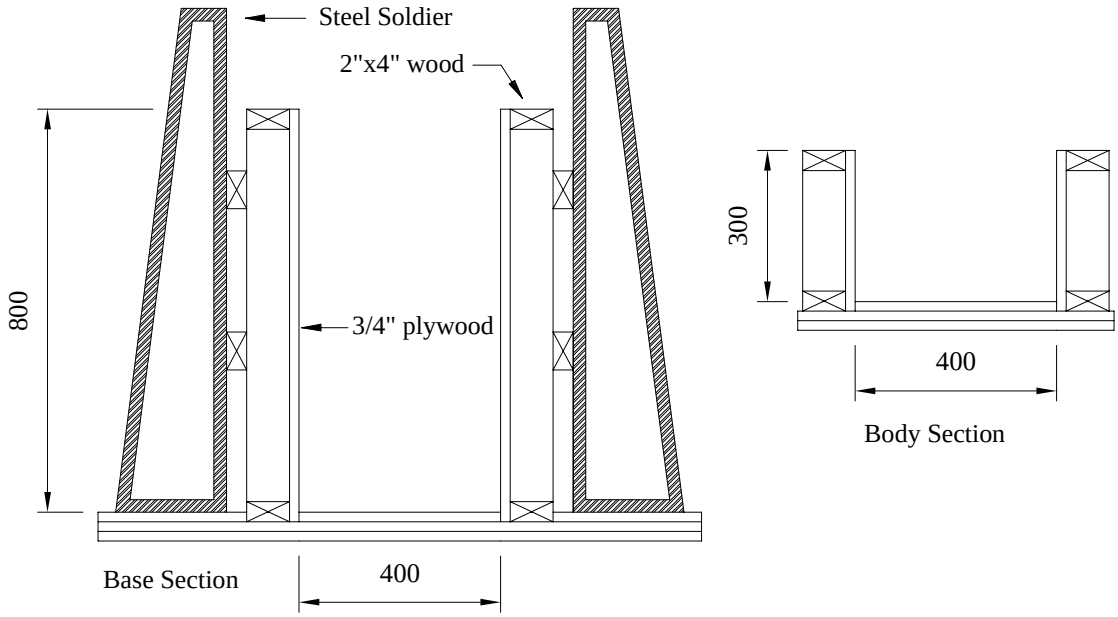

Base and Body Formwork Cross Sections

Step 1: Cut 2"x4" wood to length

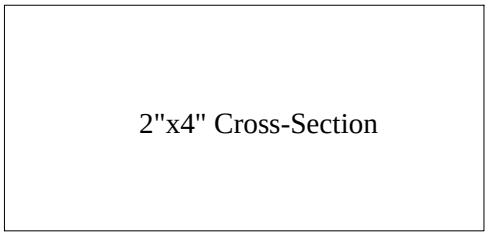

Step 2: Taper sides

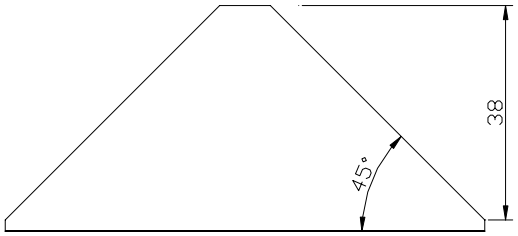

Step 3: Rout sides and cut in half

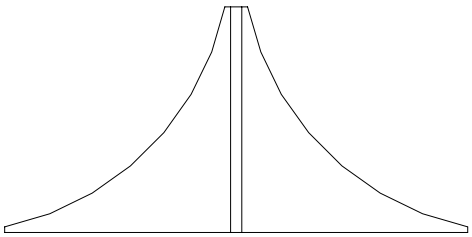

Final Section

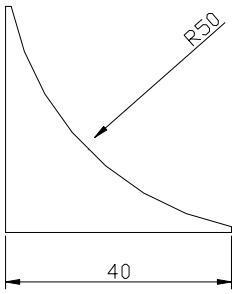

Corner Moulding Details and Fabrication Sequence

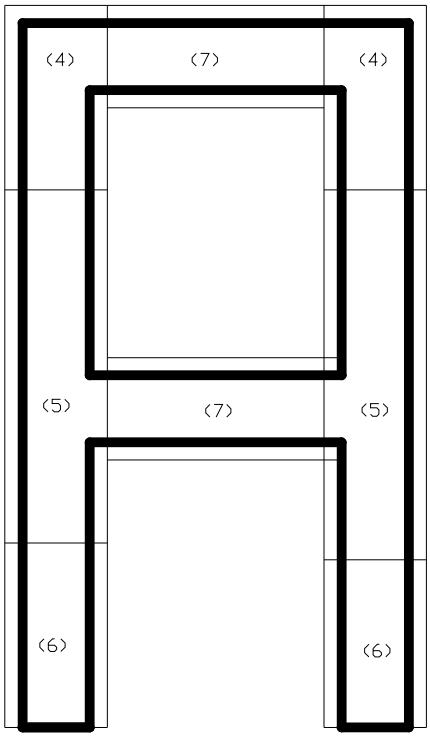

Body: 1st plywood layer

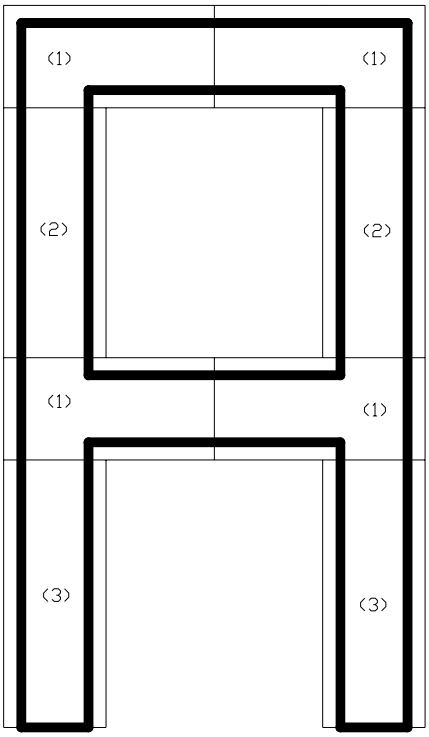

Body: 2nd plywood layer

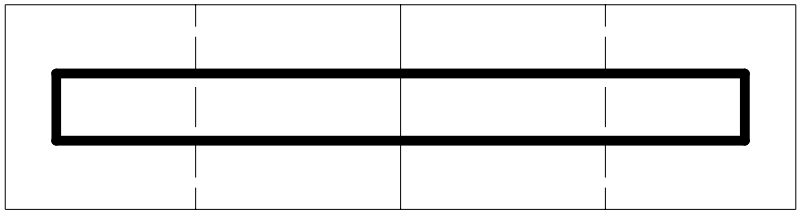

Base: 1st & 2nd plywood layers

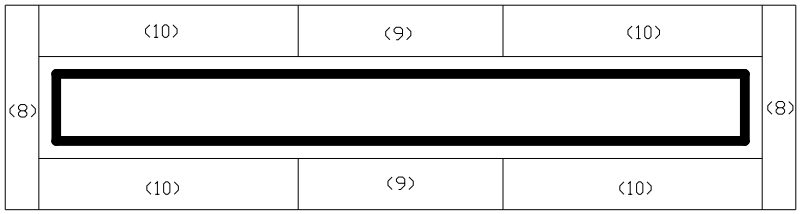

Base: Bearing plywood panels

Formwork Design: Bottom Plywood Panels

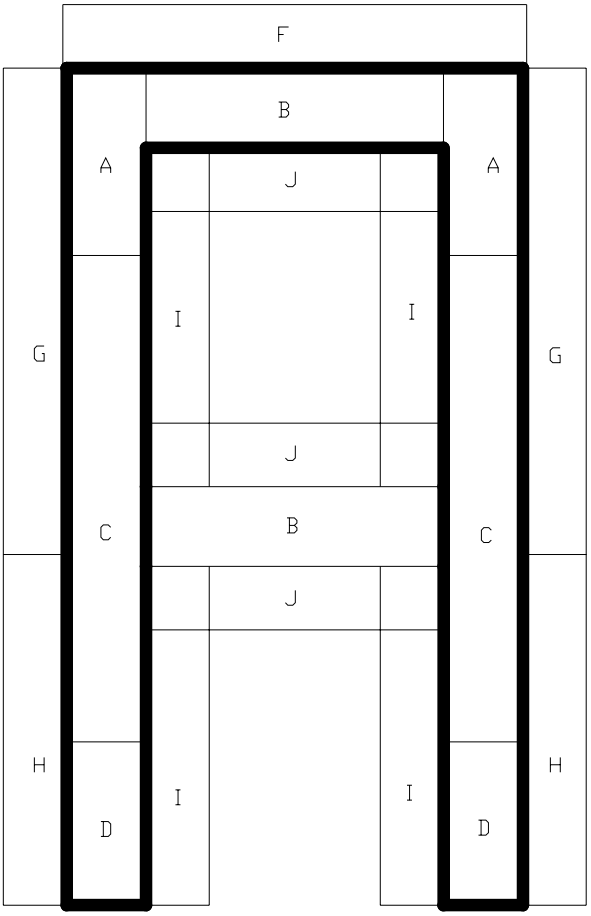

A 400 x 940
B 400 x 1500
C 400 x 2440
D 400 x 820
E 400 X 2050
F 319 X 2338
G 319 X 2440
H 319 X 1760
I 319 X 1700
J 319 X 1462
K 819 X 2440
L 819 X 1660
M 819 X 1500
N 819 X 900
O 438 X 819
Q 400 X 250
R 400 X 269

(1) 610 x 1255
(2) 610 x 1490
(3) 610 x 1595
(4) 610 x 1100
(5) 610 x 2105
(6) 610 x 1100
(7) 610 x 1290
(8) 200 x 1220
(9) 305 x 1220
(10) 305 x 1544

Body: Side plywood planels

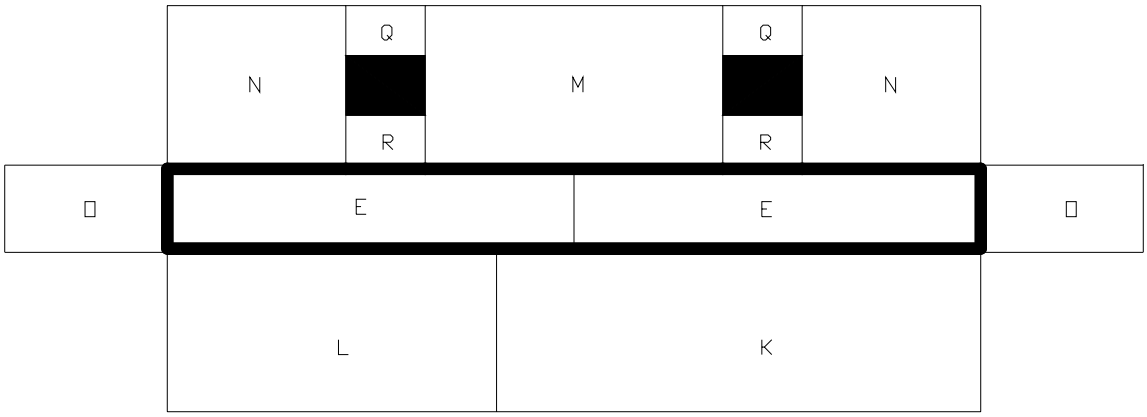

Base: Side plywood panels

Formwork Design: Side Plywood Panels

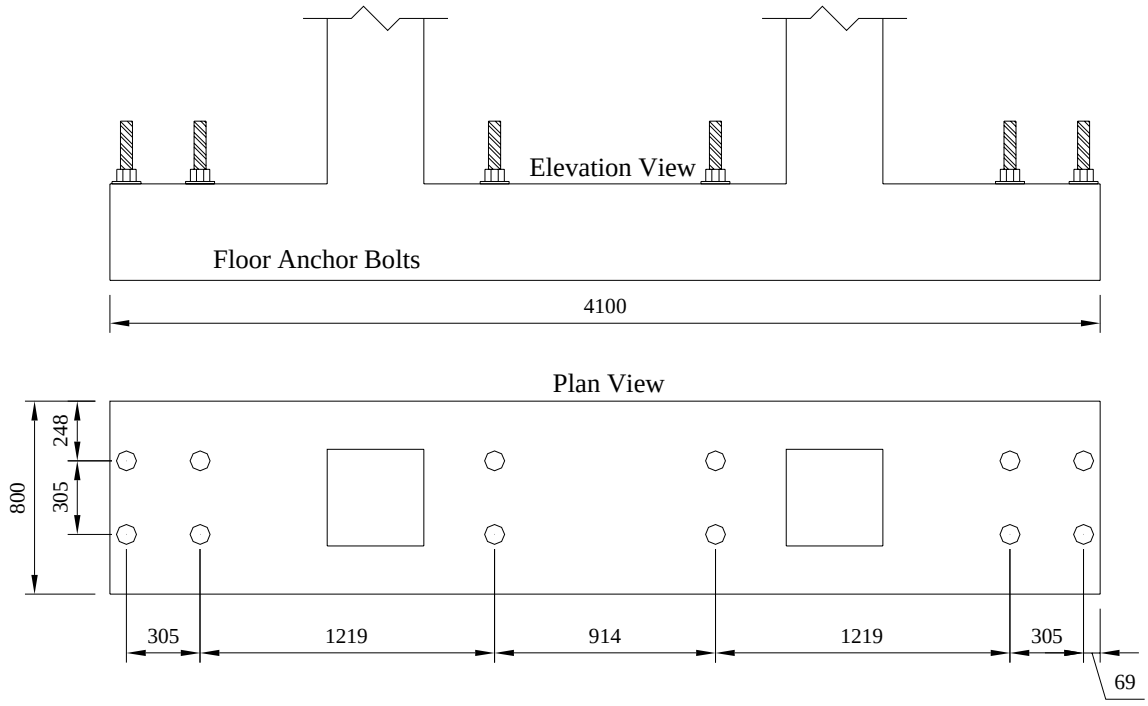

Base Floor Anchor Bolt Layout

APPENDIX B

Sample Calculations

B.1 Estimation of V_f in the First-Storey Beam (Phase A) using CSA A23.3 2004

B.2 Estimation of V_f and V_c in the First-Storey Beam (Phase B)

B.3 Estimation of V_r of the Repaired Beam

B.4 Derivation of Zurich Surface Strain

B.5 Derivation of Displacement Ductility

B.1 Estimation of V_f in the First-Storey Beam (Phase A) using CSA A23.3 2004:

From the experimentation results (at load stage 14):

- Net lateral load: 325 kN.
- Average second-storey displacement: 32.3 mm.
- Shear failure crack width in first-storey beam: 4.0 mm orthogonal (around 7 mm vertically).
- Shear failure crack angle: between 32-35 degrees from the horizontal.
- Flexural steel just yielded (from strain gauges placed 30 mm from the beam-column interface).
- First-storey beam elongation: ~2.0 mm

Stress in the beam stirrup:
If the beam stirrup's initial gauge length was assumed to be approximately 300 mm (around d_v), the strain in the steel at peak load was:

$$\frac{7}{300} = 23.3\times10^{-3}\varepsilon$$

Since ε_{sh} = 28.3 x 10^{-3} for US No.3 bar (beam stirrup), on average, the stress in the stirrup did not reach strain hardening. For the purpose of calculating V_s, the stirrup was assumed the yield stress of 506 MPa. Although the stirrup gauge length was assumed to be 300 mm, a lower estimate of this length may indicate that stirrup strain hardening took place. Even so, the steel stress would not increase significantly during the early stages of strain hardening.

Induced compressive force in first-storey beam:
It was difficult to assess the actual compression force in the first-storey beam. From, a lower beam elongation of approximately 2.0 mm, an induced compression force from the column restraint was calculated and used as a lower limit for the beam axial compression.

$$P = \frac{12EI}{h^3}\Delta;$$

where $E \approx 3320\sqrt{f'c} + 6900 = 28,700\,MPa$

$I = 0.5bh^3/12 = 0.8\times10^{-9}\,mm^4$

$(50\%\,\text{cracked column inertia was assumed})$

$\Delta = \text{half of } 2.0\,mm \text{ for each column} = 1.0\,mm$

$h = \text{first storey column height} = 1900\,mm$

$P = 40\,kN$ (compression)

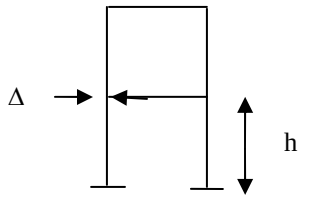

Column: 300x400 mm

Vf is critical at d_v away from the beam-column interface:

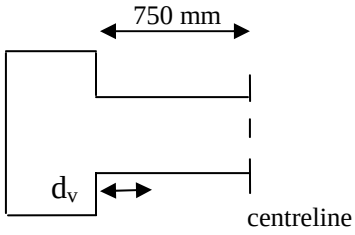

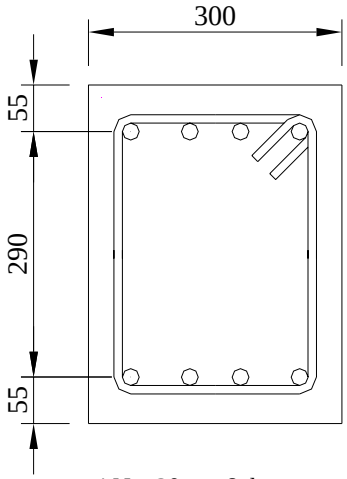

4 No. 20 top & bottom
No. 3 stirrups @ 300 mm
f'c = 42.9 MPa
fy = 447 MPa, fv = 506 MPa

$b_w = 300\,mm$

$d = 400 - \text{rebar depth} = 345\,mm$

$dv = 0.9d = 310\,mm$

$M/V = 440\,mm$

$$\varepsilon_{x1} = \frac{M_f / d_v + V_f + 0.5N_f}{2E_s A_s} = \frac{1.415Vf + Vf + 0.5(-40,000)}{2(198,400)(1200)}$$

$$V_r = V_c + V_s$$

$$V_c = \beta\sqrt{f'c}\, b_w d_v = \frac{0.4}{1+1500\varepsilon_x}\sqrt{43}\times 300\times 310$$

$$V_s = \frac{A_v f_y}{s} d_v \cot\theta = \frac{142\times 506}{300}\times 310\times\cot(29+7000\varepsilon_x)$$

Solving...

$$\varepsilon_{x1} = 0.99\times 10^{-3},\quad \theta = 35.9°,\quad V_c = 98.8\,kN,\quad V_s = 102.7\,kN,\quad V_r = V_f = 202\,kN$$

$$F_{lt} = \frac{M_f}{d_v} + 0.5N_f + (V_f - 0.5V_s)\cot\theta = 473\,kN < F_y = 536\,kN$$

Results were calculated for other assumed beam axial forces:

Axial Force (kN)	**V_r (kN)**	**V_c (kN)**	**V_s (kN)**	**θ (degrees)**	**F_{lt} (kN)**
0	199	97.1	102	36.1	485
-40	202	98.8	103	35.9	473
-100	205	101	104	35.6	455

The CSA A23.3 2004 prediction of the beam shear capacity beam was a good estimation for several reasons which correlated the predicted results to the experimental observations:

1. The predicted shear failure angle θ of 35.9 degrees was agreeable with the measured failure angle (between 32-35 degrees).
2. Using the yield stress of the stirrup as measured from the experiment, the beam shear strength was calculated. The correlated longitudinal flexural reinforcement at d_v away from the beam-column interface was 88% of yield. At 30 mm away from the interface where the moment was slightly greater, strain gauges indicated that flexural yielding took place. Therefore, the stresses in the longitudinal steel between the predicted and experimental result were reasonable.
3. The shear capacity and failure angle of the beam was not sensitive to the magnitude of the axial compression force present.

B.2 Estimation of V_f and V_c in the First-Storey Beam (Phase B):

From the experimental results (at $\pm$ 3.0Δ_y):

- The first-storey beams hinged at both ends.
- The plastic hinge region was estimated to be at least 150 mm long and extended from the beam-column interface. This region was evident by the 3.5 mm wide flexural crack at the interface, and 2 mm wide flexural crack immediately adjacent to the 150 mm wide CFRP wrap.
- To calculate the shear force V_f, the moment at 150 mm away from the beam-column interface was conservatively assumed to reach M_y. The flexural steel had yielded, but it was uncertain if strain hardening was reached.
- The stirrups have yielded, but did not reach strain hardening. The CFRP wrap provided vertical confinement that prevented further increase in the stirrup strain.
- The axial force in the beam was estimated to be around -40 kN (from B.1).

At $\pm$ 3.0Δ_y, the Moment and Shear Force Diagrams were estimated to be:

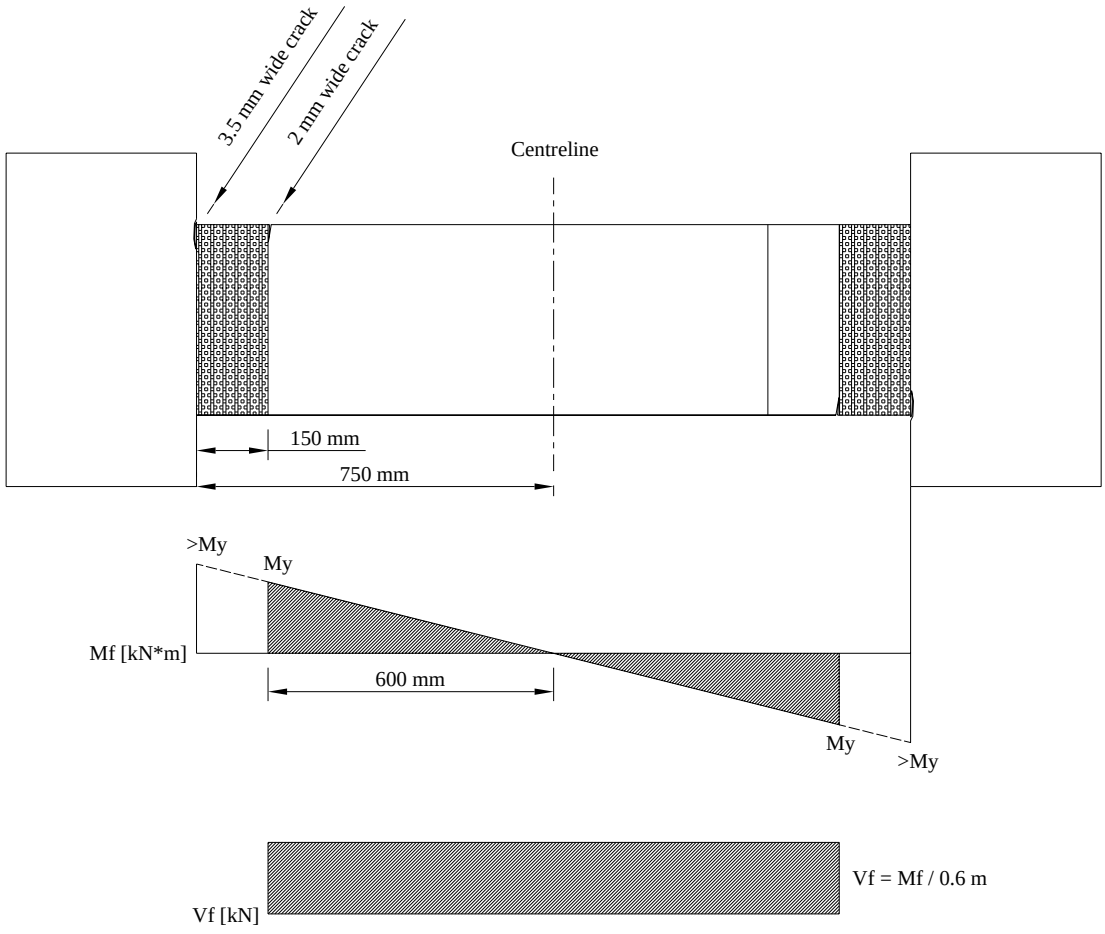

Calculation of M_y and V_f:

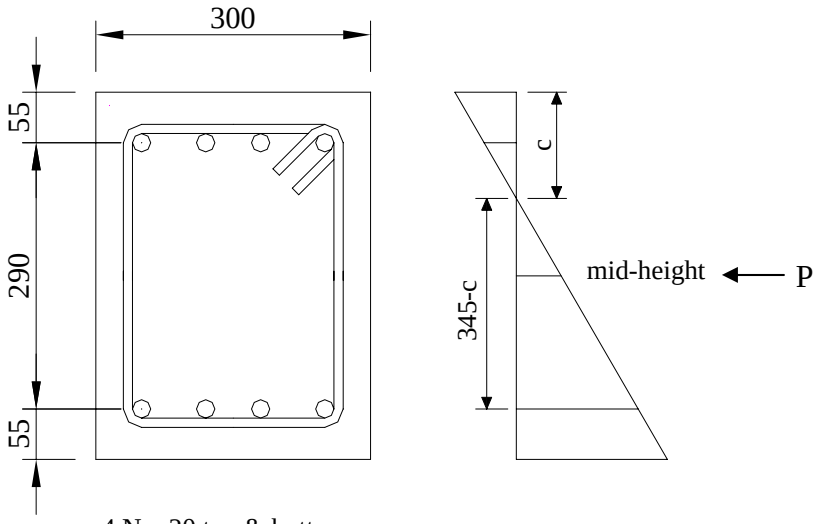

4 No. 20 top & bottom
No. 3 stirrups @ 300 mm
f'c = 42.9 MPa
fy = 447 MPa, fv = 506 MPa

Using the Parabolic concrete stress-strain relationship (Collins and Mitchell, 1991):

let $a = \dfrac{\varepsilon_t}{\varepsilon'_c}$

$\beta_1 = \dfrac{4-a}{6-2a}, \quad \alpha_1\beta_1 = a - \dfrac{a^2}{3}$

$Cc = \alpha \bullet (f'c) \bullet (\beta_1 c) \bullet (b_w)$

$T_s = \varepsilon_s \bullet E_s \bullet A_s$

$C_s = \varepsilon'_s \bullet E_s \bullet A_s$

$P = 40\,kN\,(\text{compression})$

solving...

$\varepsilon_s = \varepsilon_y = 0.00225\,(\text{steel has yielded at } M_y)$

$c = 96.1\,mm$

$\varepsilon'_s = 0.00070$

$T_s = 536\,kN$

$C_s = 408\,kN$

$C_c = 88.7\,kN$

$M_y = 158.6\,kN \bullet m$

$V_f = M_y / 0.60m = 264\,kN$

Calculation of V_{frp}:

The CFRP strains were recorded along the depth of each wrap. The strain indicated by the middle strain gauge was assumed to be effective for 90 mm (the total tributary length between the top and middle gauges and between the middle and bottom gauges). Since the CFRP was fully wrapped, the strains indicated by the top and bottom gauges were assumed to be effective up to the beam edges. The strain indicated by the top strain gauge was assumed to be effective for 140 mm (the tributary length between the top and middle gauges to the top of the beam). Similarly, the strain gauge at the bottom was effective for 140 mm.

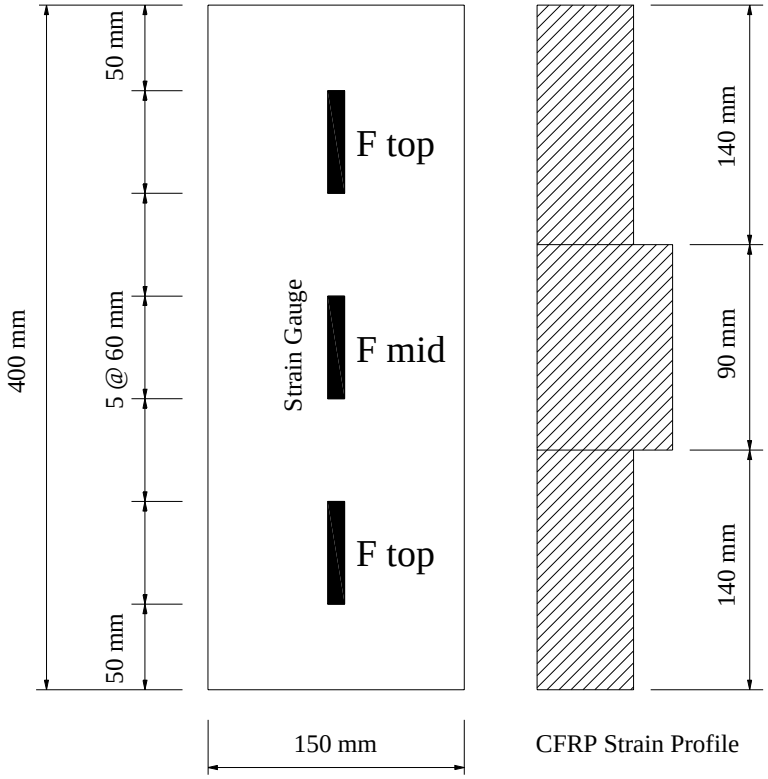

Tyfo® SCH41S (CFRP composite):

f't = 876 MPa
E = 72.4 GPa
ε_{ult} = 12.1 x10^{-3}
Thickness = 1.0 mm on each side of the beam.

The wraps were 150 mm wide (fully wrapped) and spaced apart at 187.5 mm.

Strain gauges were 60 mm long and positioned as illustrated.

$$V_{frp} = E_{frp} \bullet \varepsilon_{frpe} \bullet \frac{A_{frp}}{S_{frp}} \bullet h$$

$$= 72{,}400 \times (140\varepsilon_{top} + 90\varepsilon_{mid} + 140\varepsilon_{bot}) \times \frac{150}{150+187.5} \times 2 \quad \text{for the interior wrap}$$

$$\text{or} \quad = 72{,}400 \times (140\varepsilon_{top} + 90\varepsilon_{mid} + 140\varepsilon_{bot}) \times \frac{150}{150+93.4} \times 2 \quad \text{for the end wrap}$$

For several CFRP wraps, the mid depth strains were recorded on both sides. The average strains ($\varepsilon_{mid\ avg}$) were taken for these cases and used in the V_{frp} equation above. Where only the mid depth strain was recorded, this strain was assumed effective for the entire depth of the beam (400 mm). Where either only the top or bottom strain was recorded, this strain was assumed to effective for the top and bottom of the beam (280 mm).

Calculation of peak V_c:

$$V_c = V_f - V_s - V_{frp}$$
$$V_f = 264\,kN$$
$$V_s = 103\,kN \ (\text{assuming as similar failure angle to Phase A})$$

Using the average shear stress of the CFRP wraps along the lower beam at $\pm 3.0\ \Delta y$:

$$V_{frp} = 83.4\,kN \ (\sigma_{frp} \simeq 200\,MPa)$$
$$V_c = 264 - 103 - 83.4 = 77.6\,kN$$

The peak V_c calculated was 77.6 kN in Phase B, which was lower than the V_c obtained in Phase A at failure (98.8 kN). Since the beams were structurally repaired after Phase A, and because the frame in Phase B was moment critical, it was reasonable to assume that the concrete shear capacity was not reached in Phase B.

It is important to illustrate the sensitivity of the plastic hinge region on the V_f calculation. The moment at 150 mm away from the beam-column interface was assumed conservatively to reach M_y. If the plastic hinge region extended to 400 mm away from the interface (height of beam) and M_y was assumed here:

$$V_f = \frac{M_y}{0.750 - 0.400} = 453\,kN$$
$$V_c = V_f - V_s - V_{frp} = 453 - 103 - 83.4 = 267\,kN$$

A concrete shear strength of 77.6 kN is the lower end estimate, while 267 kN as the upper end is probably excessive (even with the increased concrete shear strength from the CFRP confinement).

B.3 Estimation of V_r of the Repaired Beam:

$V_r = V_c + V_s + V_{frp}$

$V_s = 103\,kN$ (assuming a similar failure angle to Phase A)

$$V_{frp}\ \text{(at rupture)} = E_{frp} \bullet \varepsilon_{frp\,ult} \bullet \frac{A_{frp}}{s} \bullet h$$

$$= 72{,}400 \times 12.1 \times 10^{-3} \times \frac{150 \times 2}{150 + 187.5} \times 400$$

$$= 311\,kN$$

$V_c = 0\,kN$ (conservative assumption)

$Vr = 103 + 311 = 414\,kN$

The moment capacity required to obtain this shear resistance in the beam at the beam-column interface is approximately:

$M_r = 0.75 V_r = 310\,kN \bullet m$

or an increase in the moment capacity of:

$M_r - M_y = 152\,kN \bullet m$

B.4 Derivation of Zurich Surface Strain:

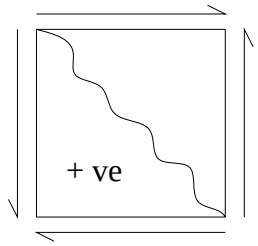

Sign Convention

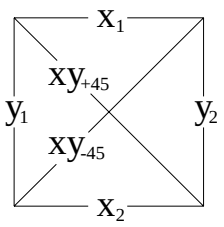

Initial State

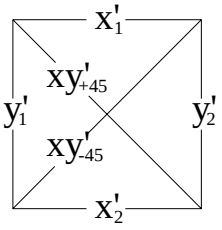

Final State

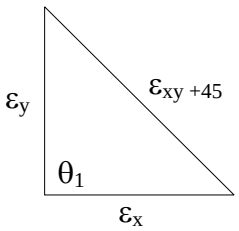

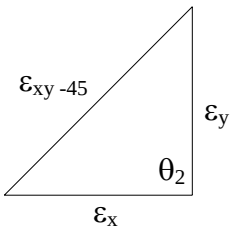

Horizontal Strain :

$$\varepsilon'_x = \frac{\frac{X'_1 + X'_2}{2} - \frac{X_1 + X_2}{2}}{\frac{X_1 + X_2}{2}}$$

Vertical Strain:

$$\varepsilon'_y = \frac{\frac{Y'_1 + Y'_2}{2} - \frac{Y_1 + Y_2}{2}}{\frac{Y_1 + Y_2}{2}}$$

Shear Strain:

$$\gamma = \frac{(\theta'_2 - \theta_2) - (\theta'_1 - \theta_1)}{2};$$

$$\theta_1 = \mathbf{cos}^{-1}\left(\frac{\varepsilon_x^{\,2} + \varepsilon_y^{\,2} - \varepsilon_{xy+45}^{\,2}}{2\varepsilon_x\varepsilon_y}\right);$$

$$\varepsilon_{xy+45} = \frac{XY'_{45} - XY_{45}}{XY_{45}}$$

θ_2 is calculated in a similar manner.

B.5 Derivation of Displacement Ductility:

(with reference to Sheikh and Khoury, 1993)

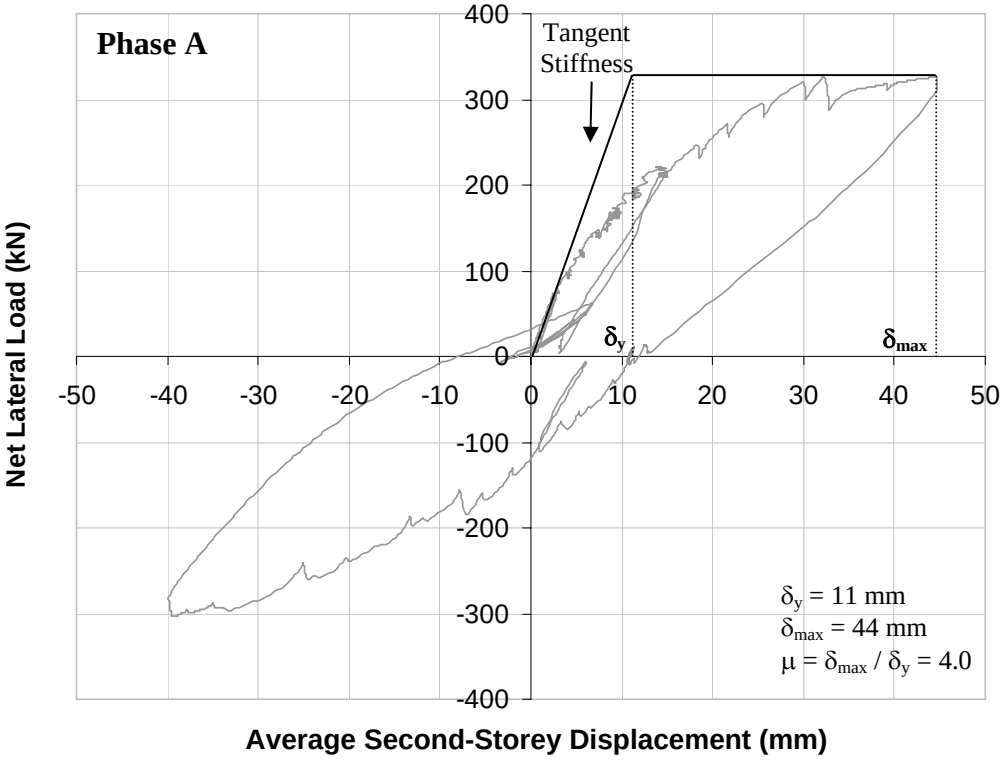

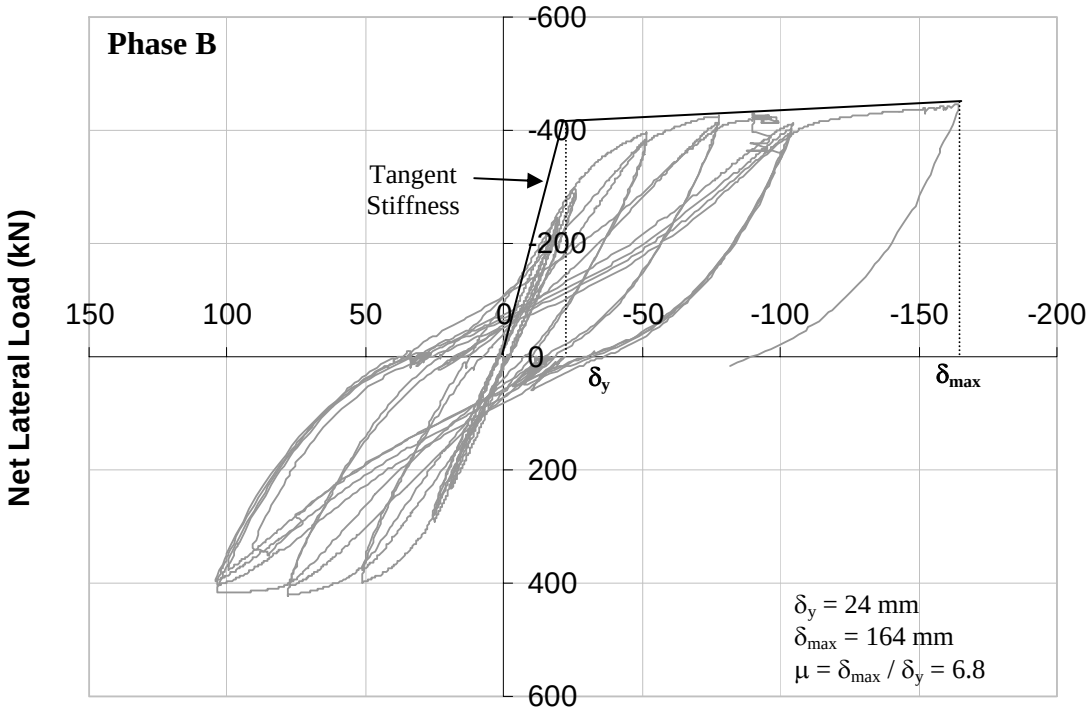

Lateral Load vs. Second-Storey Displacement: Phase A and B

The displacement ductility is defined as the ratio of the ultimate displacement divided by the yield placement:

$$\mu = \frac{\delta_{\max}}{\delta_y}$$

The methodology used to determine the displacement ductility followed the steps suggested by Sheikh and Khoury (1993). For each lateral load-displacement curve, an elastoplastic or bilinear curve was superimposed onto the original curve. The bilinear curve was constructed by two lines: the tagent stiffness and yield plateau. The yield plateau was a line drawn tangent to the lateral load-displacement curve near the peak load.

The yield displacement (δ_y) was determined as the intersection point of the tangent stiffness and yield plateau lines. The maximum displacement (δ_{max}) in this experiment corresponded to the peak lateral displacement. The displacement ductilities reported were estimates since failure did not take place. The ductility determined for Phase A should be close to the actual value since the beam was heavily damaged in shear. The ductility calculated for Phase B was inclusive since the frame was expected to displace further while maintaining the peak load; the reported values were the lower limits.

The displacement ductility was also calculated with reference to Paulay and Priestley (1992) as shown in the figure below. Instead of a tangent initial stiffness, a secant stiffness was constructed according to the location where the first sectional yielding took place.

Derivation of Displacement Ductility:
(with reference to Paulay and Priestley, 1992)

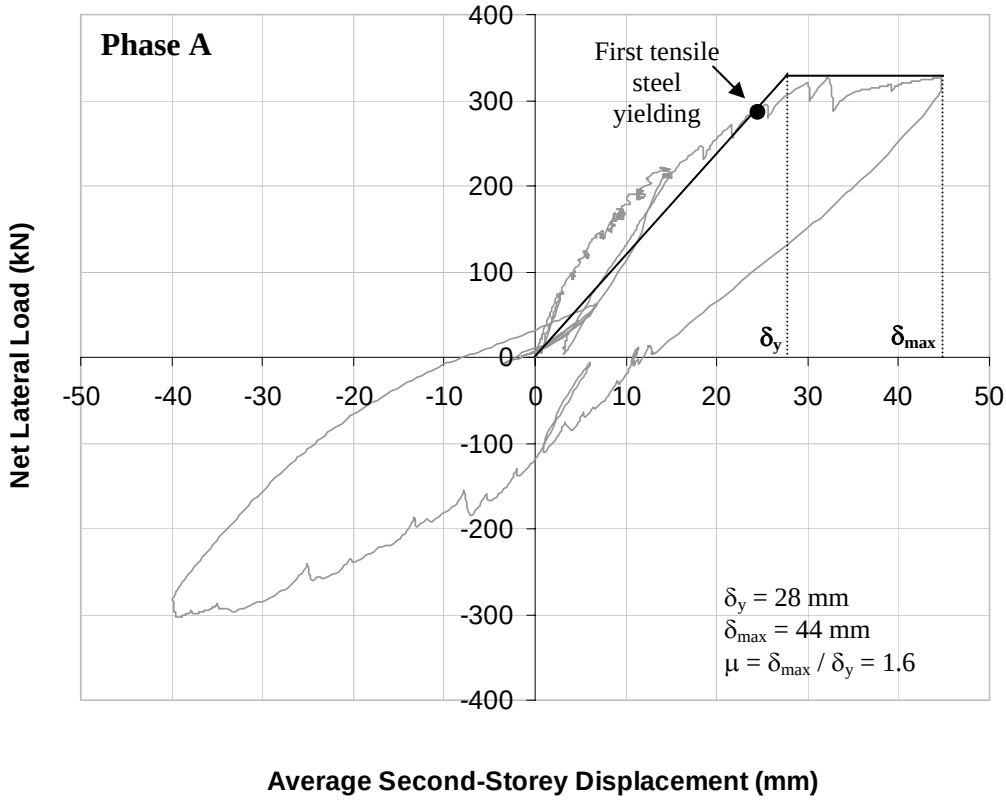

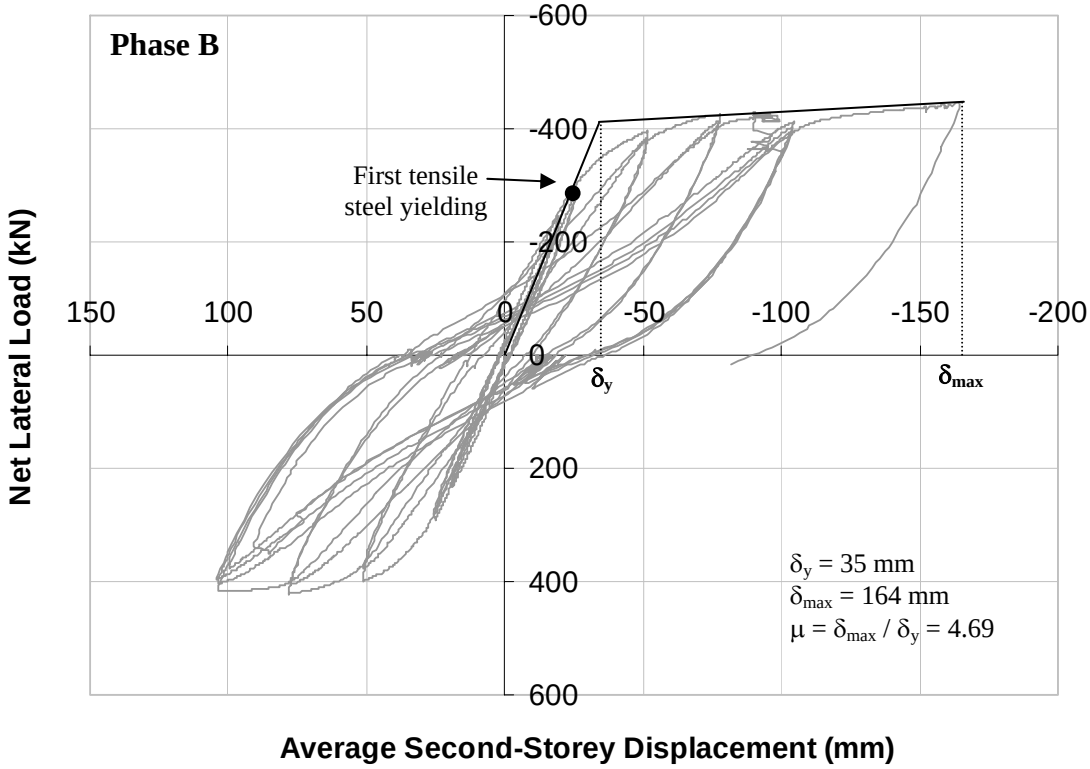

APPENDIX C

Graphs from Experimental and Numerical Results
Condensed Tables of Experimental Results

C.1 Lateral Load vs. Column Base Longitudinal Steel Strain (Experimental):

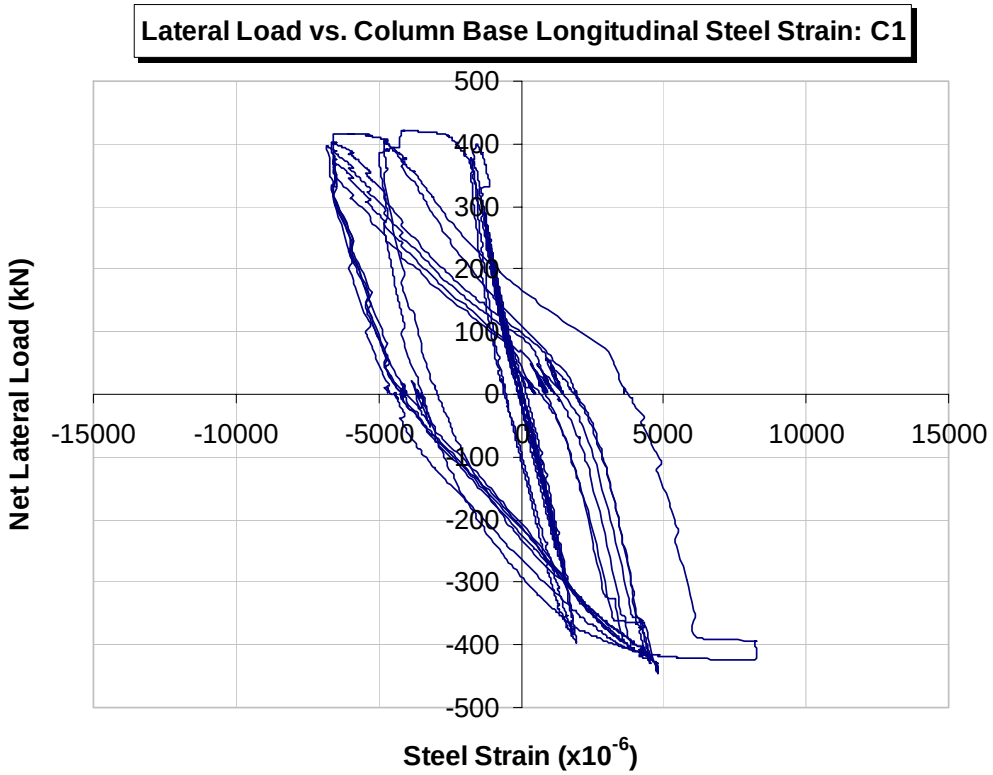

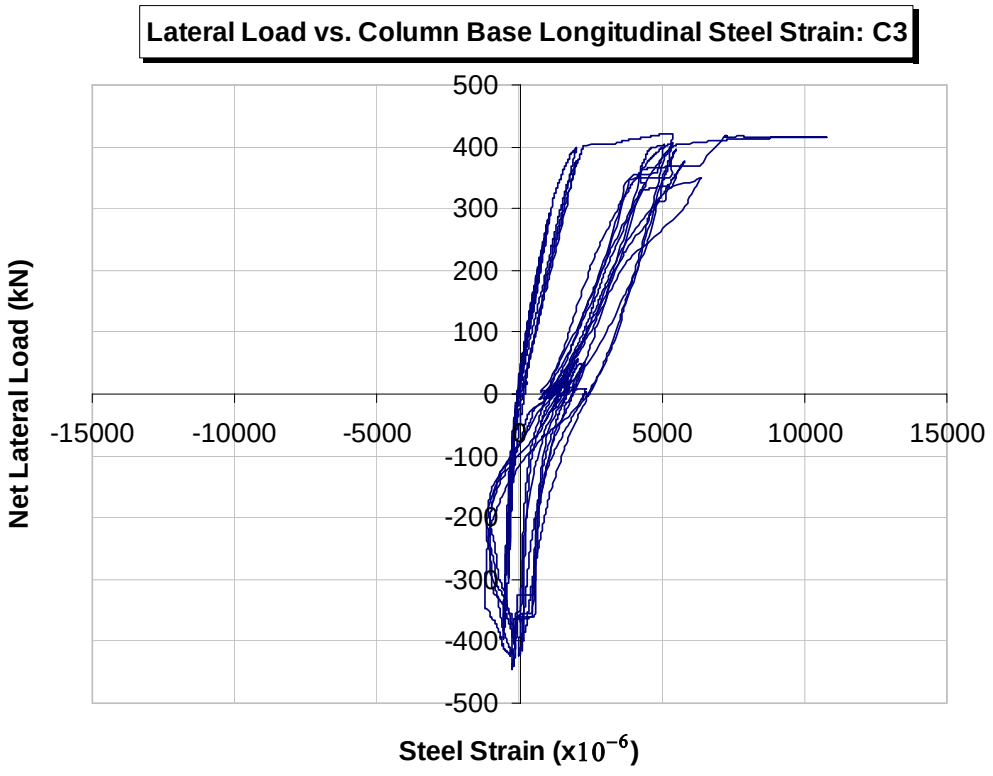

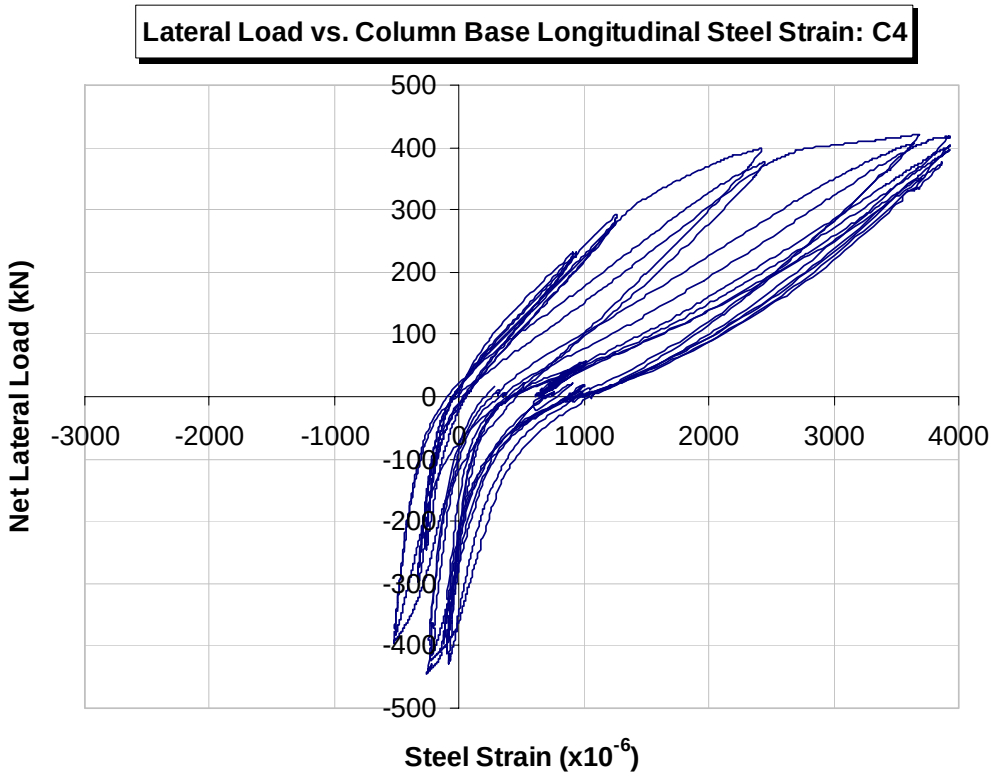
Lateral Load vs. Column Base Longitudinal Steel Strain: C4
Net Lateral Load (kN)
500
400
300
200
100
0
-100
-200
-300
-400
-500
-3000
-2000
-1000
0
1000
2000
3000
4000
Steel Strain (x10-6)

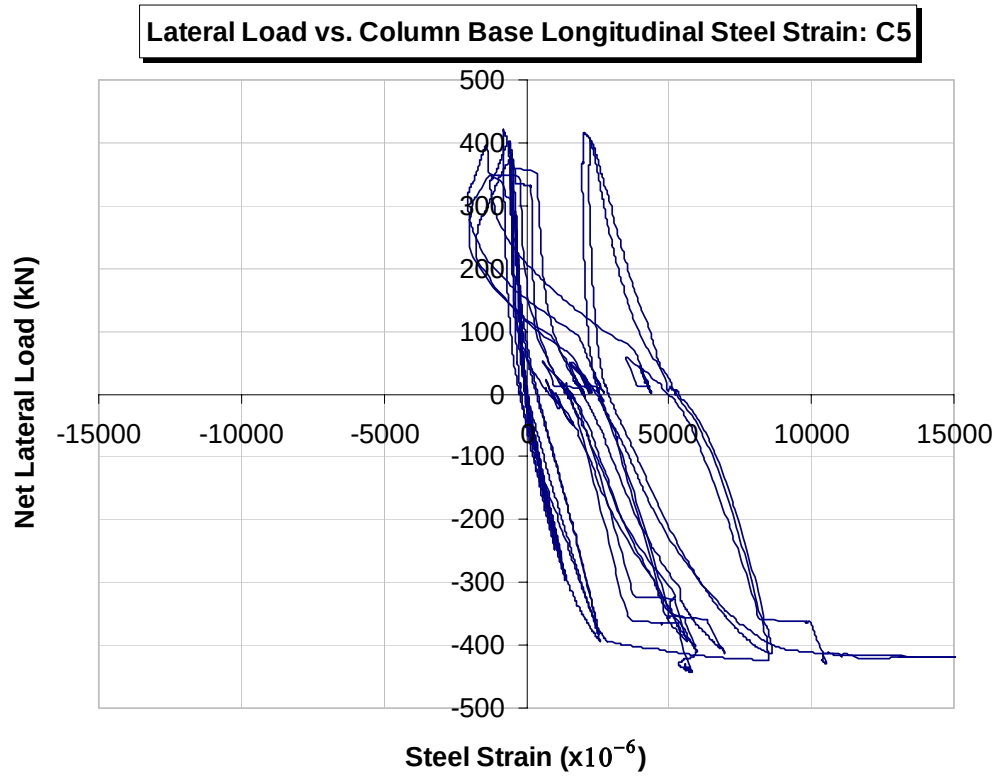
Lateral Load vs. Column Base Longitudinal Steel Strain: C5
Net Lateral Load (kN)
500
400
300
200
100
0
-100
-200
-300
-400
-500
-15000
-10000
-5000
0
5000
10000
15000
Steel Strain (x10−6)

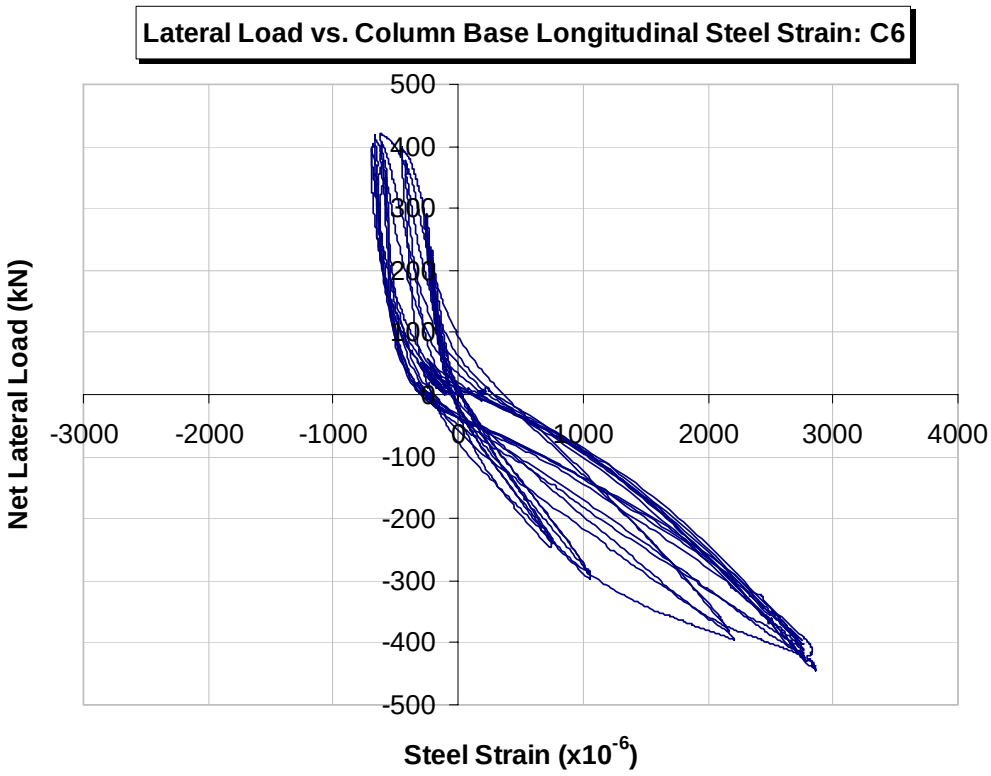
Lateral Load vs. Column Base Longitudinal Steel Strain: C6
Net Lateral Load (kN)
500
400
300
200
100
0
-100
-200
-300
-400
-500
-3000
-2000
-1000
0
1000
2000
3000
4000
Steel Strain (x10-6)

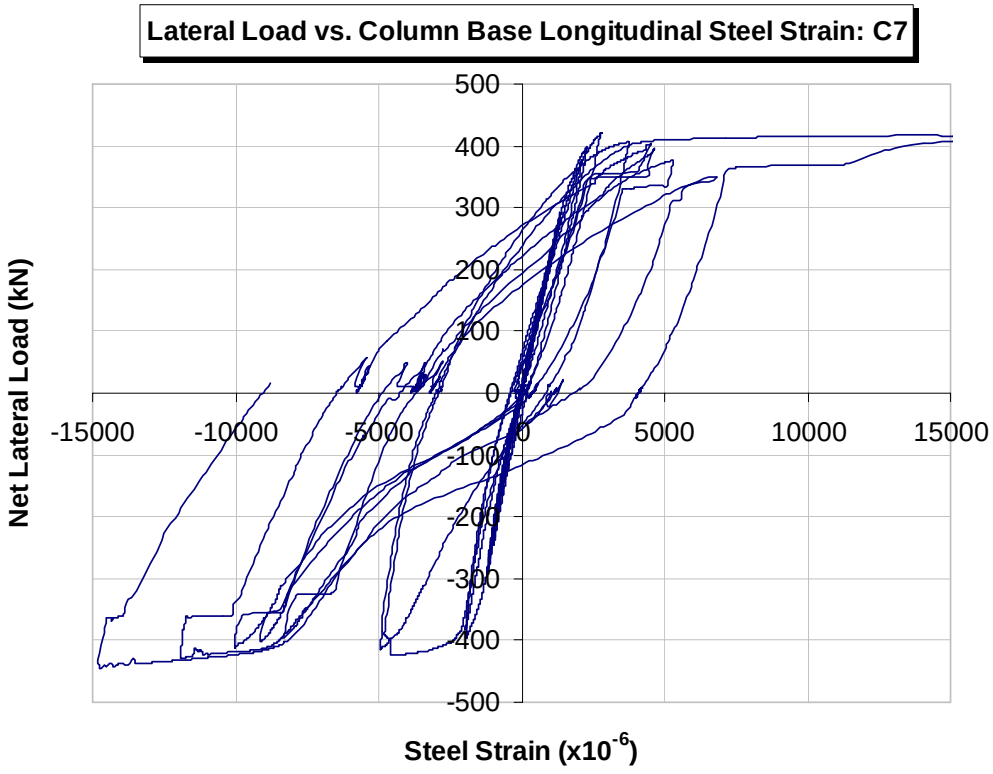
Lateral Load vs. Column Base Longitudinal Steel Strain: C7
Net Lateral Load (kN)
500
400
300
200
100
0
-100
-200
-300
-400
-500
-15000
-10000
-5000
0
5000
10000
15000
Steel Strain (x10-6)

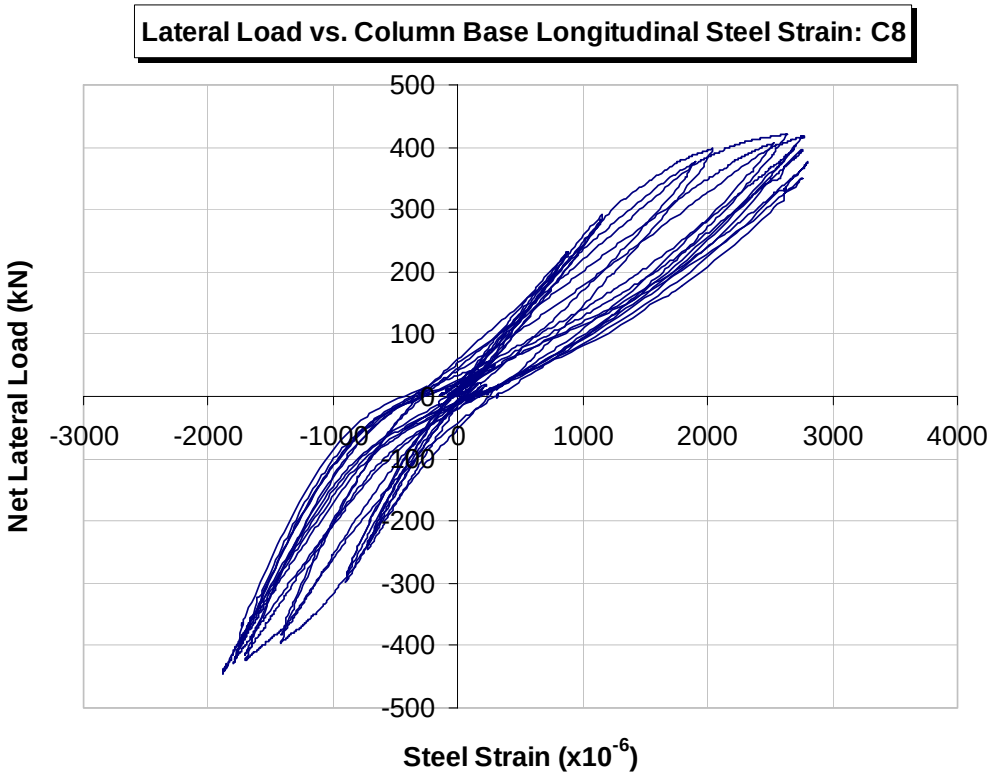
Lateral Load vs. Column Base Longitudinal Steel Strain: C8
Net Lateral Load (kN)
500
400
300
200
100
0
-100
-200
-300
-400
-500
-3000
-2000
-1000
0
1000
2000
3000
4000
Steel Strain (x10-6)

C.2 Lateral Load vs. Beam Longitudinal Steel Strain (Experimental):

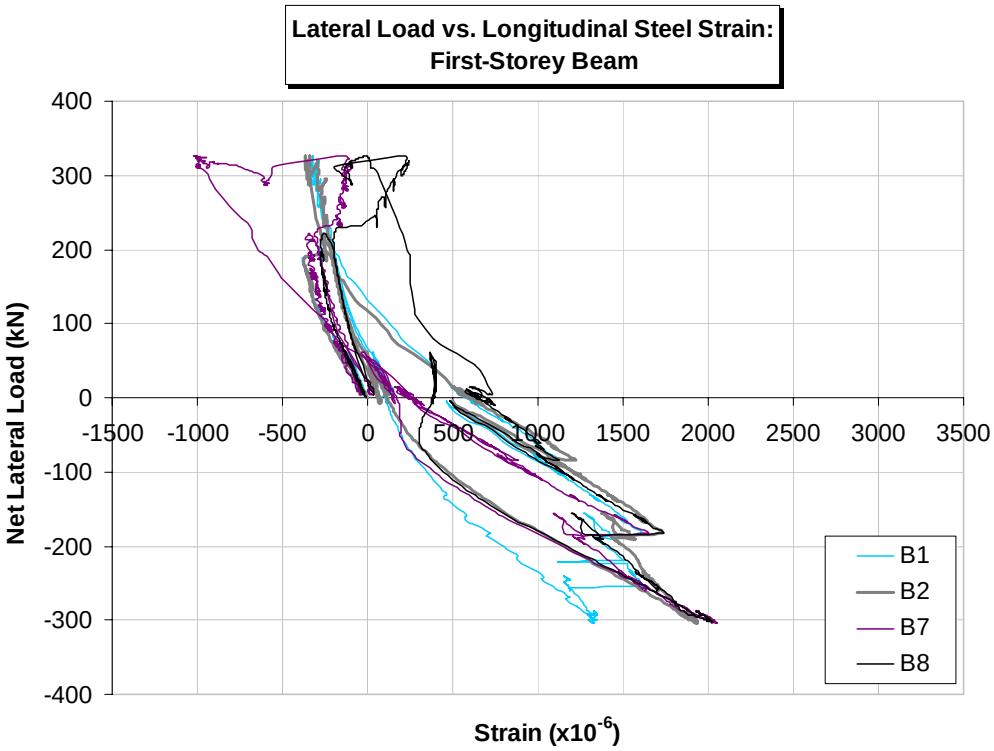

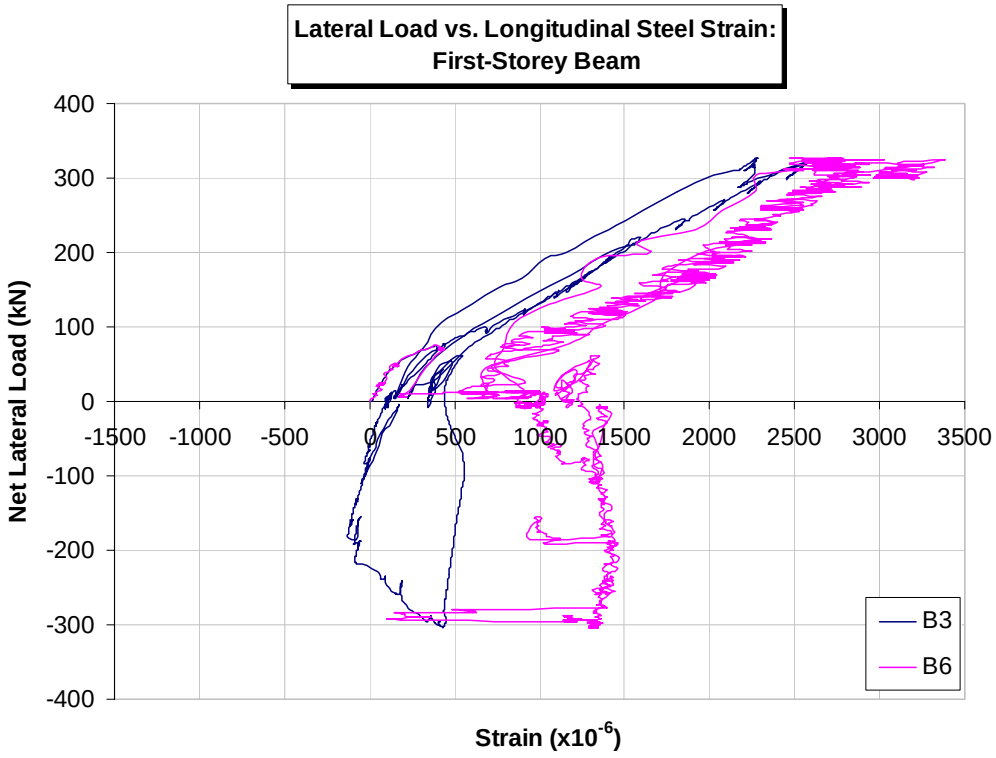

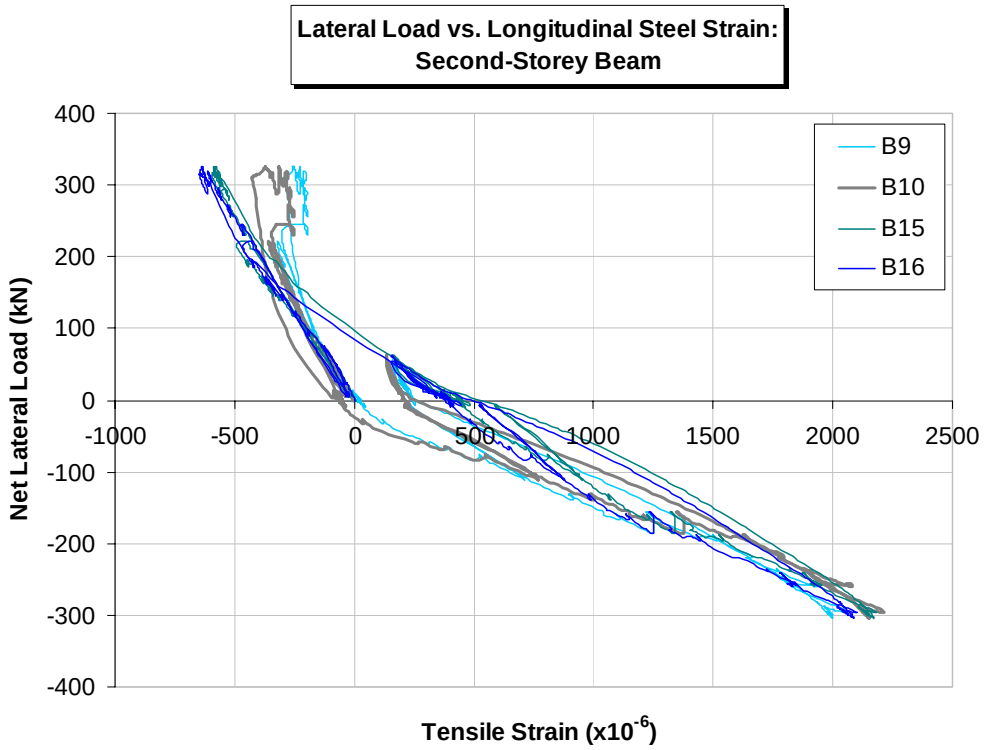
Lateral Load vs. Longitudinal Steel Strain: Second-Storey Beam
Net Lateral Load (kN)
400
300
200
100
0
-100
-200
-300
-400
-1000
-500
0
500
1000
1500
2000
2500
B9
B10
B15
B16
Tensile Strain (x10-6)

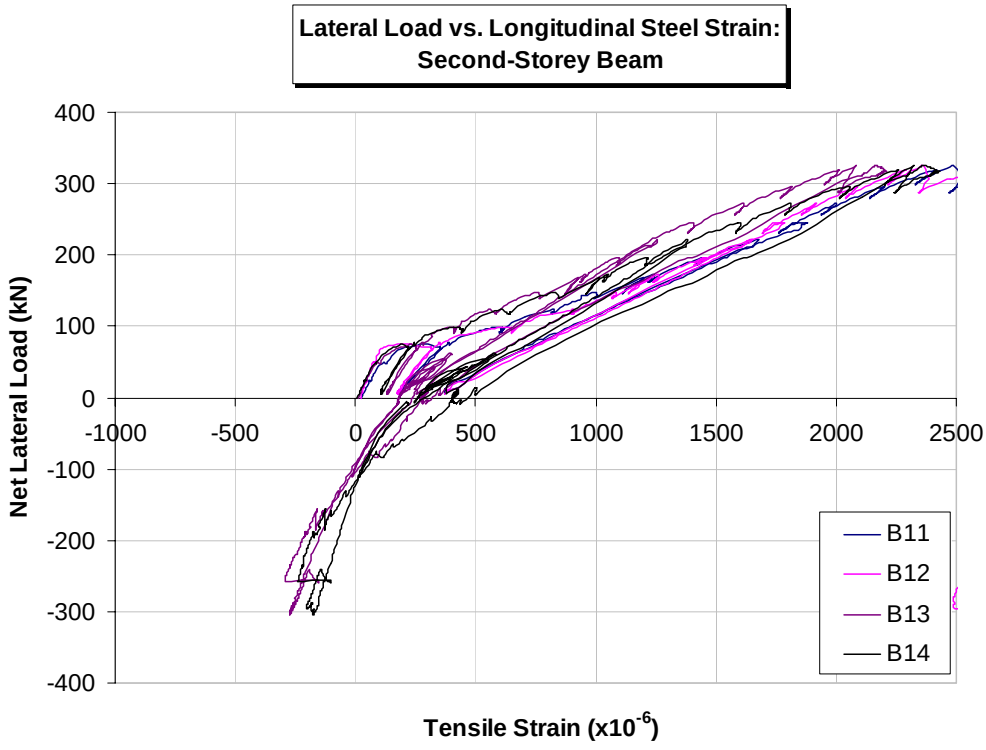
Lateral Load vs. Longitudinal Steel Strain: Second-Storey Beam
Net Lateral Load (kN)
400
300
200
100
0
-100
-200
-300
-400
-1000
-500
0
500
1000
1500
2000
2500
B11
B12
B13
B14
Tensile Strain (x10-6)

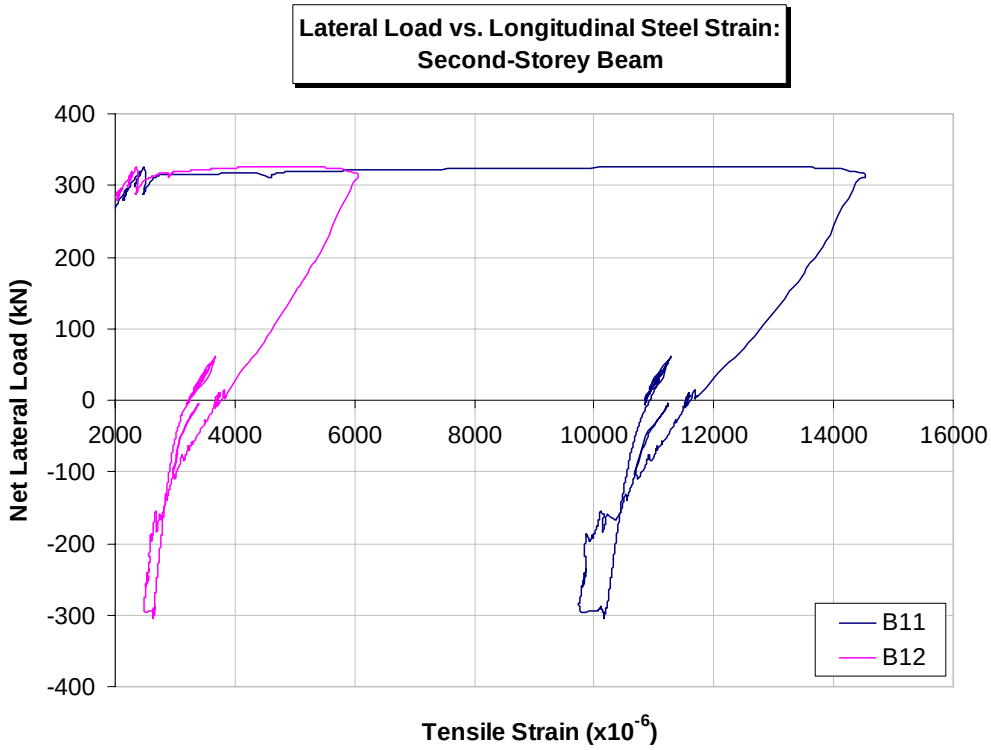
Lateral Load vs. Longitudinal Steel Strain:
Second-Storey Beam
Net Lateral Load (kN)
400
300
200
100
0
-100
-200
-300
-400
2000
4000
6000
8000
10000
12000
14000
16000
Tensile Strain (x10-6)
B11
B12

C.3 Lateral Load vs. Stirrup Steel Strain (Experimental):

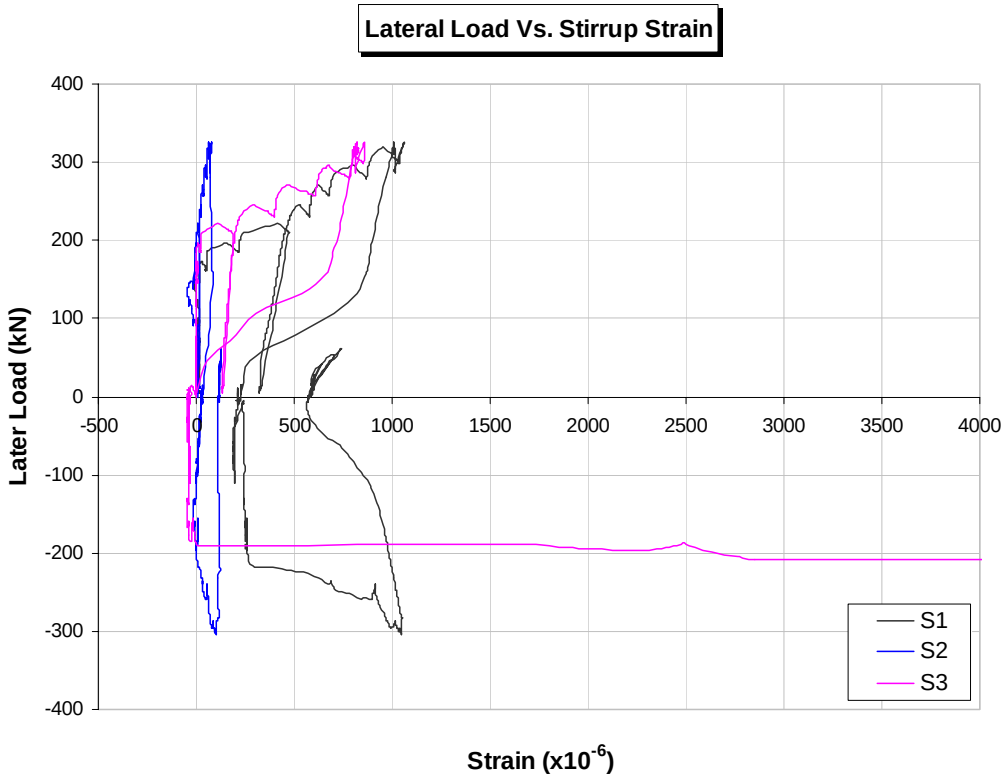

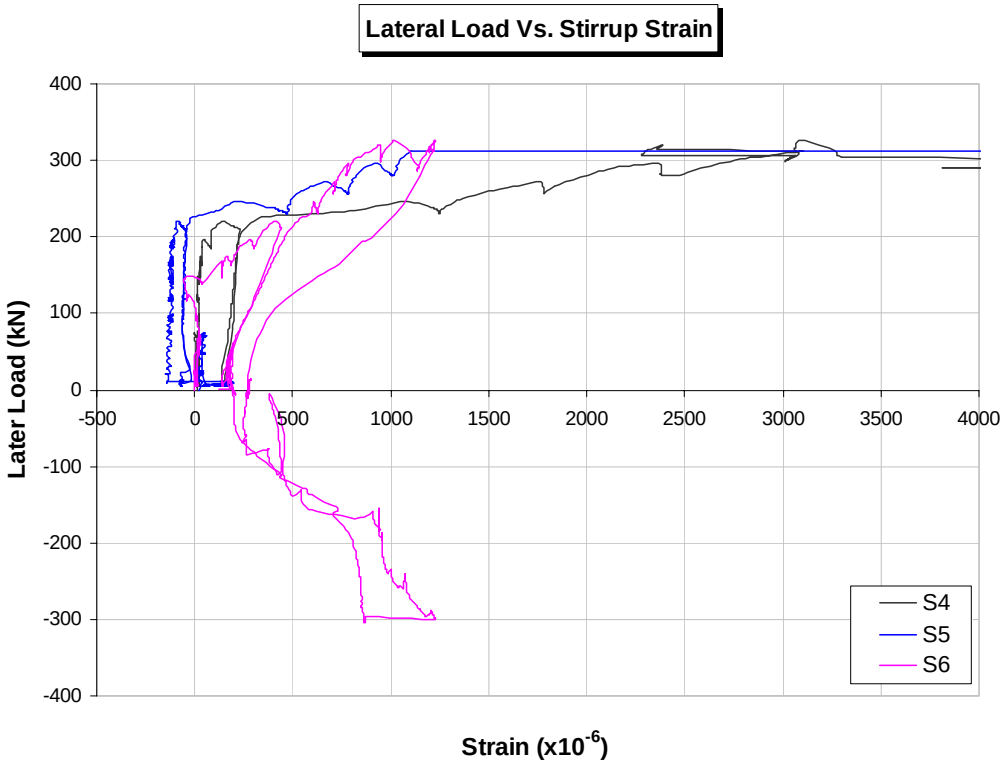

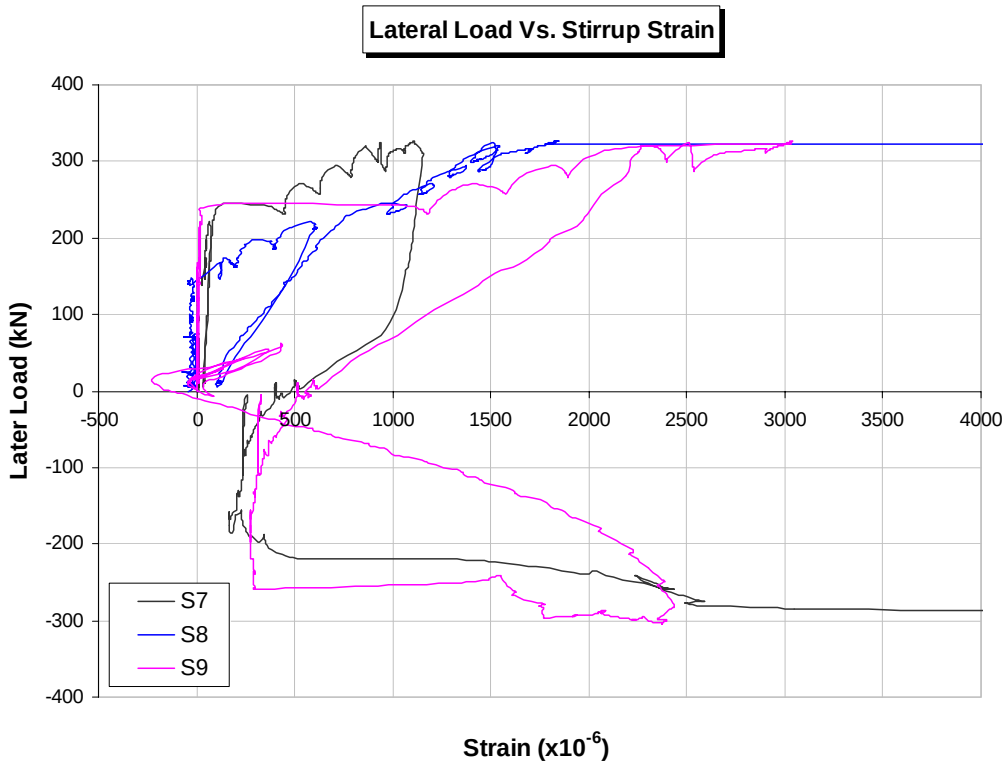
Lateral Load Vs. Stirrup Strain
Later Load (kN)
400
300
200
100
0
-100
-200
-300
-400
-500
0
500
1000
1500
2000
2500
3000
3500
4000
S7
S8
S9
Strain (x10-6)

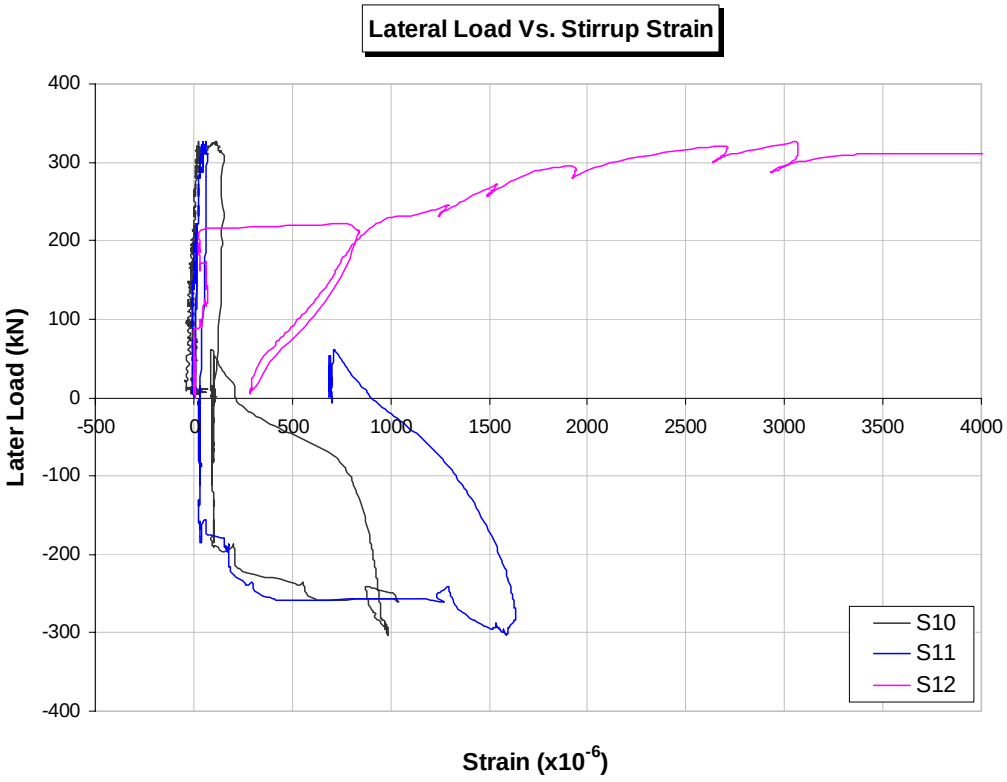
Lateral Load Vs. Stirrup Strain
Later Load (kN)
400
300
200
100
0
-100
-200
-300
-400
-500
0
500
1000
1500
2000
2500
3000
3500
4000
S10
S11
S12
Strain (x10-6)

C.4 Lateral Load vs. First-Storey Beam Displacement (Experimental vs. Analytical):

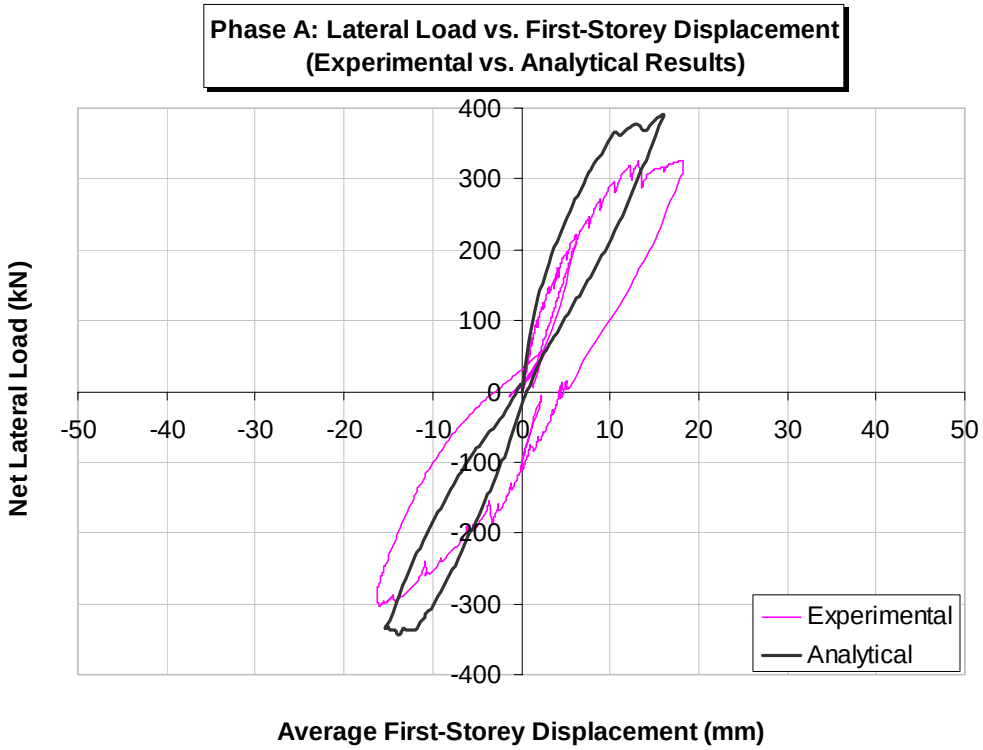

C.5 Lateral Displacement vs. Beam Curvature (Experimental):

The graphs below summarize the second-storey lateral displacement versus beam curvature relationship. The curvatures were calculated at both ends of the first and second-storey beams, at the beam-column interfaces and at the beam-column joints. The curvatures were computed from the horizontal Zurich surface gauge readings. Using the relative horizontal strains at the top and bottom of each given grid (taking the reference strain after the column axial loads were applied), the distance "c" measured from the top to the location of zero strain was calculated. A positive curvature indicated tension at the bottom and compression at the top. In the case where both the top and bottom were in either tension or in compression, a positive curvature indicated either a higher tensile strain or lower compressive strain at the bottom.

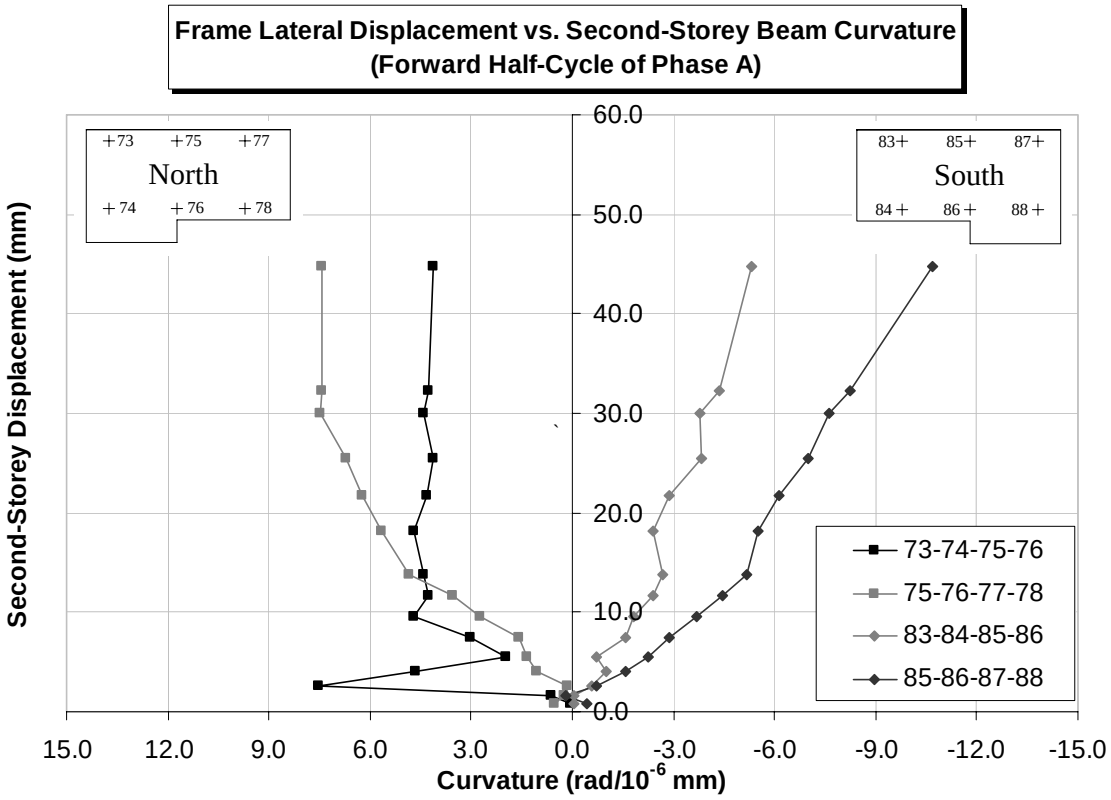

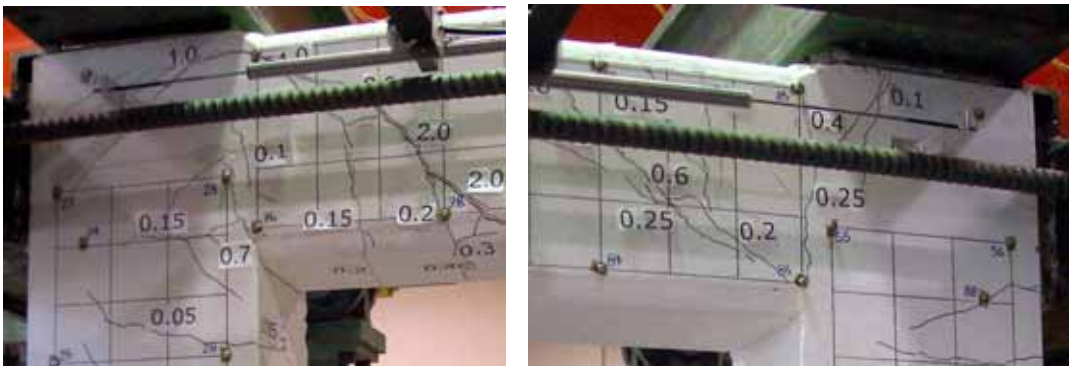

North **South**

Second-Storey Beam at Δ = 44 mm

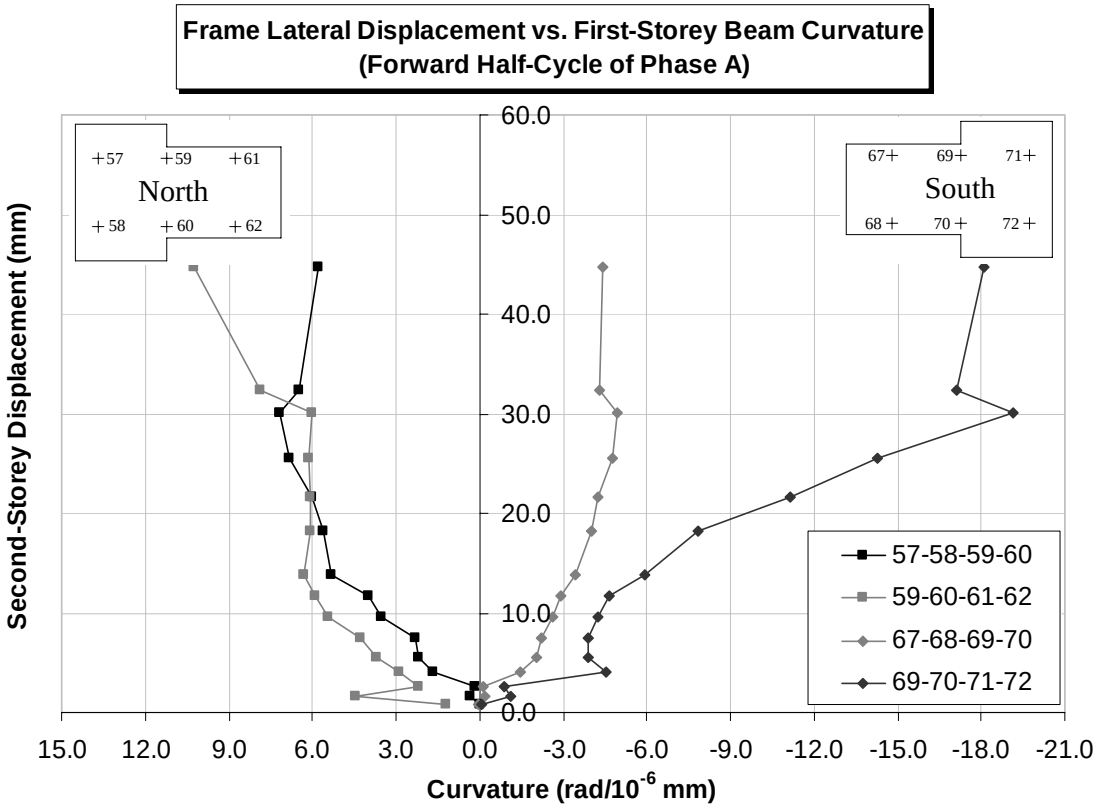

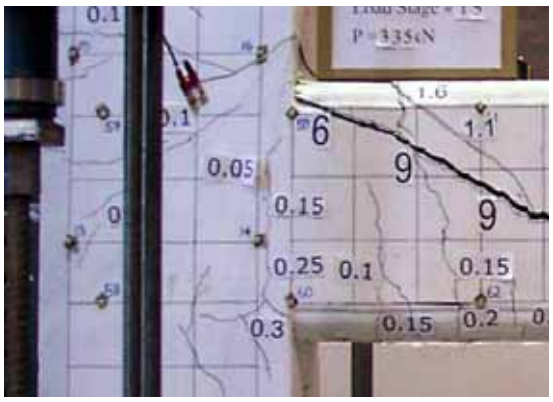

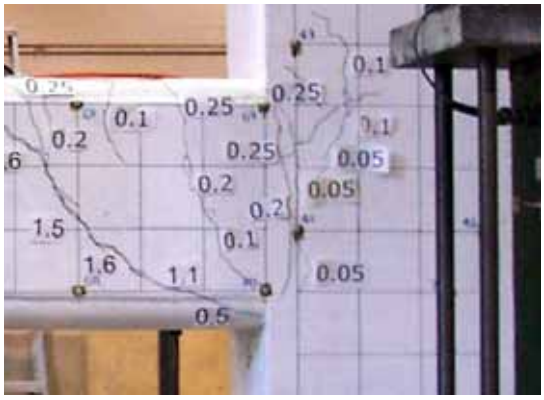

North **First-Storey Beam at Δ = 44 mm** **South**

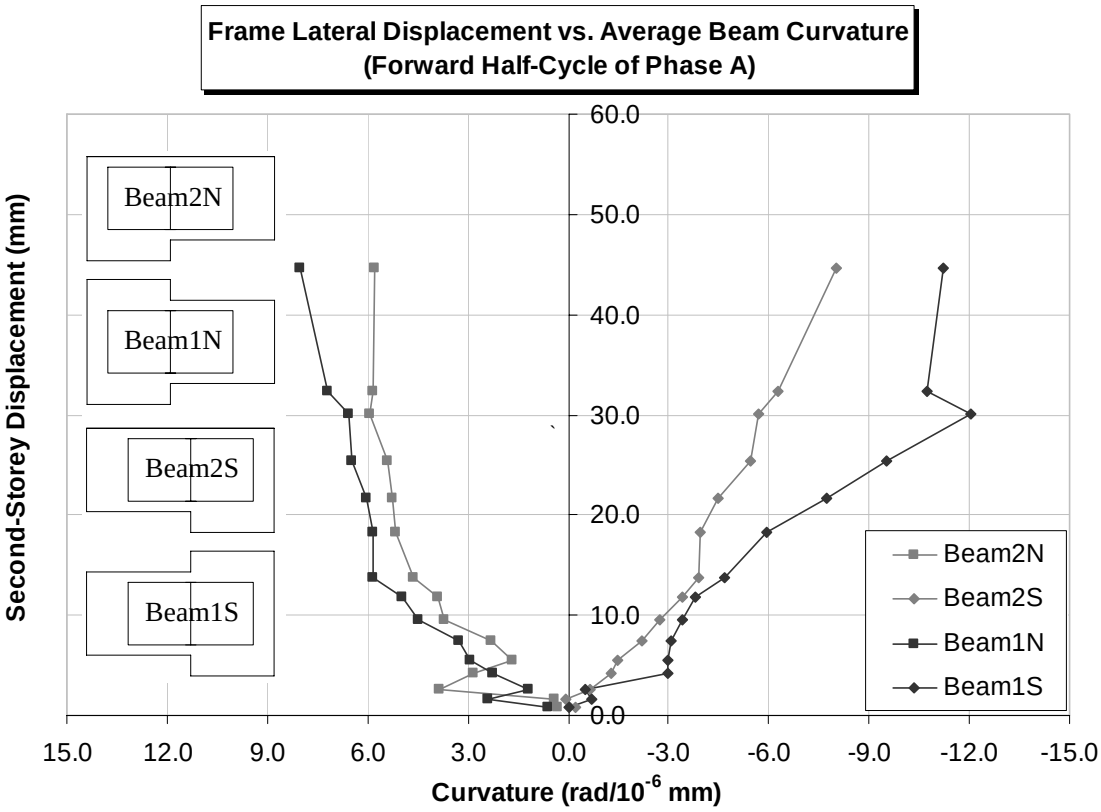
Frame Lateral Displacement vs. Average Beam Curvature
(Forward Half-Cycle of Phase A)
Second-Storey Displacement (mm)
60.0
50.0
40.0
30.0
20.0
10.0
0.0
Beam2N
Beam1N
Beam2S
Beam1S
Beam2N
Beam2S
Beam1N
Beam1S
15.0
12.0
9.0
6.0
3.0
0.0
-3.0
-6.0
-9.0
-12.0
-15.0
Curvature (rad/10-6 mm)

C.6 Phase A (Forward-Half Cycle): Summary of Experimental Results

Net			Second-Storey Beam			Beam Δ	Lateral	First-Storey Beam			Beam Δ		
MTSLOAD	DATASET	Load	North Hoz.	South Hor.	Avg. Beam	Length	Drift	NHM	SHM	Avg. Beam	Length	NHB	SHB
(kN)	(#)	Stage	δ (mm)	δ (mm)	δ (mm)	(mm)	%	(mm)	(mm)	δ (mm)	(mm)	(mm)	(mm)
0	1												
0	20												
0	46	Col. Axial Load	0.00	0.00	0.00	0.00	0.00	0.00	0.00	0.00	0.00	0.00	0.00
-25	55	LS1	0.77	0.75	0.76	-0.02	0.02	0.34	0.35	0.34	0.01	0.00	0.00
-51	74	LS2	1.58	1.62	1.60	0.04	0.04	0.73	0.75	0.74	0.02	0.01	0.00
-75	95	LS3	2.57	2.72	2.65	0.14	0.07	1.19	1.25	1.22	0.06	0.04	0.02
-99	215	LS4	4.17	4.10	4.13	-0.06	0.10	1.71	1.91	1.81	0.20	0.05	0.01
-125	251	LS5	5.20	5.71	5.46	0.51	0.14	2.34	2.60	2.47	0.27	0.09	0.03
-148	296	LS6	7.45	7.37	7.41	-0.08	0.19	2.98	3.41	3.19	0.43	0.15	0.07
-174	325	LS7	9.64	9.55	9.60	-0.09	0.24	3.82	4.44	4.13	0.62	0.17	0.08
-197	388	LS8	11.77	11.71	11.74	-0.06	0.29	4.63	5.43	5.03	0.79	0.18	0.11
-221	419	LS9	12.91	14.74	13.83	1.82	0.35	5.71	6.73	6.22	1.02	0.24	0.14
-232	578	B6 yielded	16.62	16.68	16.65	0.06	0.42	6.34	7.58	6.96	1.24	0.20	0.18
-246	583	LS10	18.15	18.26	18.20	0.11	0.46	6.89	8.24	7.57	1.35	0.21	0.20
-272	622	LS11	21.55	21.80	21.67	0.25	0.54	8.16	9.72	8.94	1.56	0.24	0.24
-289	654	B3 yielded	24.14	24.46	24.30	0.32	0.61	9.15	10.87	10.01	1.72	0.30	0.26
-295	657	LS12	25.33	25.60	25.46	0.28	0.64	9.56	11.36	10.46	1.81	0.32	0.28
-280	671	S4 yielded	25.45	25.77	25.61	0.32	0.64	9.67	11.44	10.56	1.76	0.31	0.28
-302	680	B11 yielded	26.97	27.31	27.14	0.35	0.68	10.24	12.12	11.18	1.88	0.31	0.30
-314	685	S12, B12, S5 broke	28.73	29.10	28.92	0.37	0.72	10.91	12.88	11.90	1.97	0.31	0.32
-320	688	LS13	29.84	30.22	30.03	0.38	0.75	11.31	13.33	12.32	2.02	0.32	0.33
-308	719	S9 yielded	30.52	30.89	30.70	0.37	0.77	11.65	13.60	12.63	1.96	0.35	0.35
-325	725	LS14	32.10	32.50	32.30	0.40	0.81	12.22	14.28	13.25	2.06	0.35	0.38
-312	756	S12 broke	35.80	36.26	36.03	0.46	0.90	14.09	15.75	14.92	1.66	0.37	0.38
-327	820	LS15	44.50	44.85	44.68	0.35	1.12	17.48	18.90	18.19	1.42	0.46	0.44
-320	828	S8 broke	44.53	44.88	44.70	0.35	1.12	17.49	18.89	18.19	1.40	0.46	0.45
-281	846		42.60	42.88	42.74	0.28	1.07	16.77	17.98	17.37	1.21	0.48	0.45
-199	850		34.99	35.25	35.12	0.26	0.88	13.98	14.85	14.41	0.87	0.47	0.39
-107	855		24.73	24.87	24.80	0.14	0.62	9.96	10.51	10.24	0.56	0.34	0.28

Net	Out-of-plane						NVT-				SVT-						
MTSLOAD	NHTOP	SHTOP	BASESLIP	NVT	NVM	NVB	NVB	SVT	SVM	SVB	SVB	S1	S2	S3	S4	S5	S6
(kN)	(mm)	(mm)	(mm)	(mm)	(mm)	(mm)	(mm)	(mm)	(mm)	(mm)	(mm)	10^{-6}	10^{-6}	10^{-6}	10^{-6}	10^{-6}	10^{-6}
0	-0.13	-0.04	0.00	-0.01	-0.02	0.00	-0.01	0.01	0.00	0.00	0.01	0	-1	1	8	0	0
0	0.14	1.44	-0.02	0.56	0.31	-0.06	0.62	0.62	0.38	-0.13	0.75	2	3	0	7	-6	-1
0	-0.40	1.55	-0.02	0.68	0.38	-0.08	0.76	0.76	0.46	-0.17	0.92	2	5	1	11	25	-1
-25	-0.49	1.56	-0.02	0.65	0.35	-0.07	0.72	0.79	0.49	-0.18	0.96	3	6	1	7	23	-1
-51	-0.64	1.50	-0.02	0.61	0.32	-0.06	0.68	0.83	0.52	-0.19	1.02	7	9	0	4	40	13
-75	-0.71	1.48	-0.02	0.57	0.29	-0.05	0.62	0.84	0.54	-0.20	1.05	16	11	1	2	51	22
-99	-0.76	1.54	-0.02	0.54	0.27	-0.05	0.59	0.91	0.59	-0.22	1.13	14	-8	3	21	-114	10
-125	-0.85	1.67	-0.01	0.50	0.23	-0.04	0.54	0.91	0.60	-0.23	1.14	4	-35	-2	17	-129	-30
-148	-0.91	1.60	-0.01	0.44	0.18	-0.04	0.48	0.94	0.61	-0.24	1.18	-17	-28	-2	17	-122	-36
-174	-1.07	1.54	-0.01	0.34	0.11	-0.02	0.37	0.95	0.61	-0.25	1.20	23	-8	4	30	-107	165
-197	-1.29	1.51	-0.01	0.24	0.03	-0.01	0.25	0.95	0.61	-0.26	1.22	140	0	9	45	-106	278
-221	-1.83	1.37	-0.01	0.03	-0.09	0.00	0.03	0.92	0.58	-0.28	1.19	415	9	106	143	-88	413
-232	-2.26	1.30	0.00	-0.14	-0.18	0.01	-0.16	0.85	0.55	-0.29	1.14	483	19	229	759	96	600
-246	-2.57	1.23	0.00	-0.26	-0.25	0.02	-0.29	0.82	0.53	-0.29	1.11	520	20	290	1052	202	609
-272	-3.10	1.33	0.00	-0.50	-0.40	0.04	-0.53	0.77	0.51	-0.30	1.08	626	30	470	1762	677	717
-289	-3.74	1.24	0.00	-0.74	-0.56	0.06	-0.80	0.71	0.48	-0.32	1.03	727	41	639	2136	862	761
-295	-4.00	1.26	0.00	-0.86	-0.62	0.06	-0.93	0.68	0.46	-0.32	1.00	795	44	672	2364	932	788
-280	-4.05	1.23	0.01	-0.87	-0.63	0.07	-0.93	0.68	0.47	-0.32	1.00	869	52	779	2434	1005	773
-302	-4.26	1.23	0.01	-0.97	-0.70	0.08	-1.05	0.66	0.46	-0.33	0.99	888	56	795	2786	1051	817
-314	-4.78	1.15	0.01	-1.12	-0.80	0.09	-1.21	0.60	0.43	-0.33	0.94	921	58	800	2360	25625	911
-320	-5.11	1.12	0.01	-1.21	-0.86	0.10	-1.31	0.57	0.40	-0.33	0.90	956	60	804	2386	25625	943
-308	-5.29	1.09	0.02	-1.24	-0.88	0.11	-1.35	0.58	0.42	-0.34	0.92	1042	73	860	3079	2775	959
-325	-5.62	1.07	0.02	-1.36	-0.96	0.12	-1.47	0.55	0.40	-0.34	0.89	1063	76	863	3095	4405	1020
-312	-6.04	1.18	0.02	-1.43	-1.08	0.13	-1.55	0.43	0.32	-0.33	0.76	1015	69	824	8405	-3777	1189
-327	-7.42	0.69	0.03	-1.52	-1.44	0.19	-1.71	0.10	0.08	-0.32	0.41	1007	66	818	5873	-3833	1227
-320	-7.45	0.67	0.03	-1.51	-1.44	0.19	-1.70	0.09	0.08	-0.32	0.41	1005	66	815	5394	-8889	1223
-281	-7.23	0.75	0.03	-1.36	-1.35	0.18	-1.53	0.14	0.10	-0.31	0.45	967	71	783	4474	-7784	1153
-199	-6.39	0.93	0.02	-0.84	-0.99	0.12	-0.96	0.33	0.21	-0.30	0.63	902	78	717	4602	12625	904
-107	-3.98	1.48	0.02	-0.22	-0.47	0.05	-0.26	0.60	0.36	-0.28	0.88	703	73	303	4072	4300	411

Net																				
MTSLOAD	S7	S8	S9	S10	S11	S12	B1	B2	B3	B6	B7	B8	B9	B10	B11	B12	B13	B14	B15	B16
(kN)	10^{-6}	10^{-6}	10^{-6}	10^{-6}	10^{-6}	10^{-6}	10^{-6}	10^{-6}	10^{-6}	10^{-6}	10^{-6}	10^{-6}	10^{-6}	10^{-6}	10^{-6}	10^{-6}	10^{-6}	10^{-6}	10^{-6}	10^{-6}
0	5	-33	1	1	-4	2	-13	-18	15	22	-23	-12	-10	-10	9	9	12	9	-9	-10
0	12	-59	0	-1	-2	3	-1	-7	13	26	-11	-9	-10	-9	19	18	12	7	2	-2
0	12	-39	1	3	-2	5	2	-1	14	1	-7	-7	-9	-7	24	21	12	7	6	2
-25	13	-38	2	2	-2	5	-43	-58	66	89	-66	-53	-43	-43	60	47	44	40	-32	-36
-51	10	-21	2	10	-2	5	-104	-126	151	143	-124	-107	-82	-81	116	76	93	84	-74	-76
-75	4	-8	5	10	-4	-1	-175	-201	386	399	-181	-155	-128	-128	289	200	232	196	-128	-126
-99	4	-33	3	-19	-4	35	-241	-259	675	1012	-243	-204	-183	-190	581	603	381	403	-196	-192
-125	5	-13	2	-28	-4	57	-291	-302	919	1463	-279	-232	-222	-233	823	907	560	610	-258	-248
-148	17	-24	0	-26	-4	64	-335	-341	1116	1746	-292	-256	-256	-272	994	1088	755	826	-321	-307
-174	45	141	8	-2	7	60	-369	-363	1296	1902	-335	-271	-283	-304	1241	1264	959	1050	-390	-373
-197	52	285	13	-2	3	22	-293	-271	1430	2020	-343	-275	-308	-336	1453	1455	1087	1206	-448	-428
-221	65	575	17	11	18	779	-246	-256	1594	2134	-336	-260	-324	-359	1677	1652	1252	1377	-459	-437
-232	93	794	22	2	21	1061	-227	-236	1715	2326	-221	-49	-305	-346	1809	1731	1305	1484	-444	-444
-246	148	953	208	9	23	1297	-240	-242	1846	2207	-175	43	-265	-323	1880	1784	1398	1592	-467	-470
-272	536	1198	1420	8	26	1545	-271	-251	2091	2506	-164	92	-208	-271	2001	1919	1617	1813	-523	-528
-289	673	1320	1734	10	29	1752	-290	-258	2261	2732	-148	137	-208	-270	2141	2038	1759	1970	-555	-566
-295	714	1372	1828	15	30	1916	-278	-248	2305	2595	-140	156	-205	-269	2202	2091	1820	2058	-545	-570
-280	786	1292	1892	11	32	1923	-298	-286	2227	2657	-123	151	-203	-270	2141	2041	1769	2016	-522	-558
-302	801	1362	1970	9	34	2160	-303	-290	2355	2861	-133	171	-216	-286	2263	2158	1869	2114	-551	-589
-314	836	1459	2101	12	38	2460	-293	-291	2495	2882	-93	225	-215	-288	2368	2252	1967	2213	-563	-604
-320	862	1541	2312	16	40	2696	-285	-296	2573	2861	-88	241	-208	-283	2416	2290	2014	2260	-570	-613
-308	925	1425	2418	21	41	2708	-320	-344	2496	3274	-151	203	-223	-304	2370	2256	1984	2233	-567	-618
-325	938	1514	2512	22	44	3057	-319	-341	2602	3383	-142	214	-228	-313	2487	2362	2085	2322	-590	-641
-312	993	1602	2714	35	48	10525	-337	-364	2267	2696	-760	-130	-242	-341	2679	2607	2162	2391	-592	-647
-327	1111	1831	3036	108	65	14838	-340	-366	2275	2554	-1004	-1	-255	-375	13413	5383	2166	2362	-579	-636
-320	1126	25625	2274	123	65	13925	-332	-361	2235	2493	-997	12	-259	-382	14363	5936	2141	2336	-572	-631
-281	1141	25625	2190	138	66	11288	-296	-327	1813	2267	-897	100	-280	-412	14250	5855	1898	2108	-504	-575
-199	1102	25625	1807	144	61	9713	-199	-246	1159	1648	-640	231	-249	-377	13681	5363	1417	1648	-352	-440
-107	1019	25625	1211	134	48	8341	110	53	426	848	-262	293	-184	-299	12825	4662	823	1023	-33	-92

Net								
MTSLOAD	C1	C2	C3	C4	C5	C6	C7	C8
(kN)	10^{-6}	10^{-6}	10^{-6}	10^{-6}	10^{-6}	10^{-6}	10^{-6}	10^{-6}
0	-16	-13	6	5	-6	-1	22	14
0	-93	-88	-46	-75	-120	-108	-92	-96
0	-111	-107	-60	-95	-147	-133	-120	-117
-25	-165	-151	-34	-73	-173	-147	-68	-69
-51	-229	-204	-5	-41	-202	-166	-2	-14
-75	-298	-260	34	-1	-232	-188	69	42
-99	-386	-332	83	58	-275	-223	154	126
-125	-473	-400	138	133	-309	-253	252	220
-148	-570	-477	211	245	-346	-283	362	337
-174	-684	-564	323	373	-382	-312	491	478
-197	-790	-643	433	504	-416	-339	619	613
-221	-916	-736	565	687	-452	-363	790	764
-232	-995	-792	644	805	-473	-378	868	839
-246	-1057	-836	709	897	-489	-387	943	911
-272	-1204	-934	827	1084	-519	-402	1082	1029
-289	-1320	-1009	914	1220	-539	-413	1198	1126
-295	-1358	-1034	959	1284	-543	-414	1242	1161
-280	-1367	-1030	913	1261	-544	-412	1214	1133
-302	-1434	-1078	994	1348	-564	-426	1305	1214
-314	-1495	-1120	1068	1444	-576	-433	1389	1294
-320	-1528	-1142	1103	1494	-583	-437	1435	1337
-308	-1566	-1154	1072	1481	-599	-444	1434	1341
-325	-1623	-1197	1150	1570	-615	-456	1518	1418
-312	-1673	-1253	1238	1713	-698	-533	1655	1561
-327	-1822	-1388	1453	1998	-805	-617	1971	1868
-320	-1818	-1384	1434	1986	-809	-615	1957	1859
-281	-1715	-1299	1211	1785	-780	-593	1743	1670
-199	-1482	-1125	872	1418	-719	-554	1364	1338
-107	-1052	-807	391	811	-583	-460	720	754

C.7 Phase A (Reverse-Half Cycle): Summary of Experimental Results

Net			Second-Storey Beam			Beam Δ	Lateral	First-Storey Beam			Beam Δ		
MTSLOAD	DATASET	Load	North Hoz.	South Hor.	Avg. Beam	Length	Drift	NHM	SHM	Avg. Beam	Length	NHB	SHB
(kN)	(#)	Stage	δ (mm)	δ (mm)	δ (mm)	(mm)	%	(mm)	(mm)	δ (mm)	(mm)	(mm)	(mm)
2	1248	LS16	10.71	10.85	10.78	0.14	0.27	4.09	4.56	4.32	0.47	0.11	0.12
32	1263	LS17	9.04	9.17	9.10	0.13	0.23	3.33	3.84	3.58	0.52	0.09	0.11
69	1284	LS18	5.50	5.63	5.56	0.13	0.14	1.77	2.36	2.07	0.59	0.02	0.08
82	1292		4.25	4.40	4.33	0.15	0.11	1.23	1.84	1.54	0.61	-0.01	0.07
84	1293	LS19	4.01	4.16	4.09	0.15	0.10	1.12	1.75	1.43	0.63	-0.02	0.07
81	1294		3.63	3.79	3.71	0.16	0.09	0.92	1.60	1.26	0.68	-0.03	0.07
111	1311	LS20	0.91	1.13	1.02	0.23	0.03	-0.27	0.45	0.09	0.73	-0.07	0.05
139	1420	LS21	-1.94	-1.62	-1.78	0.32	-0.04	-1.53	-0.62	-1.07	0.90	-0.14	0.03
168	249	LS22	-5.16	-4.73	-4.94	0.42	-0.12	-2.92	-1.91	-2.41	1.01	-0.20	-0.05
185	1450	LS23	-7.35	-6.86	-7.10	0.48	-0.18	-3.86	-2.77	-3.32	1.09	-0.26	-0.06
164	1451		-7.85	-7.36	-7.61	0.49	-0.19	-4.10	-3.03	-3.56	1.06	-0.26	-0.06
197	1472	LS24	-13.29	-12.59	-12.94	0.70	-0.32	-6.45	-5.26	-5.86	1.19	-0.32	-0.05
214	1486		-15.56	-14.81	-15.18	0.75	-0.38	-7.49	-6.23	-6.86	1.26	-0.36	-0.08
217	1487	S3 bust	-15.95	-15.18	-15.56	0.76	-0.39	-7.67	-6.39	-7.03	1.28	-0.37	-0.08
219	1488		-16.40	-15.63	-16.01	0.78	-0.40	-7.87	-6.57	-7.22	1.30	-0.38	-0.08
260	1511	LS25	-25.27	-23.99	-24.63	1.28	-0.62	-11.54	-10.05	-10.79	1.49	-0.52	-0.15
286	1537		-31.29	-29.71	-30.50	1.58	-0.76	-13.91	-12.27	-13.09	1.64	-0.60	-0.21
296	1572		-37.08	-35.41	-36.24	1.67	-0.91	-15.85	-14.07	-14.96	1.78	-0.66	-0.24
304	1603	LS26	-40.29	-38.62	-39.45	1.67	-0.99	-16.99	-15.17	-16.08	1.82	-0.70	-0.27
195	1655		-34.24	-32.78	-33.51	1.46	-0.84	-14.45	-13.04	-13.75	1.41	-0.64	-0.27
95	1675		-24.16	-23.00	-23.58	1.16	-0.59	-10.15	-9.21	-9.68	0.94	-0.48	-0.18
-2	1703		-7.79	-7.08	-7.43	0.71	-0.19	-3.13	-2.45	-2.79	0.68	-0.21	-0.04

Net	Out-of-plane						NVT-				SVT-						
MTSLOAD	NHTOP	SHTOP	BASESLIP	NVT	NVM	NVB	NVB	SVT	SVM	SVB	SVB	S1	S2	S3	S4	S5	S6
(kN)	(mm)	(mm)	(mm)	(mm)	(mm)	(mm)	(mm)	(mm)	(mm)	(mm)	(mm)	10^{-6}	10^{-6}	10^{-6}	10^{-6}	10^{-6}	10^{-6}
2	-1.20	2.32	0.00	0.54	0.21	-0.06	0.60	0.85	0.54	-0.27	1.12	210	26	-44	3130	25625	268
32	-1.20	2.40	0.00	0.66	0.29	-0.07	0.73	0.87	0.54	-0.26	1.13	198	20	-47	3102	25625	255
69	-1.18	2.44	0.00	0.74	0.36	-0.09	0.83	0.83	0.52	-0.25	1.07	189	7	-36	3102	25625	241
82	-1.10	2.50	0.00	0.75	0.37	-0.10	0.85	0.82	0.51	-0.24	1.06	191	3	-34	3118	25625	266
84	-1.10	2.50	0.00	0.76	0.37	-0.10	0.86	0.82	0.51	-0.24	1.06	191	3	-34	3132	25625	261
81	-1.09	2.51	0.00	0.77	0.38	-0.10	0.87	0.82	0.52	-0.24	1.06	190	6	-31	3564	25625	328
111	-1.12	2.61	0.00	0.84	0.43	-0.11	0.95	0.80	0.51	-0.23	1.03	195	2	-33	3761	25625	422
139	-0.78	2.92	0.00	0.89	0.48	-0.12	1.01	0.74	0.47	-0.22	0.96	245	-10	-39	3755	25625	499
168	-0.60	3.04	0.00	0.96	0.54	-0.14	1.09	0.68	0.43	-0.21	0.88	249	-18	-46	3742	25625	814
185	-0.32	3.22	0.00	0.97	0.56	-0.15	1.12	0.62	0.38	-0.21	0.83	256	7	-24	3961	25625	941
164	-0.24	3.21	0.00	0.96	0.55	-0.14	1.10	0.65	0.41	-0.21	0.86	256	7	-22	3961	25625	941
197	-0.10	3.31	0.00	0.96	0.56	-0.15	1.12	0.49	0.32	-0.20	0.69	255	-1	2236	5291	25625	953
214	0.08	3.44	0.01	0.90	0.53	-0.16	1.06	0.39	0.26	-0.19	0.58	276	6	9103	3878	25625	956
217	0.10	3.46	0.01	0.90	0.52	-0.16	1.06	0.38	0.25	-0.19	0.57	290	9	13409	3875	25625	957
219	0.17	3.51	0.01	0.89	0.52	-0.16	1.05	0.36	0.24	-0.19	0.54	314	14	20733	3870	25625	959
260	0.67	3.93	0.03	0.79	0.47	-0.17	0.96	0.04	0.01	-0.14	0.19	901	52	25625	3920	25625	1063
286	0.82	3.96	0.05	0.69	0.41	-0.18	0.87	-0.16	-0.14	-0.12	-0.03	971	71	25625	3927	25625	1142
296	1.18	4.13	0.06	0.61	0.35	-0.17	0.78	-0.28	-0.27	-0.11	-0.17	1025	88	25625	5463	3951	1219
304	1.22	4.11	0.07	0.56	0.31	-0.17	0.73	-0.37	-0.34	-0.10	-0.27	1047	98	25625	25625	-13773	865
195	1.38	4.49	0.07	0.67	0.37	-0.16	0.83	0.06	-0.07	-0.15	0.21	980	115	25625	25625	25625	798
95	1.39	4.48	0.05	0.82	0.45	-0.14	0.96	0.55	0.28	-0.23	0.78	836	109	25625	25625	25625	361
-2	0.95	4.24	0.03	0.87	0.49	-0.11	0.98	1.00	0.62	-0.29	1.29	577	113	25625	25625	25625	193

Net																				
MTSLOAD	S7	S8	S9	S10	S11	S12	B1	B2	B3	B6	B7	B8	B9	B10	B11	B12	B13	B14	B15	B16
(kN)	10^{-6}	10^{-6}	10^{-6}	10^{-6}	10^{-6}	10^{-6}	10^{-6}	10^{-6}	10^{-6}	10^{-6}	10^{-6}	10^{-6}	10^{-6}	10^{-6}	10^{-6}	10^{-6}	10^{-6}	10^{-6}	10^{-6}	10^{-6}
2	400	25625	513	104	33	6038	592	622	99	1029	256	658	17	-62	11525	3679	273	403	437	394
32	337	25625	442	103	32	5988	796	841	38	1013	472	847	122	37	11359	3501	211	316	538	488
69	265	25625	384	99	32	5820	1035	1116	-12	1103	757	1033	386	371	11063	3234	125	161	720	650
82	250	25625	364	98	31	5769	1113	1202	-30	1147	859	1105	474	485	10975	3164	91	119	773	697
84	248	25625	360	97	32	5752	1129	1222	-34	1130	887	1123	494	508	10956	3149	85	111	789	714
81	246	25625	354	98	32	5727	1011	1093	-3	1238	808	1048	517	535	10938	3134	75	101	806	733
111	238	25625	323	96	33	5713	1183	1284	-47	1328	1025	1215	709	769	10731	2992	-12	15	952	875
139	218	25625	298	100	27	5731	1364	1473	-81	1368	1241	1408	913	1001	10544	2864	-74	-41	1073	992
168	174	25625	275	103	30	5706	1524	1644	-114	1425	1524	1640	1108	1219	10358	2773	-137	-103	1226	1144
185	180	25625	273	98	37	5775	1354	1464	-75	945	1168	1277	1249	1378	10150	2697	-165	-130	1340	1253
164	194	25625	274	100	39	5777	1334	1444	-70	966	1148	1256	1248	1377	10153	2696	-166	-129	1341	1253
197	314	25625	274	149	170	5795	1383	1486	-71	1429	1277	1394	1520	1655	9936	2614	-214	-175	1545	1447
214	437	25625	275	211	182	5838	1476	1575	-83	1437	1388	1497	1640	1775	9833	2569	-238	-201	1640	1545
217	472	25625	276	215	183	5844	1490	1583	-82	1433	1402	1510	1662	1797	9831	2567	-241	-204	1660	1567
219	594	25625	278	225	184	5850	1504	1589	-77	1383	1417	1521	1665	1798	9831	2568	-245	-209	1683	1592
260	2408	25625	292	1038	1270	6427	1186	1709	173	1359	1624	1698	1934	2081	9798	2514	-151	-104	1926	1831
286	4156	25625	1763	945	1438	6556	1293	1830	285	206	1837	1846	2007	2158	9747	2486	-244	-193	2116	2030
296	7419	25625	2155	976	1553	6578	1315	1916	378	1325	1996	1988	1988	2141	10144	2657	-268	-184	2134	2048
304	7350	25625	2372	989	1590	6583	1326	1934	433	1293	2050	2029	2000	2153	10163	2626	-273	-176	2173	2089
195	6467	25625	2138	906	1545	6498	757	1119	490	1436	1095	1128	1524	1650	10367	2764	-151	-71	1723	1645
95	5750	25625	1179	780	1315	6213	328	445	556	1348	362	423	920	1006	10561	2912	-6	35	1208	1142
-2	5369	25625	-157	208	897	6338	104	109	440	1220	167	385	257	245	10947	3246	241	294	512	473

Net								
MTSLOAD	C1	C2	C3	C4	C5	C6	C7	C8
(kN)	10^{-6}	10^{-6}	10^{-6}	10^{-6}	10^{-6}	10^{-6}	10^{-6}	10^{-6}
2	-528	-436	124	286	-386	-327	113	211
32	-439	-363	69	224	-329	-288	17	125
69	-245	-224	-25	98	-215	-208	-153	-26
82	-172	-171	-47	59	-175	-180	-209	-74
84	-157	-159	-52	52	-166	-172	-220	-84
81	-149	-147	-58	39	-149	-157	-232	-97
111	26	-3	-107	-39	-59	-96	-350	-195
139	249	161	-147	-104	64	-20	-479	-301
168	479	348	-187	-170	274	90	-613	-413
185	617	476	-225	-235	409	198	-685	-487
164	616	477	-226	-237	410	200	-684	-487
197	899	755	-293	-337	725	450	-868	-653
214	1017	868	-312	-372	841	540	-958	-724
217	1040	888	-317	-377	863	557	-971	-735
219	1065	908	-321	-381	888	581	-986	-747
260	1450	1248	-404	-475	1278	948	-1252	-961
286	1703	1486	-462	-539	1518	1192	-1430	-1095
296	1883	1664	-514	-588	1688	1395	-1547	-1182
304	1994	1769	-548	-621	1790	1504	-1618	-1239
195	1534	1394	-488	-584	1291	1142	-1379	-1036
95	943	881	-379	-486	726	683	-1003	-750
-2	82	116	-87	-188	60	96	-375	-252

.

C.8 Phase B: Summary of Experimental Results

Net			Second-Storey Beam		Avg.	Lateral	First-Storey Beam		Avg.
MTSLOAD	DATASET	Load	North Hoz.	South Hor.	Beam	Drift	NHM	SHM	Beam
(kN)	(#)	Stage	δ (mm)	δ (mm)	δ (mm)	%	(mm)	(mm)	δ (mm)
0	0		0.00	0.00	0.00		0.00	0.00	0.00
233	73	LC1: +0.75Dy	18.78	18.83	18.81	0.47	7.46	8.60	8.03
1	150		2.02	2.05	2.04	0.05	0.76	0.83	0.80
-247	230	LC1: -0.75Dy	-19.52	-18.96	-19.24	-0.48	-8.96	-8.03	-8.49
1	295		-1.68	-1.55	-1.62	-0.04	-0.77	-0.60	-0.68
233	423	LC2: +0.75Dy	19.27	19.38	19.32	0.48	7.63	8.86	8.24
-1	479		1.33	1.40	1.37	0.03	0.46	0.56	0.51
-241	548	LC2: -0.75Dy	-19.87	-19.27	-19.57	-0.49	-9.12	-8.13	-8.62
1	616		-1.37	-1.25	-1.31	-0.03	-0.63	-0.50	-0.56
291	690	LC3 +1.0Dy	25.10	25.34	25.22	0.63	9.92	11.52	10.72
-2	752		1.90	1.97	1.93	0.05	0.65	0.79	0.72
-298	835	LC3: -1.0Dy	-26.07	-25.27	-25.67	-0.64	-11.86	-10.38	-11.12
-1	908		-2.28	-2.13	-2.20	-0.06	-1.02	-0.77	-0.90
283	968	LC4: +1.0Dy	25.28	25.53	25.41	0.64	9.94	11.60	10.77
0	1023		1.70	1.75	1.72	0.04	0.55	0.72	0.63
-289	1091	LC4: -1.0Dy	-26.13	-25.34	-25.73	-0.64	-11.87	-10.38	-11.12
-1	1158		-1.99	-1.87	-1.93	-0.05	-0.92	-0.68	-0.80
399	1277	LC5: +2.0Dy	50.47	51.80	51.13	1.28	18.48	22.33	20.40
-3	1422		11.78	12.48	12.13	0.30	3.50	5.55	4.52
-395	1567	LC5: -2.0Dy	-52.71	-50.64	-51.68	-1.29	-22.99	-17.85	-20.42
-1	1638		-11.00	-9.27	-10.14	-0.25	-5.60	-1.82	-3.71
377	1742	LC6: +2.0Dy	50.10	52.08	51.09	1.28	17.47	22.93	20.20
0	1811		7.05	8.62	7.84	0.20	0.74	4.76	2.75
-384	1918	LC6: -2.0Dy	-52.65	-50.46	-51.55	-1.29	-23.17	-17.51	-20.34
1	1999		-8.31	-6.47	-7.39	-0.18	-4.76	-0.50	-2.63
422	2148	LC7: +3.0Dy	75.94	79.91	77.93	1.95	26.59	34.69	30.64
1	2227		21.21	24.28	22.75	0.57	5.55	11.89	8.72
-424	2374	LC7: -3.0Dy	-79.53	-75.32	-77.42	-1.94	-34.38	-24.81	-29.60
-1	2441		-20.36	-16.42	-18.39	-0.46	-10.36	-2.47	-6.41
406	2818	LC8: +3.0Dy	75.52	79.68	77.60	1.94	25.50	35.36	30.43
-3	2881		14.43	18.00	16.21	0.41	1.87	10.15	6.01
-414	2993	LC8: -3.0Dy	-79.90	-75.52	-77.71	-1.94	-34.94	-24.66	-29.80
-1	3058		-16.77	-12.57	-14.67	-0.37	-9.36	-0.84	-5.10
417	3240	LC9: +4.0Dy	100.59	106.69	103.64	2.59	36.21	48.30	42.26
1	3326		35.18	40.22	37.70	0.94	10.71	20.87	15.79
-422	3568	LC9: -4.0Dy	-101.90	-95.17	-98.53	-2.46	-45.17	-31.65	-38.41
0	3697		-39.63	-32.99	-36.31	-0.91	-19.95	-8.27	-14.11
403	3891	LC10: +4.0Dy	100.22	106.54	103.38	2.58	35.51	48.96	42.24
-1	3966		26.92	32.95	29.94	0.75	7.19	18.92	13.05
-412	4093	LC10: -4.0Dy	-107.94	-100.85	-104.40	-2.61	-48.10	-34.03	-41.06
2	4134		-34.35	-27.67	-31.01	-0.78	-18.11	-6.17	-12.14
397	4349	LC11: +4.0Dy	101.06	107.24	104.15	2.60	36.12	49.67	42.89
1	4394		26.48	32.02	29.25	0.73	7.03	18.92	12.97
-403	4500	LC11: -4.0Dy	-106.93	-100.40	-103.66	-2.59	-47.79	-33.72	-40.76
-1	4540		-33.12	-26.85	-29.99	-0.75	-17.79	-5.93	-11.86
377	4682	LS12: +4.0	81.44	104.58	93.01	2.33	35.34	48.54	41.94
-1	4880		28.11	33.62	30.86	0.77	7.64	19.43	13.54
-395	4979	LS12: -4.0Dy	-106.41	-100.37	-103.39	-2.58	-47.70	-33.69	-40.70
2	5028		-31.19	-25.23	-28.21	-0.71	-17.14	-5.21	-11.17
-369	5338		-100.63	-94.54	-97.58	-2.44	-45.42	-31.60	-38.51
-444	5441	LS13	-167.81	-159.74	-163.77	-4.09	-76.68	-59.84	-68.26
-185	5470		-141.60	-133.69	-137.64	-3.44	-65.40	-49.89	-57.65
15	0		-85.68	-77.67	-81.68	-2.04	-42.74	-27.18	-34.96

Net			Out-of-Plane								
MTSLOAD	NHB	SHB	NHTOP	SHTOP	BASESLIP	NVT	NVM	NVB	SVT	SVM	SVB
(kN)	(mm)	(mm)	(mm)	(mm)	(mm)	(mm)	(mm)	(mm)	(mm)	(mm)	(mm)
0	0.00	0.00	0.00	0.00	0.00	0.00	0.00	0.00	0.00	0.00	0.00
233	-0.24	0.21	-0.75	3.42	0.04	-0.37	-0.24	0.04	1.01	0.70	-0.38
1	-0.06	0.01	0.16	3.66	0.03	0.80	0.45	-0.08	1.13	0.74	-0.32
-247	0.44	-0.27	0.92	4.57	0.06	0.91	0.60	-0.16	0.16	0.05	-0.15
1	0.08	-0.08	0.72	4.33	0.03	0.92	0.54	-0.09	1.13	0.72	-0.31
233	-0.21	0.24	-0.55	3.79	0.04	-0.40	-0.26	0.05	1.02	0.70	-0.38
-1	-0.01	-0.02	0.32	3.92	0.03	0.78	0.46	-0.08	1.13	0.74	-0.33
-241	0.48	-0.29	0.93	4.58	0.06	0.86	0.58	-0.15	0.14	0.05	-0.16
1	0.10	-0.06	0.69	4.28	0.03	0.89	0.53	-0.09	1.12	0.72	-0.32
291	-0.29	0.29	-1.72	3.40	0.04	-0.93	-0.58	0.09	0.88	0.62	-0.39
-2	-0.03	0.00	0.19	3.85	0.03	0.78	0.46	-0.08	1.15	0.75	-0.33
-298	0.57	-0.27	1.11	4.79	0.08	0.79	0.55	-0.16	-0.21	-0.17	-0.11
-1	0.12	-0.06	0.84	4.45	0.03	0.92	0.55	-0.09	1.11	0.72	-0.31
283	-0.29	0.29	-1.91	3.48	0.05	-0.92	-0.57	0.09	0.90	0.63	-0.39
0	-0.03	0.00	0.09	3.82	0.03	0.78	0.47	-0.07	1.15	0.76	-0.33
-289	0.57	-0.27	0.99	4.77	0.08	0.78	0.54	-0.16	-0.20	-0.15	-0.12
-1	0.11	-0.06	0.71	4.36	0.03	0.92	0.56	-0.09	1.14	0.74	-0.32
399	-0.51	0.61	-7.15	1.81	0.10	-2.50	-1.69	0.26	0.18	0.12	-0.42
-3	-0.07	0.16	-1.05	3.36	0.06	0.51	0.29	-0.06	0.98	0.63	-0.36
-395	1.04	-0.36	1.27	5.78	0.15	0.18	0.10	-0.13	-1.24	-0.75	-0.02
-1	0.41	-0.01	1.36	5.91	0.07	0.84	0.49	-0.09	1.14	0.79	-0.37
377	-0.40	0.66	-6.26	3.21	0.11	-2.31	-1.55	0.24	0.32	0.18	-0.43
0	0.08	0.17	-1.12	4.29	0.07	0.54	0.36	-0.07	1.16	0.76	-0.39
-384	1.08	-0.35	1.20	6.03	0.16	0.20	0.10	-0.12	-1.15	-0.68	-0.03
1	0.41	0.02	1.30	6.22	0.07	0.89	0.52	-0.09	1.26	0.85	-0.39
422	-0.66	1.23	-10.68	1.64	0.15	-3.39	-2.58	0.47	-0.42	-0.53	-0.42
1	-0.09	0.69	-2.25	3.89	0.08	0.39	0.07	-0.02	0.88	0.40	-0.39
-424	1.82	-0.26	2.72	8.65	0.22	-0.18	-0.45	-0.02	-1.67	-1.31	0.10
-1	1.05	0.33	3.52	9.81	0.09	0.98	0.37	-0.04	1.57	0.72	-0.37
406	-0.29	1.50	-9.96	4.25	0.15	-3.25	-2.59	0.50	0.30	-0.45	-0.42
-3	0.46	0.80	-1.11	6.16	0.07	0.62	0.12	0.01	1.63	0.54	-0.42
-414	2.05	-0.15	3.44	9.30	0.22	0.03	-0.46	0.01	-0.63	-1.25	0.09
-1	1.17	0.52	3.89	11.01	0.08	1.25	0.42	-0.02	2.52	0.82	-0.41
417	-0.61	2.94	-14.92	4.23	0.15	-4.29	-3.75	0.66	0.16	-1.25	-0.43
1	0.06	2.17	-2.50	7.17	0.06	0.22	-0.57	0.05	1.80	-0.06	-0.44
-422	2.83	0.84	5.93	12.72	0.23	-0.16	-1.09	0.05	-1.16	-1.96	0.14
0	2.20	1.48	7.01	16.48	0.08	1.03	-0.25	0.00	2.65	0.12	-0.40
403	-0.11	3.69	-10.57	10.76	0.14	-4.03	-3.79	0.65	1.71	-1.16	-0.44
-1	0.92	2.80	-0.70	11.35	0.05	0.28	-0.80	0.05	3.11	-0.03	-0.46
-412	3.56	1.30	5.53	13.28	0.22	-0.25	-1.32	0.08	-0.85	-2.13	0.14
2	2.59	2.45	6.52	17.57	0.09	1.24	-0.24	0.02	2.89	0.16	-0.41
397	0.31	4.62	-13.87	10.92	0.15	-4.24	-4.06	0.68	1.69	-1.24	-0.43
1	1.43	3.61	-1.33	11.91	0.06	0.33	-0.91	0.06	3.15	-0.02	-0.47
-403	3.75	1.86	5.48	14.54	0.23	-0.18	-1.35	0.10	-0.39	-2.07	0.12
-1	2.79	2.87	5.95	17.90	0.08	1.34	-0.25	0.03	2.98	0.16	-0.43
377	0.59	4.78	25.63	9.02	0.13	-5.27	-5.03	0.71	1.58	-1.30	-0.43
-1	1.58	3.81	-9.44	10.08	0.05	-0.21	-1.39	0.07	2.98	-0.14	-0.47
-395	3.89	1.97	2.74	13.56	0.21	-0.39	-1.49	0.11	-0.43	-2.08	0.10
2	2.92	3.11	3.75	17.88	0.06	1.21	-0.36	0.03	3.07	0.14	-0.43
-369	3.92	2.28	0.26	13.78	0.19	-0.41	-1.50	0.12	-0.10	-1.89	0.05
-444	6.32	2.61	1.85	12.98	0.23	-2.54	-3.41	0.13	-3.30	-4.39	0.29
-185	6.31	2.80	2.35	14.21	0.11	-1.66	-2.91	0.11	-1.26	-3.07	-0.07
15	5.43	3.74	3.45	18.75	0.03	-0.47	-2.00	0.05	1.16	-1.43	-0.39

Net												
MTSLOAD	S1	S2	S6	S7	S9	S10	S11	B1	B2	B3	B6	B8
(kN)	10^{-6}	10^{-6}	10^{-6}	10^{-6}	10^{-6}	10^{-6}	10^{-6}	10^{-6}	10^{-6}	10^{-6}	10^{-6}	10^{-6}
0	0	0	0	0	0	0	0	0	0	0	0	0
233	1636	2594	1369	5486	-125	108	651	-358	-226	2265	-2561	384
1	683	657	498	5350	-122	105	655	46	73	404	1035	465
-247	1682	1528	584	6325	-103	522	1292	1910	2184	21	32	2587
1	717	889	488	5461	-119	210	798	56	112	411	-8613	683
233	1748	2986	1568	5681	-71	154	694	-333	-237	2307	-16881	581
-1	668	806	600	5383	-85	150	708	107	91	404	-6869	678
-241	1656	1663	599	6391	-79	623	1384	1871	2103	25	-5428	2534
1	623	790	484	5406	-101	176	770	81	79	408	-9688	652
291	2225	5363	2105	5888	82	149	688	-387	-258	2942	25625	596
-2	655	2792	666	5413	44	149	705	147	140	603	-8930	687
-298	1791	4017	694	6925	-9	934	1838	2208	2467	201	-3825	4747
-1	610	2923	536	5444	-38	184	870	107	106	613	-4228	2713
283	2224	5569	2239	5919	426	139	717	-384	-284	2984	-695	2498
0	593	2915	672	5381	77	136	730	148	132	587	243	2673
-289	1761	4172	719	6920	15	920	1902	2129	2381	213	1306	5063
-1	571	2965	505	5400	-16	144	815	112	108	594	1891	2733
399	2295	7398	2517	6313	1897	961	1641	-244	86	25625	25625	2922
-3	930	4703	490	5428	211	284	1053	578	672	25625	25625	3120
-395	2469	6756	1056	12419	177	1013	3071	13897	11188	25625	25625	16978
-1	779	4646	856	10113	143	124	909	7563	4743	25625	25625	9086
377	2961	7306	15583	11258	2117	887	1802	3830	1588	25625	25625	6031
0	446	3327	7744	10169	217	105	894	5606	4014	25625	25625	7525
-384	2296	5341	7875	12594	276	1346	3080	9719	8083	25625	25625	10361
1	434	3325	7331	10194	191	59	733	4879	3014	25625	25625	6744
422	1295	4827	13011	11492	2604	1096	1932	2916	1393	25625	25625	5581
1	136	3065	6900	10050	222	52	791	4970	3611	25625	25625	6703
-424	2127	6647	7542	15463	747	1019	2928	11311	6619	25625	25625	10820
-1	43	3504	6831	8400	338	-111	10	4872	2336	25625	25625	5913
406	1827	4570	12769	9038	2784	1127	1993	-898	-456	25625	25625	2453
-3	44	2757	7031	7311	257	-174	420	1732	2431	25625	25625	3637
-414	2159	6138	7284	9664	1169	1036	15558	7263	4761	25625	25625	7788
-1	-21	3080	6600	6781	350	-193	11700	2845	1859	25625	25625	4114
417	1285	4653	8341	8250	3472	1276	25625	-2311	-477	25625	25625	1373
1	-65	2799	6544	6513	801	-210	21270	197	2340	25625	25625	2298
-422	1571	6519	6948	8925	2839	1060	25625	7581	5088	25625	25625	7438
0	-144	3222	5869	5913	904	-354	25625	2239	1739	25625	25625	3054
403	1188	4475	6981	7675	13305	1106	25625	-2284	-680	25625	25625	989
-1	-134	2787	6128	6069	9888	-287	25625	661	2206	25625	25625	1950
-412	1488	5239	6681	8144	12309	1058	25625	6375	4590	25625	25625	6947
2	-154	3051	5591	5763	9994	-379	25625	1727	1599	25625	25625	2909
397	1063	4407	6564	7572	12575	1062	25625	-2075	-893	25625	25625	1871
1	-148	2804	5914	5900	6563	-326	25625	878	1847	25625	25625	2953
-403	1361	5011	6425	7838	8825	1100	25625	5588	4184	25625	25625	6742
-1	-165	2995	5663	5831	6345	-329	25625	1768	1915	25625	25625	3359
377	741	4346	6044	7338	9481	961	25625	-1544	-727	25625	25625	2531
-1	-130	2673	5881	5763	6038	-347	25625	1065	1754	25625	25625	3316
-395	958	4799	25625	7669	7688	1120	25625	5188	3888	25625	25625	6544
2	-170	3018	5470	5700	5688	-341	25625	1400	1442	25625	25625	3186
-369	836	4602	25625	7667	7800	1241	25625	4718	3813	25625	25625	6400
-444	1313	4744	25625	7825	8013	1239	25625	6736	5431	25625	25625	9145
-185	249	3506	25625	6169	6375	215	25625	2572	1960	25625	25625	4631
15	-118	3128	25625	5448	5292	-499	25625	1519	1528	25625	25625	3433

Net													
MTSLOAD	B9	B10	B13	B14	B15	B16	C1	C3	C4	C5	C6	C7	C8
(kN)	(ue)	(ue)	(ue)	(ue)	(ue)	(ue)	(ue)	(ue)	(ue)	(ue)	(ue)	(ue)	(ue)
0	0	0	0	0	0	0	0	0	0	0	0	0	0
233	-106	-177	1410	1751	-192	-193	-1189	722	834	-417	-292	767	737
1	221	162	219	324	326	312	-249	-117	-24	-158	-131	-215	-87
-247	1517	1608	-217	-91	1373	1336	1070	-410	-344	897	661	-1245	-858
1	324	284	189	270	440	430	-117	-115	-122	-71	-54	-326	-187
233	-94	-170	1457	1805	-179	-173	-1192	730	862	-423	-297	781	750
-1	252	189	215	315	370	359	-212	-137	-51	-145	-118	-238	-109
-241	1526	1619	-198	-71	1388	1351	1077	-417	-354	906	677	-1243	-858
1	302	263	193	275	426	414	-114	-115	-122	-88	-70	-311	-175
291	-135	-217	1901	2272	-292	-288	-1430	981	1181	-480	-336	1087	1022
-2	245	182	232	339	364	354	-227	-150	-36	-154	-132	-231	-97
-298	1943	2057	-193	-66	1707	1676	1400	-469	-405	1252	969	-1459	-1031
-1	351	321	202	275	461	447	-86	-122	-139	-62	-44	-343	-205
283	-125	-208	1868	2230	-285	-280	-1422	960	1174	-481	-340	1064	1006
0	254	195	236	334	371	359	-226	-149	-46	-149	-126	-234	-102
-289	1910	2019	-188	-58	1702	1673	1385	-477	-412	1240	966	-1455	-1025
-1	335	306	192	268	445	431	-98	-125	-141	-67	-59	-342	-206
399	-37	-177	10569	11025	-443	-456	-1669	1917	2343	-704	-534	2015	1908
-3	285	204	9955	8605	355	335	-653	100	362	-279	-283	-75	100
-395	18527	13275	4320	4841	12406	25625	1754	-656	-605	2480	2128	-2215	-1555
-1	12541	7370	5663	6075	5842	24369	34	-108	-182	294	288	-667	-451
377	7669	3366	15322	15020	1760	15119	-1909	1934	2369	-676	-508	1843	1766
0	9261	5194	12413	5175	3960	17039	-727	39	306	-99	-125	-279	-87
-384	12080	10800	6313	2190	7861	25625	1678	-639	-593	2434	2094	-2230	-1550
1	7963	4968	7806	3758	3642	23423	-92	-34	-103	235	205	-625	-407
422	5611	3435	25028	8519	1520	15544	-4222	5308	3610	-931	-708	2507	2505
1	6923	5025	19131	2863	3573	17945	-3636	2370	973	-344	-322	-129	169
-424	12295	25625	10514	-2050	7595	25625	7770	-94	-321	8225	2678	-4753	-1841
-1	8469	3954	12248	1140	2867	25625	3645	918	173	5145	222	-3172	-507
406	3405	1577	25625	4352	-3537	15816	-4963	5281	3561	2117	-698	3466	2397
-3	5193	4143	25625	795	95	18323	-3045	2267	802	2788	-269	520	5
-414	10298	25625	11031	-2868	4921	25625	4336	-2	-296	8497	2633	-5189	-1839
-1	6913	3128	12881	605	1460	25625	1804	1091	237	5253	155	-3261	-473
417	3535	1710	25625	4909	-2818	16838	-6753	7148	3837	1882	-749	15678	2628
1	5047	4574	25625	1159	404	19261	-4741	2243	934	2439	-348	3867	52
-422	12066	25625	13575	-3576	4953	25625	4417	-405	-154	11600	2685	-11355	-1921
0	7856	3004	17886	293	1132	25625	1705	1611	332	4861	90	-6731	-508
403	2145	1317	25625	3717	-1882	25625	-6764	4964	3850	-709	-763	4213	2573
-1	4379	4820	25625	1129	891	25625	-4377	894	798	1881	-324	-291	-34
-412	10019	25625	13942	-2456	4707	25625	4205	-216	-180	6828	2684	-10313	-1903
2	6331	4266	25625	555	1014	25625	1304	1775	367	2326	21	-5105	-410
397	2566	780	25625	3955	-1898	25625	-7000	5431	3847	-1510	-771	4356	2619
1	4323	3975	25625	1218	777	25625	-4202	991	791	1292	-352	-134	-19
-403	9200	25625	13547	-2091	4443	25625	3706	-273	-188	5838	2680	-9406	-1896
-1	5817	5336	25625	556	1560	25625	1086	1261	344	2468	19	-4525	-411
377	2929	1445	25625	3085	-1596	25625	-6709	5713	3788	-602	-672	5033	2663
-1	4528	4267	25625	997	995	25625	-4203	1070	871	1394	-362	89	-33
-395	8806	25625	13481	-1443	4307	25625	3423	-229	-208	5550	2668	-8550	-1885
2	5494	4731	25625	1016	806	25625	471	1845	354	1448	-6	-3931	-378
-369	8206	25625	13545	-966	4087	25625	2739	-695	-198	5350	2563	-7811	-1821
-444	12598	25625	11503	-675	5173	25625	4658	-351	-337	5684	2778	-15006	-2019
-185	7888	25625	11411	232	1606	25625	2181	580	-211	2512	1456	-12163	-1447
15	6431	25625	18463	1537	640	25625	465	1831	204	1119	-104	-9050	-388

Net													
MTSLOAD	F1	F2	F3	F4	F5	F7	F8	F9	F10	F11	F12	F13	F14
(kN)	10^{-6}	10^{-6}	10^{-6}	10^{-6}	10^{-6}	10^{-6}	10^{-6}	10^{-6}	10^{-6}	10^{-6}	10^{-6}	10^{-6}	10^{-6}
0	0	0	0	0	0	0	0	0	0	0	0	0	0
233	80	28	818	3	9	92	1806	55	13	5	36	110	2
1	90	-3	296	6	-3	55	357	178	15	-3	25	40	3
-247	141	5	627	7	1	138	638	424	37	49	104	71	221
1	75	27	328	6	-1	162	292	185	4	86	435	46	66
233	318	36	1241	6	10	156	1674	959	23	48	283	204	26
-1	140	12	316	8	-3	121	345	345	11	45	240	136	28
-241	218	163	746	10	1	646	596	698	14	663	2130	122	258
1	110	90	355	4	-2	170	261	286	17	341	330	104	60
291	717	85	1878	10	11	419	1879	1864	58	252	347	1594	28
-2	294	58	430	15	-6	306	464	477	37	235	254	421	30
-298	573	1940	939	10	7	1118	754	898	1660	2039	2070	1297	480
-1	304	677	444	0	1	283	336	380	465	458	485	504	128
283	888	504	2135	34	11	985	2088	2103	360	341	490	1777	64
0	328	480	420	11	-5	437	466	488	276	289	293	438	57
-289	725	2561	928	0	14	1150	782	909	1875	2125	2160	1441	530
-1	340	604	399	-7	2	344	350	382	431	417	487	453	110
399	1128	520	2830	538	15	2889	3506	3150	763	700	822	2113	1288
-3	412	811	365	204	-12	743	759	682	677	702	772	437	429
-395	1825	3524	1069	231	103	1635	1363	1312	2466	2654	2811	2011	1717
-1	505	634	437	118	14	779	870	838	450	466	482	463	443
377	1469	636	3148	1006	11	3596	4385	3917	961	956	1282	2128	1583
0	520	664	330	263	-6	930	947	922	533	569	638	488	417
-384	2199	3560	1197	318	119	2106	1639	1605	2528	2713	2945	2252	1995
1	596	632	435	160	11	929	964	959	521	526	630	520	398
422	2497	784	3246	1311	10	3928	4450	4288	1306	1317	1633	2954	1867
1	792	889	478	272	4	1116	998	1031	764	792	981	660	415
-424	3302	4156	2087	893	151	3114	2771	2530	3043	3217	3394	3138	2528
-1	859	878	534	343	16	1061	1039	1152	678	657	850	766	623
406	3321	1089	3802	1497	15	4705	5125	4927	1627	1602	1951	3781	2900
-3	860	875	530	348	10	1154	1119	1075	703	688	951	828	707
-414	3322	4083	2453	1303	166	3289	3100	2753	3037	3197	3448	3296	2806
-1	847	964	544	417	16	1141	1136	1178	725	665	946	857	778
417	3650	1428	3801	1820	24	4893	5306	5041	1854	1844	2347	4281	2684
1	972	930	525	444	16	1138	1193	1102	720	694	986	991	813
-422	3691	4447	2902	2980	197	3663	3733	3211	3745	3864	4583	3767	3340
0	1267	1777	903	788	41	1471	1516	1330	1489	1400	2159	1252	966
403	4518	2371	4238	2598	161	5625	5825	5519	2211	2273	3192	5734	3438
-1	1225	1348	763	684	105	1491	1454	1280	879	908	1578	1299	1110
-412	3403	4278	2742	3250	277	3550	3694	3080	3756	3897	4590	3568	3433
2	1147	1583	703	705	108	1381	1458	1216	1283	1229	1953	1291	1052
397	4828	2677	3906	2822	411	5506	5663	5322	2339	2450	3422	6206	3554
1	1313	1513	821	693	149	1605	1548	1339	975	1032	1709	1427	1122
-403	3332	4121	2840	3369	340	3513	3682	3003	3778	3919	4645	3430	3439
-1	1125	1439	669	683	150	1389	1472	1173	1234	1180	1900	1274	1064
377	4428	2598	3367	2725	422	5483	5538	5219	2393	2525	3536	6431	3586
-1	1339	1602	938	755	149	1727	1645	1400	1098	1177	1876	1573	1164
-395	3285	3919	2972	3433	353	3469	3678	2940	3655	3844	4609	3286	3436
2	1116	1384	788	682	150	1360	1454	1140	1061	1100	1836	-23972	1017
-369	3116	3532	2944	3375	349	3350	3514	2764	3304	3501	4265	3070	3312
-444	4094	4174	4214	3553	437	4464	4640	3764	3965	4311	5156	3738	3706
-185	3096	2968	3153	2613	337	3209	3328	2664	3102	3248	4042	2720	2604
15	1596	1694	1239	786	200	1596	1625	1236	1581	1605	2386	1588	1153

Net													
MTSLOAD	F15	F16	F17	F18	F19	F20	F21	F22	F23	F24	F25	F26	F27
(kN)	10^{-6}	10^{-6}	10^{-6}	10^{-6}	10^{-6}	10^{-6}	10^{-6}	10^{-6}	10^{-6}	10^{-6}	10^{-6}	10^{-6}	10^{-6}
0	0	0	0	0	0	0	0	0	0	0	0	0	0
233	13	3	15	51	36	64	33	-18	-55	-8	13	3	33
1	2	-2	16	14	17	98	9	9	13	13	14	15	43
-247	25	15	33	160	23	160	9	851	1390	68	230	675	117
1	10	6	18	59	16	86	7	282	327	28	135	162	65
233	15	0	21	71	50	192	34	100	43	6	85	71	213
-1	3	-4	20	29	27	165	11	149	117	16	75	67	142
-241	28	18	43	188	34	192	16	993	1438	65	463	596	156
1	10	4	21	46	17	150	6	258	263	22	131	132	99
291	21	3	26	83	102	332	43	97	34	40	83	61	771
-2	7	-2	25	28	67	239	14	158	110	30	78	63	287
-298	39	31	59	304	57	278	30	1339	1872	74	975	694	265
-1	21	12	31	65	31	197	11	336	320	25	293	168	195
283	29	7	35	93	202	487	51	98	25	64	133	55	1042
0	11	1	29	35	89	238	19	171	109	30	143	66	344
-289	49	41	73	314	70	281	36	1365	1796	72	1333	609	262
-1	25	14	37	55	37	189	13	322	290	25	276	168	205
399	154	77	89	125	1853	1547	52	111	-16	2602	135	32	1616
-3	35	33	60	33	433	369	24	837	112	596	772	396	428
-395	1042	148	231	657	263	423	96	2991	2273	471	1986	2347	2002
-1	416	53	130	126	242	312	37	536	223	463	431	697	610
377	376	101	185	194	2201	1768	988	1408	37	2515	1672	1492	1710
0	226	44	121	77	425	454	316	687	92	772	686	709	731
-384	1373	177	282	779	319	576	244	3250	2226	537	2539	2945	2847
1	382	56	153	148	279	415	234	789	188	448	512	693	650
422	428	133	254	245	2530	2006	2912	2090	34	2890	2203	1986	2206
1	259	66	148	97	351	497	672	867	104	532	783	887	1007
-424	1287	229	606	1222	546	1618	1440	4095	2939	998	3470	3978	3870
-1	354	68	296	205	371	681	752	963	322	498	594	803	738
406	405	167	441	305	1863	2157	3071	2535	370	3060	2480	2263	2489
-3	249	68	232	170	345	523	722	849	364	584	703	750	906
-414	1353	264	813	1673	642	2172	1764	4046	2968	1201	3414	3798	3768
-1	317	72	329	253	355	616	694	887	354	486	576	719	694
417	428	373	1019	2186	1809	2271	3740	3579	699	3601	3505	3131	3422
1	231	143	384	531	396	523	836	856	371	720	814	788	984
-422	1527	456	1282	2168	1609	3237	2132	4058	3418	1492	3409	3888	3838
0	396	172	608	634	449	803	757	1004	537	552	672	819	808
403	456	1359	1675	2739	2156	2789	3675	3654	1514	3493	3539	3203	3520
-1	301	444	521	663	459	761	786	885	477	658	670	704	922
-412	1658	950	1529	2839	2220	3126	2253	3847	3453	1764	3109	3567	3552
2	444	384	668	765	571	922	744	988	549	546	677	809	814
397	746	1817	1897	3022	2464	3092	3521	3608	1871	3467	3594	3263	3575
1	383	461	563	773	601	889	736	892	512	645	688	733	986
-403	1657	1588	1646	3040	2348	3281	2216	3760	3523	1808	2922	3380	3423
-1	418	404	693	805	565	975	756	976	578	515	668	759	849
377	929	2064	2035	3214	2592	3359	3185	3243	1962	2981	3663	3359	3713
-1	444	479	674	841	650	1090	723	925	595	626	772	816	1091
-395	1645	1664	1723	3117	2382	3392	2164	3714	3624	1830	2841	3316	3367
2	476	427	724	877	610	1107	793	988	622	530	725	836	895
-369	1569	1591	1707	3039	2354	3314	2060	3618	3671	1858	2754	3197	3298
-444	2072	2202	2254	3429	2581	3796	3006	4413	4282	3057	3425	4197	4044
-185	1351	1436	2024	2728	2053	3041	2361	3749	3486	2710	2855	3442	3327
15	529	535	1077	950	659	1248	1117	1481	951	787	803	1164	1086

Net				
MTSLOAD	F28	F29	F31	F32
(kN)	10^{-6}	10^{-6}	10^{-6}	10^{-6}
0	0	0	0	0
233	80	6	-104	-45
1	37	6	-10	-10
-247	47	157	1496	923
1	17	61	236	251
233	93	38	-57	35
-1	41	37	66	77
-241	58	179	1540	1092
1	17	55	165	197
291	117	56	-85	21
-2	51	39	41	71
-298	75	225	2004	1627
-1	21	69	232	262
283	138	61	-90	3
0	57	43	49	62
-289	75	232	1998	1639
-1	24	63	199	220
399	226	2058	-66	-22
-3	61	467	60	47
-395	1304	1246	2264	2116
-1	277	642	146	303
377	2098	2584	909	14
0	800	868	359	82
-384	1695	1395	2068	2213
1	670	631	159	343
422	3284	2775	1407	3
1	843	803	342	215
-424	2081	2308	2486	2474
-1	739	771	431	274
406	3888	2887	1899	1616
-3	736	911	648	473
-414	2055	2313	2188	2203
-1	647	728	439	250
417	4419	2050	2478	2336
1	836	881	712	506
-422	2269	1764	2327	2156
0	658	587	557	390
403	4007	1889	3108	3060
-1	718	574	714	542
-412	2409	1967	2611	2456
2	601	538	573	398
397	3932	1887	3340	3343
1	667	526	696	634
-403	2272	1961	2692	2573
-1	592	486	533	454
377	3988	2104	3649	3708
-1	673	522	862	810
-395	2178	1999	2758	2636
2	637	459	607	485
-369	2033	1973	2625	2547
-444	3152	2517	3088	2981
-185	2303	2130	2430	2259
15	811	710	726	614

APPENDIX D

VecTor2 Input Files

D.1 Vector.job

D.2 Case1.s2r

D.3 Case2.s2r

D.4 Struct.s2r

D.1 Vector.job

(Model 3a)

Refer to Tables 6.4 and 6.6

```
                              * * * * * * * * * * * *
                              *     V E C T O R     *
                              *   J O B   D A T A   *
                              * * * * * * * * * * * *

Job Title       (30 char. max.)        : KV1A
Job File Name   ( 8 char. max.)        : Vector
Date            (30 char. max.)        : May 2005

STRUCTURE DATA
--------------
Structure Type                         : 2
File Name       ( 8 char. max.)        : Struct

LOADING DATA
------------
No. of Load Stages                     : 85
Starting Load Stage No.                : 1
Load Series ID  ( 5 char. max.)        : KV1

Load   File Name                                Factors
Case   (8 char. max.)        Initial    Final    LS-Inc  Type Reps    C-Inc
  1    Case1                 1.000    40.000     1.000    3    1     0.000
  2    Case2              1.000000  1.000000  0.000000    1    1  0.000000
  3    NULL               0.000000  0.000000  0.000000    1    1  0.000000
  4    NULL               0.000000  0.000000  0.000000    1    1  0.000000
  5    NULL               0.000000  0.000000  0.000000    1    1  0.000000

ANALYSIS PARAMETERS
-------------------
Analysis Mode                          (1-2) : 1
Seed File Name      (8 char. max.)             : NULL
Convergence Limit                     (>1.0) : 1.000100
Averaging Factor                      (<1.0) : 0.750
Maximum No. of Iterations                    : 40
Convergence Criteria                   (1-5) : 2
Results Files                          (1-4) : 1
Output Format                          (1-3) : 1

MATERIAL BEHAVIOUR MODELS
-------------------------
Concrete Compression Base Curve        (0-3) : 3
Concrete Compression Post-Peak         (0-3) : 2
Concrete Compression Softening         (0-8) : 1
Concrete Tension Stiffening            (0-6) : 1
Concrete Tension Softening             (0-3) : 2
Concrete Tension Splitting             (0-1) : 1
Concrete Confined Strength             (0-2) : 1
Concrete Dilation                      (0-1) : 1
Concrete Cracking Criterion            (0-4) : 1
Concrete Crack Slip Check              (0-2) : 1
Concrete Crack Width Check             (0-2) : 4
Concrete Bond or Adhesion              (0-3) : 1
Concrete Creep and Relaxation          (0-1) : 1
Concrete Hysteresis                    (0-2) : 2
Reinforcement Hysteresis               (0-2) : 1
Reinforcement Dowel Action             (0-1) : 1
Reinforcement Buckling                 (0-1) : 1
Element Strain Histories               (0-1) : 1
Element Slip Distortions               (0-4) : 1
Strain Rate Effects                    (0-1) : 1
Structural Damping                     (0-1) : 1
Geometric Nonlinearity                 (0-1) : 1
Crack Allocation Process               (0-1) : 1


<<< JOB FILE NOTES>>>
```

Summary of Material Behaviour Models:

MATERIAL BEHAVIOUR MODELS	1a	1b	1c	1d	1e	1f	1g	1h	1i	1j	1k
Concrete Compression Base Curve	3	3	3	3	3	3	3	3	3	3	3
Concrete Compression Post-Peak	2	2	2	2	2	2	2	2	2	2	2
Concrete Compression Softening	1	1	1	1	1	1	1	1	1	1	1
Concrete Tension Stiffening	1	1	1	1	1	1	1	1	1	1	1
Concrete Tension Softening	2	2	2	2	2	2	2	2	2	2	2
Concrete Tension Splitting	1	1	1	1	1	1	1	1	1	1	1
Concrete Confined Strength	1	1	1	1	1	1	1	1	1	1	1
Concrete Dilation	1	1	1	1	1	1	1	1	1	1	1
Concrete Cracking Criterion	1	1	1	1	1	1	1	1	1	1	1
Concrete Crack Slip Check	1	1	1	1	1	1	1	1	1	1	1
Concrete Crack Width Check	1	4	4	1	1	4	4	4	0	4	0
Concrete Bond or Adhesion	1	1	1	1	1	1	1	1	1	1	1
Concrete Creep and Relaxation	1	1	1	1	1	1	1	1	1	1	1
Concrete Hysteresis	2	2	2	2	2	2	2	2	2	2	2
Reinforcement Hysteresis	1	1	1	1	1	1	1	1	1	1	1
Reinforcement Dowel Action	1	2	0	1	1	2	0	1	1	1	1
Reinforcement Buckling	1	1	1	1	1	1	1	1	1	1	1
Element Strain Histories	1	1	1	1	1	1	1	1	1	1	1
Element Slip Distortions	1	1	1	1	1	1	1	1	1	1	1
Strain Rate Effects	1	1	1	1	1	1	1	1	1	1	1
Structural Damping	1	1	1	1	1	1	1	1	1	1	1
Geometric Nonlinearity	1	1	1	1	1	1	1	1	1	1	1
Crack Allocation Process	1	1	1	1	1	1	1	1	1	1	1

MATERIAL BEHAVIOUR MODELS	2a	2b	2c	3a	3b	3c
Concrete Compression Base Curve	3	3	3	3	3	3
Concrete Compression Post-Peak	2	2	2	2	2	2
Concrete Compression Softening	1	1	1	1	1	1
Concrete Tension Stiffening	1	1	1	1	1	1
Concrete Tension Softening	2	2	2	2	2	2
Concrete Tension Splitting	1	1	1	1	1	1
Concrete Confined Strength	1	1	1	1	1	1
Concrete Dilation	1	1	1	1	1	1
Concrete Cracking Criterion	1	1	1	1	1	1
Concrete Crack Slip Check	1	1	1	1	1	1
Concrete Crack Width Check	4	4	4	4	4	4
Concrete Bond or Adhesion	1	0	1	1	1	1
Concrete Creep and Relaxation	1	1	1	1	1	1
Concrete Hysteresis	2	2	2	2	2	2
Reinforcement Hysteresis	1	1	1	1	1	1
Reinforcement Dowel Action	1	1	1	1	1	1
Reinforcement Buckling	1	1	1	1	1	1
Element Strain Histories	1	1	1	1	1	1
Element Slip Distortions	1	1	1	1	1	1
Strain Rate Effects	1	1	1	1	1	1
Structural Damping	1	1	1	1	1	1
Geometric Nonlinearity	1	1	1	1	1	1
Crack Allocation Process	1	1	1	1	1	1

D.2 Case1.l2r

(Model 3a)

Refer to Figure 6.7

```
                          * * * * * * * * * * * * *
                          *     V e c T o r 2     *
                          *   L O A D   D A T A   *
                          * * * * * * * * * * * * *

                            LOAD CASE PARAMETERS
                            ********************

Structure Title      (30 char. max.)     : Enter Structure Title
Load Case Title      (30 char. max.)     : Lateral Load
Load Case File Name   (8 char. max.)     : Case1
No. of Loaded Joints                     : 0
No. of Prescribed Support Displacements  : 1
No. of Elements with Gravity Loads       : 0
No. of Elements with Temperature Loads   : 0
No. of Elements with Concrete Prestrain  : 0
No. of Elements with Ingress Pressure    : 0
No. of Element Surfaces w/ Thermal Load  : 0
No. of Nodes with Lumped Masses          : 0
No. of Nodes with Impulse Forces         : 0
Ground Acceleration Record  (0-1)        : 0

                               JOINT LOADS
                               ***********
<NOTE:>  UNITS:  KIPS OR KN
<<<<< FORMAT >>>>>
NODE    Fx    Fy    [ #NODE d(NODE) d(Fx) d(Fy) ] /
/
                           SUPPORT DISPLACEMENTS
                           *********************
<NOTE:> UNITS: MM OR IN
<<<<< FORMAT >>>>>
JNT  DOF  DISPL   [ #JNT d(JNT) ] /
  3052   1   1.000  1   1/
/

ETC.
<<< LOAD FILE NOTES >>>
```

D.3 Case2.l2r

(Model 3a)

Refer to Figure 6.7

```
                          * * * * * * * * * * * * *
                          *     V e c T o r 2     *
                          *   L O A D   D A T A   *
                          * * * * * * * * * * * * *

                            LOAD CASE PARAMETERS
                            ********************

Structure Title      (30 char. max.)     : Enter Structure Title
Load Case Title      (30 char. max.)     : Col & PT Load
Load Case File Name   (8 char. max.)     : Case2
No. of Loaded Joints                     : 24
No. of Prescribed Support Displacements  : 0
No. of Elements with Gravity Loads       : 0
No. of Elements with Temperature Loads   : 0
No. of Elements with Concrete Prestrain  : 0
No. of Elements with Ingress Pressure    : 0
No. of Element Surfaces w/ Thermal Load  : 0
No. of Nodes with Lumped Masses          : 0
No. of Nodes with Impulse Forces         : 0
Ground Acceleration Record  (0-1)        : 0

                              JOINT LOADS
                              ***********
<NOTE:>  UNITS:  KIPS OR KN
<<<<< FORMAT >>>>>
NODE    Fx    Fy    [ #NODE d(NODE) d(Fx) d(Fy) ] /
  698   0.000  -71.000  1   1   0.000   0.000/
  705   0.000  -71.000  1   1   0.000   0.000/
  731   0.000  -71.000  1   1   0.000   0.000/
  749   0.000  -71.000  1   1   0.000   0.000/
  775   0.000  -71.000  1   1   0.000   0.000/
  782   0.000  -71.000  1   1   0.000   0.000/
  3308  0.000  -46.670  1   1   0.000   0.000/
  3309  0.000  -46.670  1   1   0.000   0.000/
  3310  0.000  -46.670  1   1   0.000   0.000/
  3311  0.000  -46.670  1   1   0.000   0.000/
  3312  0.000  -46.670  1   1   0.000   0.000/
  3313  0.000  -46.670  1   1   0.000   0.000/
  3314  0.000  -46.670  1   1   0.000   0.000/
  3315  0.000  -46.670  1   1   0.000   0.000/
  3316  0.000  -46.670  1   1   0.000   0.000/
  3348  0.000  -46.670  1   1   0.000   0.000/
  3349  0.000  -46.670  1   1   0.000   0.000/
  3350  0.000  -46.670  1   1   0.000   0.000/
  3351  0.000  -46.670  1   1   0.000   0.000/
  3352  0.000  -46.670  1   1   0.000   0.000/
  3353  0.000  -46.670  1   1   0.000   0.000/
  3354  0.000  -46.670  1   1   0.000   0.000/
  3355  0.000  -46.670  1   1   0.000   0.000/
  3356  0.000  -46.670  1   1   0.000   0.000/
/
                            SUPPORT DISPLACEMENTS
                            *********************
<NOTE:> UNITS: MM OR IN
<<<<< FORMAT >>>>>
JNT  DOF  DISPL   [ #JNT d(JNT) ] /
/

ETC.
<<< LOAD FILE NOTES >>>
```

D.4 Struct.s2r

(Model 3a)

Refer to Figures 6.1 to 6.6, and Tables 6.1 to 6.3

```
                  * * * * * * * * * * * * * * * * * * *
                  *          V e c T o r 2            *
                  *   S T R U C T U R E    D A T A   *
                  * * * * * * * * * * * * * * * * * * *

                            STRUCTURAL PARAMETERS
                            *********************

Structure Title        (30 char. max.)     : Enter Structure Title
Structure File Name    ( 8 char. max.)     : Struct
No. of R.C. Material Types                 : 5
No. of Steel Material Types                : 6
No. of Bond Material Types                 : 0
No. of Rectangular Elements                : 3048
No. of Quadrilateral Elements              : 0
No. of Triangular Elements                 : 0
No. of Truss Bar Elements                  : 938
No. of Linkage Elements                    : 0
No. of Contact Elements                    : 0
No. of Joints                              : 3357
No. of Restraints                          : 124

                          MATERIAL SPECIFICATIONS
                          ***********************

                          (A) REINFORCED CONCRETE
                          -----------------------
<NOTE:> TO BE USED IN RECTANGULAR AND TRIANGULAR ELEMENTS ONLY

CONCRETE
--------
MAT  Ns    T    f'c  [ f't    Ec    e0     Mu   Cc   Agg   Dens   Kc ] [Sx  Sy]
TYP  #    mm    MPa    MPa   MPa    me          /C    mm  kg/m3  mm2/s  mm  mm
 1   1   800.0  43.0   0.0   0.0   2.31   0.0   0.0  10.0   0.0   0.0   0.0   0.0
 2   1   300.0  43.0   0.0   0.0   2.31   0.0   0.0  10.0   0.0   0.0   0.0   0.0
 3   0   300.0  43.0   0.0   0.0   2.31   0.0   0.0  10.0   0.0   0.0   0.0   0.0
 4   0   225.0  43.0   0.0   0.0   2.31   0.0   0.0  10.0   0.0   0.0   0.0   0.0
 5   0   800.0  43.0   0.0   0.0   2.31   0.0   0.0  10.0   0.0   0.0   0.0   0.0
/
REINFORCEMENT COMPONENTS
------------------------
MAT  REF  DIR   As  Db   Fy   Fu    Es    Esh   esh   Cs   Dep
TYP  TYP  deg    %  mm   MPa  MPa   MPa   MPa   me    /C    me
 1   1    90.0  0.429  11.3  455.0  583.0  192400.0  1195.0  22.8  0.0  0.0
 2   1    0.0   1.018  11.3  455.0  583.0  192400.0  1195.0  22.8  0.0  0.0
/
                                  (B) STEEL
                                  ---------
<NOTE:> TO BE USED FOR TRUSS ELEMENTS ONLY
MAT  REF    AREA   Db    Fy    Fu     Es    Esh   esh   Cs   Dep
TYP  TYP     mm2   mm   MPa   MPa    MPa    MPa    me   /C    me
  1   1    2400.0   19.5   447.0   603.0   198400.0   1372.0   17.1   0.0   0.0
  2   1    1200.0   19.5   447.0   603.0   198400.0   1372.0   17.1   0.0   0.0
  3   1    900.0    19.5   447.0   603.0   198400.0   1372.0   17.1   0.0   0.0
  4   1    600.0    19.5   447.0   603.0   198400.0   1372.0   17.1   0.0   0.0
  5   1    300.0    19.5   447.0   603.0   198400.0   1372.0   17.1   0.0   0.0
  6   1    142.0    9.5    506.0   615.0   210000.0   1025.0   28.3   0.0   0.0
/
                                  (C) BOND
                                  --------
<NOTE:> TO BE USED FOR EXTERIOR/INTERIOR BONDED ELEMENTS
MAT  REF  { Ao   U1    U2    U3    S1    S2    S3 }/{ CPF   Cmin   No.  HOOK }
TYP  TYP   mm^2  MPa   MPa   MPa   mm    mm    mm     0-1    mm    LYR   0/1
/

ETC.
<<< STRUCTURE FILE NOTES >>>
```

(Model 3c)

```
                    * * * * * * * * * * * * * * * * * * *
                    *          V e c T o r 2            *
                    *   S T R U C T U R E     D A T A   *
                    * * * * * * * * * * * * * * * * * * *

                           STRUCTURAL PARAMETERS
                           *********************

Structure Title        (30 char. max.)     : Enter Structure Title
Structure File Name    ( 8 char. max.)     : Struct
No. of R.C. Material Types                 : 6
No. of Steel Material Types                : 8
No. of Bond Material Types                 : 0
No. of Rectangular Elements                : 3648
No. of Quadrilateral Elements              : 0
No. of Triangular Elements                 : 0
No. of Truss Bar Elements                  : 1318
No. of Linkage Elements                    : 0
No. of Contact Elements                    : 0
No. of Joints                              : 3357
No. of Restraints                          : 124

                         MATERIAL SPECIFICATIONS
                         ***********************

                         (A) REINFORCED CONCRETE
                         -----------------------
<NOTE:> TO BE USED IN RECTANGULAR AND TRIANGULAR ELEMENTS ONLY

CONCRETE
--------
MAT  Ns    T    f'c  [ f't    Ec    e0     Mu   Cc   Agg   Dens   Kc ] [Sx  Sy]
TYP  #    mm    MPa    MPa   MPa    me          /C    mm  kg/m3  mm2/s  mm  mm
 1   1   800.0  43.0   0.0   0.0   2.31   0.0   0.0  10.0   0.0   0.0   0.0   0.0
 2   1   300.0  43.0   0.0   0.0   2.31   0.0   0.0  10.0   0.0   0.0   0.0   0.0
 3   0   300.0  43.0   0.0   0.0   2.31   0.0   0.0  10.0   0.0   0.0   0.0   0.0
 4   0   225.0  43.0   0.0   0.0   2.31   0.0   0.0  10.0   0.0   0.0   0.0   0.0
 5   0   800.0  43.0   0.0   0.0   2.31   0.0   0.0  10.0   0.0   0.0   0.0   0.0
 6   1   225.0  43.0   0.0   0.0   2.31   0.0   0.0  10.0   0.0   0.0   0.0   0.0
/
REINFORCEMENT COMPONENTS
------------------------
MAT  REF  DIR   As  Db   Fy   Fu    Es    Esh   esh   Cs   Dep
TYP  TYP  deg    %  mm   MPa  MPa   MPa   MPa   me    /C    me
 1   1    90.0  0.429  11.3  455.0  583.0  192400.0  1195.0  22.8  0.0  0.0
 2   1    0.0   1.018  11.3  455.0  583.0  192400.0  1195.0  22.8  0.0  0.0
 6   1    361.0 2.000  1.0   876.0  877.0  72400.0   72400.0 12.10 0.0  0.0
/
                              (B) STEEL
                              ---------
<NOTE:> TO BE USED FOR TRUSS ELEMENTS ONLY
MAT  REF    AREA   Db    Fy    Fu     Es    Esh   esh   Cs   Dep
TYP  TYP     mm2   mm   MPa   MPa    MPa    MPa    me   /C    me
  1   1    2400.0   19.5   447.0   603.0   198400.0   1372.0   17.1   0.0   0.0
  2   1    1200.0   19.5   447.0   603.0   198400.0   1372.0   17.1   0.0   0.0
  3   1     900.0   19.5   447.0   603.0   198400.0   1372.0   17.1   0.0   0.0
  4   1     600.0   19.5   447.0   603.0   198400.0   1372.0   17.1   0.0   0.0
  5   1     300.0   19.5   447.0   603.0   198400.0   1372.0   17.1   0.0   0.0
  6   1     142.0   9.5    506.0   615.0   210000.0   1025.0   28.3   0.0   0.0
  7   1     100.0   1.0    876.0   877.0   72400.0    72400.0  12.1   0.0   0.0
  8   1      50.0   1.0    876.0   877.0   72400.0    72400.0  12.10  0.0   0.0
/
                              (C) BOND
                              --------
<NOTE:> TO BE USED FOR EXTERIOR/INTERIOR BONDED ELEMENTS
MAT  REF  { Ao   U1    U2    U3    S1    S2    S3 }/{ CPF   Cmin   No.  HOOK }
TYP  TYP   mm^2  MPa   MPa   MPa   mm    mm    mm     0-1    mm    LYR   0/1
/

ETC.
<<< STRUCTURE FILE NOTES >>>
```

(Model 2c)

```
                    * * * * * * * * * * * * * * * * * * *
                    *          V e c T o r 2            *
                    *   S T R U C T U R E     D A T A   *
                    * * * * * * * * * * * * * * * * * * *

                           STRUCTURAL PARAMETERS
                           *********************

Structure Title        (30 char. max.)     : Enter Structure Title
Structure File Name    ( 8 char. max.)     : Struct
No. of R.C. Material Types                 : 6
No. of Steel Material Types                : 8
No. of Bond Material Types                 : 3
No. of Rectangular Elements                : 3048
No. of Quadrilateral Elements              : 0
No. of Triangular Elements                 : 0
No. of Truss Bar Elements                  : 1318
No. of Linkage Elements                    : 418
No. of Contact Elements                    : 0
No. of Joints                              : 3775
No. of Restraints                          : 124

                         MATERIAL SPECIFICATIONS
                         ***********************

                         (A) REINFORCED CONCRETE
                         -----------------------
<NOTE:> TO BE USED IN RECTANGULAR AND TRIANGULAR ELEMENTS ONLY

CONCRETE
--------
MAT  Ns    T    f'c  [ f't    Ec    e0     Mu   Cc   Agg   Dens   Kc ] [Sx  Sy]
TYP  #    mm    MPa    MPa   MPa    me          /C    mm  kg/m3  mm2/s  mm  mm
 1   1   800.0  43.0   0.0   0.0   2.31   0.0   0.0  10.0   0.0   0.0   0.0   0.0
 2   1   300.0  43.0   0.0   0.0   2.31   0.0   0.0  10.0   0.0   0.0   0.0   0.0
 3   0   300.0  43.0   0.0   0.0   2.31   0.0   0.0  10.0   0.0   0.0   0.0   0.0
 4   0   225.0  43.0   0.0   0.0   2.31   0.0   0.0  10.0   0.0   0.0   0.0   0.0
 5   0   800.0  43.0   0.0   0.0   2.31   0.0   0.0  10.0   0.0   0.0   0.0   0.0
 6   1   225.0  43.0   0.0   0.0   2.31   0.0   0.0  10.0   0.0   0.0   0.0   0.0
/
REINFORCEMENT COMPONENTS
------------------------
MAT  REF  DIR   As  Db   Fy   Fu    Es    Esh   esh   Cs   Dep
TYP  TYP  deg    %  mm   MPa  MPa   MPa   MPa   me    /C    me
 1   1    90.0  0.429  11.3  455.0  583.0  192400.0  1195.0  22.8  0.0  0.0
 2   1    0.0   1.018  11.3  455.0  583.0  192400.0  1195.0  22.8  0.0  0.0
 6   1    361.0 2.000  1.0   876.0  877.0  72400.0   72400.0 12.10 0.0  0.0
/
                              (B) STEEL
                              ---------
<NOTE:> TO BE USED FOR TRUSS ELEMENTS ONLY
MAT  REF    AREA   Db    Fy    Fu     Es     Esh   esh   Cs   Dep
TYP  TYP     mm2   mm   MPa   MPa    MPa    MPa    me   /C    me
  1   1    2400.0   19.5   447.0   603.0   198400.0   1372.0   17.1   0.0   0.0
  2   1    1200.0   19.5   447.0   603.0   198400.0   1372.0   17.1   0.0   0.0
  3   1     900.0   19.5   447.0   603.0   198400.0   1372.0   17.1   0.0   0.0
  4   1     600.0   19.5   447.0   603.0   198400.0   1372.0   17.1   0.0   0.0
  5   1     300.0   19.5   447.0   603.0   198400.0   1372.0   17.1   0.0   0.0
  6   1     142.0   9.5    506.0   615.0   210000.0   1025.0   28.3   0.0   0.0
  7   1     100.0   1.0    876.0   877.0   72400.0    72400.0  12.1   0.0   0.0
  8   1      50.0   1.0    876.0   877.0   72400.0    72400.0  12.10  0.0   0.0
/
                              (C) BOND
                              --------
<NOTE:> TO BE USED FOR EXTERIOR/INTERIOR BONDED ELEMENTS
MAT  REF  { Ao   U1    U2    U3    S1    S2    S3 }/{ CPF   Cmin   No.  HOOK }
TYP  TYP   mm^2  MPa   MPa   MPa   mm    mm    mm     0-1    mm    LYR   0/1
  1   3   2000.0  10.0  0.01  0.0  0.038  0.20  0.201 0.0  0.0   0   0
  2   3   2000.0  4.37  0.01  0.0  0.038  0.20  0.201 0.0  0.0   0   0
  3   3   1000.0  4.37  0.01  0.0  0.038  0.20  0.201 0.0  0.0   0   0
/
ETC.
<<< STRUCTURE FILE NOTES >>>
```

APPENDIX E

Experimental Photos

E.1 Phase A: Forward Half-Cycle

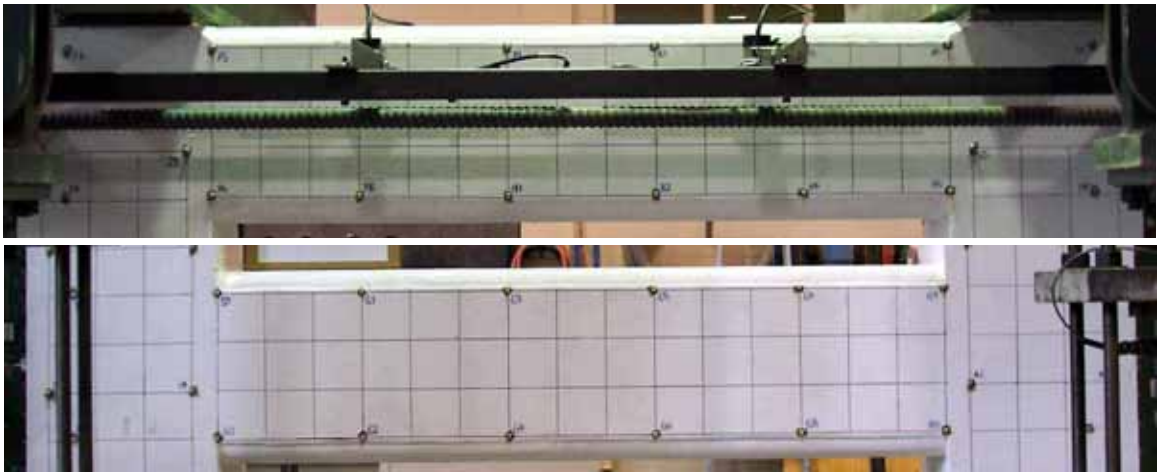

LS1

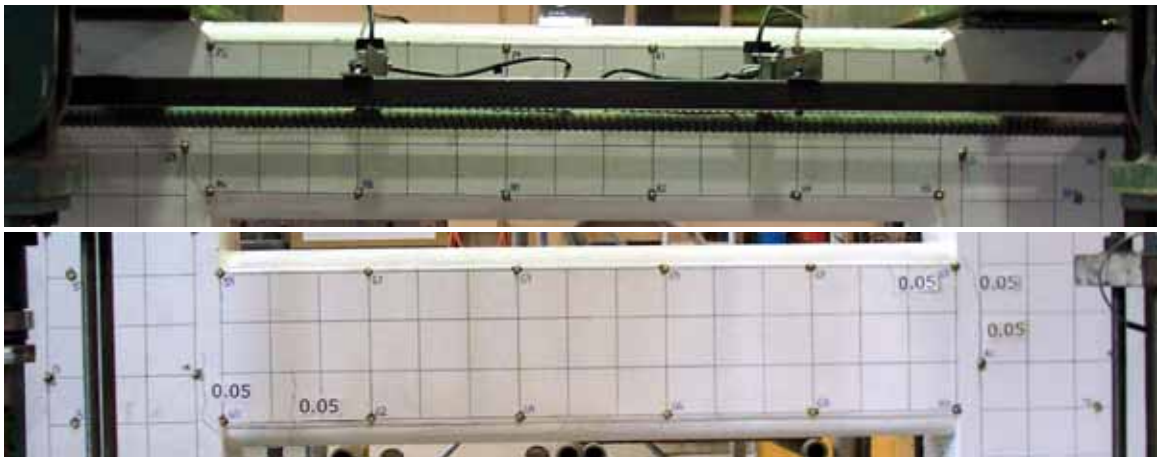

LS3

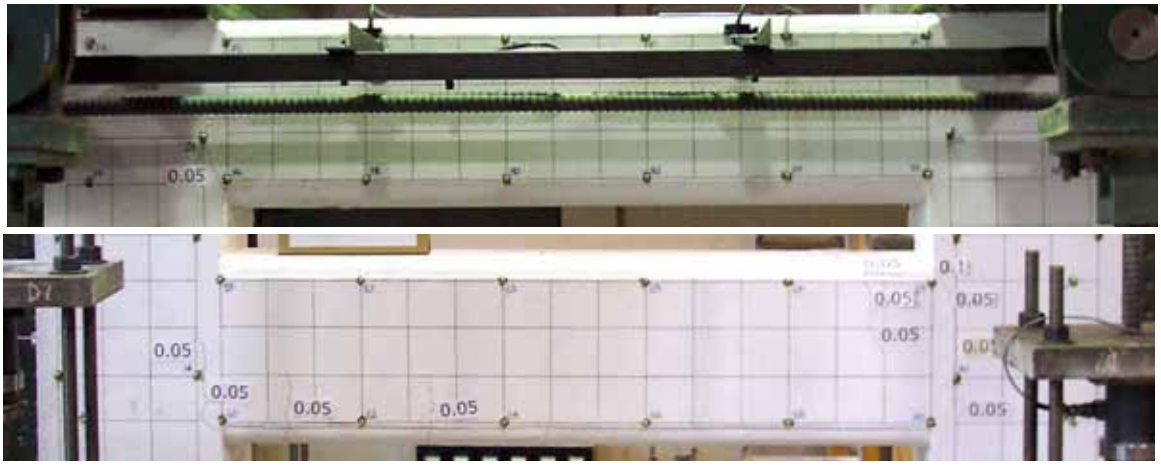

LS4

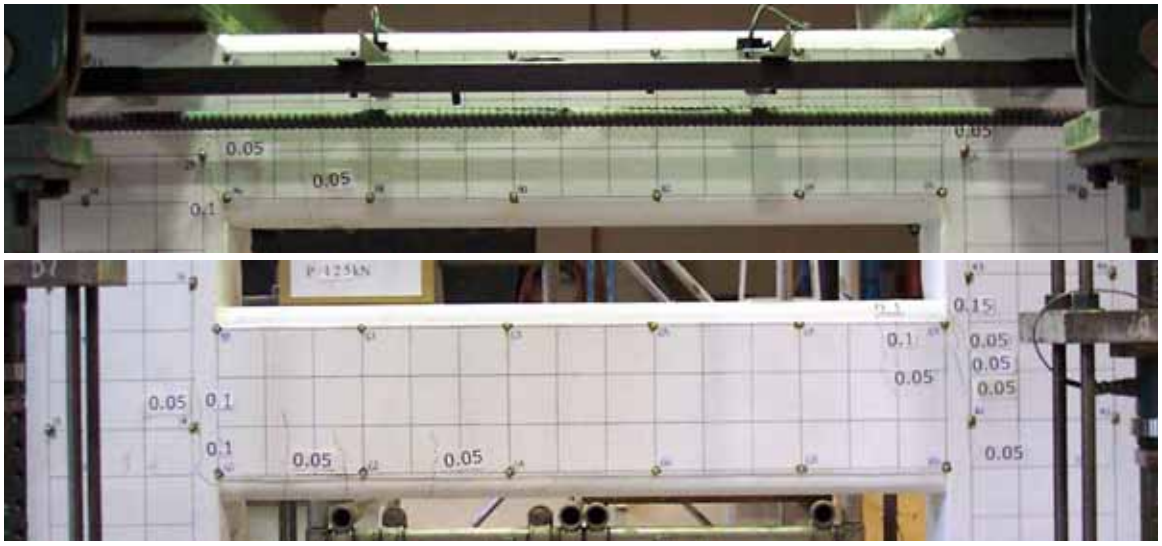
0.05
0.05
0.1
0.05
0.15
0.1
0.05
0.05
0.05
0.05
0.1
0.1
0.05
0.05
0.05

LS5

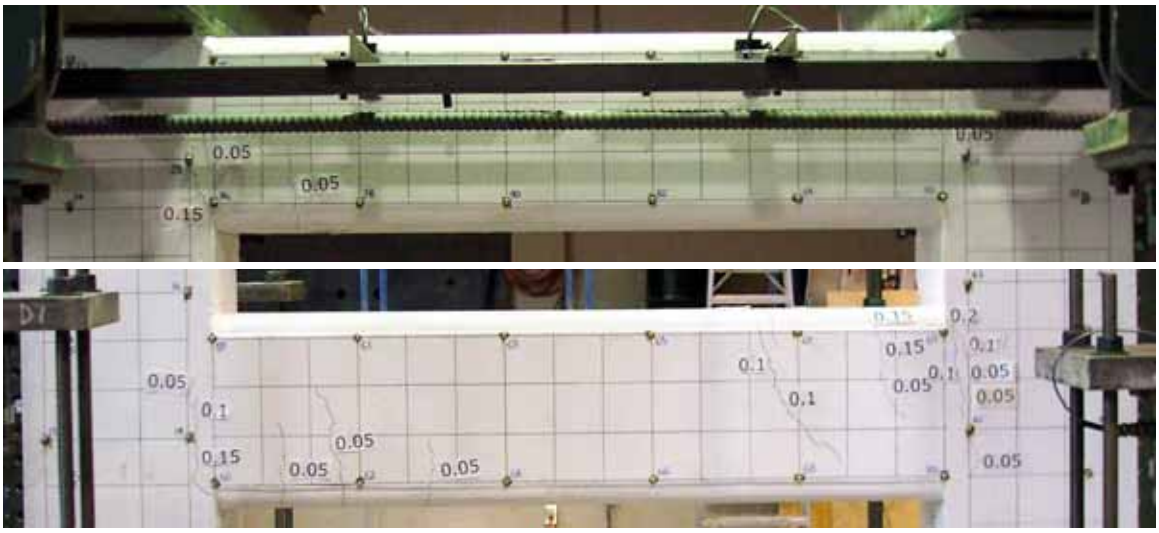
0.05
0.05
0.15
0.05
0.2
0.15
0.1
0.1
0.05
0.05
0.1
0.05
0.1
0.15
0.05
0.05
0.05
0.05

LS6

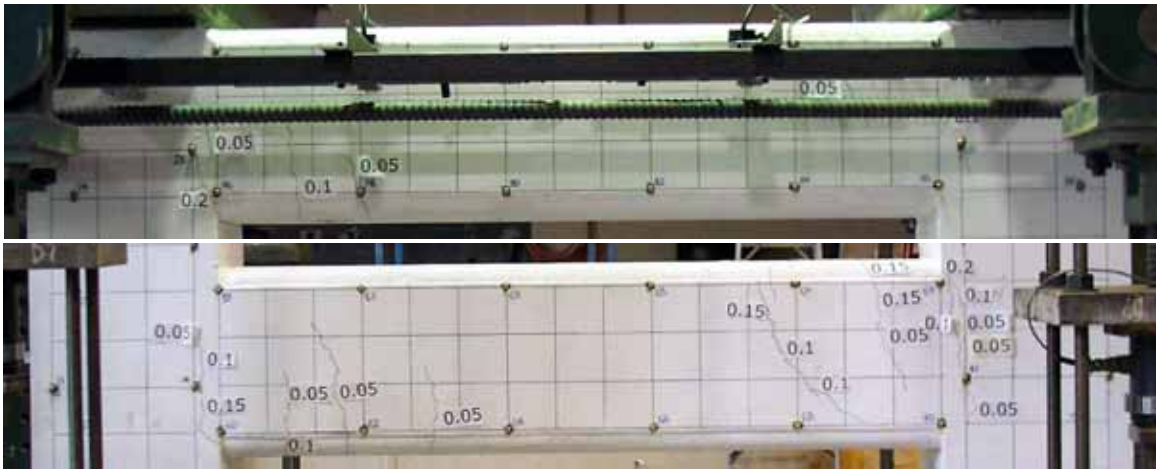
0.05
0.05
0.05
0.2
0.1
0.2
0.15
0.15
0.1
0.05
0.05
0.05
0.1
0.1
0.15
0.05
0.05
0.05
0.1

LS7

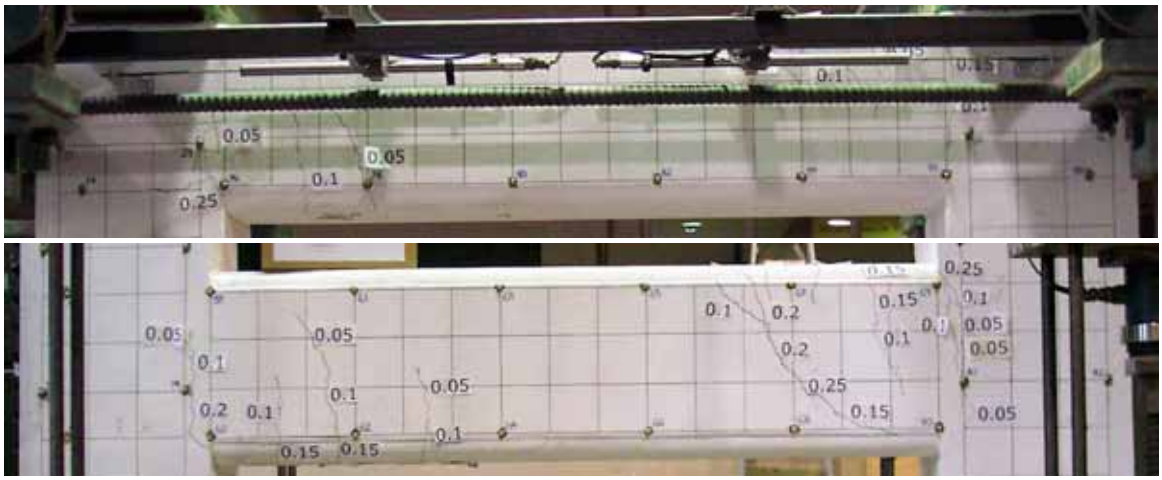

LS8

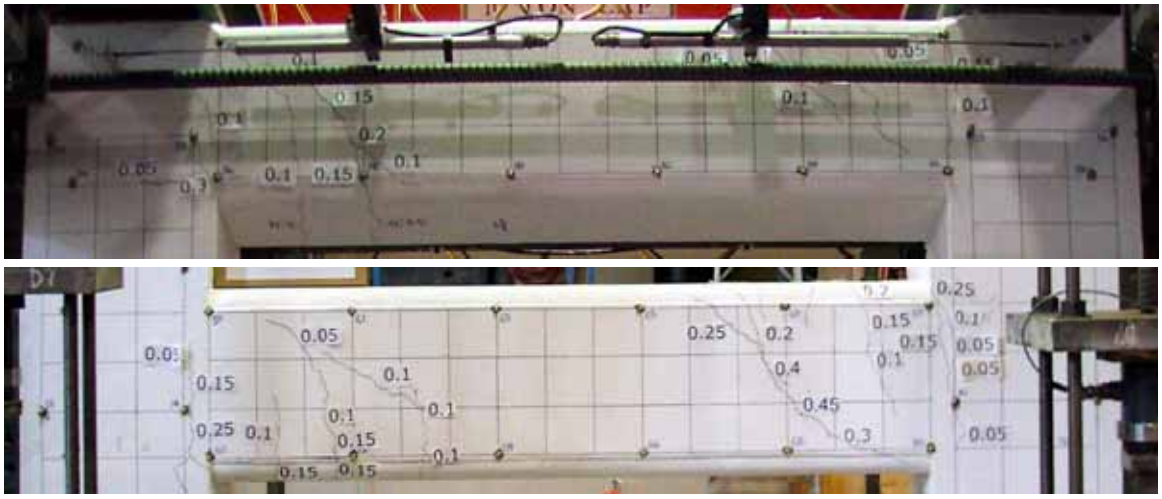

LS9

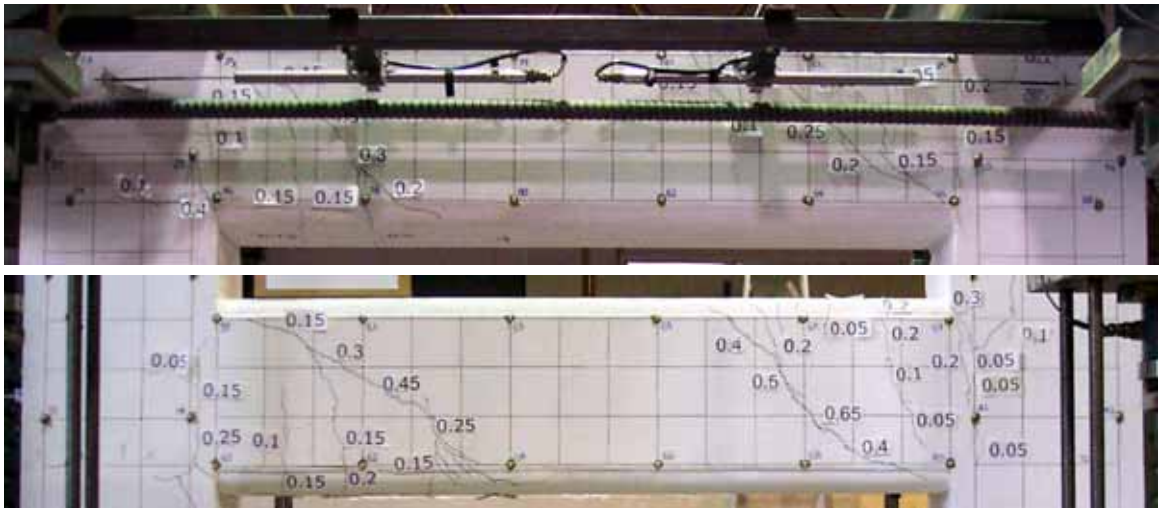

LS10

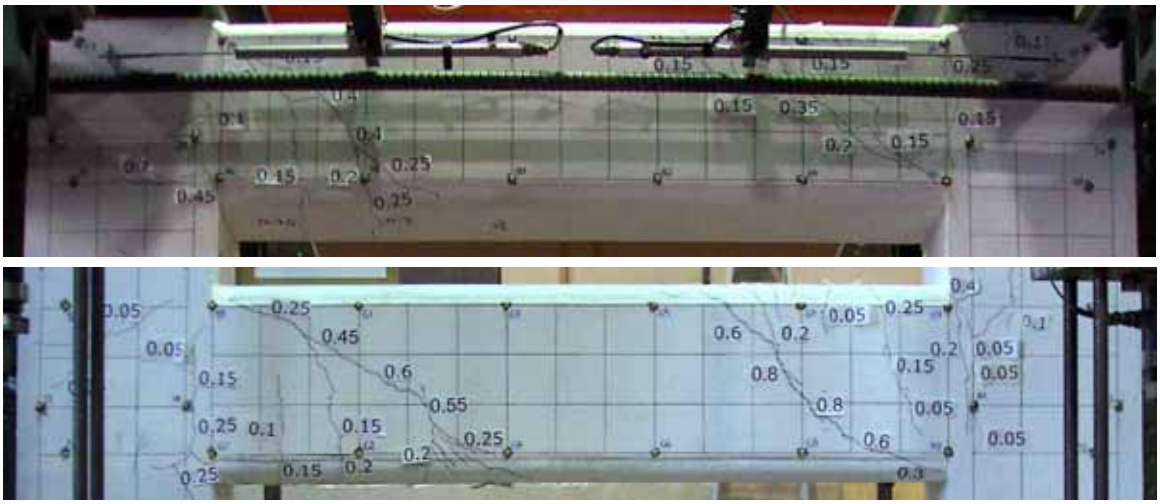

LS11

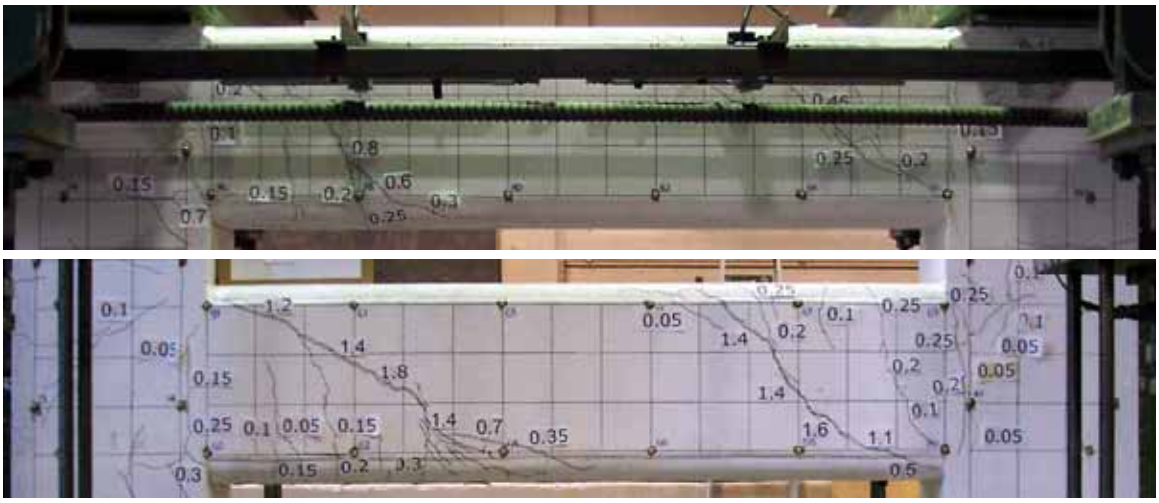

LS13

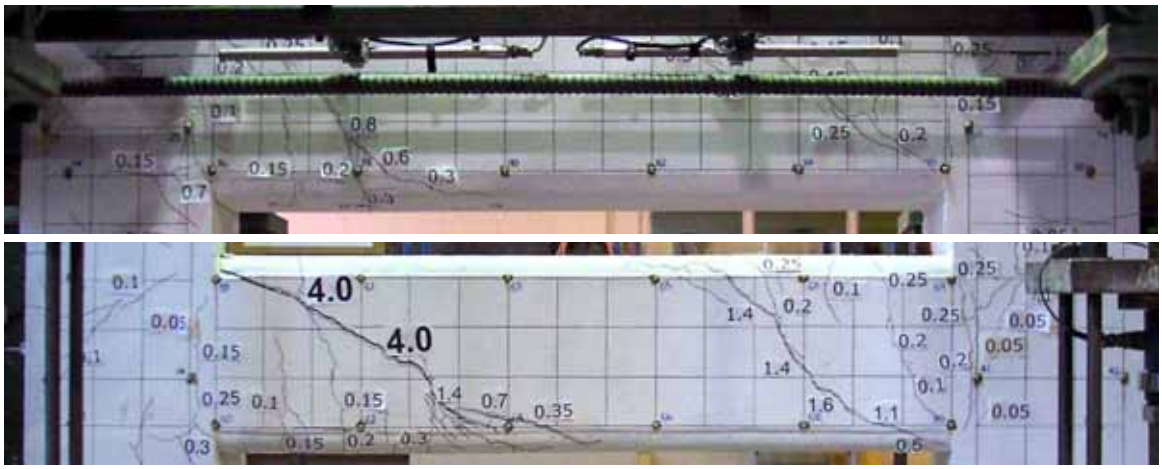

LS14

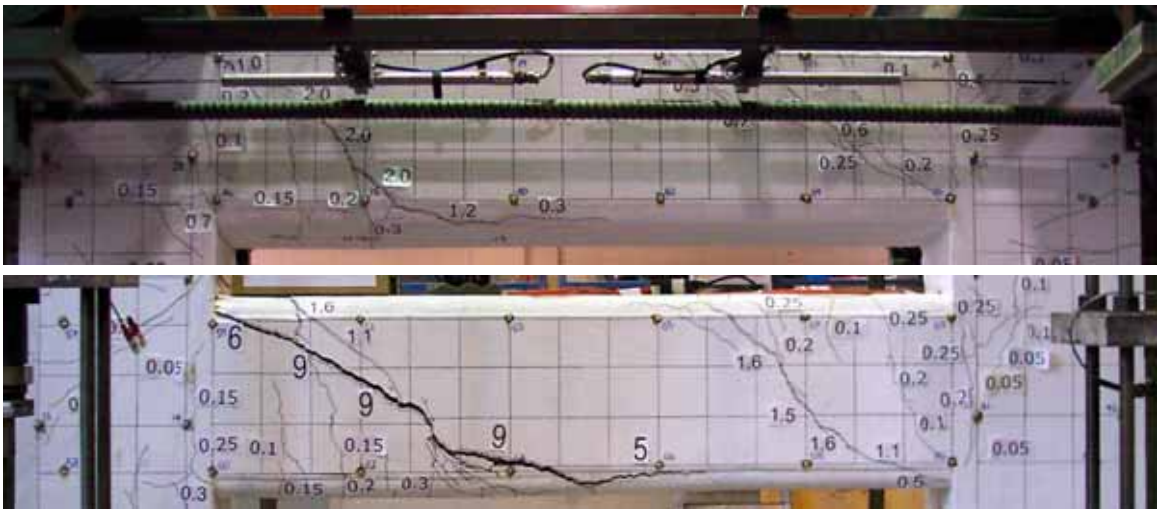

LS15

E.2 Phase A: Reverse Half-Cycle

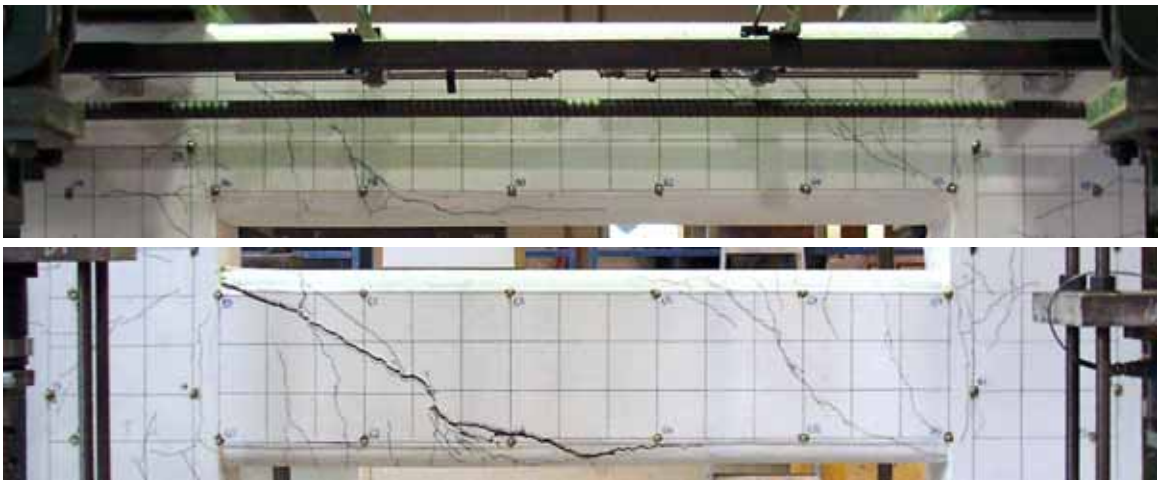

LS16

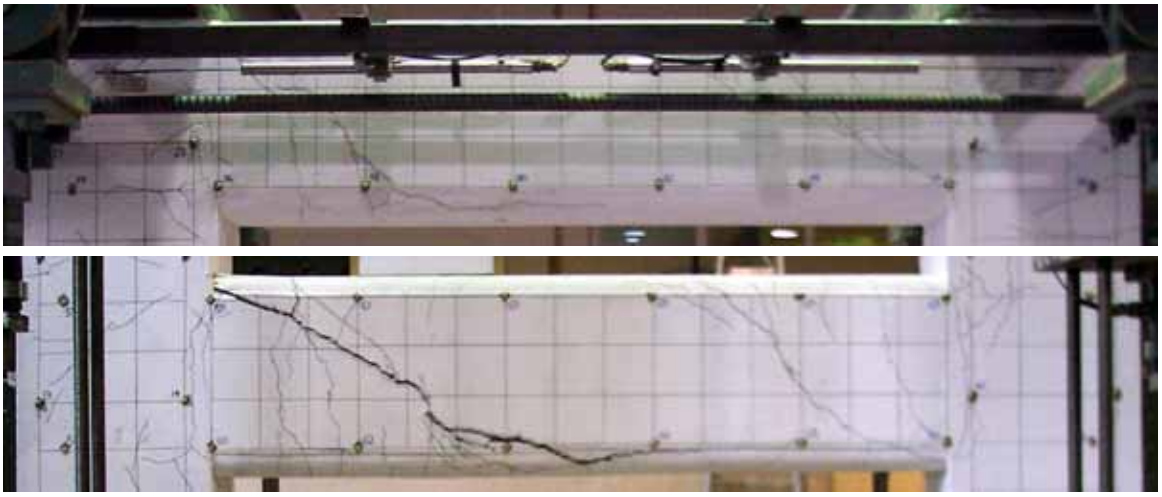

LS18

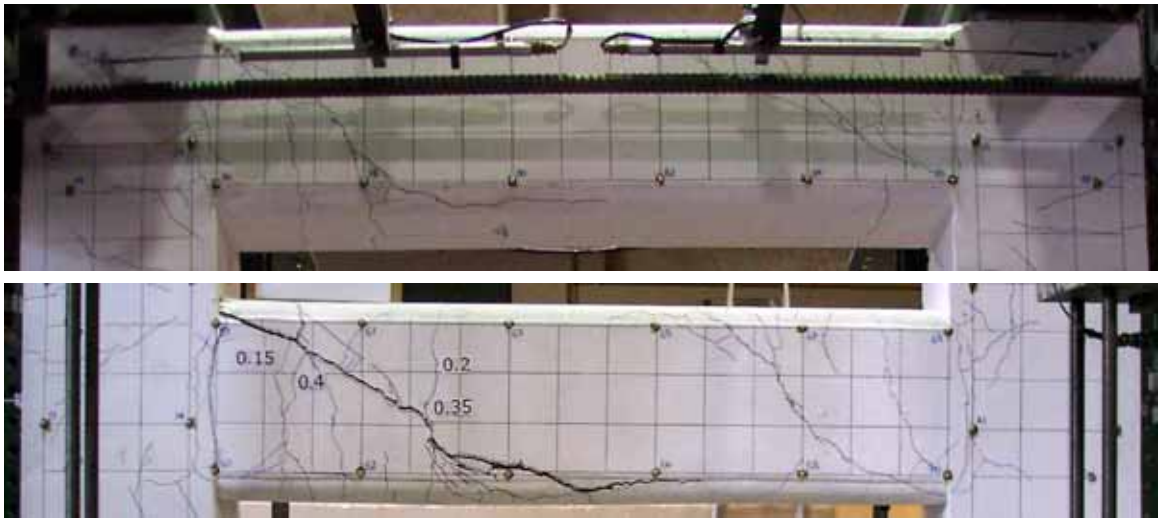

LS19

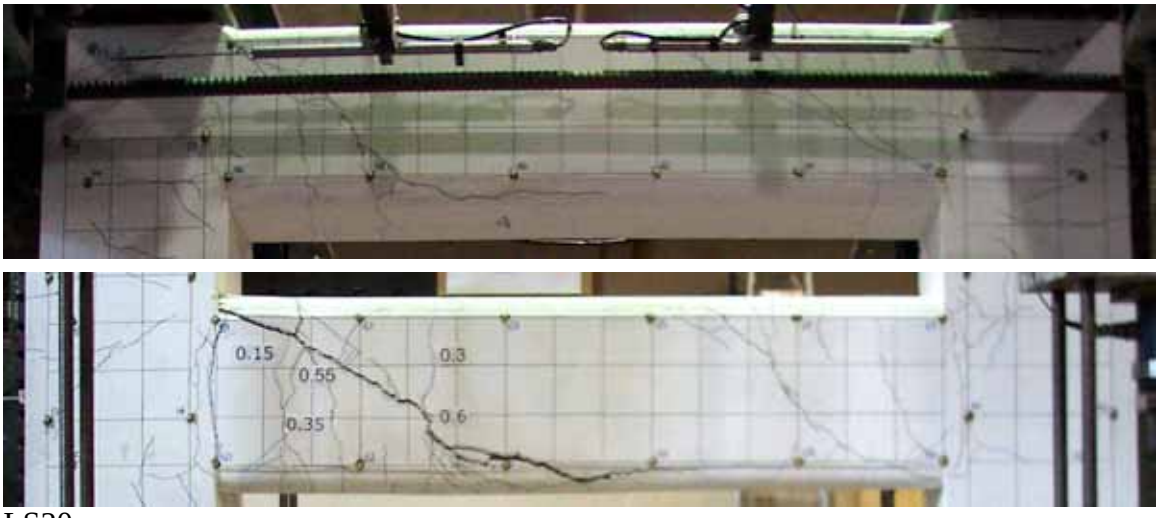

LS20

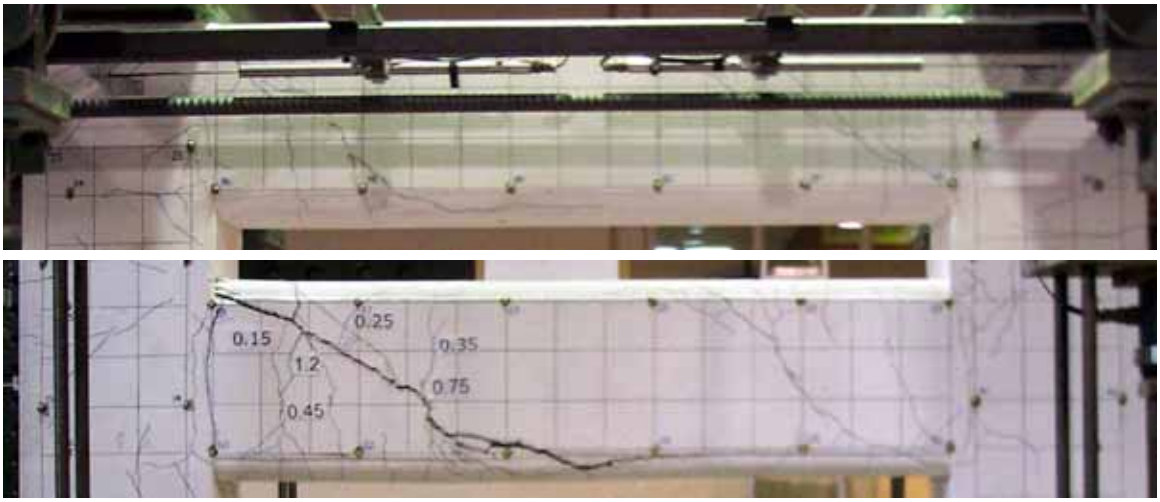

LS21

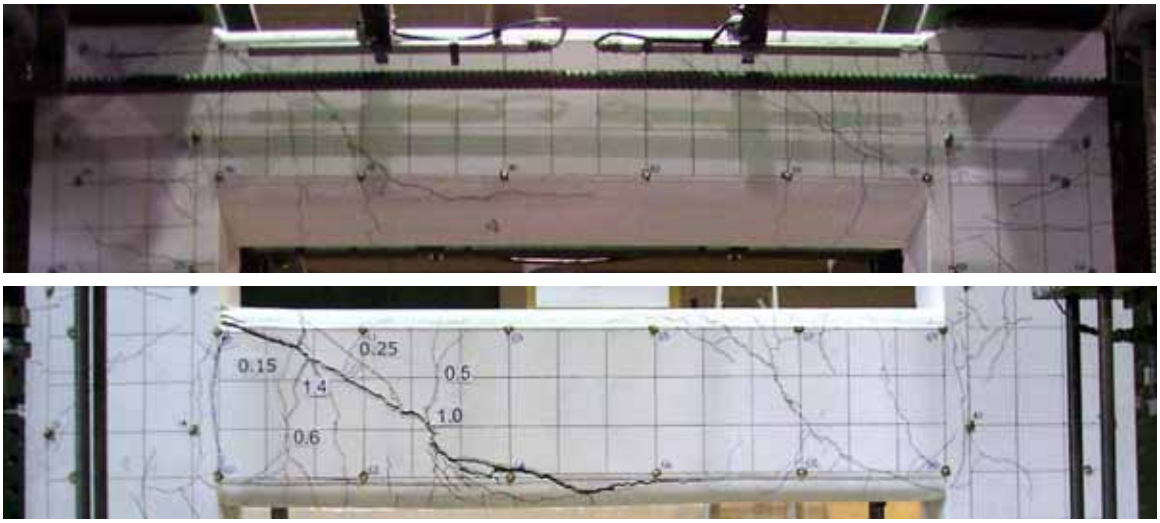

LS22

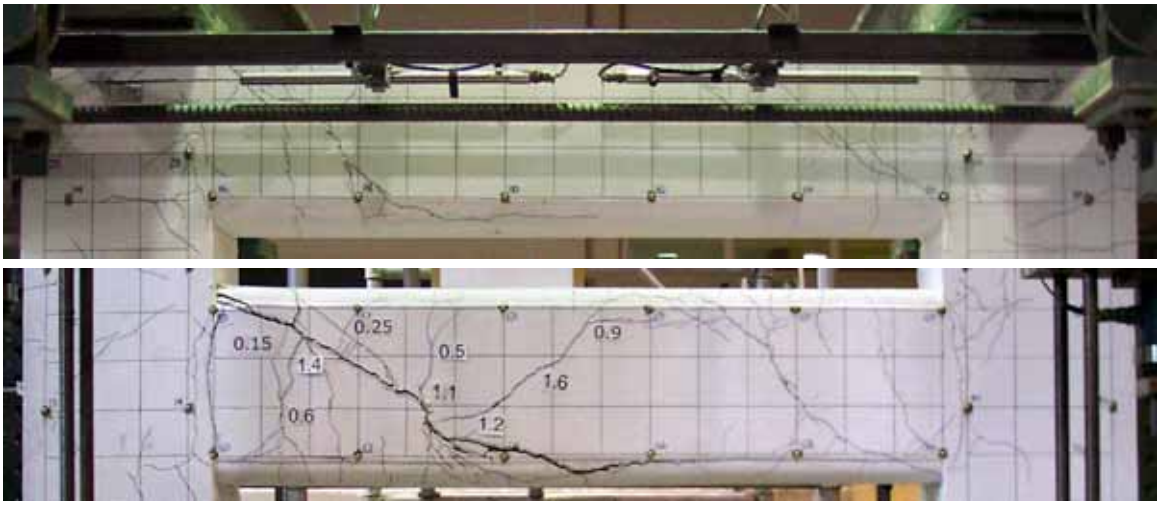

LS23

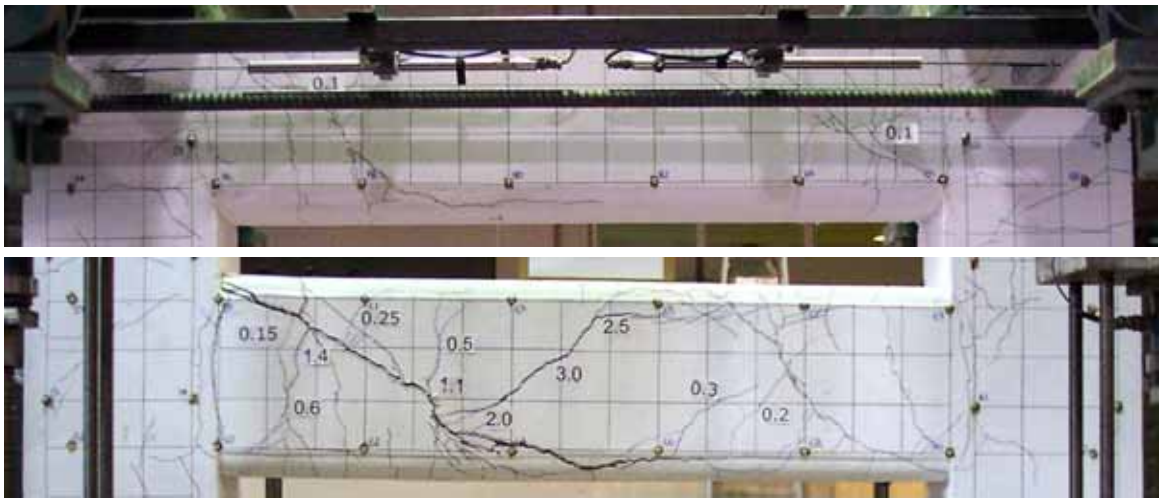

LS24

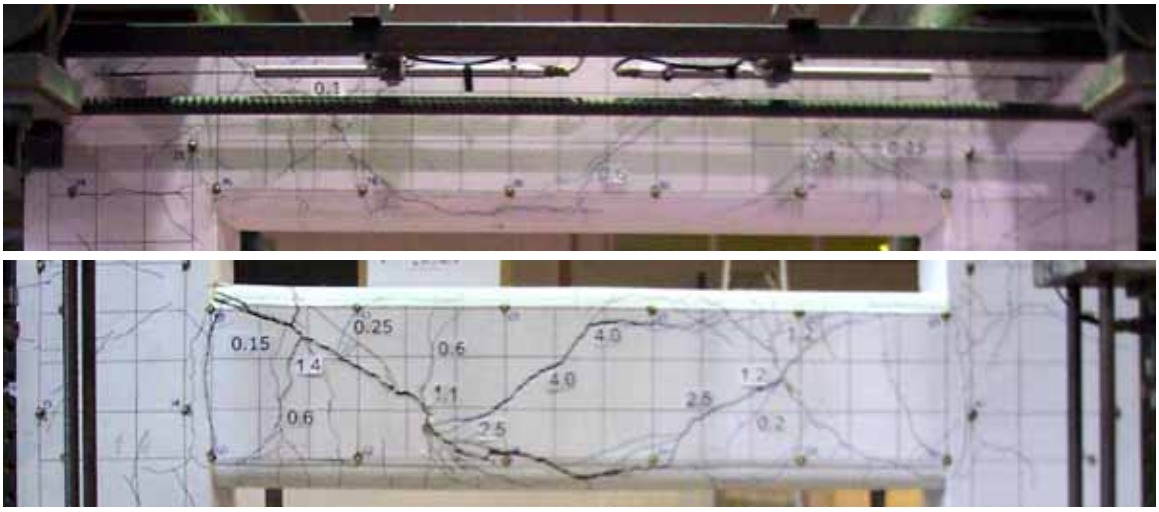

LS25

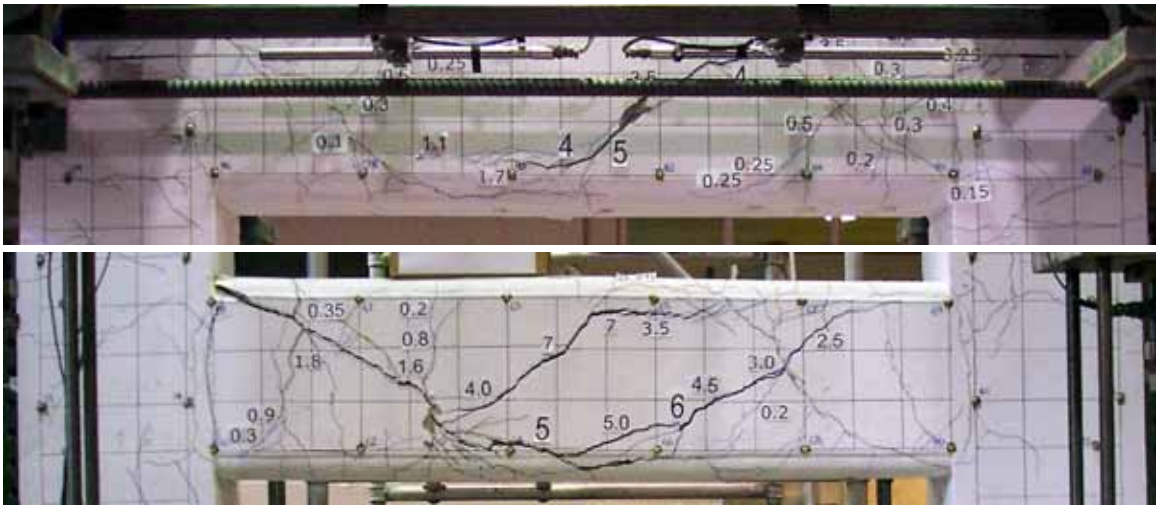

LS26

E.3 Phase B: Cyclic Loading

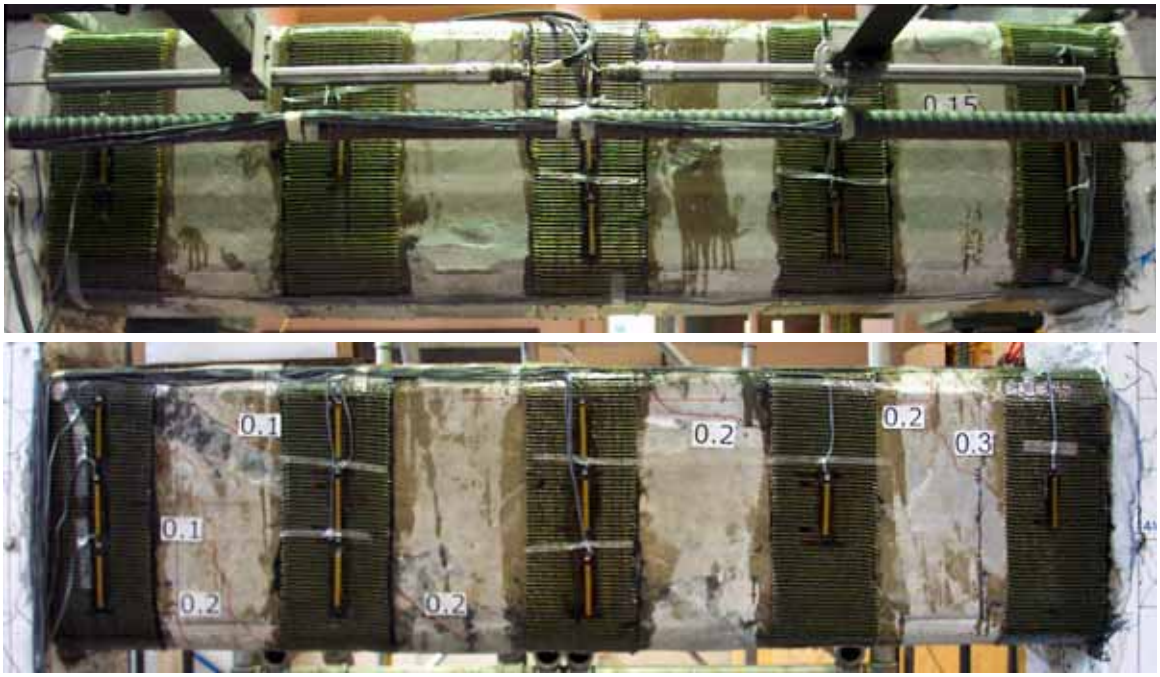

LC1: +0.75 Δ_y

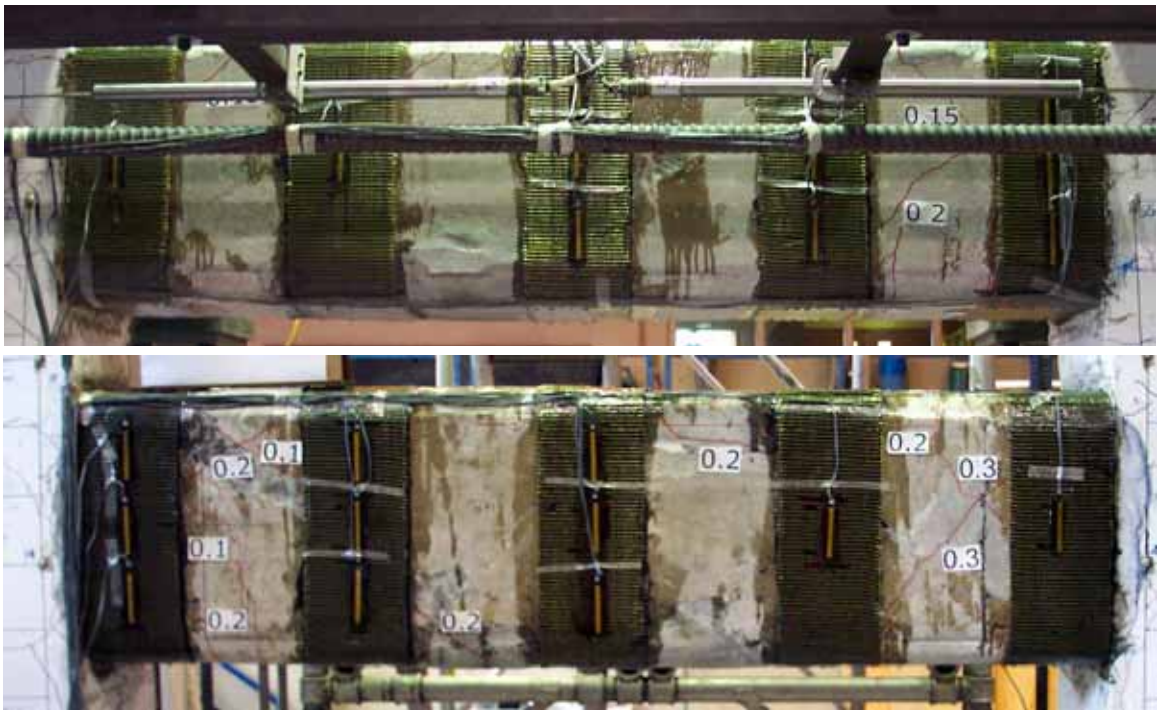

LC1: -0.75 Δ_y

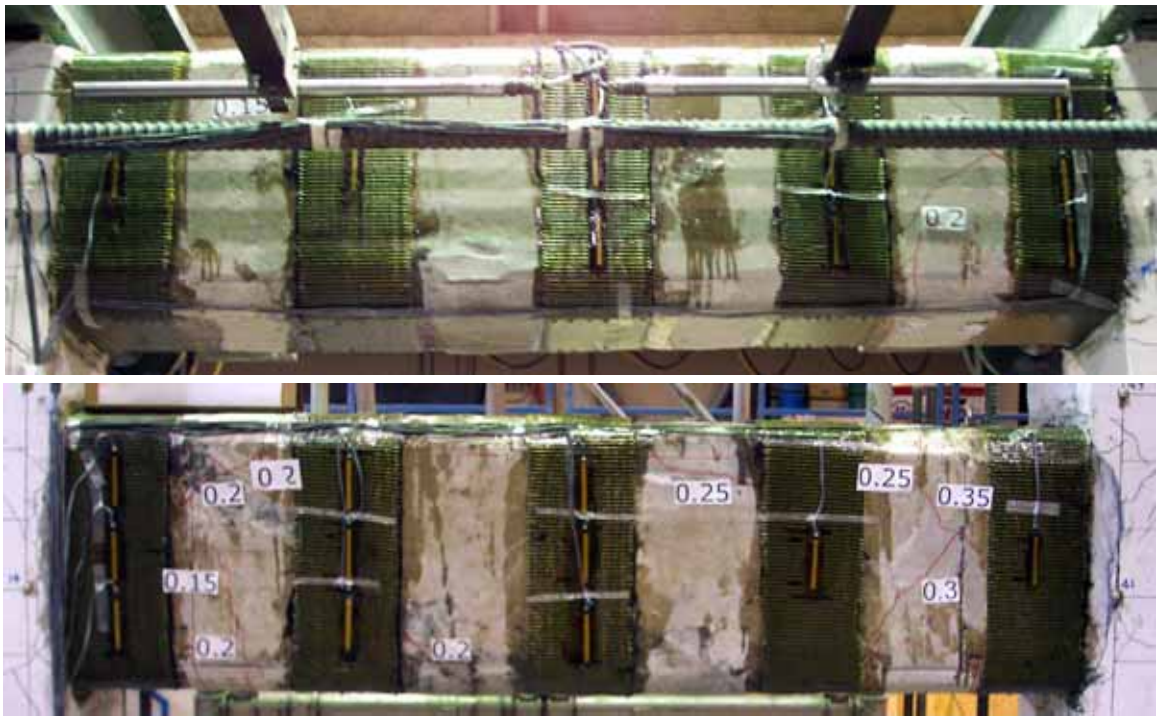

LC2: +0.75 Δ_y

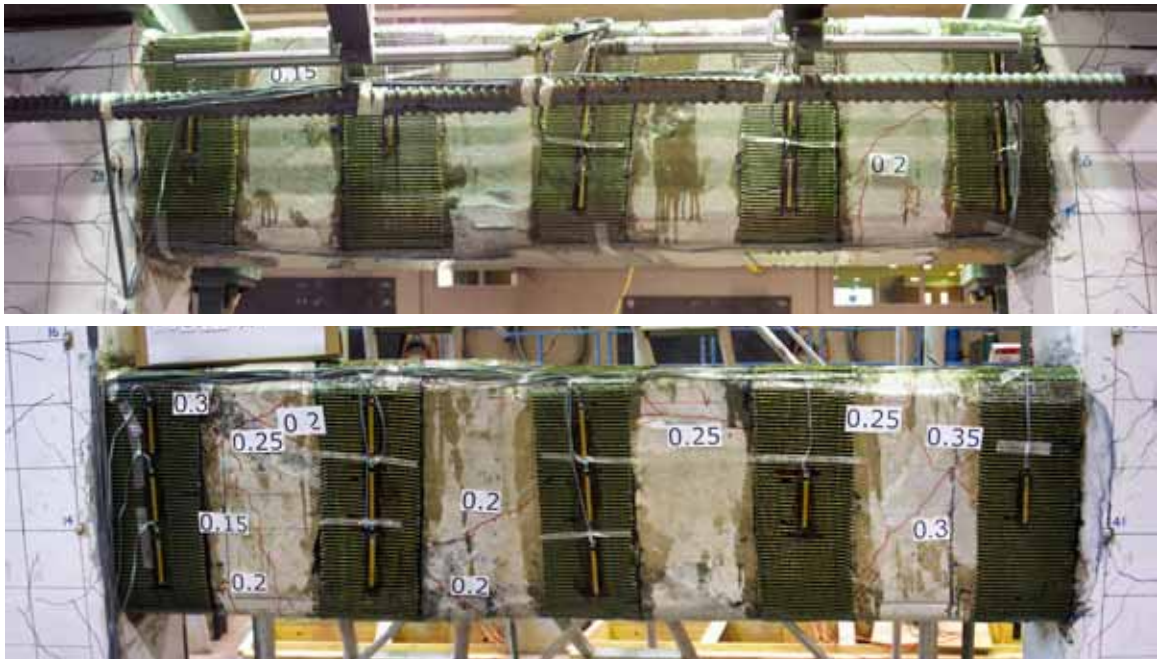

LC2: -0.75 Δ_y

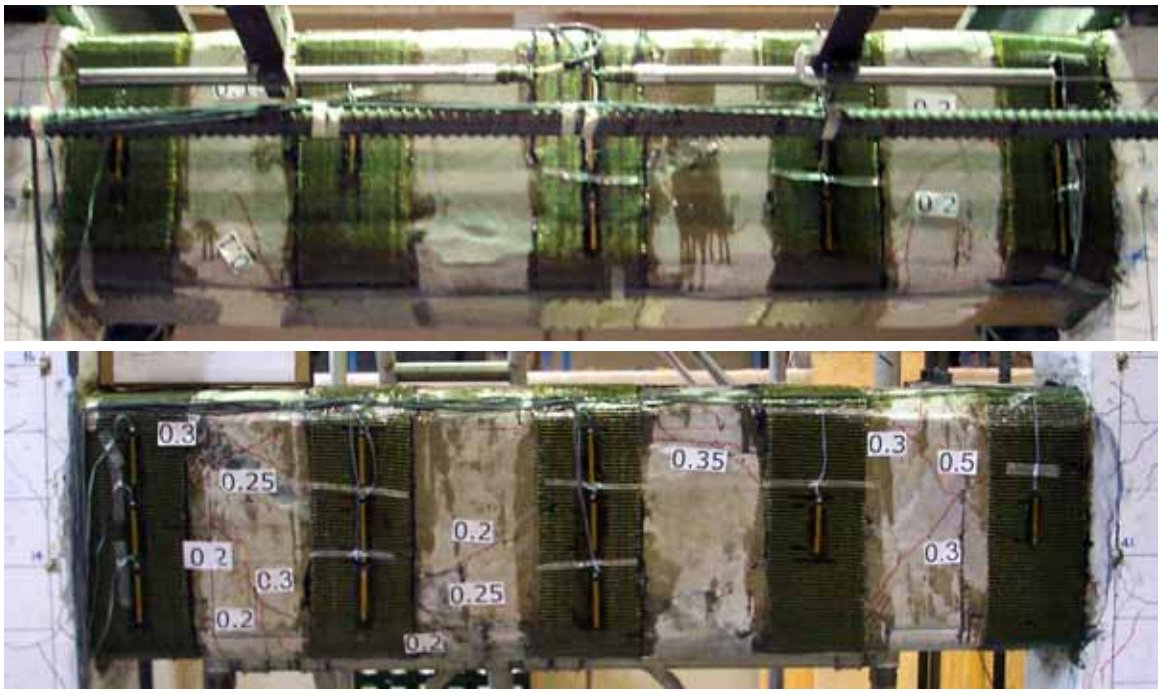

LC3: +1.0 Δ_y

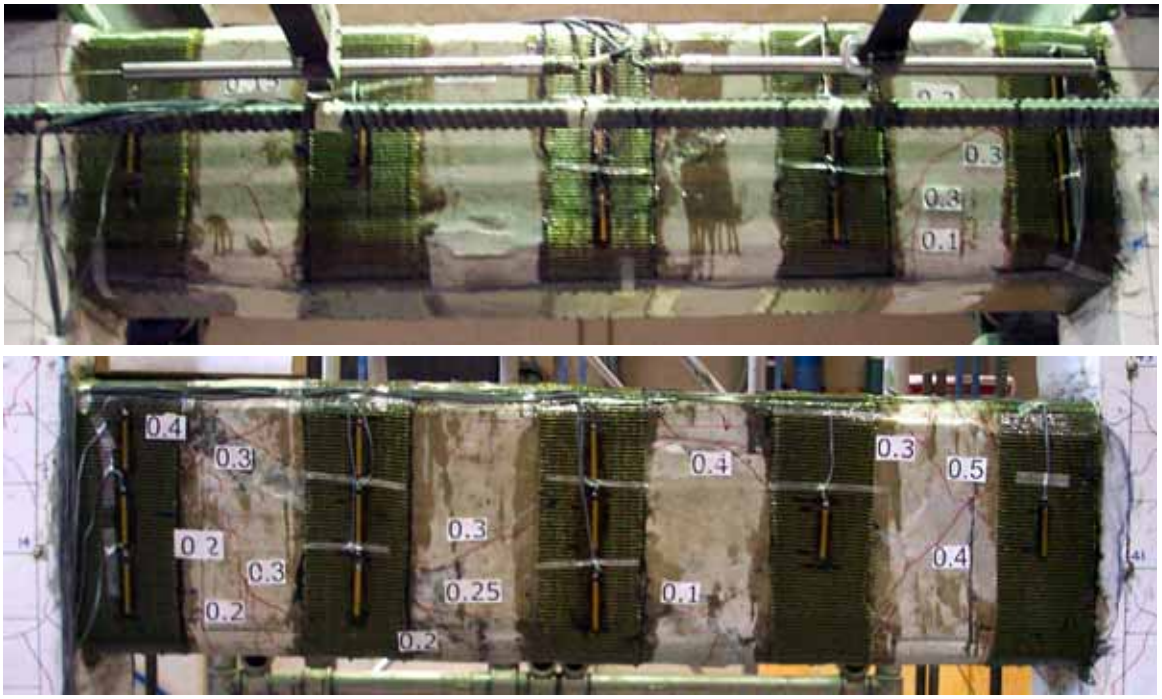

LC3: -1.0 Δ_y

LC4: +1.0 Δ_y

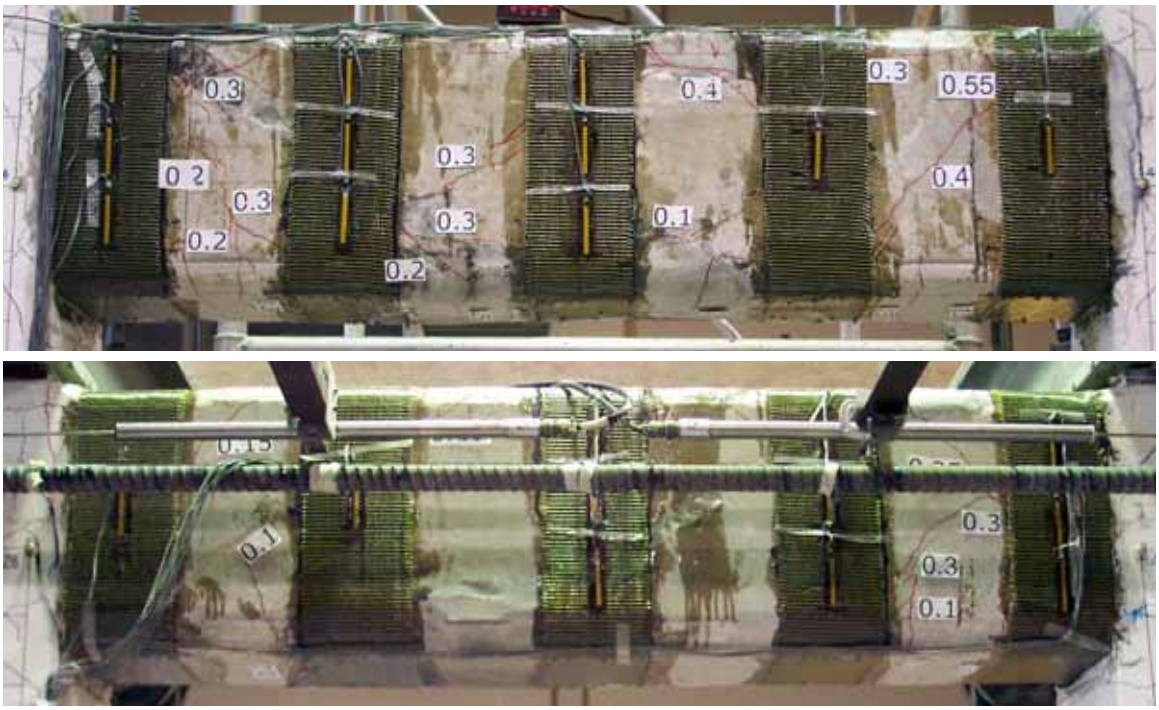

LC4: -1.0 Δ_y

LC5: +2.0 Δ_y

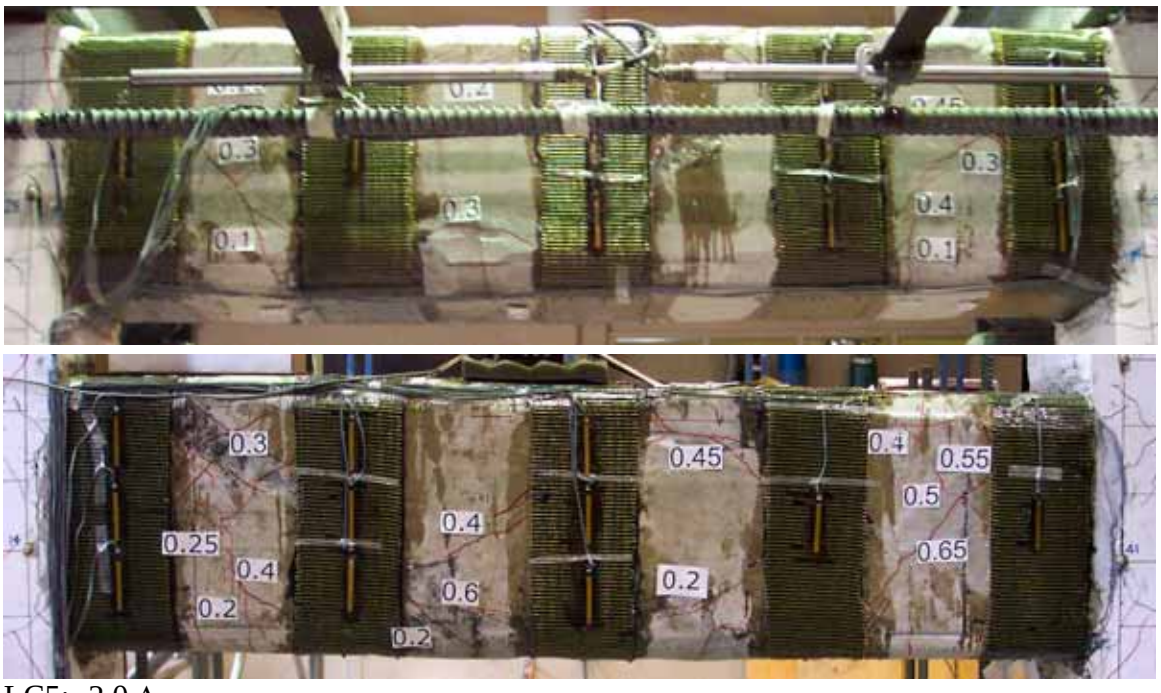

LC5: -2.0 Δ_y

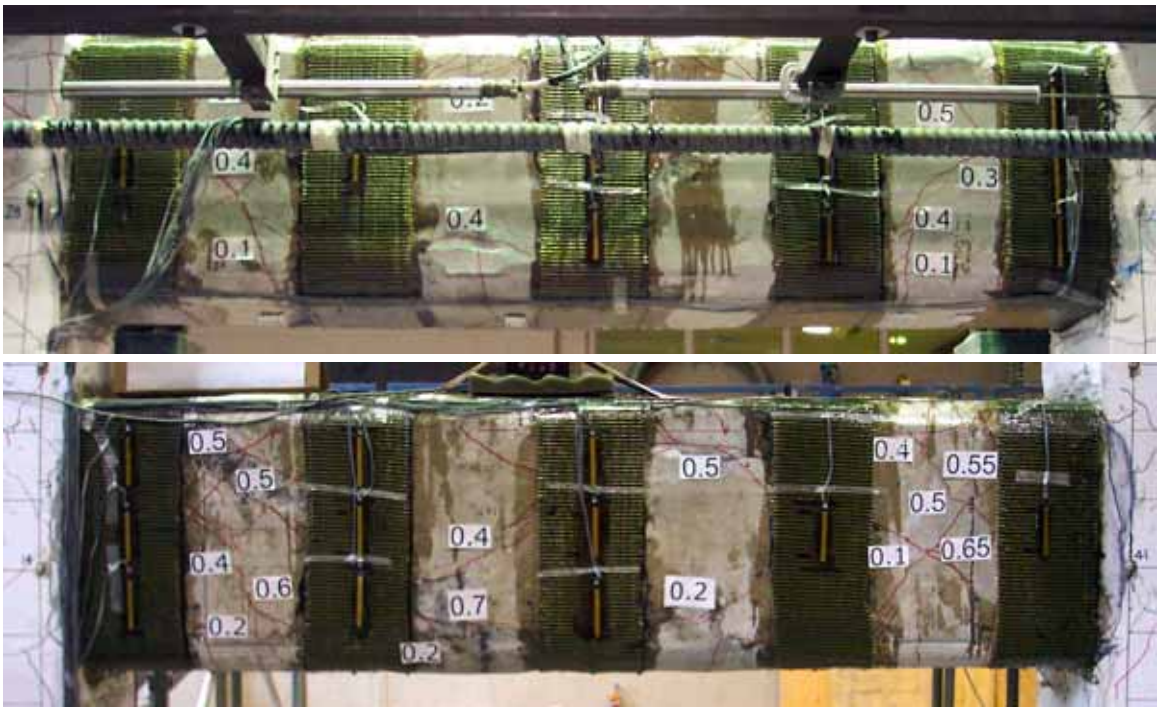

LC6: +2.0 Δ_y

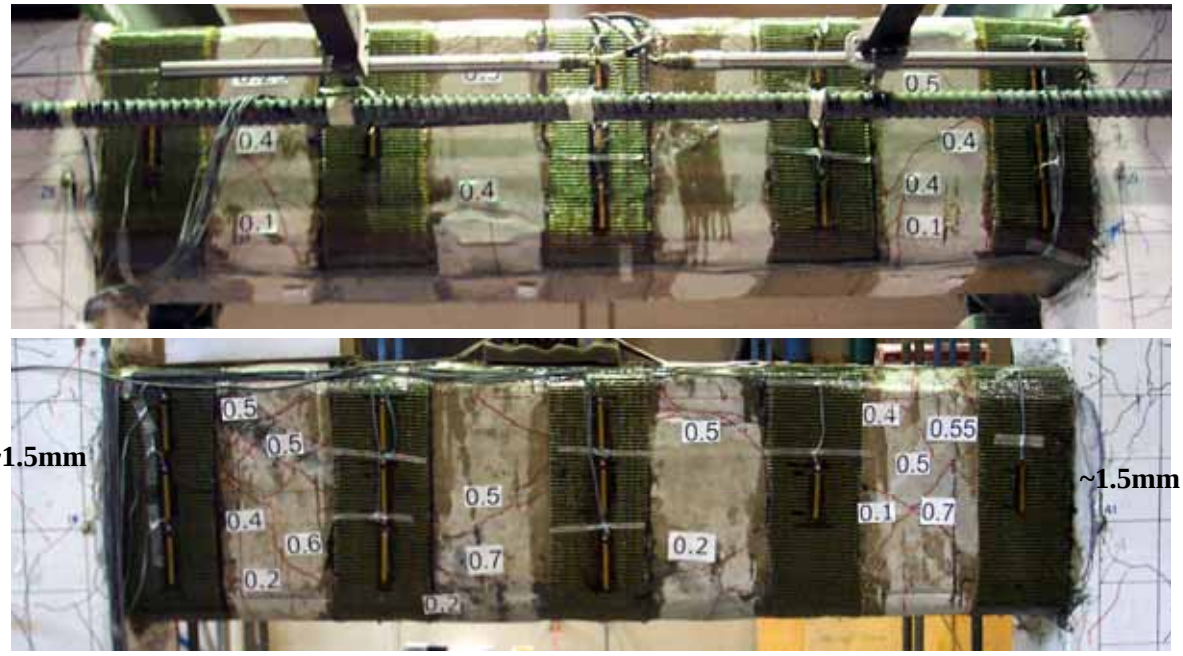

~1.5mm **~1.5mm**

LC6: -2.0 Δ_y

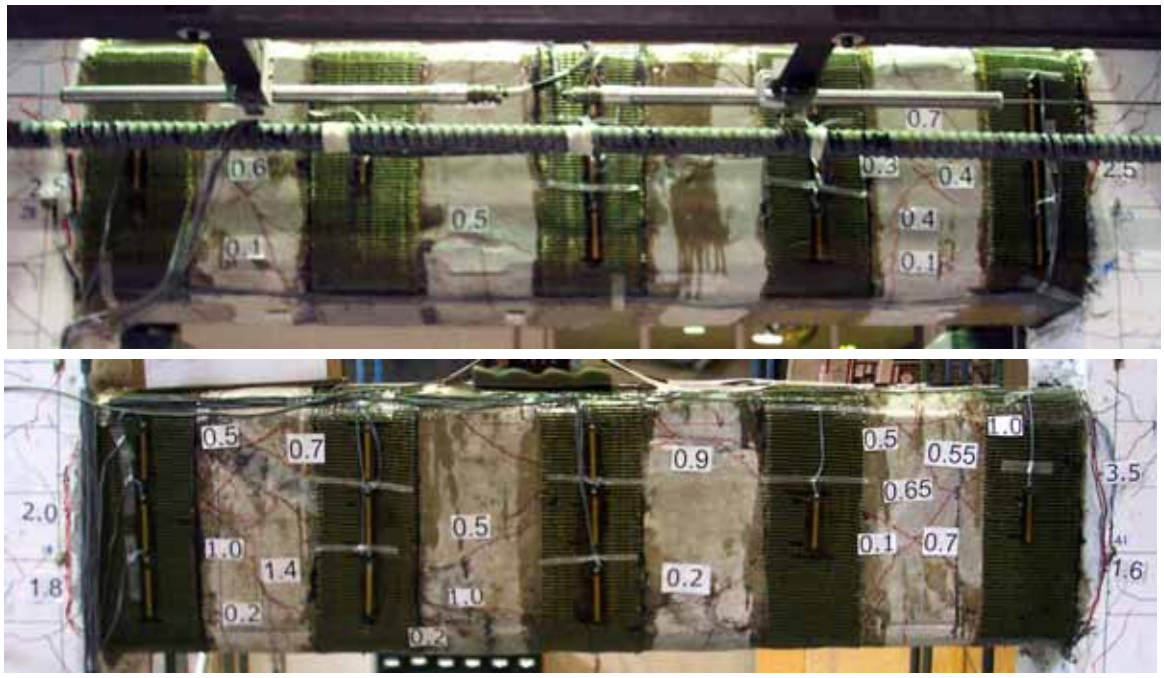

LC7: +3.0 Δ_y

LC7: -3.0 Δ_y

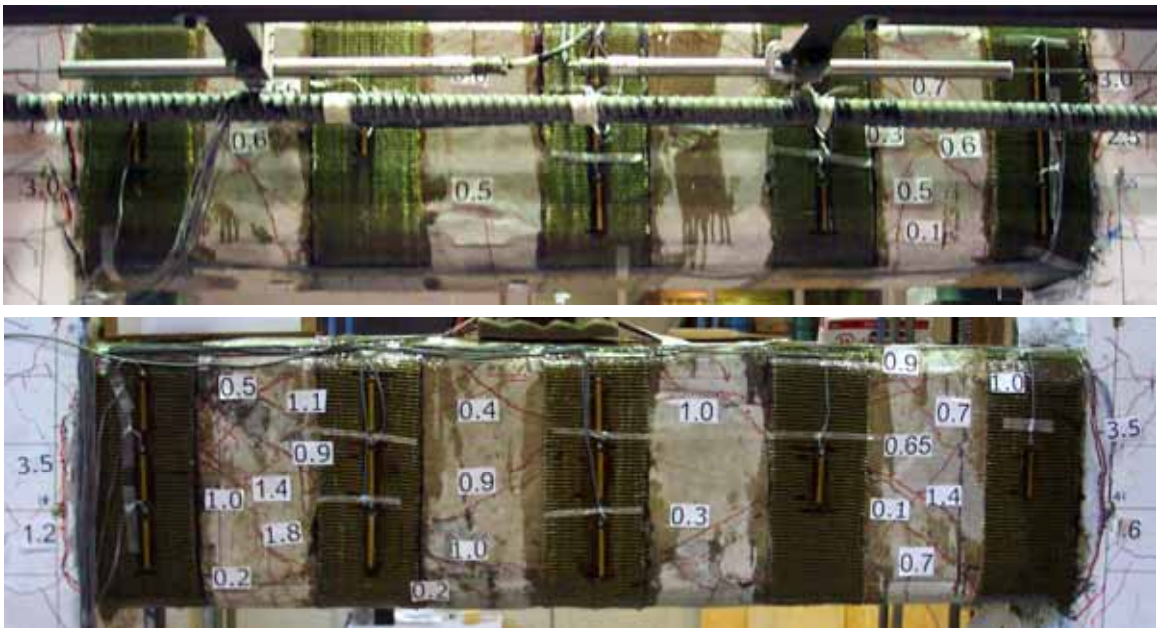

LC8: +3.0 Δ_y

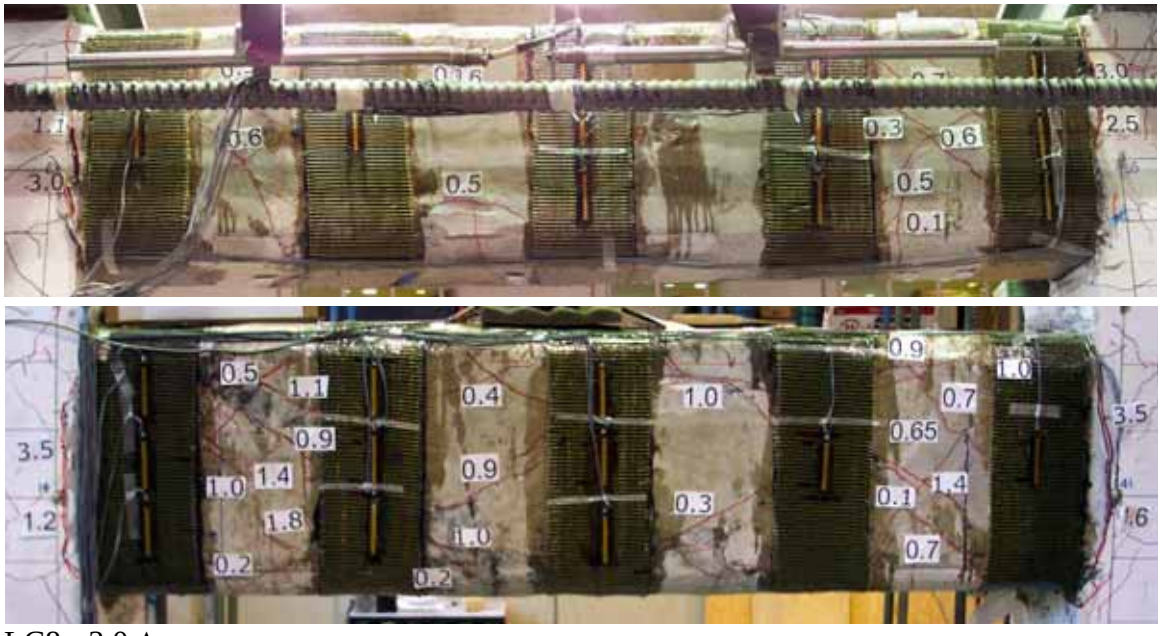

LC8: -3.0 Δ_y

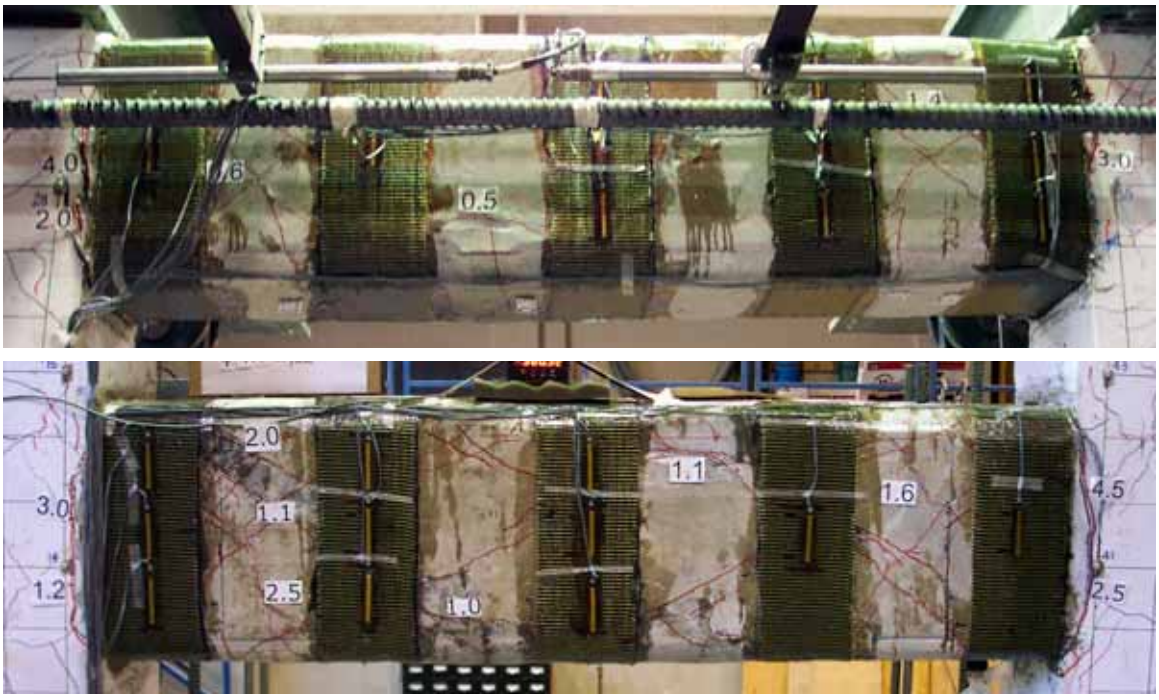

LC9: +4.0 Δ_y

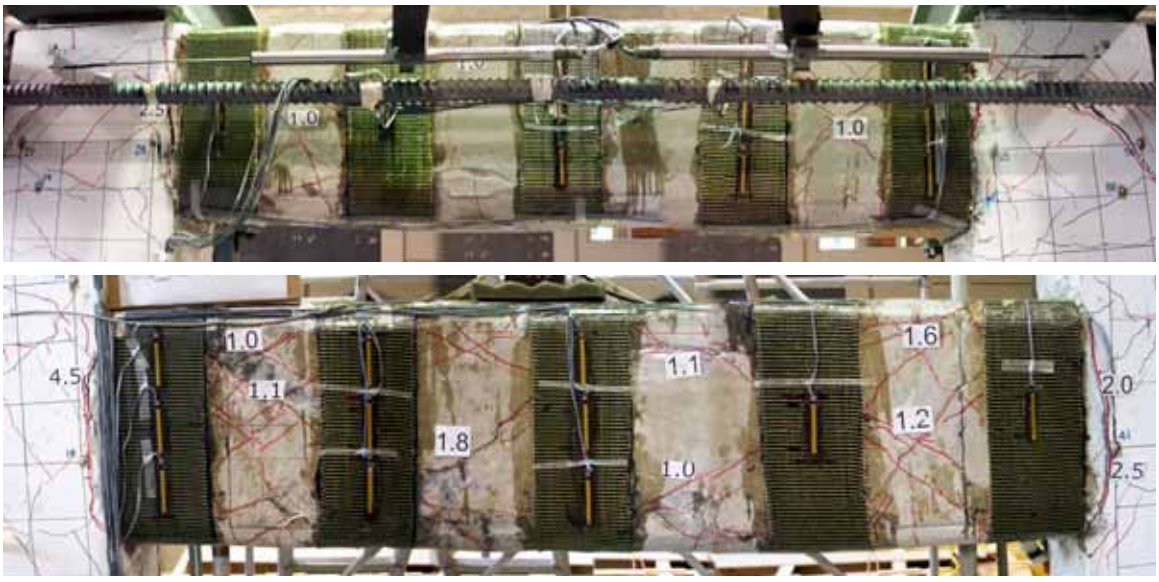

LC9: -4.0 Δ_y

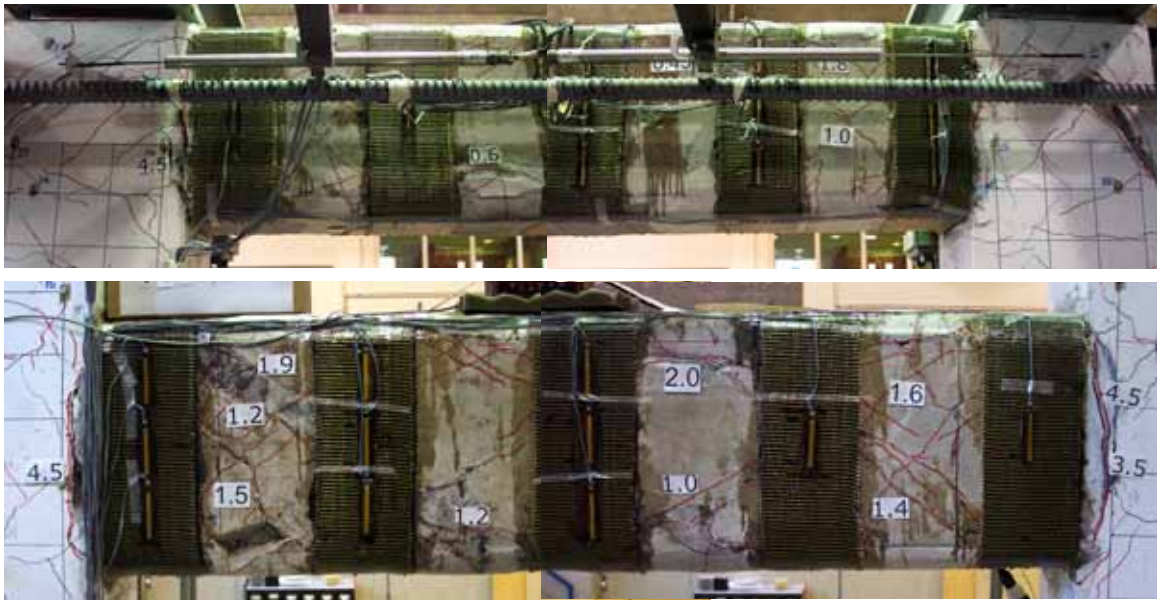

LC11: +4.0 Δ_y

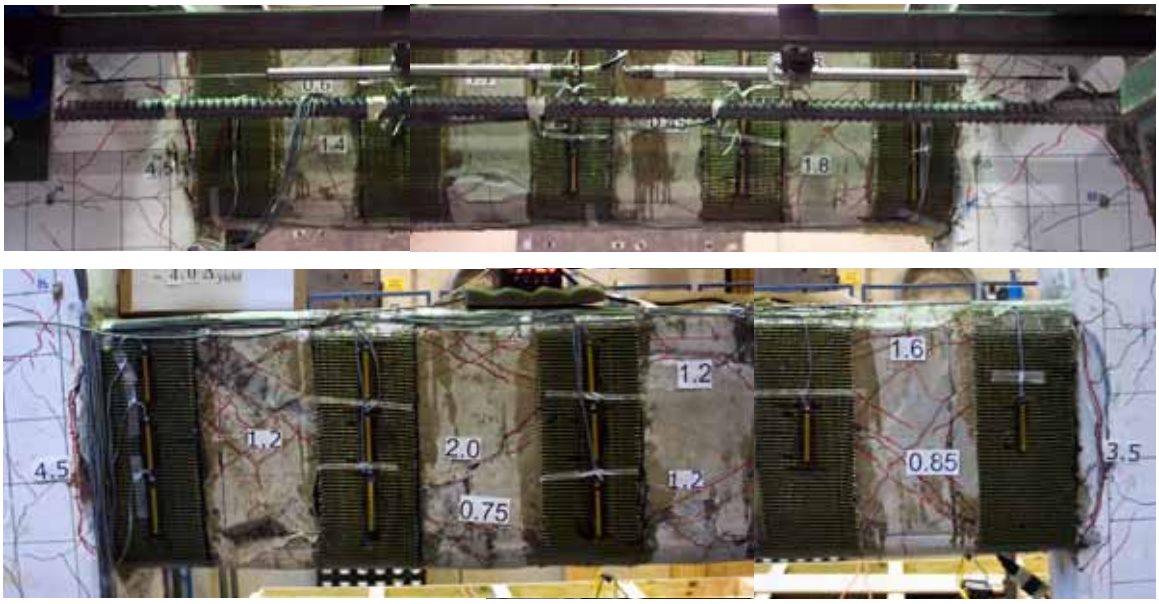

LC12: -4.0 Δ_y

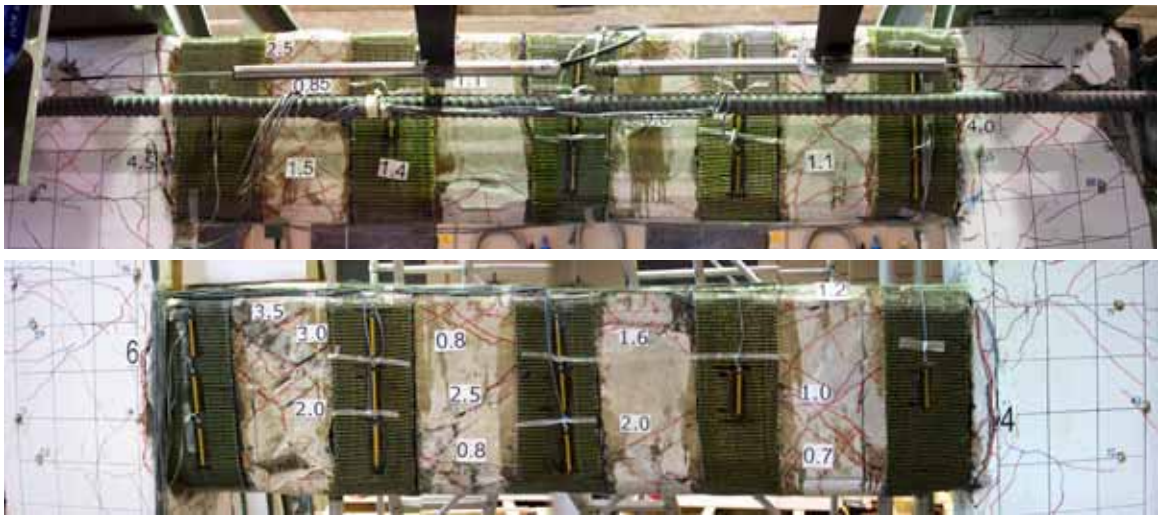

LC13: -6.6 Δ_y